The role of the TRPM4 channel in hippocampal synaptic transmission and the development of genetically-encoded tools for mapping neuronal and synaptic activity.

Dissertation

Submitted by

Brenna C. Fearey

Los Alamos, New Mexico, USA

July 3, 2020

The following evaluators recommend the admission of the dissertation:

Prof. Dr. Christian Lohr

Abteilung Neurophysiologie

Zoologisches Institut an der Universität Hamburg

Dr. Christine E. Gee

Institute of Synaptic Physiology

Center for Molecular Neurobiology-Hamburg

University Medical Center Hamburg-Eppendorf

Oral defense: September 18th, 2020

Without memory, time would be unarmed against us

John Steinbeck

Table of Contents

Table of Figures

Paper 1:

Summary

In the brain, calcium plays a crucial role in neural activity and downstream signaling pathways that can lead to long term changes to connectivity. In dysfunction calcium plays a role in the different pathways leading to cell death. In this thesis I present two projects connected to calcium signaling in neurons. In project 1, I hypothesized that the monovalent cationic transient receptor potential melastatin 4 (TRPM4) channel, which activated by internal calcium, may boost excitatory synaptic transmission in the healthy hippocampus. Using calcium imaging and electrophysiology I found no effect of the TRPM4 antagonists 9-phenanthrol and glibenclamide on synaptic transmission in hippocampal slices from healthy mice. TRPM4 is reported to contribute to disease severity in the murine experimental autoimmune encephalomyelitis (EAE) model of multiple sclerosis and to neuronal cell death in models of excitotoxicity and traumatic brain injury. In slices from wild type EAE mice, glibenclamide reduced excitatory synaptic potentials. This effect was absent in TRPM4 deficient mice. I conclude that TRPM4 plays a limited role in basal hippocampal synaptic transmission but in EAE a glibenclamide-sensitive TRPM4 effect is apparent.

It is well-established in systems neuroscience that distinct neuronal ensembles participate in the formation of memory or drive action however it remains challenging to follow or label these ensembles with high spatial and temporal resolution. Recently the tool CaMPARI was developed which

permanently photoconverts from green to red only the presence of both elevated calcium and violet

light (395 nm-405nm). CaMPARI enables marking of active neuronal however it photoconverts in low

calcium, exhibits slow kinetics and following fixation most fluorescence is lost. My collaborates and I

developed CaMPARI2 with improved brightness, higher photoconversion contrast and improved

amenability for immunohistochemical methods, including an antibody specifically against the red

CaMPARI2 species.

In addition to neuronal ensembles, synaptic ensembles are hypothesized to mediate the

changes in connectivity that occurs during learning or other plasticity-related behaviors. However, it

remains technically challenging to identify all of the active synapses in tissue. My co-authors and I

created SynTagMA, a synaptic tag for mapping activity, by targeting CaMPARI2 to the pre- or

postsynapse. All synapses active within 2 seconds before violet light illumination will be photoconverted

from green to red. PreSynTagMA can be used to discriminate between active and inactive axons.

PostSynTagMA can be used to take a snapshot of synapses active just prior to photoconversion. As

SynTagMA allows for high resolution activity mapping, we demonstrated how to identify and follow the

fluorescence of synapses over time in an automated fashion. These photoconvertible tools allow for a

new method for iteratively mapping active neurons and synapses *in vitro* and *in vivo.*

Zussammenfassung

Im Gehirn spielt Kalzium eine entscheidende Rolle bei der neuronalen Aktivität und den

nachgeschalteten Signalwegen, die zu langfristigen Veränderungen der Konnektivität führen können. Bei

Funktionsstörungen spielt Kalzium eine Rolle in den verschiedenen Bahnen, die zum Zelltod führen. In

dieser Arbeit stelle ich zwei Projekte vor, die im Zusammenhang mit der Kalzium-Signalübertragung in

Nervenzellen stehen. In Projekt 1 stellte ich die Hypothese auf, dass der durch internes Kalzium

aktivierte monovalente kationische Transientenrezeptorpotenzial-Kanal Melastatin 4 (TRPM4) die exzitatorische synaptische Übertragung im gesunden Hippocampus verstärken könnte. Mit Hilfe von Kalzium-Bildgebung und Elektrophysiologie fand ich keine Wirkung der TRPM4-Antagonisten 9-Phenanthrol und Glibenclamid auf die synaptische Übertragung in Hippocampusschnitten von gesunden Mäusen. Es wird berichtet, dass TRPM4 zur Schwere der Erkrankung im experimentellen Modell der experimentellen Autoimmunenzephalomyelitis (EAE) der Multiplen Sklerose bei Mäusen und zum neuronalen Zelltod in Modellen von Exzitotoxizität und traumatischen Hirnverletzungen beiträgt. In Schnitten von EAE-Wildtyp-Mäusen reduzierte Glibenclamid exzitatorische synaptische Potentiale. Dieser Effekt fehlte bei TRPM4-defizienten Mäusen. Ich schließe daraus, dass TRPM4 eine begrenzte Rolle bei der basalen synaptischen Übertragung im Hippocampus spielt, aber bei EAE zeigt sich ein Glibenclamid-sensitiver TRPM4-Effekt.

Es ist in der Systemneurologie gut etabliert, dass verschiedene neuronale Ensembles an der Bildung von Gedächtnis- oder Antriebsaktionen beteiligt sind, aber es bleibt eine Herausforderung, diese Ensembles mit hoher räumlicher und zeitlicher Auflösung zu verfolgen oder zu etikettieren. Vor kurzem wurde das Werkzeug CaMPARI entwickelt, das permanent nur das Vorhandensein von sowohl erhöhtem Kalzium als auch violettem Licht (395 nm-405nm) von grün nach rot photokonvertiert. CaMPARI ermöglicht die Markierung aktiver Neuronen, wandelt jedoch in kalziumarmes Licht um, weist eine langsame Kinetik auf und nach der Fixierung geht die meiste Fluoreszenz verloren. Meine Mitarbeiter und ich entwickelten CaMPARI2 mit verbesserter Helligkeit, höherem Photokonversionskontrast und verbesserter Zugänglichkeit für immunhistochemische Methoden, einschließlich eines Antikörpers, der spezifisch gegen die rote CaMPARI2-Spezies gerichtet ist.

Zusätzlich zu den neuronalen Ensembles werden synaptische Ensembles angenommen, um die Veränderungen der Konnektivität zu vermitteln, die während des Lernens oder anderer

plastizitätsbezogener Verhaltensweisen auftreten. Es bleibt jedoch technisch anspruchsvoll, alle aktiven Synapsen im Gewebe zu identifizieren. Meine Koautoren und ich schufen SynTagMA, ein synaptisches Tag zur Kartierung der Aktivität, indem wir CaMPARI2 auf die Prä- oder Postsynapse zielten. Alle Synapsen, die innerhalb von 2 Sekunden vor der Beleuchtung mit violettem Licht aktiv sind, werden von grün nach rot photokonvertiert. PreSynTagMA kann zur Unterscheidung zwischen aktiven und inaktiven Axonen verwendet werden. PostSynTagMA kann verwendet werden, um eine Momentaufnahme von Synapsen zu machen, die unmittelbar vor der Fotokonversion aktiv waren. Da SynTagMA ein hochauflösendes Aktivitäts-Mapping ermöglicht, haben wir gezeigt, wie die Fluoreszenz von Synapsen automatisch identifiziert und über die Zeit verfolgt werden kann. Diese photokonvertierbaren Werkzeuge ermöglichen eine neue Methode zur iterativen Kartierung aktiver Neuronen und Synapsen *in vitro* und *in vivo*.

Introduction

1.0 Ion channels shape signal transduction

How do neurons sense their local environments and transduce signals, like light, heat, tension, taste? Neurons are surrounded by protein-rich plasma membranes embedded with ion channels and when these channels are activated by particular stimuli, downstream signaling pathways give rise to physiological processes. These channels conduct specific ions and their opening and closing is dependent on a number of chemical, mechanical and electrical stimuli (Hille, 1987). Seminal experiments conducted by Hodgkins and Huxley in the 1950's (Hodgkin & Huxley, 1952), determined that changes in ion concentration across a membrane were responsible for action potential generation and that those changes were ion species and concentration dependent. Ion conductance in the cell is tightly regulated by expression of a number of functionally different ion channels and the local ionic

concentration gradient (Kandel, Schwartz, & Jessell, 2000, Chapter 9). Those ion channels are often anchored to a specific subcellular locale and the spatial distribution and expression pattern varies between cell types and can change depending on their current environment (Bezanilla, 2008). While one typically thinks of excitable cells when considering changes in ionic concentrations between the extra- and intracellular spaces, ion channels are also crucial for signaling in non-excitable cells. For example, voltage-dependent Ca^{2+}-activated K^+ channels are typically activated by intracellular calcium release. Activation of these channels result in hyperpolarization and increase the driving force for calcium (Nilius & Droogmans, 2001).

In the last fifty years, considerable progress has been made in describing these channels due to the advancement of patch clamp electrophysiology, single-channel recordings, and overexpression systems, which allow us to study the behavior and pharmacology of individual channels. In addition, incredible advances in cryo-electron microscopy in the last decade have made it possible to resolve the crystal structures of membrane-bound proteins, which were notoriously difficult to purify (Madej & Ziegler, 2018). While it is important to study ion channels in a "vacuum" to determine their particular properties, another direction of research has focused on studying these channels in the context of normal physiology in living tissue. These studies are crucial to understand how certain channelopathies can develop and give rise to disease.

1.1 A calcium-activated nonselective cation current

Shortly after the advent of single channel recordings in 1981 (Hamill, Marty, Neher, Sakmann, & Sigworth, 1981), the first calcium-activated non-selective cation current was described in cultured cardiac cells (Colquhoun, Neher, Reuter, & Stevens, 1981). Shortly thereafter, numerous studies described this current; referred to as either the non-selective cation current of the Ca^{2+}-activated type (NSC_{Ca}) or the calcium-activated nonselective cation current (I_{CAN}). This thesis will predominately use the

I_{CAN} nomenclature. Early studies described a current with minimal voltage sensitivity, equal permeability

to K^+ and Na^+, Ca^{2+} impermeable, activation by intracellular calcium, inhibition by intracellular

AMP>ADP>ATP and antagonism by flufenamic acid (Endo, Kurachi, & Mishina, 2000, Chapter 25; Nilius &

Droogmans, 2001; L. Donald Partridge, Müller, & Swandulla, 1994). I_{CAN} has been described in both

excitable and non-excitable cells including but not limited to epithelial cells (Popp & Gögelein, 1992),

pancreatic secretory cells (Sturgess, Nicholas Hales, & Ashford, 1986), cardiomyocytes (Guinamard et al.,

2004), and neurons (L. Donald Partridge et al., 1994). However, the channel(s) responsible for these

currents remain enigmatic. One particular superfamily of ion channels came into focus as a potential

source of I_{CAN}: the transient receptor potential (TRP) superfamily.

1.2   The transient receptor potential superfamily

In mammals, the transient receptor potential (TRP) ion channel superfamily is made up of 28

different channels split into six protein families based on their homology: canonical TRPs (TRPC),

vanilloid TRPs (TRPV), melastatin TRPs (TRPM), mucolipin TRPs (TRPMLs), polycystins TRPs (TRPPs), and

the ankyrin TRP (TRPA) (Fig. 1A) (Gees, Colsoul, & Nilius, 2010). Similar to voltage-gated channels, TRP

channels have six transmembrane (TM) domains with the pore-forming loop between TM5 and TM6.

Both N- and C-termini are intracellular. The structural and functional domains vary considerably

between TRP channels. The channels likely form tetramers and there have been reports of both

homomeric and heteromeric TRP channels (Vetter & Lewis, 2011). TRP channels are found in both

excitable and non-excitable tissues. Their function has been linked to chemo-, thermo-, and mechano-

sensation, metabolic regulation, and cell homeostasis (Gees et al., 2010). All TRP channels conduct

monovalent and divalent cations with the exception of TRPM4 and TRPM5, who only conduct

monovalent cations. TRP channels are often involved in feedback loops regulating internal calcium

concentrations (Fig. 1B-C). In 2002, the TRPM4 channel was cloned and described. It has a 25 pS

conductance, direct activation by internal Ca^{2+}, permeable to Na^+ and K^+ but not Ca^{2+}; suggestive that

TRPM4 could be the molecular identity of I_{CAN} (Launay et al., 2002). The years following provided evidence supporting TRPM4 as the molecular identity of I_{CAN}. To clearly introduce TRPM4, I will briefly discuss its characterization in the central nervous system and in pathophysiology.

1.3   Characterization of TRPM4 in overexpression models

The first study to clone TRPM4 channel found expression in numerous tissue types; the highest being heart, prostate and colon (Xu, Moebius, Gill, & Montell, 2001). HEK-293 cells overexpressing the TRPM4 clone showed higher basal calcium levels than controls and increased intracellular calcium upon exposure to high extracellular calcium. The study concluded that the channel may be permeable to calcium or at least involved in a feedback-mechanism for calcium influx. This was a first hint at possible TRPM4 channel regulation by internal calcium concentrations. A year later, another group cloned and characterized the TRPM4 channel (Launay et al., 2002). It expresses on the membrane and forms homomers in overexpressing HEK-293 cells. In whole-cell patch clamp and single channel recordings, TRPM4 is activated by >300 nM internal Ca^{2+}, has a 25 pS conductance and is permeable only to monovalent cations. Interestingly, they also report endogenous expression of TRPM4 in HEK-293 cells. The gene variant cloned in the 2002 study is named TRPM4b as it is 174 amino acids longer than the gene cloned by Xu et al (2001), which is named TRPM4a. It is hypothesized that TRPM4a is a splice variant and the TRPM4b is the full-length gene. The majority of existing studies use the full-length TRPM4b variant overexpressed in HEK-293 cells (Mathar et al., 2014). The N- and C-termini of TRPM4 contain several protein kinase-C (PKC) phosphorylation sites, two ATP-binding cassette transporter-like motifs, four Walker B sites (putatively ATP-binding), a putative phosphatidylinositol 4,5-bisphosphate (PIP$_2$), and five calmodulin-binding sites (Vennekens & Nilius, 2007) (Fig. 1C). Indeed, TRPM4 is inhibited by intracellular ATP (Nilius et al., 2005; Nilius, Prenen, Voets, & Droogmans, 2004) and channel desensitization can be rescued by PIP$_2$ (Nilius et al., 2006; Zhang, Okawa, Wang, & Liman, 2005). Calmodulin and PKC binding increase TRPM4 sensitivity to Ca^{2+} but not exclusively as mutations to all

binding sites do not prevent TRPM4 opening (Nilius et al., 2005). TRPM4 opening probability is also temperature sensitive, similar to many TRP channels (Talavera et al., 2005).

Although TRPM4 has a number of the described I_{CAN} characteristics, it should be noted that TRPM5 shares approximately 50% homology with TRPM4 and unsurprisingly the two channels share a few properties. Briefly, TRPM5, like TRPM4, is calcium-activated, selective for monovalent cations and modulated by PIP_2 (Fig. 1D). In contrast to TRPM4, TRPM5 is has a higher affinity for intracellular calcium (EC_{50} of 0.7 µM versus 20 µM of TRPM4) and is insensitive to ATP (Ullrich et al., 2005). Unlike TRPM4, TRPM5 expression is less ubiquitous. It is predominately expressed in taste receptor cells, olfactory neurons and other chemosensory tissues (Liman, 2014). To distinguish the action of these channels from each other and many others, particularly in tissue, specific and potent pharmacology is necessary.
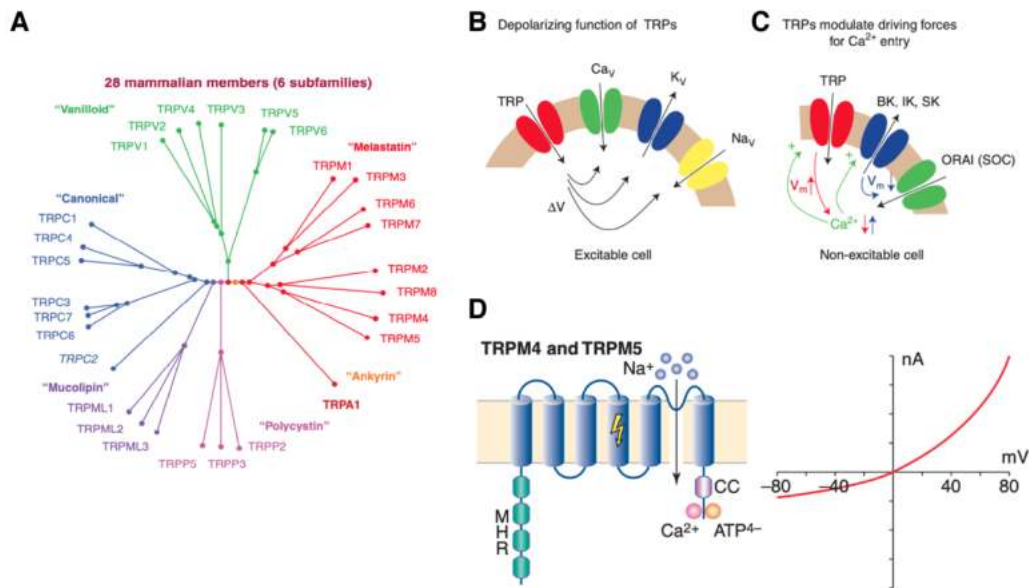
Figure 1: **The TRP family and TRPM4/5**

A) The TRP family tree B) TRP channels depolarize excitable cells by activating voltage gated channels and C) modulate driving force for calcium in non-excitable cells. Depolarization reduces calcium entry by ORAI channels. Hyperpolarization by K^+ channels increases calcium entry. This feedback loop is tightly regulated, in part, by TRP channels. D)TRPM4 and TRPM5 share 50% homology including regions on the N-termini (MHR) and the steady-state current–voltage relationship is characterized by outward rectification with slight voltage dependence (CC, coiled-coil region).

Adapted from: (Fleig & Penner, 2004; Gees et al., 2010)

1.5 Pharmacology for TRPM4

A particular challenge when studying TRPM4 is the availability of potent and specific antagonists. While overexpression studies show inhibition of TRPM4 by intracellular ATP (Fig. 2A), directly manipulating ATP concentration in the cell could have far-reaching effects on many cellular processes and likely engage multiple cellular processes, not only TRPM4 antagonism. Instead, pharmacological agents are a better option for studying TRPM4 in tissue.

Flufenamic acid (FFA) is a non-steroidal anti-inflammatory drug (NSAID), whose limited effectiveness in comparison to other NSAIDs coupled with deleterious side effects resulted in the discontinuation of its use in patients in the 1970s (Guinamard, Simard, & Del Negro, 2013). However, it found new purpose when it proved useful in the study of ion channels. Early studies describing I_{CAN} found FFA was an extremely effective antagonist for the current in multiple cell types (Endo et al., 2000; Nilius & Droogmans, 2001; L D Partridge & Swandulla, 1988). Unfortunately, FFA blocks both TRPM4 and TRPM5 currents (Ullrich et al., 2005) (Fig. 2B). In fact, FFA is an effective agonist or antagonist for numerous TRP channels, Cl^- channels, Na^+ channels and K^+ channels (reviewed in depth here: Guinamard et al., 2013). While FFA is reported to have relatively high affinity for TRPM4 (EC_{50}=2.8 μM) in comparison to other channels, its promiscuity with other channels and receptors makes it an insufficient antagonist to exclusively study TRPM4 currents (Guinamard et al., 2013).
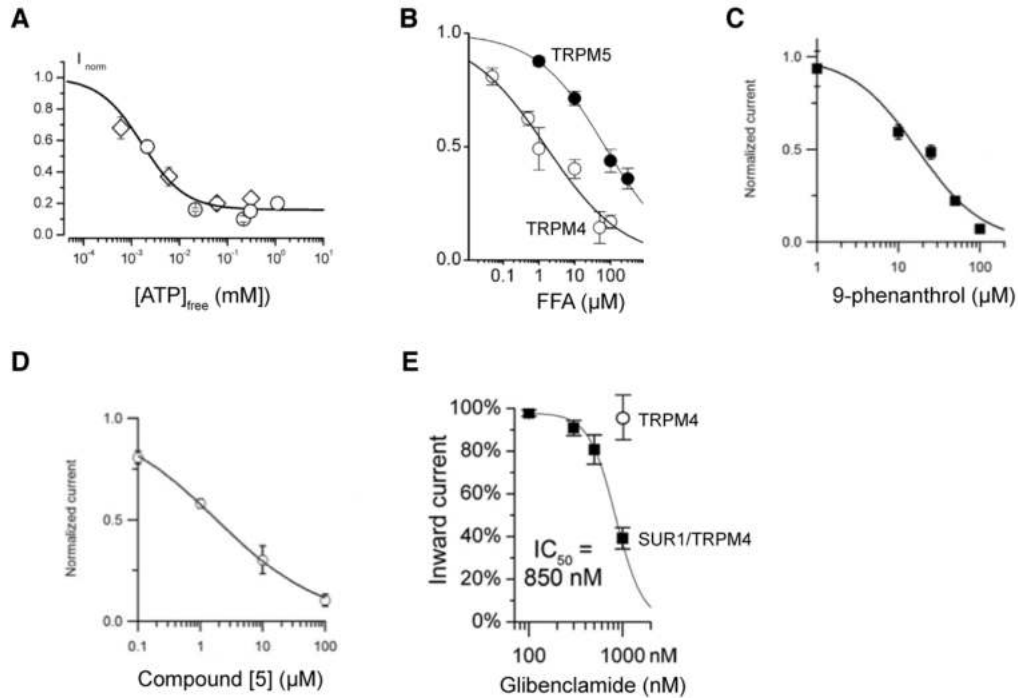
Figure 2: Pharmacology for TRPM4

Concentration-response curves for TRPM4 antagonists Normalized current amplitudes versus A) free ATP concentration. B) FFA for TRPM4 (open circles) and TRPM5 (black squares) C) 9-phenanthrol and D) compound [5]. E) Current versus glibenclamide for the SUR/TRPM4 (black squares) and TRPM4 alone (open circle). Note that the IC_{50} for SUR1/TRPM4 does not antagonize TRPM4 alone.

Adapted from: A: (Nilius, Prenen, Voets, et al., 2004), B & D: (Ozhathil et al., 2018), C: (Ullrich et al., 2005) E: (Woo, Kwon, Ivanov, Gerzanich, & Simard, 2013)

In 2008, a new compound, 9-phenanthrol, was shown to specifically antagonize TRPM4 but not

TRPM5 (Grand et al., 2008). 9-phenanthrol rapidly and reversibly inhibits TRPM4 at an IC_{50} of 20 µM and

specifically blocks native TRPM4 currents in HEK-293 cells (Fig. 2C) (Amarouch, Syam, & Abriel, 2013)

and in cardiac cells with TRPM4-like currents (C. Simard, Hof, Keddache, Launay, & Guinamard, 2013).

The majority of TRPM4 studies have used 9-phenanthrol as a selective inhibitor however it important to

note its reported off-target effects. In cardiac cells, 9-phenanthrol, at concentrations above 100 µM,

reduces L-type calcium channel currents and delayed outward rectifier potassium currents (C. Simard,

Sallé, Rouet, & Guinamard, 2012). Additional off-target effects of 9-phenanthrol include antagonism of

the calcium-activated chloride channel, TMEM16A, with an IC_{50} of 12 µM (Burris, Wang, Bulley, Neeb, & Jaggar, 2015) and activation of the calcium-activated potassium channel $K_{Ca}3.1$ (Garland et al., 2015).

Another interesting TRPM4 antagonist is glibenclamide. Glibenclamide is a sulfonylurea that targets ATP-sensitive K^+ channels (K_{ATP}). It is a commonly used as an anti-diabetic drug because K_{ATP} channels regulate insulin secretion in pancreatic cells (Ashcroft, 2005). They are hetero-octomeric channels made up of the inward-rectifier potassium channel, Kir6.2, and sulfonylurea receptor, SUR1. SUR receptors are members of the ATP-binding cassette (ABC) transporter family and SUR1 acts as an ion channel regulator rather than a transporter (Aittoniemi et al., 2009). Glibenclamide was first linked to TRPM4 blockade in a study of (Demion, Bois, Launay, & Guinamard, 2007). Sino-atrial-node cells express TRPM4 and FFA and glibenclamide (both at 100 µM) block TRPM4-like I_{CAN} in sino-atrial-node cells and TRPM4 overexpressing HEK-293 cells. The block of TRPM4-like currents by glibenclamide suggests a possible interaction of TRPM4 with SUR1. In 2013, SUR1 amd TRPM4 were shown to forms a heteromeric channel (Woo et al., 2013). Interestingly, in COS-7 cells overexpressing either SUR1/TRPM4 or TRPM4 alone, glibenclamide antagonizes the SUR1/TRPM4 channel more efficiently than TRPM4 alone (IC_{50} of 850 nM versus ~100 µM, Fig. 2E). The coupling of TRPM4 and SUR1 has been predominately associated with disease states and will be reviewed in-depth later in this thesis. Although glibenclamide is a TRPM4 antagonist, it will also target K_{ATP} channels, whose action is hyperpolarizing whereas TRPM4 is depolarizing and its potency is modulated by its channel composition.

Recently, compound [5], a chemical analogue of flufenamic acid, showed high specificity and selectivity for TRPM4 (Ozhathil et al., 2018). Compound [5] has an IC_{50} of ~1 µM for TRPM4 (Fig. 2D). Electrophysiology and radio-ligand binding assays showed high specificity of compound [5] for TRPM4. Compound [5] showed no to little interaction with these channels: TRPM5, TRPM7, TRPM8, TRPV1, TRPV6, $GABA_A$-α1 subunit, *N*-methyl-D-aspartate (NMDA) receptor, L-type and N-type Ca^{2+} channels, and

hERG channels, even at concentrations 10-100 times higher than the IC_{50} for TRPM4. This was the first evidence of what appears to be a truly selective and potent inhibitor specifically for the TRPM4. Further studies will tell whether this inhibitor retains its crown as a selective and potent TRPM4 antagonist. Compound [5] is available commercially as CBA (4-Chloro-2-[[2-(2-chlorophenoxy)acetyl] amino]benzoic acid). Few studies, as of now, have used CBA to study TRPM4 channels (Bianchi, Smith, & Abriel, 2018; O'Malley, Seibt, Chin, & Beierlein, 2020), however I expect this to rapidly change in the coming years. The crystal structures of mouse and human TRPM4, with or without calcium, ATP and decavanadate were recently resolved and I expect further development of precise pharmacology for the channel in the future (Autzen et al., 2017; Duan et al., 2018; Guo et al., 2017; Winkler, Huang, Sun, Du, & Lü, 2017).

1.6   TRPM4 in the nervous system

1.6.1 Sensation

TRP channels are associated with numerous sensory processes and TRPM4 has been linked to olfaction and taste (Vetter & Lewis, 2011). Olfaction is a critical sensory modality that conveys information important for mating via pheromones, food, and stress. The olfactory system transduces these chemical signals to give rise to relevant behaviors. It can be split into the main and accessory olfactory systems (Bakker & Leinders-Zufall, 2015). Briefly, the vomeronasal sensory neurons (VSNs) of the vomeronasal organ (VNO) sense the chemicals and send their axons and synapse onto the mitral neurons of the accessory olfactory bulb (AOB), who project to higher brain areas (Bakker & Leinders-Zufall, 2015). AOB mitral neurons can undergo prolonged excitation and persistent firing (PF). Strong synaptic stimulation drives PF lasting up to several minutes in AOB mitral neurons. PF can also be induced by $GABA_A$ blockade, likely due to a local inhibitory network controlling AOB firing. Intracellular calcium chelation, FFA and 9-phenanthrol reduces PF in AOB neurons and these neurons also express

TRPM4; suggesting that TRPM4 is at least partially responsible for PF in these cells (Shpak, Zylbertal, Yarom, & Wagner, 2012).

Upstream of the AOB, the VNO also expresses TRPM4. Specifically, vomeronasal sensory neurons express TRPM4 in the somata and dendrites with little to no expression in the axons (Eckstein et al., 2020). This expression pattern was determined using a TRPM4-IRES-Cre knock-in mouse line crossed with a tauGFP reporter line, which reports recent promotor activity. Interestingly, differential expression levels in female mice is linked to the estrus cycle with the highest expression occurring at the proestrus and estrus stages. TRPM4 seems to be involved in the transduction of chemical information specifically related to mating and pheromones. Future study will have to determine the physiology of TRPM4 at these neurons.

Although TRPM5 remains the better studied channel in in taste sensation, TRPM4 has also been linked to taste (Dutta Banik, Martin, Freichel, Torregrossa, & Medler, 2018). Taste receptor cells sit inside of the taste buds on the tongue. Type II receptor cells detect umami, sweet and bitter stimuli. Specifically, in these cells, taste is transduced by G-protein coupled receptor (GPCR) activation of the phospholipase C pathway (PLC), which triggers calcium release from internal stores. The resulting rise in internal calcium, in turn, triggers TRPM5 activation and drives further depolarization (Guinamard, Sallé, & Simard, 2011). Although it is well-established that TRPM5 is crucial for detection of the bitter, sweet and umami tastes, there remained the possibility of TRPM4 in mediating taste transduction. Using careful pharmacology, immunohistochemistry, single and double genetic deletion of TRPM4 and TRPM5, it was shown that both channels mediate detection of taste in type II cells (Dutta Banik et al., 2018). Double knock-out of these channels eliminated taste-evoked Na^+ currents and behaving animals show an absence of sweet/umami/bitter taste detection. The rise time of TRPM5 is faster than TRPM4, suggesting that TRPM4 requires a higher internal calcium concentration to open; matching previous

single channel calcium sensitivity measurements of TRPM4/5 (Dutta Banik et al., 2018; Ullrich et al., 2005) Taste perception is also modulated by temperature and both TRPM5 and TRPM4 are similarly activated by heat (Talavera et al., 2005).

1.6.2 preBötzinger Complex

The role of TRPM4 in synaptic transmission and bursting is probably best described in the preBötzinger Complex (preBötC) compared to other brain areas. Breathing is a fundamental behavior that is generated by a complex network of cellular, molecular and network mechanisms. The preBötC is a medullary microcircuit at the core of the central pattern generator responsible for inspiration. One well-studied subpopulation of neurons in the preBötC are the glutamatergic neurons, whose precursors express developing brain homeobox 1 (DBX1). DBX1$^+$ neurons have rhythmic membrane properties (C. A. Del Negro, Funk, & Feldman, 2018). How inspiration is generated has been a subject of debate and one popular hypothesis includes the existence of pacemaking neurons in the preBötC. The proposed mechanism for pacemaker cells is the presence of cell-intrinsic currents including I$_{Na+}$ and I$_{CAN}$. Blockade of those currents ceased bursting but enhancing of cell excitability was enough to recover this block (C. a. Del Negro et al., 2005). Rather than pacemakers driving inspiratory rhythm generation, accumulating evidence supports an emergent network burstlet model, in which a relatively quiet network becomes increasingly excited via spontaneous activity of a few locally connected preBötC neurons. This activity eventually drives inspiratory bursting with an underlying 20-40 mV drive potential mediated by I$_{CAN}$ (C. A. Del Negro et al., 2018). In preBötC neurons, intracellular PIP$_2$ rescues I$_{CAN}$ desensitization, I$_{CAN}$ is blocked by FFA, 9-phenanthrol, and ATP, it is activated downstream of NMDA and mGlu5 receptors, I$_{CAN}$ conductance is ~24 pS, and I$_{CAN}$ is activated by calmodulin and may be downstream of IP$_3$-modulated endoplasmic reticulum (ER) calcium release (Crowder et al., 2007; Mironov, 2008, 2013; Pace, Mackay, Feldman, & Del Negro, 2007). These features point strongly at TRPM4 as the molecular candidate underlying the I$_{CAN}$ inspiratory drive potential but, only recently, two studies directly studied the impact

of TRPM4 knock-out or knock-down on inspiration *in vivo* and inspiratory bursting *in vitro* (Koizumi et al., 2018; Picardo et al., 2019). They determined that indeed, TRPM4 is responsible for the drive potential in DBX1+ neurons in the preBötC. Knock-down of TRPM4 increased breathing frequency and decreased volume of breath leading to gasping and sometimes death. Both studies conclude that although TRPM4 currents are crucial to inspiratory bursting, they do not drive the rhythmogenesis of those bursts. They suggest rather that TRPM4 contributes to the first stage of bursting.

1.6.3 Basal ganglia

In the substania nigra, tonic and phasic dopamine release are thought to underlie behaviors like motivation, movement and reward learning (Cox & Witten, 2019). Neurons in both the substantia nigra pars compacta (SNc) and the substantia nigra pars reticulata (SNr) exhibit tonic and burst firing. The sustained depolarization required for burst firing is hypothesized to be mediated by I_{CAN}. It remains unclear what channels are responsible for these currents and the variation could be in part due to anatomical differences. In the SNr, H_2O_2 and FFA modulate burst firing and introducing TRPM2-specific antibodies intracellularly blocked burst firing (Lee, Machold, Witkovsky, & Rice, 2013). However, the authors acknowledge that the described current fits well with TRPM4 features and that TRPM4 has been implicated in near identical currents in the SNc. In the SNc, TRPM2 and TRPM4 mRNA is expressed specifically in the GABAergic-positive neurons and FFA and 9-phenanthrol reduce tonic and burst firing (Mrejeru, Wei, & Ramirez, 2011).

1.6.4 Hippocampal formation

The hippocampal formation includes the hippocampus, entorhinal cortex, presubiculum, parasubiculum and subiculum (Andersen, Morris, Amaral, Bliss, & O'Keefe, 2006, Chapter 3). The entorhinal cortex (6-layers) bidirectionally connects the hippocampus to cortical areas (Valero & de la Prida, 2018). The hippocampus; a tri-synaptic circuit consisting of the dentate gyrus (DG), CA3, and CA1;

is one of the most highly studied structures in the brain crucial to learning and memory. Milner's work

with patient HM, who could no longer form new declarative memories, demonstrated the importance of

the hippocampus in memory and the discovery of long-term potentiation (LTP) gave a potential

mechanism for learning and memory (Andersen et al., 2006, Chapter 1; Bliss & Lømo, 1973). Since then,

there have been thousands of studies describing types of LTP, necessary molecular components for its

expression, and linking LTP to behavior (Nicoll, 2017). One required component for the expression of LTP

is calcium-dependent depolarization at the postsynaptic neuron (Lynch, Larson, Kelso, Barrionuevo, &

Schottler, 1983).

Being activated by intracellular calcium and having a slight voltage dependence at positive

potentials suggests that TRPM4 could contribute to the expression of synaptic plasticity by boosting

depolarization. In TRPM4 knock-out mice, theta-burst LTP is impaired and high-frequency LTP is partially

impaired (Menigoz et al., 2016). The theta-burst LTP phenotype could be rescued in TRPM4 knock-outs

by depolarizing the postsynaptic neuron; suggesting that TRPM4 boosts depolarization downstream

from NMDARs. No differences in spine density, dendritic complexity, input/output curves, and basic cell

parameters were reported between wild-type and TRPM4 knock-out animals. Another study from the

same group showed that when LTP is induced using implanted electrodes *in vivo*, LTP in TRPM4 knock-

out rats decay faster in comparison to wild-type animals (Bovet-Carmona et al., 2018). Additionally,

TRPM4 knock-out rats have a weak albeit specific memory impairment in the Barnes maze. Knock-out

animals perform worse than control animals, as they revisited holes more often and failed to learn new

escape tunnel locations. These all indicate impairments in working-memory and spatial reference,

although they did not perform differently than wild-type rats in the Morris water maze. Finally, low-

frequency stimulation of the Schaffer collaterals using implanted electrodes *in vivo*, causes a delayed

and less pronounced blood oxygenation levels in the target regions compared to wild-type animals

(Bovet-Carmona et al., 2019). These are the only studies of TRPM4 in the hippocampus.

Expanding the search for TRPM4-like currents in the hippocampal formation to include the keyword I$_{CAN}$, I found a number of studies focused on intrinsic excitability and persistent firing. While the identity of I$_{CAN}$ in some brain areas like the preBötC focused predominately on TRPM4, in the hippocampus the TRPC channel family was hypothesized to mediate I$_{CAN}$ currents, specifically related to persistent firing.

Persistent firing (PF) is defined by prolonged activity of the postsynaptic neuron after an input is finished, typically in the presence of neuromodulator. It is thought to be a cellular mechanism for short-term memory formation (Debanne, Inglebert, & Russier, 2019; Vetter & Lewis, 2011, Chapter 31). In acute slice preparations of hippocampus and entorhinal cortex, carbachol-driven PF has been described in CA1, CA3, and medial entorhinal cortex (Arboit, Reboreda, & Yoshida, 2020; Egorov AV, Hamam BN, Fransen E, Hasselmo ME, & AA., 2002; Jochems & Yoshida, 2013; Knauer, Jochems, Valero-Aracama, & Yoshida, 2013; L. Donald Partridge & Valenzuela, 2000; Yoshida, Knauer, & Jochems, 2012). Most studies link TRPC3/4/5 channels to the depolarizing current underlying PF as it is blocked by FFA and the nonspecific TRP/TRPC antagonist SKF96365 (Singh, Hildebrand, Garcia, & Snutch, 2010; Tai, Hines, Choi, & MacVicar, 2011). Recently, it has become evident that TRPC channels may not exclusively carry I$_{CAN}$. In medial entorhinal pyramidal cells, carbachol-induced PF is not eliminated in either TRPC1/4/5 triple knock-out or complete TRPC1/2/3/4/5/6/7 hepta knock-out mice (Egorov et al., 2019). Most antagonists used to study PF are non-specific; i.e. FFA and the TRPC antagonist, SKF96365, which has not been tested for off-target effects on TRPM4. In layer 5 neurons of the entorhinal cortex, gabazine-induced bursting was reduced by 9-phenanthrol but not SKF96365. The reduction in bursting by 9-phenanthrol was more pronounced when puffed close to the soma (E. C. Lin, Combe, & Gasparini, 2017). In general, the underlying ion channel(s) responsible for I$_{CAN}$ involved in PF in the hippocampal formation remains unknown but studies in other brain areas hint at a role of TRPM4.

1.6.5 Prefrontal cortex & thalamus

Persistent firing in the presence of neuromodulators, including carbachol, has also been described in the prefrontal cortex and a component of PF is the slow afterdepolarization (sADP) (Haj-dahmane & Andrade, 1998; Yan, Villalobos, & Andrade, 2009). In layer 5 pyramidal neurons of the mouse prefrontal cortex TRPM5, not TRPM4, was found to modulate at least 40% of the current responsible for sADP (Lei et al., 2014). Interestingly, 9-phenanthrol reduces sADP in wild-type and TRPM4 knock-out mice indicative of clear off-target effects of 9-phenanthrol. TRPM4 is expressed predominately at the soma and primary apical dendrite of excitatory and inhibitory neurons in layer 2/3 of the mouse prefrontal cortex and TRPM4-like currents are blocked only when 9-phenanthol is puffed at the proximal portion of these neurons (Riquelme et al., 2018).

Slow rhythmic activity in the thalamocortical system has been linked to sleep spindle generation, plasticity and memory consolidation (Beenhakker & Huguenard, 2009; Diekelmann & Born, 2010). Neurons in the thalamic reticular nucleus (TRN) generate this slow rhythmic firing and there is some evidence for it being supported by I_{CAN} (Crunelli & Hughes, 2010). In the TRN, a subset of neurons display PF and the proportion of neurons displaying this behavior is increased when small-conductance calcium-activated K^+ (SK) channels are blocked (O'Malley et al., 2020). The initial generation of PF is dependent on calcium influx via T-type Ca^{2+} channels. Although TRPC channels have long been implicated in PF, TRPC3 and TRPC1/4/5/6 quadruple knock-out revealed no elimination of PF in the TRN. Instead, PF depolarization is sustained by TRPM4 activation. However, it cannot be ruled out that the TRPM4-dependent effect on PF may be due to off-target effects of 9-phenanthrol, glibenclamide or CBA but the consistent elimination of PF by all three TRPM4 antagonists is promising. Again, I_{CAN}, previously thought to be mediated by TRPCs in these brain areas, may involve TRPM4 as well.

1.6.6 Cerebellum

The cerebellum shows relatively high mRNA expression of TRPM4 in the Allen Brain Atlas *in situ* hybridization and Purkinje cells express TRPM4 and TRPM5 in the soma and dendrites. Following either a brief burst of depolarizing steps or burst activation of climbing fiber synapses, Purkinje cells exhibit an inward current called DISC (depolarization induced slow current), which may be mediated by I_{CAN} (Shin, Kim, Worley, & Linden, 2009). DISC is blocked by 9-phenanthrol, glibenclamide and FFA but TRPM4 or TRPM5 single knock-out or a TRPM4/5 double knock-out reveals that DISC is specifically but only partially (~40%) mediated by TRPM4. The partial block of DISC is not due to complete TRPM4 knock-out as acute knock-down also only partially blocks DISC (Y. S. Kim et al., 2013).

Another recent study found a role of TRPM4 in another cerebellar cell type, the granule cell (GrC). Granule cells receive input from the mossy fiber cells and their axons make up the parallel fibers (Kandel et al., 2000). GrCs display regular non-adapting spiking behavior however a new modeling study suggests that GrCs may exhibit other firing patterns when given long (2 second) depolarizing current injections (Masoli et al., 2017). A follow-up study tested the model experimentally and found three types of firing behavior in these cells: non-adapting, adapting and accelerating. 9-phenanthrol only blocked firing in accelerating-type cells. Accelerating has a similar phenotype as that for persistent firing. Interestingly, the differentiation of spiking behavior is only apparent when the mossy fibers are driven at low frequencies, i.e. ~20 Hz (Masoli, Tognolina, & Angelo, 2019).

1.7 TRPM4 in pathophysiology

Above, I described the diverse signaling processes that TRPM4 has been linked to in normal physiology and it is unsurprising that TRPM4 is involved in a pathophysiology as well. TRPM4 mutations, including both gain and loss of function variants, have been found in patients with progressive familial heart block and Brugada syndromes (Guinamard et al., 2015). TRPM4 has also been linked to some

cancers and tumorigenesis (Gao & Liao, 2019). However, the focus of this thesis is the nervous system and I will not go into further details on these disorders.

1.7.1   Central nervous system injury

Injury to the central nervous system (CNS) can arise from acute traumas, often by blunt force, leading to hemorrhage, edema (i.e. brain swelling), ischemia, and secondary injury events. Traumatic brain and spinal cord injuries effect a broad swath of the population; emphasizing the importance of preclinical and clinical studies on the mechanisms underlying both the acute and long-term effects of such trauma (Ghajar, 2000). TRPM4 has been extensively implicated in types of acute brain injury.

Brain injury can be split into primary and secondary injury. Generally, it's thought that clinical intervention for primary injury is not feasible however intervention is possible for secondary injury. Secondary injury includes cerebral edema and contusion expansion and are considered to be potentially more damaging than the initial event (Jha et al., 2020; Jha, Kochanek, & Simard, 2019). Brain swelling and hemorrhage trigger a number of cellular and molecular pathways that ultimately can lead to cell death. TRPM4 sensitivity to Ca^{2+} is facilitated by ATP depletion, which typically occurs when a cell enters a depleted metabolic state that accompanies accidental necrosis; a form of cell death (Nilius et al., 2005; J. M. Simard, Woo, & Gerzanich, 2012). TRPM4 is also strongly activated by the reactive oxygen species (ROS), H_2O_2 (Leiva-Salcedo, Riquelme, Cerda, & Stutzin, 2017a; Simon et al., 2010). Whereas TRPM4 usually desensitizes shortly after exposure to high internal calcium, H_2O_2 blocks this desensitization and the H_2O_2-induced TRPM4-dependent current is blocked by both FFA and glibenclamide. If TRPM4 is continuously active when the cell is in state of severe ATP depletion and ROS are being generated, this could result in chronic depolarization of the cell. Chronic depolarization can lead to cell swelling and ultimately oncotic cell death. In COS-7 cells, TRPM4 overexpression coupled with ATP depletion leads to cell swelling, blebbing and oncotic death (Gerzanich et al., 2009).

1.7.1.1 The TRPM4/SUR1 channel and brain injury

In 2001, a SUR1-NSC$_{Ca}$ current (i.e. I$_{CAN}$) was described in astrocytes exposed to sodium azide, a metabolic toxin that induces chemical hypoxia (Mingkui Chen & Marc Simard, 2001). This current was activated by intracellular Ca^{2+} and ATP depletion and could be blocked by glibenclamide (M Chen, Dong, & Simard, 2003). SUR1 is the regulatory subunit that associates with either the Kir6.1 or Kir 6.2 subunits to form the K$_{ATP}$ channel (Karschin, Ecke, Ashcroft, & Karschin, 1997). However, KATP channels would cause hyperpolarization and to generate the SUR1-NSC$_{Ca}$ current, SUR1 likely couples with a different channel (Fig. 3).
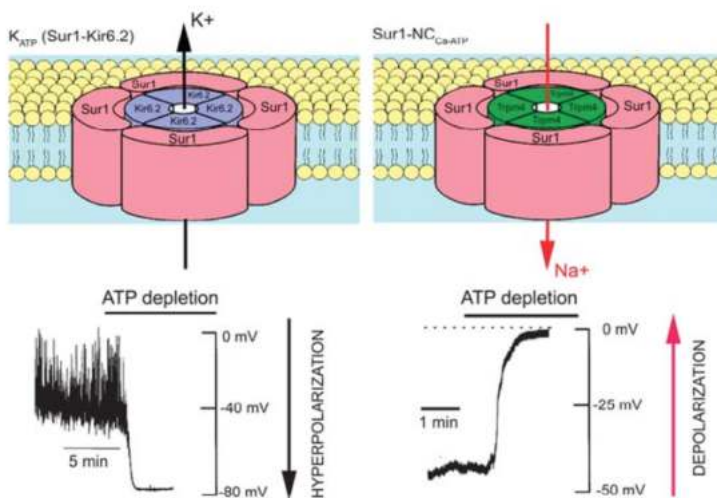
Figure 3: Opposing actions of SUR1 coupling to either Kir6.2 or NSC$_{Ca}$/TRPM4

The K$_{ATP}$ channel (SUR1/Kir6.2) hyperpolarizes upon ATP depletion as opposed to the SUR/TRPM4, which depolarizes upon ATP depletion.

Adapted from: (J. M. Simard, Woo, Schwartzbauer, & Gerzanich, 2012)

In a rodent model for stroke, SUR1 is upregulated at the sites of injury in neurons (NeuN+), astrocytes (GFAP+) and capillary endothelial cells (J. M. Simard et al., 2006). Interestingly, in this study, neither Kir6.1 nor Kir6.2 are upregulated with the SUR1 subunit; suggesting that indeed, SUR1 couples with another channel particularly when there is an injury. Neuron-like cells freshly dissociated from injury sites express a functional SUR1-NSC$_{Ca}$ current that is blocked by glibenclamide. Finally, using glibenclamide as a treatment reduced injury size and edema in a rodent model for stroke. Unsurprisingly, the potential molecular partner of SUR1 in the SUR1-NSC$_{Ca}$ heteromer, would be TRPM4.

In a similar study as described above, TRPM4 is upregulated in a rodent model of spinal cord injury

(Gerzanich et al., 2009). Although TRPM4 upregulation was visible in many cell types at the core injury

site, outside of the core TRPM4 expression was restricted to capillaries. The extent of injury was

alleviated by antisense TRPM4, TRPM4 knock-out and FFA. These studies together implicate the

existence of a SUR1/TRPM4 channel.

Indeed, using co-immunoprecipitation and FRET, a process in which one fluorophore's (the donor)

emission will excite the acceptor fluorophore, if the acceptor is within approximately 10 nanometers of

the donor, SUR1 and TRPM4 were shown to co-associate in both cell culture overexpression systems

and in tissue (Woo et al., 2013). The channel exhibited the classic hallmarks of I_{CAN}/TRPM4: 23-25 pS

conductance, activation by internal Ca^{2+} and ATP depletion. Interestingly, the SUR1/TRPM4 heteromer is

antagonized by lower concentrations of glibenclamide (~480nM) than TRPM4 alone (~100 µM). Further,

the heteromer confers a higher sensitivity to ATP and Ca^{2+} than TRPM4 alone. It should be noted that all

existing studies confirming association of SUR1 and TRPM4 come from the same lab and another lab has

disputed the SUR1/TRPM4 association using FRET as well (Sala-Rabanal, Wang, & Nichols, 2012).

SUR1/TRPM4 channel expression is upregulated in spinal cord injury, traumatic brain injury,

ischemia, hypoxia, and HIV infection (Jha et al., 2020; Leiva-Salcedo, Riquelme, Cerda, & Stutzin, 2017b;

Li et al., 2020; Tosun et al., 2013). The cell types in which the SUR1/TRPM4 channel is shown to be

expressed includes astrocytes, microglia, and endothelial cells (Kurland et al., 2016; Stokum et al., 2018).

In neurons, the Simard lab has reported upregulation of SUR1 in NeuN+ cells from both rodents and

humans and presumably there would be corresponding TRPM4 expression in those cells, however this

remains to be shown (Martínez-Valverde et al., 2015; J. M. Simard et al., 2006). In a model of blunt force

hippocampal injury, SUR1 was upregulated diffusely in the hippocampus and glibenclamide reduced

expression of activated caspase-3 (a marker for cell death) compared to untreated. The spatial learning

impairment seen in controls was alleviated in glibenclamide-treated animals (Patel, Gerzanich, Geng, &

Simard, 2010).

1.7.2 Multiple Sclerosis

Multiple sclerosis (MS) is a chronic neuroinflammatory disease of the brain and spinal cord that

effects approximately 2.5 million individuals worldwide (Compston & Coles, 2008). The disease onset is

rather young, on average 30 years of age, and therefore incurs a heavy burden on healthcare and

economy. The pathogenesis begins with a CNS inflammatory cascade, predominately caused by auto-

activated T-cells against myelin and myelin-making oligodendrocytes. These T-cells manage to cross the

blood-brain-barrier (BBB) and drive local inflammatory responses resulting in lesions; characterized by

demyelination, gliosis, and neurodegeneration (Dendrou, Fugger, & Friese, 2015). The presence of

lesions is used as a diagnostic tool in MS patients. Determining the mechanisms of disease progression

remains at the heart of MS research and it is thought that inflammation and neurodegeneration

together drive this progression. Presently there is no cure for MS and although the use of

immunomodulators can reduce relapse frequency, it does not appear to prevent disease progression.

This hints that our understanding of the underlying disease mechanisms is still lacking and that the

immune system may not be the only driver of MS. The underlying cause(s) of MS remain unclear but

genetic susceptibility in combination with environmental factors seem to influence disease penetrance

(Dendrou et al., 2015). However, it is difficult to experimentally test the role of a particular gene or

environmental factor on MS disease progression when working with patients. This led to the

development of an animal model for MS called experimental autoimmune encephalomyelitis (EAE)

(Glatigny & Bettelli, 2018). A myelin-related protein and a pathogen is injected, and an inflammatory

response is triggered. The resulting autoimmune response specifically causes axonal damage and

neurological deficits, mimicking MS in humans. Although there is more than one EAE model, the most

common injects myelin-oligodendrocyte glycoprotein (MOG); a protein that is expressed on the CNS

myelin surface and T-cells reactive to this protein have been found in MS patients (Raddassi et al., 2011). MOG-induced EAE leads to a chronic disease phenotype in C57BL/6 mice.

Dysregulation of ion channel expression is a prominent feature of MS (Schattling, Eggert, & Friese, 2014). Although ion channels are often associated with excitable cells, like neurons, they also play a fundamental role in non-excitable cells by tightly controlling ionic gradients across the membrane and consequently influence regulatory mechanisms in the cell (Nilius & Droogmans, 2001). Changes to expression and distribution of a number of ion channels has been described in MS. Unsurprisingly, in MS these changes can be found in immune cells, neuronal and glial cells and at the BBB and have been linked to potential MS disease mechanisms. One interesting channel, that has been reported in many of these cell types is TRPM4.

In a mouse model of multiple sclerosis, knock-out of TRPM4 was protective against disease progression severity (Schattling et al., 2012) (Fig. 4). TRPM4 protein is upregulated in mouse spinal cord neurons and axons and in active lesions from MS patients. Channel deletion does not alter the immune response under EAE suggesting that TRPM4-mediated action is independent of immune response to EAE. Instead, TRPM4 may contribute to disease progression by exacerbating excitotoxicity. In a glutamate excitotoxicity assay using hippocampal neurons from TRPM4 knock-out mice were less susceptible to cell swelling and death in comparison to the wild-type (Fig. 4B-C). Finally, glibenclamide, a non-specific TRPM4 antagonist, replicates the protective effects of TRPM4 knock-out in clinical severity and disease progression.
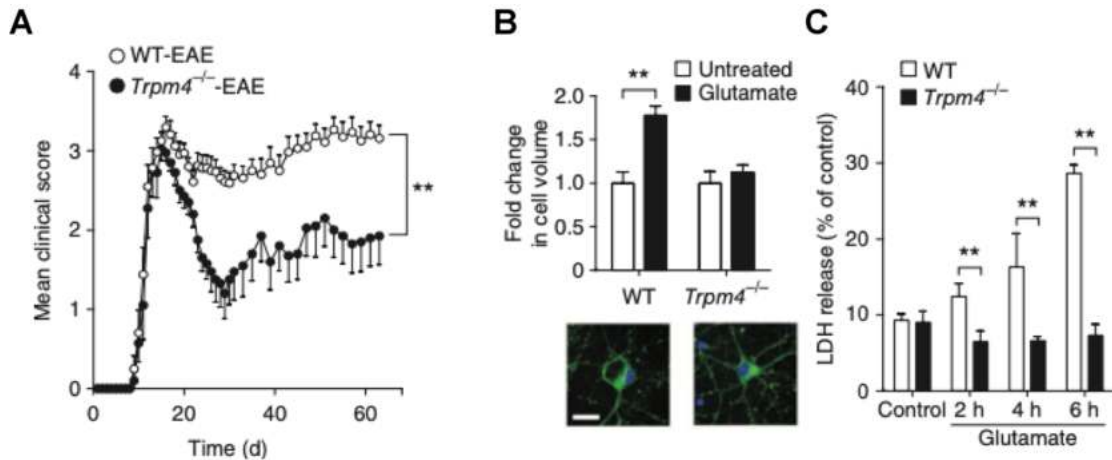
Figure 4: TRPM4 in EAE

A) Disease progression in a mouse model for multiple sclerosis (EAE). TRPM4 knock-out mice partly recover from EAE in comparison to wildtypes. B) In a glutamate excitotoxicity assay, wildtype neurons increase in cell volume but TRPM4 knockouts retain their size. The presence of lactate dehydrogenase (LDH) release is a measure of cell integrity, which is compromised in continued presence of glutamate in wild-type but not TRPM4 knock-out mice.

Adapted from: (Schattling et al., 2012)

A few additional studies have since expanded on these findings. They show that SUR1 in addition to TRPM4 expression is upregulated in EAE (Bianchi et al., 2018; Gerzanich et al., 2017; Makar et al., 2015). Blocking TRPM4 with 9-phenanthrol, glibenclamide or CBA reduces cell death in a glutamate excitotoxicity assay. Similar to TRPM4 knock-out, knock-out of SUR1 or treatment with glibenclamide reduces disease severity in EAE. SUR1/TRPM4 channels are upregulated; predominately in reactive astrocytes (Gerzanich et al., 2017; Makar et al., 2015). Unlike the study from Schattling et al (2012), these studies report peripheral immune cell infiltration of the CNS and an increase in pro-inflammatory cytokine production in spinal cord from EAE wild-type animals. The authors hypothesize that the action of SUR1/TRPM4 in EAE is predominantly via reactive astrocytes, who regulate pro-inflammatory cytokine excretion (TNF alpha, NOS2). The exact role of TRPM4 in MS and EAE remains unclear but it is evident that its activation is involved in molecular pathways driving disease progression in MS.

1.8 Calcium signaling in neurons

The previous sections dealt namely with the TRPM4 ion channel and its role in a number of calcium-dependent cellular processes. Many ion channels, including TRPM4, either directly or indirectly mediate calcium influx/efflux. The downstream action of calcium, as a secondary messenger, can lead to changes in the metabolic state, gene expression, protein regulation, and post-transcriptional protein modification among many other critical functions (Clapham, 2007). What's more is that these processes are autoregulatory as calcium can both activate and consequently stop these processes in a calcium-concentration dependent manner. For this reason, calcium dynamics can inform us about the activity status of a cell.

Figure 5 illustrates the numerous sources of calcium in a neuron, although it ignores the complex anatomy of a neuron. These include voltage-gated calcium channels (VGCCs), ligand-gated receptors, and store-operated calcium channels. VGCCs are highly selective for calcium and are split into L-, P/Q-, N-, R-, and T-type channels (Simms & Zamponi, 2014). Their distribution depends the cell type and compartment but in hippocampal pyramidal neurons, L- and R-type VGCCs are found at the dendritic spines although the exact composition varies spine to spine (Bloodgood & Sabatini, 2007). More generally, VGCCs are responsible for action potential generation and back-propagation into the dendrite (Jaffe et al., 1992; G. Stuart, Spruston, Sakmann, & Hausser, 1997). NMDA receptors are voltage-dependent ionotropic glutamate receptors and sit predominately at the post-synapse. The calcium influx through NMDARs has been linked to numerous processes associated with mechanisms of synaptic plasticity and NMDAR-dependent calcium influx has been shown to drive activity-dependent gene transcription (M. J. Higley & Sabatini, 2012; Josselyn & Tonegawa, 2020). Metabotropic glutamate receptors (mGluRs) are GPCRs whose downstream effectors (PLC and IP_3) can drive calcium release from the endoplasmic reticulum (ER), otherwise known as store-operated release. The mechanism of ER calcium reuptake and release is one of the many calcium buffering that the cell uses to further tightly

regulate calcium concentrations (Brini, Calì, Ottolini, & Carafoli, 2014; Grienberger & Konnerth, 2012;

Ross, 2012)
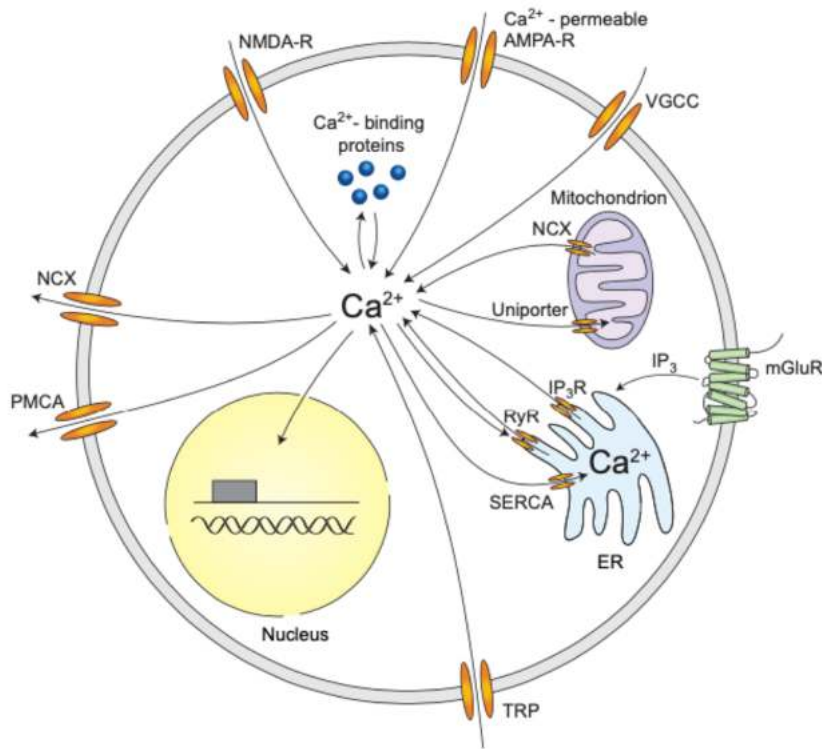
Figure 5: Sources of calcium in neurons

Calcium influx via NMDA and GluA1-homomeric AMPA receptors is gated by glutamate. Depolarization opens VGCCs, some TRP channels and NMDARs. Indirectly, mGluR activation drives calcium release from the ER via IP_3 receptors and ryanodine (RyR) receptors. Calcium efflux is also crucial and mediated by plasma-membrane calcium ATPase (PMCA), the sarco/endoplasmic reticulum calcium ATPase (SERCA) pump, and the sodium-calcium exchanger (NCX). Calcium binding proteins act to buffer calcium concentrations at particularly at microdomains. All these channels and binding proteins work to maintain calcium concentration gradients within the cell. This diagram does not highlight the complex anatomy of neurons.

Adapted from (Grienberger & Konnerth, 2012)

In neurons internal calcium concentrations at rest is approximately 50-100 nM but activity can

transiently increase the internal concentrations up to 10-100 times higher (Berridge, Lipp, & Bootman,

2000). The complex anatomy of neurons with their numerous bifurcating dendrites and axons creates

subcellular compartments in which local calcium gradients can be markedly different at any given

moment and often relay specific information to the cell (Brini et al., 2014). Calcium influx at the

presynaptic terminal triggers neurotransmitter release and calcium influx at the postsynapse regulates

synaptic plasticity. These examples are short-term consequences of calcium influx but on an expanded

timescale, calcium can trigger complex molecular cascades that can modify neurotransmitter release probability, synapse stability and receptor composition, and of course, calcium at the nucleus can alter gene expression, particularly activity-related genes like cFos and Arc.

Monitoring neuronal and synaptic activity is possible with a number of methods. A gold standard is electrophysiological recordings of synaptic potentials, which can estimate the contribution of presynaptic release or postsynaptic strength and the balance of excitatory and inhibitory transmission of a single neuron. But these recordings are spatially limited to, at maximum, a handful of neurons at once, and are temporally limited due to the terminal nature of whole-cell recordings. Recordings at the soma are a sum of all participating synapses and it is therefore extremely difficult to tease apart the "where" of participating synapses. The advent of calcium imaging methods makes it possible to survey calcium activity in groups of neurons or even subcellular compartments, like spines, dendrites and axons (Humeau & Choquet, 2019). This thesis is concerned with the creation of a two new types of calcium sensors called CaMPARI2 and SynTagMA. In order to contextualize their advantages over existing methods, I will introduce both the development of calcium sensors and the instrumentation required to conduct these experiments.

1.9 Advances in imaging for neuroscience

The utility of a particular sensor is limited by the experimental conditions and the available technology to measure and quantify the data collected. Two important considerations when live-cell imaging is spatial and temporal resolution. One-photon fluorescence imaging includes confocal laser scanning microscopy and direct imaging using charge coupled device array detectors (CCD) or photodiode arrays (Grienberger & Konnerth, 2012). Direct imaging requires weakly scattering and relatively flat preparations, like cell culture, to obtain reasonable signal to noise ratio (SNR) as the entire sample is simultaneously illuminated, and emitted photons are recorded by the CCD or array (Fig. 6A-C)

(Homma et al., 2009). As the emitted fluorescence is collected from the entire preparation at once, this allows for a high temporal resolution but is limited by poor axial resolution and high background due to excitation of objects outside of the focal plane and light scatter. Laser scanning microscopy tackles the issue of axial resolution by focusing the excitation scanning beam into a so-called cone (Fig. 6D), which can then move across the preparation in a raster pattern (Fig. 6G). Although the excitation beam is now focused, fluorophores outside the focus are still excited. In confocal microscopy, a pinhole placed in front of the detector, set to reflect the diffraction limit of the objective, rejects all fluorescence coming from outside the focal spot (Fig. 6E) (Lichtman & Conchello, 2005). Although this rejection affords effectively high spatial/axial resolution, excitation outside the focal plane is still occurring, albeit "invisible" to the user resulting in photobleaching and "photon waste".
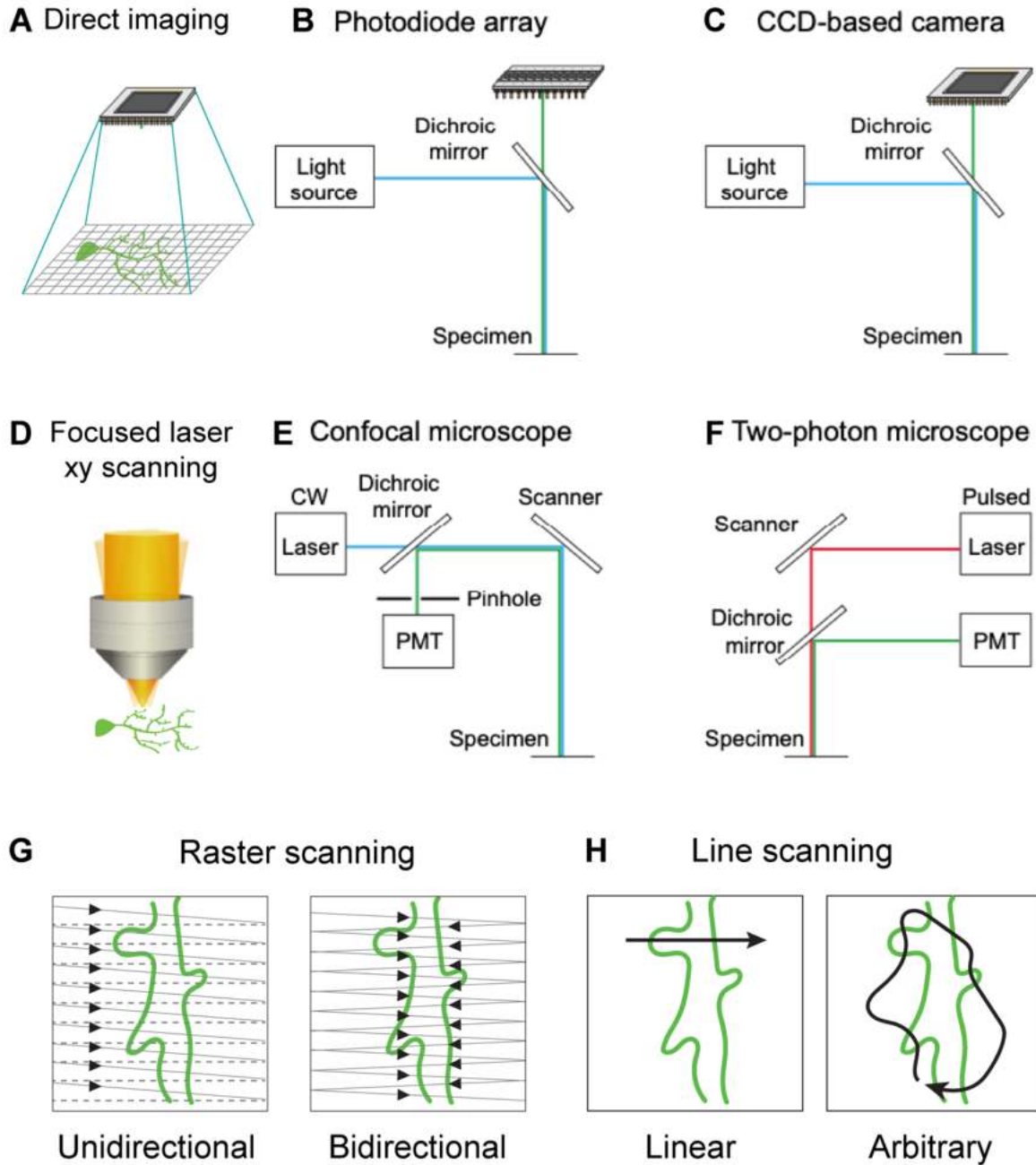
Figure 6: One-photon and two-photon imaging

A) Scheme of direct imaging using either photodiode (B) or CCD-based cameras (C). Note the grid over the sample indicating the corresponding chip detectors. Light source can be mercury lamps or LEDs D) Scheme of focused x-y laser scanning. E) Confocal imaging with a focused continuous laser. Emitted fluorescence inside the focal point collected and all fluorescence outside is rejected by the pinhole before reaching the photomultiplier tubes (PMTs). F) 2PLSM uses a near-infrared pulsed laser and collects all emitted photons. Laser scanning microscopy can steering the laser beam in a rastering pattern (G) or using either linear line scanning (essentially 1 line raster) or user-directed arbitrary line scanning.

Adapted from: (Grienberger & Konnerth, 2012; Ji, Freeman, & Smith, 2016)

Approximately thirty years ago, two-photon laser scanning microscopy (2PLSM) was introduced (Fig. 7F) (Denk, Strickler, & Webb, 1990). 2PLSM uses infrared wavelengths to excite a fluorescence molecule. Photons at longer wavelengths have a lower energy and consequently a fluorophore requires concurrent absorption of two photons to reach its excited state. The likelihood of such an event occurring is dramatically lower than with one-photon excitation. Due to the nonlinearity of two-photon excitation, the absorption rate depends on the laser intensity. Laser intensity is highest at the focus and drops off dramatically outside the focus. These principles achieve a very small diffraction limited excitation volume (0.1 to 1 μm^3) depending on the numerical aperture of the objective) (Svoboda & Yasuda, 2006). Light scattering in tissue is a barrier to both the excitation source (i.e. laser) and the emitted photons from the sample. The long wavelengths (near infrared) used in 2PLSM penetrate tissue better than the shorter wavelengths used in 1P and the small excitation volume achieved means that all photons collected constitute useful signals. One limitation to laser scanning microscopy is that raster scanning is relatively slow and some of the scanning time is spent collecting irrelevant or empty signal. There have been further developments to work around these issues. For example, arbitrary line scanning, as used in this thesis, (Fig. 6H) and the use of spatial light modulators allows the user to image in a specified area; increasing imaging speed and collecting only relevant signal (Ji et al., 2016). There have been further advances including projection or volume, tomographic, and random-access imaging (Kazemipour et al., 2019; Wu et al., 2020). All of these factors highlight the advantage of using 2PLSM for live cell imaging particularly in highly scattering brain tissue.

1.10 Synthetic calcium dyes

Although the first calcium sensor was a bioluminescent photoprotein called aequorin (Fig. 7A) (Shimomura, Johnson, & Saiga, 1962), the hybridization of calcium chelators, like EGTA or BAPTA, to

fluorescent chromophores to make calcium sensitive dyes revolutionized the field (Grynkiewicz, Poenie, & Tsien, 1985; Tsien, 1980). The calcium binding of the chelator results in a conformational change that alters the fluorophore's emission state (Fig. 7B). Since the first hybridization, numerous dyes have been developed featuring varying binding affinities and kinetics, single or dual fluorophore design, and various excitation/emission spectra; some commonly used dyes include: fura-2, Oregon-green BAPTA, Fluo-4/5 and rhodamine-2. These dyes must be introduced to the cell by some means. One method is to introduce a dye, which has been coupled to membrane-permeable acetoxymethyl (AM) esters, into cell culture media or for *in vivo* applications by micro-pressure loading. Once the dye crosses the membrane, the AM esters are cleaved, and the dye is "trapped" within the cell (Grienberger & Konnerth, 2012). However, this method does not allow targeting of a single cell. To achieve cell targeting, cells can be impaled with microelectrodes and microinjected with a dye (without AM esters), introduced through the pipette using whole-cell patch clamp or the dye can be introduced by electroporation. One advantage of using dyes is the possibility to directly quantify the calcium concentration in the cell (Helmchen, 2004; Michael J. Higley & Sabatini, 2008; Yasuda et al., 2004). However, using calcium dye has limitations. For example, specifically targeting a genetically defined population of cells is impossible and chronic imaging of a particular cell is not feasible due to eventual dye extrusion or toxicity (Hires, Tian, & Looger, 2008).

1.11 Genetically encoded calcium indicators

Targeting a cell population of interest involves using cell-type specific promotor or regulatory sequence to drive the expression of a transgene encoding an effector protein, such as a genetically-encoded calcium indicator (GECI) (Luo, Callaway, & Svoboda, 2018). Similar to synthetic dyes, GECIs are made up of two components: 1) calcium binding domains (typically calmodulin or troponin-C) fused to 2) either a single fluorescent protein (FP) or a FRET-compatible pair of FPs. Chameleon was the first GECI and is a FRET sensor (cyan-FP and yellow-FP, Fig. 7C) (Miyawaki et al., 1997). FRET sensors are ratiometric as the emission spectra changes based on proximity between the FP pair, which is

modulated by calcium binding. Advantages of using FRET-based sensors includes higher baseline fluorescence and motion artifacts are less problematic. Since the publication of Chameleon, a number of additional FRET-indicators have been developed and improved upon including the yellow-chameleon family and the twitch family (Pérez Koldenkova & Nagai, 2013). Using dual color indicators, however, makes it challenging to combine with additional fluorescent labels or optogenetic actuators with similar activation spectra to the sensor.

The other category of GECIs use a single FP in which the calcium sensing domains, most often calmodulin/M13, are fused to the N- and C- termini of the FP of interest (Fig. 7D). Whereas for FRET-based sensors the change in fluorescence upon calcium binding is calculated as the FRET ratio, single FP GECIs get brighter upon calcium binding and the change in fluorescence is calculated based on the baseline fluorescence ($F-F_0/F_0$) (Yasuda et al., 2004). The most well-known family of GECIs in this category are the GCaMPs. Using targeted mutagenesis methods the family has gone through numerous iterations: GCaMP, GCaMP1.6, GCaMP2, GCaMP3, GCaMP5, GCaMP6, of which the newest is the jGCaMP7 series (J. Akerboom et al., 2012; T.-W. Chen et al., 2013; Dana et al., 2019; Nakai, Ohkura, & Imoto, 2001; Tian et al., 2009). There are GCaMP variants with slow or fast kinetics, different signal-to-noise ratios and dynamic range, and brightness at rest (i.e. in low calcium). One particular advance is the jGCaMP7b variant, which exhibits high baseline fluorescence (allowing the user to work without an addition morphology marker) and retains a high dynamic range. These features make it an attractive variant imaging smaller compartments like spines (Dana et al., 2019).

Due to the rapid development of imaging modalities and the introduction of optogenetic techniques, there is an increasing demand for sensors in a range of colors (Zhao et al., 2011). Red-shifted indicators have received the most attention and development, in part due to the increased penetration and reduced scatter of long wavelengths in tissue, i.e. for *in vivo* imaging. Most commonly,

are R-GECO and RCaMP (Jasper Akerboom et al., 2013; Zhao et al., 2011). In the last five years, there has

been an increase in promising single-fluorophore GECIs in other colors. The X-CaMP series includes blue,

green, yellow and red variants that can be used to simultaneously monitor calcium from different cell

populations (Inoue et al., 2019). The near-infrared sensor NIR-GECO1 is excitable at 600-700 nm and

emits at 700-800 nm, yet another boon for deep tissue imaging (Qian et al., 2019). YFP-based GECIs are

also seeing more popularity as they can be used in combination with RFP-based sensors with better

spectral separation than GFP-based sensors and they can be used with less expensive, fixed long

wavelength lasers (1030-1040nm) as well (Mohr et al., 2020). Of course, there are also further efforts to

improve upon the gold-standard sensor family, i.e. GCaMP by replacing the GFP with better

fluorophores like mNeonGreen (Zarowny et al., 2020).
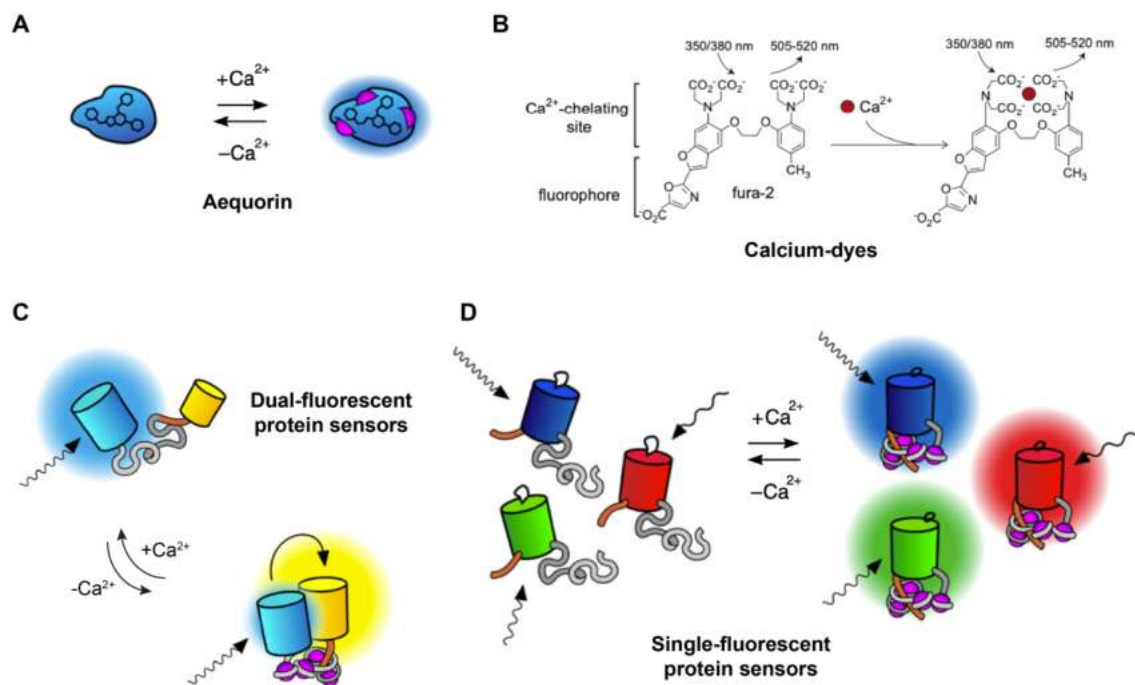
Figure 7: Available calcium sensors

A) An example chemical calcium dye, Fura-2. Note the calcium sensing/chelating and the fluorophore
domains. It is excited by UV light and its emission changes upon Ca^{2+} binding B) The chemiluminescent
protein aequorin, whose luminescence naturally changes upon Ca^{2+} binding. C) Dual-fluorescent
protein (FRET) sensors. As denoted by the drawn color cloud, the emission ratio changes upon Ca^{2+}

binding. D) Single-fluorescent protein sensors. When Ca^{2+} binds fluorescence increases. These sensors are available in a number of colors.

Adapted from: (Grienberger & Konnerth, 2012; Pérez Koldenkova & Nagai, 2013)

By using GECIs, we can select cell-type specific promotors to target, for example, dopamine receptor-1 expressing neurons or interneuron subtypes that express parvalbumin (PV). Methods for targeting GECIs include viral transduction, single cell or *in utero* electroporation or the use of transgenic mouse lines and with the expanded color palette of sensors, it is now possible to perform multiplex imaging of more than one population of cells simultaneously. Genetic targeting of sensors can also include localization of a sensor to subcellular compartments. GECIs have been targeted to the pre- and post-synapse (Dreosti, Odermatt, Dorostkar, & Lagnado, 2009; Leitz & Kavalali, 2014) and to mitochondrial or ER lumen (Henderson et al., 2015; Suzuki et al., 2014). It is important to note that calcium is used as a correlate for activity but should not be conflated as a sensor for changes in membrane potential (M. Z. Lin & Schnitzer, 2016). Both synthetic dyes and genetically encoded voltage sensors (GEVIs) have been developed alongside GECIs however this thesis will not review these sensors.

1.12 *CaMPARI: a calcium-modulated photoactivatable ratiometric integrator*

Calcium imaging using GECIs has led to the discovery of ensembles of cells whose *in vivo* activity is involved in the coordination of behaviors or play a significant role in memory formation and storage. Imaging of subcellular compartments like the dendrite and its spines have revealed that groups of synapses can respond to a particular stimulus, like the grating direction across the visual field (Jia, Rochefort, Chen, & Konnerth, 2010). Despite these advances, we are limited by the nature of the sensors and the instrumentation. Single synapse or dendritic calcium imaging requires a limited field of view, multiple trials per stimulation and fast imaging to capture the fast kinetics and achieve synaptic resolution. Similarly, *in vivo* imaging is typically limited to a single focal plane and limited field of view

and due to inherent animal movements the necessity of frame averaging further limits the temporal resolution.

An alternative approach to studying neuronal ensembles uses immediate early genes to label active ensembles but these methods suffer from poor temporal resolution, on the scale of hours. The calcium-modulated photoactivatable ratiometric integrator, CaMPARI, is a new approach for studying active neuronal ensembles (Fosque et al., 2015). CaMPARI is a sensor that permanently photoconverts from green to red only in the presences of both elevated calcium and violet light illumination (Fig 8A). By pairing violet light with epochs of activity or a behavior, active cells become increasingly red while the less active remain green (Fig. 8B). Both the green and red species of CaMPARI retain their normal calcium indicator features although their fluorescence decreases upon calcium binding as opposed to the more common increase in fluorescence. By capturing the cells that were active at a certain point in time with CaMPARI, one can read out a high-resolution image of the final activity snapshot. Because only violet light and activity are requisites for photoconversion of CaMPARI (i.e. labeling active cells), the imaging and the labeling of behavior can be decoupled. Using CaMPARI allows for the acquisition of larger high-resolution image stacks, and therefore access to a richer picture of neural activity.

This thesis concerns itself with improvements to the original CaMPARI to make CaMPARI2 and the targeting of CaMPARI2 to the pre and post synapse, to make SynTagMA.
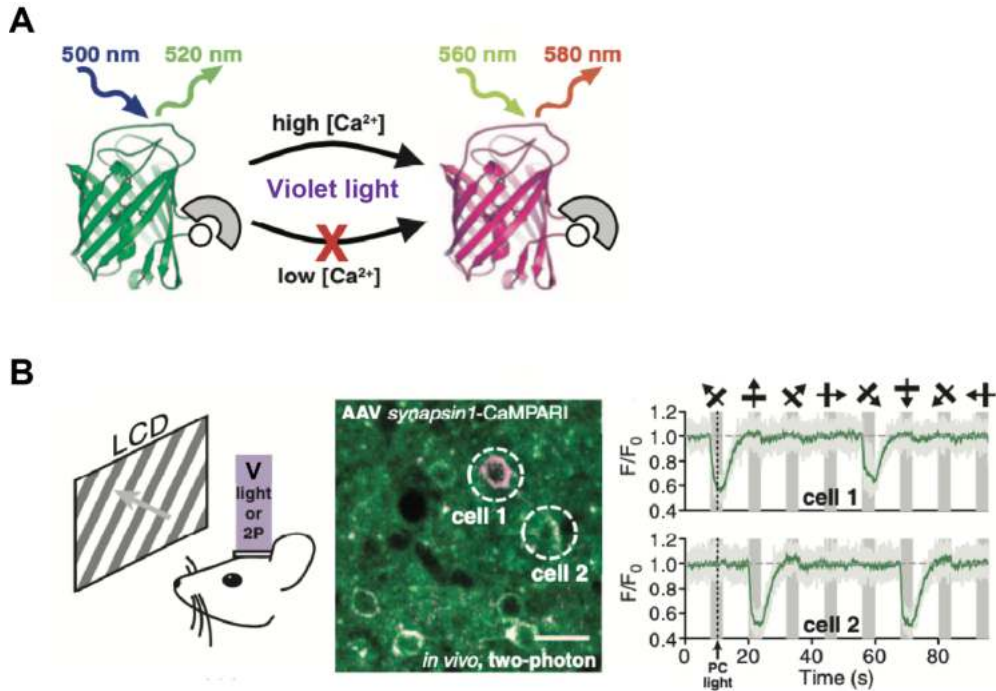
Figure 8: Taking an activity snapshot with CaMPARI

A) Design of CaMPARI. Circularly permutated mEos fused to Calmodulin and M13 calcium sensing domains. Only in the condition of both high calcium and violet light (395-405 nm) is CaMPARI irreversibly photoconverted from green to red. B) Example use of CaMPARI *in vivo*. Neurons responsive to the grating direction shown will photoconvert when the grating presentation is combined with violet light.

Adapted from: (Fosque et al., 2015)

Aims of the thesis

Project 1: The role of TRPM4 in hippocampal synaptic transmission

Because the TRPM4 channel is activated by internal Ca^{2+} and nonselectively conducts monovalent cations, I hypothesized that it would be activated downstream of NMDA receptors and boost depolarization in a feedback loop (Figure 9B). In pathophysiological states that cause excitotoxicity, like that in multiple sclerosis, TRPM4 could become deleteriously active in a feedback loop leading to

chronic calcium influx and potentially activating downstream signaling pathways that can trigger cell

death (J. M. Simard, Woo, & Gerzanich, 2012). In this project I aimed to answer these questions:

1) What is the expression pattern of TRPM4 in the hippocampus? *In situ* hybridization indicate that

   TRPM4 mRNA is present in the hippocampus (Figure 9A) and existing studies show staining for

   protein in the brain however few of these studies tested antibodies using a knock-out model.

2) Does TRPM4 contribute to excitatory postsynaptic calcium influx or excitatory postsynaptic

   potentials at the CA3->CA1 Schaffer collateral synapse?

3) In a murine model of multiple sclerosis, is the contribution of TRPM4 to excitatory postsynaptic

   potentials altered?
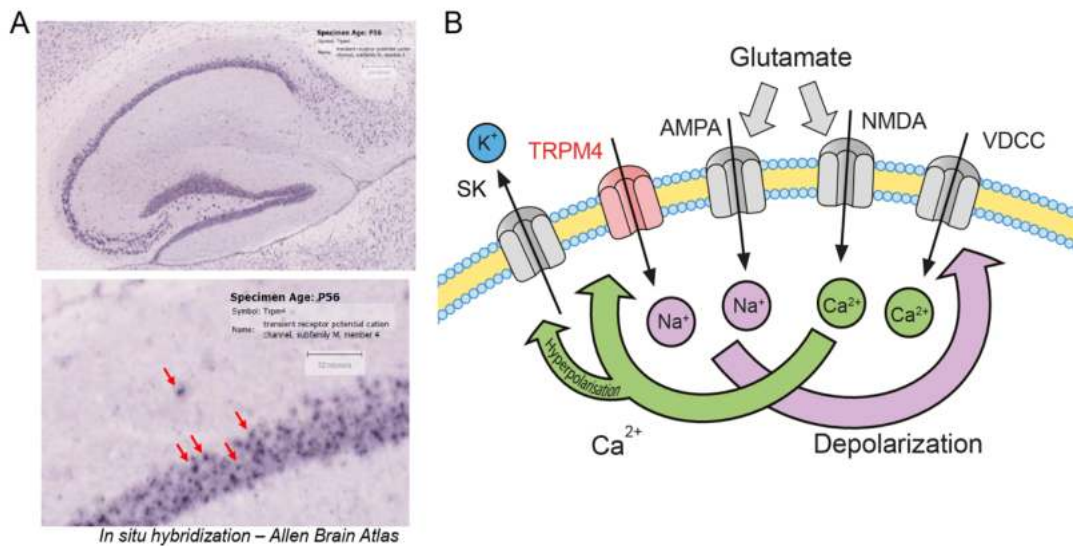
Figure 9: TRPM4 in the hippocampus

A) Evidence of TRPM4 mRNA transcripts in the hippocampus, including the CA1 cell body region and the stratum oriens. B) My hypothesis of the channels involved in TRPM4 activation. Glutamate binding activates both AMPAR and NMDARs leading to depolarization and calcium influx. The calcium should then activate TRPM4 opening which leads to further depolarization. Activation of VGCCs should drive further calcium influx and potentially maintain TRPM4 activation. The SK channels are also calcium activated and drive hyperpolarization, likely mediating the end of the depolarization feedback loop that TRPM4 may participate in.

Project 2: Labeling active neurons and synapses with CaMPARI2 and SynTagMA

CaMPARI is a new method for labelling active neurons. However, it suffers some drawbacks including photoconversion in low/zero Ca^{2+} conditions. In a collaborative project, we improved upon CaMPARI and created CaMPARI2. Our lab is interested in how synaptic activity can lead to changes in synaptic connectivity. Because calcium imaging at single synapses has limited spatial and temporal resolution, we chose to target CaMPARI to the pre and post-synapse. In doing so, we would be able to capture all the synapses active at a certain point in time (Figure 10). I specifically worked on these aims:

1) Characterize the calcium-dependent dimming of CaMPARI2 and SynTagMA and the relationship between photoconversion and violet light timing, duration and intensity.

2) Characterize SynTagMA and how it can be used to:

   a. Distinguish active from inactive synapses by using increasing back-propagating action potentials paired with violet light.

   b. Map and remap synaptically active synapses. Specifically, I was interested in turnover rate of the red species of SynTagMA and how soon relabeling of previously labeled synapses could occur.

   c. Improving the analysis pipeline in collaboration with other authors. A tool that labels a few active synapses among thousands requires sophisticated analysis solutions to detect and quantify the signals.

3) Facilitate a collaborative atmosphere that rapidly expanded our understanding of SynTagMA. I want to remark that the advancement of this project was also due to tight collaborative efforts with my co-first author, Dr. Alberto Perez-Alvarez, and the other labs whose access to certain methods, like *in vivo* imaging, made it possible to publish our paper at a high impact level. I worked hard to facilitate exchange of knowledge and help to drive the project forward. This is difficult to point at on paper despite its importance to the final outcome.

SynTagMA: a Synaptic Tag for Mapping Activity
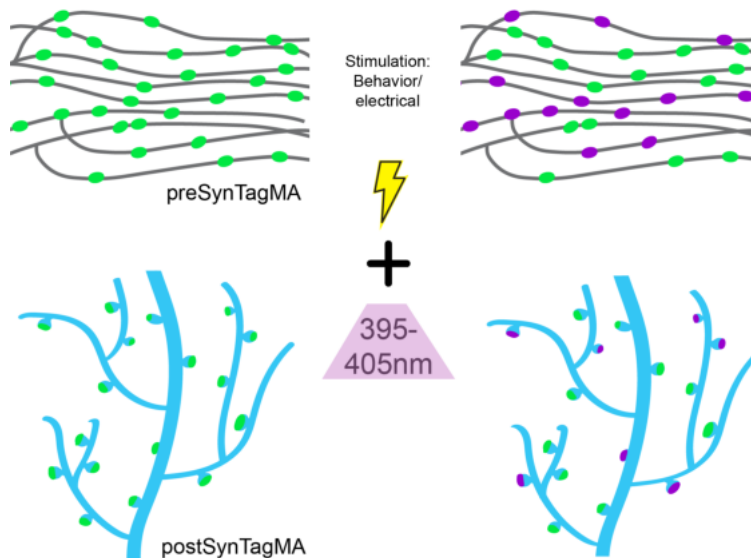
Figure 10: **SynTgMA**

Our new tool SynTagMA makes it possible to take freeze all synapses that were active within a 2 second period of the violet light illumination. This scheme visualizes this action for preSynTagMA (upper) and postSynTagMA (lower). For demonstration purposes, only a portion of the axon or dendritic arbor is shown but principally, all synapses can be labeled so long as violet light is there.

To achieve my aims for both projects, I used single cell electroporation or ballistic transfection to express GCaMP, SynTagMA or CaMPARI2 in hippocampal slice cultures. I combined 2PLSM and electrophysiology to study TRPM4 at single spines and to characterize SynTagMA or CaMPARI2. As the SynTagMA project developed, I used from simple hand drawn regions of interest on upwards of 50 synapses to the use of our in-house written software allowing automated analysis of thousands of synapses. The combination of TRPM4 antaognists in combination with a TRPM4 knock-out line made it possible to confirm that any observed effect by the antagonists is TRPM4 specific and not due to off-target effects of the drug

Publication #1: unpublished; submitted to eNeuro

Glibenclamide reduces excitatory postsynaptic currents in CA1 hippocampal neurons in a mouse model of multiple sclerosis

Brenna C. Fearey[1], Lars Binkle[2], Daniel Mensching[2], Christian Schulze[1], Manuel A. Friese[2], Thomas G. Oertner[1], Christine E. Gee[1]*

[1]Institute of Synaptic Physiology, Center for Molecular Neurobiology-Hamburg, University Medical Center Hamburg-Eppendorf, 20251 Hamburg, Germany
[2]Institute of Neuroimmunology and Multiple Sclerosis, Center for Molecular Neurobiology-Hamburg, University Medical Center Hamburg-Eppendorf, 20251 Hamburg, Germany
Affiliation: University Medical Center Hamburg-Eppendorf, Center for Molecular Neurobiology, Falkenried 94, 20251 Hamburg
*corresponding author: christine.gee@zmnh.uni-hamburg.de

Keywords: TRPM4, EAE, calcium imaging, electrophysiology

Specific contributions

I am first author on this paper, and I wrote the paper with editing from the other authors. I conducted and analyzed all of the experiments presented. Access to the animal lines and the induction of EAE was done in partnership with the collaborating authors, Dr. Lars Binkle and Dr. Daniel Mensching, in Prof. Dr. Friese's laboratory.

Abstract

The transient receptor potential melastatin 4 (TRPM4) channel has been shown to contribute to disease severity in the murine experimental autoimmune encephalomyelitis (EAE) model of multiple sclerosis and to neuronal cell death in models of excitotoxicity and traumatic brain injury. As TRPM4 is activated by intracellular calcium and conducts monovalent cations, we hypothesized that TRPM4 may also contribute to and boost excitatory synaptic transmission in the hippocampus. Using single-spine calcium imaging and electrophysiology we found no effect of the TRPM4 antagonists 9-phenanthrol and glibenclamide on synaptic transmission in hippocampal slices from healthy mice. In contrast,

glibenclamide but not 9-phenanthrol reduced excitatory synaptic potentials in slices from EAE mice, an effect that was absent in slices from EAE mice lacking TRPM4. We conclude that TRPM4 plays a limited role in basal hippocampal synaptic transmission, but a glibenclamide-sensitive TRPM4-mediated effect is upregulated by EAE.

Introduction

Transient receptor potential melastatin 4 (TRPM4) channels are non-selective monovalent cation channels activated by intracellular calcium (Launay et al. 2002; Nilius et al. 2005). TRPM4 activation is modulated by ATP, calmodulin, protein kinase-c (PKC), PIP_2 , and H_2O_2 (Nilius et al. 2004; Zhang et al. 2005; Nilius et al. 2005; Simon et al. 2010). It has been suggested that the TRPM4 channel may be responsible for the Ca^{2+}-activated nonselective cation current (I_{CAN}) described in a number of cell types (Guinamard, Sallé, and Simard 2011). TRPM4 channels are ubiquitously expressed in both excitable and non-excitable cells and their action contributes to heart sinus rhythm (C. Simard et al. 2013), boosts smooth muscle cell depolarization (Gonzales et al. 2010), and is involved in calcium regulation in T cells and dendritic cells (Launay et al. 2004). In the brain, TRPM4 antagonists reduce bursting in neurons of the substantia nigra, layer V of the medial entorhinal cortex and the thalamic reticular nucleus (E. C. Lin, Combe, and Gasparini 2017; Mrejeru, Wei, and Ramirez 2011; O'Malley et al. 2020). Similarly, in the pre-Bötzinger complex TRPM4 contributes to bursting and inspiratory drive but not breathing rhythm generation (Picardo et al. 2019; Koizumi et al. 2018; Mironov and Skorova 2011). In the hippocampus, knock-out of TRPM4 impairs long-term potentiation (LTP) of synaptic transmission specifically when induced by theta-burst stimulation (Menigoz et al. 2015) and in cerebellar Purkinje cells, both TRPM4 and TRPM5 contribute to the generation of a depolarization-induced slow current (Kim et al. 2013). As TRPM4 is activated by intracellular calcium, we hypothesized that it may be activated downstream of NMDA and metabotropic glutamate receptors to boost synaptic depolarization. Such a positive-feedback process would need to be limited as run-away depolarization would eventually lead to toxicity.

Indeed, TRPM4 is upregulated in spinal neurons, glial cells, and neuro-vasculature in response to injury (J. M. Simard et al. 2013; Kurland et al. 2016; Mehta et al. 2015). Likewise, pharmacological blockade or knockout of TRPM4 improves clinical outcomes in animal models of spinal cord injury and brain hemorrhage (Gerzanich et al. 2009; Chen et al. 2019; Tosun et al. 2013) and protects neurons against glutamate-induced excitotoxicity (Schattling et al. 2012; Bianchi, Smith, and Abriel 2018). It therefore seems maladaptive that, in both human multiple sclerosis patients and mice with experimental autoimmune encephalomyelitis (EAE), TRPM4 protein expression is upregulated when knock-out of TRPM4 improves outcome after EAE (Schattling et al. 2012; Bianchi, Smith, and Abriel 2018).

Interestingly, TRPM4 can co-assemble with the sulfonylurea receptor 1 (SUR1) (Kwon et al. 2013). SUR1 is a member of the ATP-binding cassette transporter family and co-assembles with the Kir6.2 inwardly-rectifying ATP-sensitive K^+ channel (Aittoniemi et al. 2009). It is not yet clear whether SUR1/Kir6.2 and SUR1/TRPM4 channels ae expressed concurrently or if SUR1/TRPM4 channels only form in pathological states. In spinal cord injury, SUR1 but not Kir6.2 is upregulated (J. M. Simard et al. 2007). SUR1 and TRPM4 upregulation have been reported in brain injury and in murine EAE (Schattling et al. 2012; Makar et al. 2015; Gerzanich et al. 2009; J. M. Simard et al. 2006). The anti-diabetic drug, glibenclamide, antagonizes SUR1/Kir6.2, SUR1/TRPM4 and TRPM4 channels (Woo et al. 2013) and treatment with glibenclamide has similar neuroprotective effects as TRPM4 or SUR1 knock-out in EAE and brain injury models (Schattling et al. 2012; Makar et al. 2015; Gerzanich et al. 2017; Jha et al. 2020).

In the hippocampus, little is known about the contribution of TRPM4 to basal synaptic transmission at the CA3-CA1 schaffer collateral synapse. In this study, we tested the hypothesis that NMDAR-dependent calcium influx would activate TRPM4 and drive further depolarization. We tested this hypothesis by measuring CA3-CA1 excitatory postsynaptic calcium transients (EPSCaTs) in wild-type

mouse organotypic hippocampal slice cultures and excitatory postsynaptic potentials (EPSPs) in mouse

acute hippocampal slices from wild-type and $Trpm4^{-/-}$ healthy and EAE mice. We found no evidence for

the involvement of TRPM4 in basal synaptic transmission but in EAE, TRPM4 boosts EPSPs.

Results

TRPM4 antagonism does not reduce calcium influx at individual CA1 pyramidal neuron spines or their

parent dendrites.

To study the role of TRPM4 and calcium influx at both the spine and dendritic level, mouse

organotypic hippocampal slice cultures were transduced via ballistic transfection with tdimer2 as a

morphology marker and GCaMP6f to monitor intracellular calcium at single spines and dendrites of CA1

pyramidal neurons (Figure 1A). Excitatory postsynaptic calcium transients (EPSCaTs) in response to

electrical stimulation of the Schaffer collaterals were monitored using a two-photon microscope (Figure

1B). With the expectation that TRPM4 activation requires and contributes to large calcium transients,

we aimed to induce not only isolated transients at single spines but responses at the dendrite as well

(Figure 1B-D). Washing in the TRPM4 antagonist, 9-phenanthrol, did not significantly reduce spine

EPSCaT peak amplitude (Figure 1E; $F_{(2, 26)}$ = 0.6477, p =0.53, RM-ANOVA) or area under the curve (AUC)

(Figure 1E; $F_{(2, 26)}$ = 0.5971, p =0.56, RM-ANOVA). Nor was there any reduction in dendritic EPSCaT peak

amplitude (Figure 1F; $F_{(2, 8)}$ = 0.8978, p=0.44, RM-ANOVA) or AUC (Figure 1F; $F_{(2, 8)}$ = 1.364, p =0.3, RM-

ANOVA). Thus TRPM4 does not contribute to synaptically evoked calcium transients at Schaffer

collateral synapses.

We then attempted to verify that TRPM4 protein was present in hippocampal neurons using

immunohistochemistry. All of the four antibodies tested produced indistinguishable staining patterns in

slices of $Trpm4^{+/+}$ and $Trpm4^{-/-}$ mice (Supplementary Figure 1) and are therefore not specific for TRPM4

or unsuitable for immunohistochemistry in this vicinity.
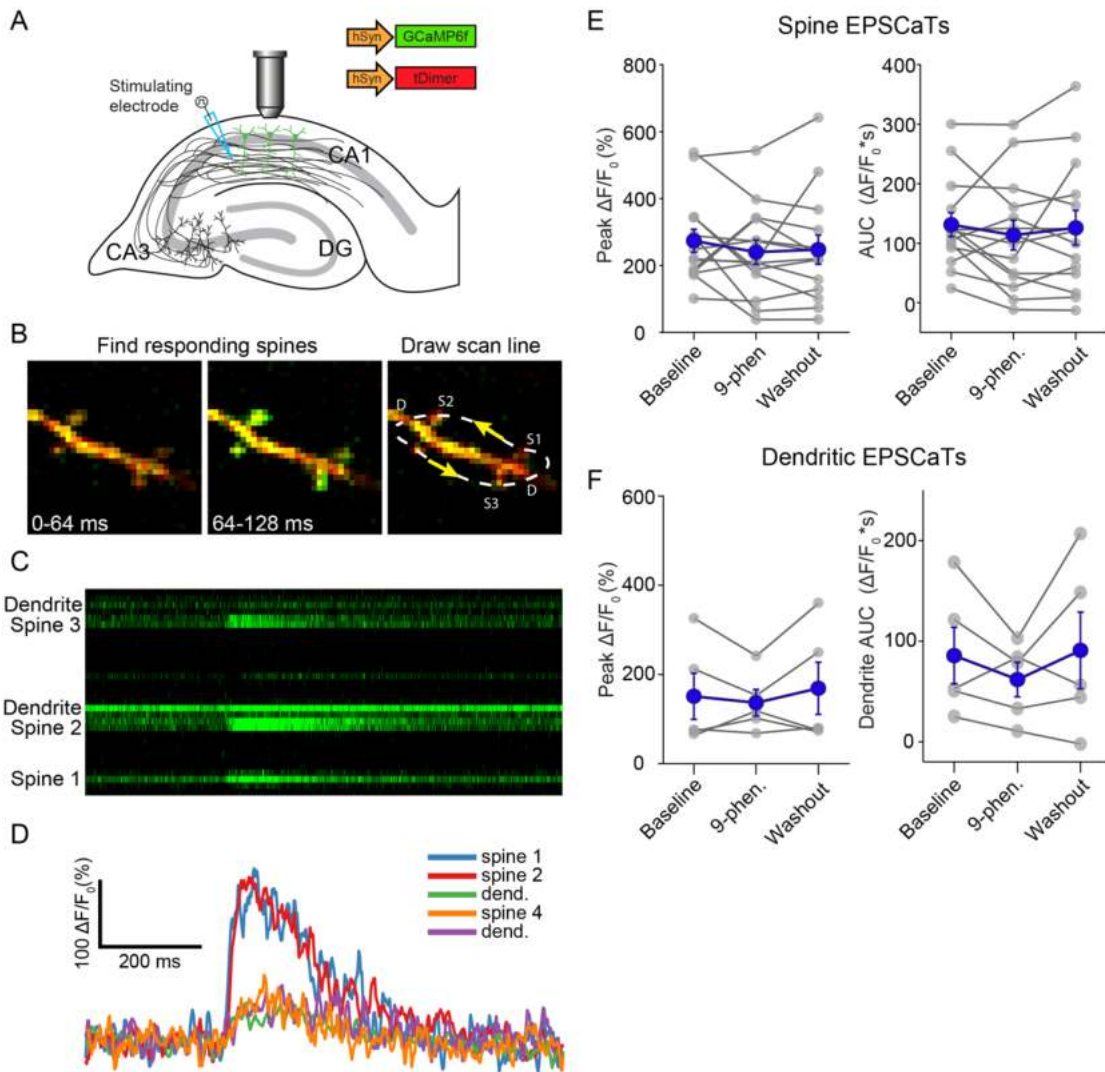
Figure 1: 9-phenanthrol does not reduce evoked excitatory postsynaptic calcium transients (EPSCaTs) at the spine or dendrite. (**A**) A monopolar stimulating electrode was placed in stratum radiatum to stimulate the Schaffer collaterals and evoke EPSCaTs in spines and dendrites of CA1 neurons expressing GCaMP6f and tdimer2. EPSCaTs were recorded by a two-photon microscope. (**B**) Example trial in frame scan mode of an EPSCaT from responding spines and the corresponding arbitrary scan line over the same responding spines (**C**) Example EPSCaT in response to Schaffer collateral stimulation from the line in B. (**D**) the corresponding plots of % $\Delta F/F_0$. (**E**) Peak amplitude and area under the curve (AUC) from spine eEPSCaTs (n = 14 spines) at baseline, 20 min after wash-in of 9-phenanthrol and following washout. (**F**) Peak and AUC from dendritic EPSCaTs (n = 5 dendrites). A one-way repeated measures

ANOVA revealed no significant differences between baseline, 9-phenanthrol or washout. Blue circles represent mean ± SEM and small grey circles represent individual spines or dendrites.

TRPM4 antagonists do not reduce CA1 excitatory synaptic potentials (EPSPs) in healthy wild-type or

***Trpm4*-deficient mice**

We next examined the contribution of TRPM4 to evoked excitatory postsynaptic potentials (EPSPs) in acute hippocampal slices prepared from adult wild-type and $Trpm4^{-/-}$ mice (always blind to genotype). As action potentials, inhibitory potentials, and calcium-activated small conductance potassium (SK) channels might mask a TRPM4-mediated component of EPSPs, QX-314 was included in the intracellular solution to block voltage-gated Na^+ channels and bicuculline in the extracellular solution to block $GABA_A$ and SK channels, respectively (Khawaled et al. 1999). D-serine was included in the extracellular solution to ensure that the glycine site of NMDA receptors was occupied. Large EPSPs (~40 mV deflections) were recorded from CA1 pyramidal neurons in response to Schaffer collateral stimulation in *stratum radiatum*. There was no effect of 9-phenanthrol on the EPSP amplitude or AUC in hippocampal slices from either wild-type (Figure 2 A–E; wilcoxon test, amplitude $p > 0.99$; AUC $p = 0.63$) or $Trpm4^{-/-}$ mice (Figure 2 A–E; wilcoxon test amplitude $p = 0.1875$; AUC $p = 0.44$). The TRPM4 antagonist glibenclamide also had no effect on the EPSP peak amplitude or AUC in either wild-type (Figure 3 A–E; wilcoxon test amplitude $p = 0.59$, AUC $p = 0.63$) or $Trpm4^{-/-}$ mice (Figure 3 A–E; wilcoxon test amplitude $p = 0.31$; AUC $p = 0.09$). Again, similar to 9-phenanthrol, there is no fast or slow effect of glibenclamide on EPSP peak or AUC (Figure 3 A–E). There were also no differences due to genotype in the cell parameters or baseline EPSP amplitude or AUC (Table 1). These results show that a TRPM4-mediated conductance does not significantly contribute to EPSPs under these steady state experimental conditions.
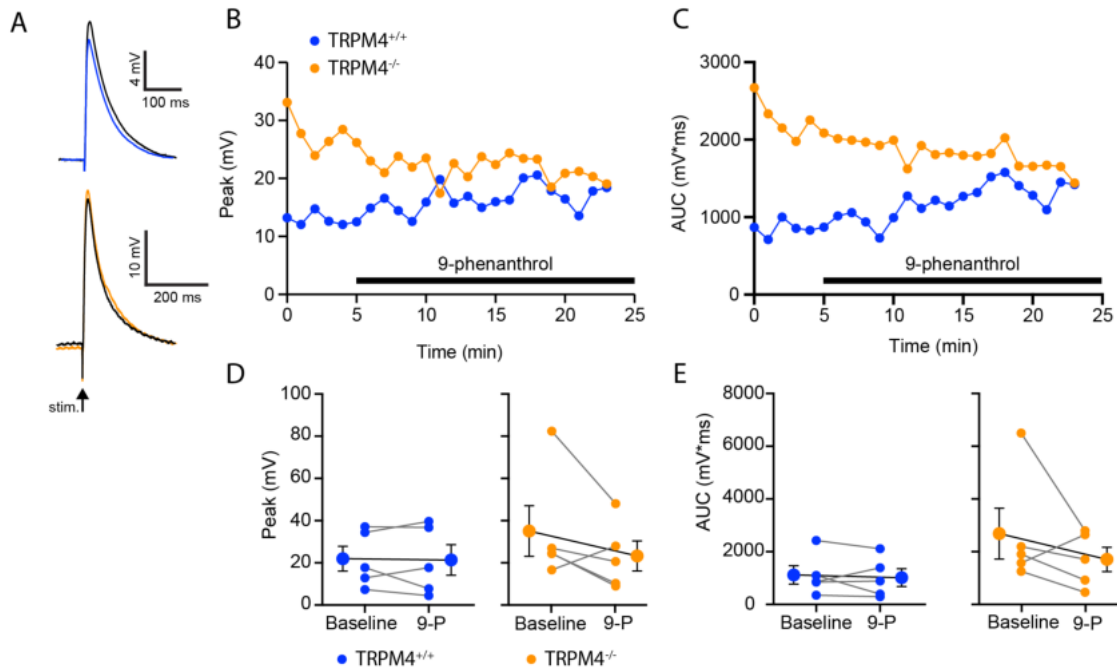
Figure 2: 9-phenanthrol does not reduce excitatory postsynaptic potentials (EPSPs) in CA1 pyramidal neurons. (A) EPSPs from representative CA1 pyramidal neurons in response to stimulation of stratum radiatum of acute slices from *Trpm4*$^{+/+}$ (upper, blue/black) or *Trpm4*$^{-/-}$ (lower orange/black) mice. After establishing a stable baseline (blue/orange traces), 9-phenanthrol (30 μM) was washed into the bath for 20 min. (black traces). Time course (**B**) and area under the curve (**C**) of the EPSPs from the same neurons in **A**. *Trpm4*$^{+/+}$ neuron (blue circles) and *Trpm4*$^{-/-}$ neuron (orange circles), black bar indicates time of 9-phenanthrol in the bath. **(D)** Summary of EPSP peak amplitudes at baseline (5 minute average) and after wash-in of 9-phenanthrol (last 5 minutes) of *Trpm4*$^{+/+}$ (blue, n = 5 neurons) and *Trpm4*$^{-/-}$ (orange, n = 5 neurons). Large filled circles are mean ± SEM and smaller circles are individual experiments. **(E)** As in D but area under the curve.
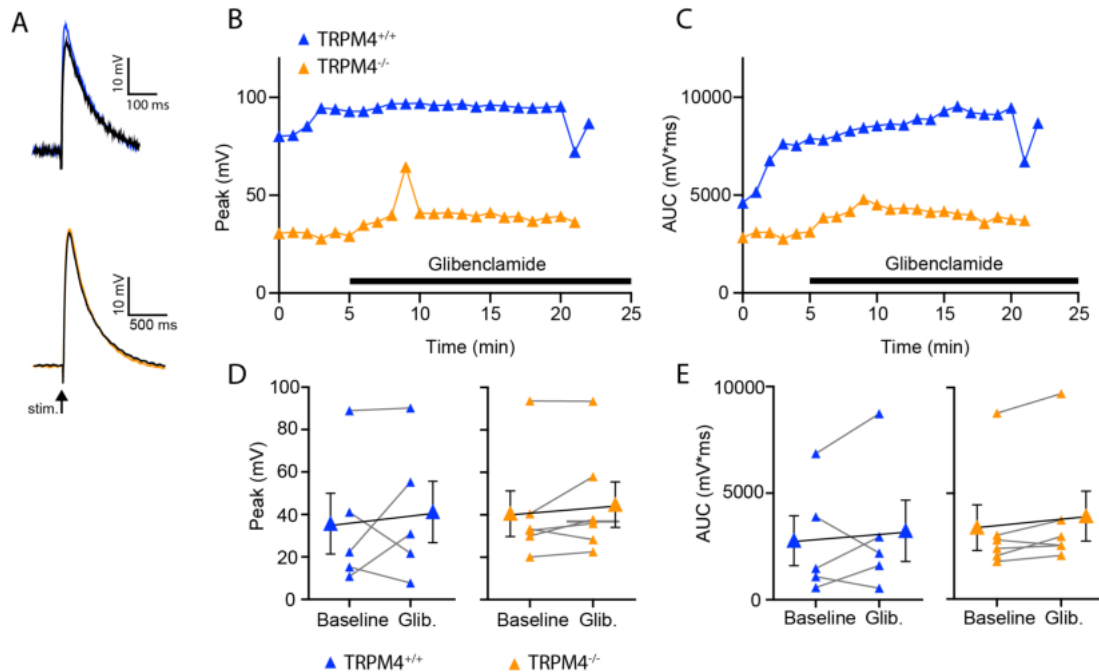
Figure 3: Glibenclamide does not reduce evoked excitatory postsynaptic potentials in CA1 pyramidal neurons. (**A**) EPSPs from representative CA1 pyramidal neurons in response to stimulation of stratum radiatum of acute slices from *Trpm4*$^{+/+}$ (upper, blue/black) or *Trpm4*$^{-/-}$ (lower orange/black) mice. After establishing a stable baseline (blue/orange traces), glibenclamide (20 µM) was washed into the bath for 20 min (black traces). Time course (**B**) and area under the curve (**C**) of the EPSPs in **A**. *Trpm4*$^{+/+}$ neuron (blue triangles) and *Trpm4*$^{-/-}$ neuron (orange triangles), black bar indicates time of glibenclamide in the bath. (**D**) EPSP peak amplitude at baseline (5 minute average) and after wash-in of 9-phenanthrol (average last 5 minutes) recorded from *Trpm4*$^{+/+}$ (blue, n = 6) and *Trpm4*$^{-/-}$ (orange, n = 6) neurons. Large filled triangles are mean ± SEM and smaller circles are individual experiments. (**E**) As in **D** but area under the curve.

Glibenclamide but not 9-phenanthrol reduces EPSP peak amplitude in wild-type EAE mice

We were surprised that blockade of TRPM4 had no impact on EPSPs in healthy mice. Several studies have shown that the channel is upregulated in diseased states; including models of multiple sclerosis (Schattling et al. 2012; Bianchi, Smith, and Abriel 2018), ischemia (Chen et al. 2019; Leiva-Salcedo et al. 2017), and brain injury (Jiang et al. 2017). Therefore, we induced EAE in *Trpm4*$^{+/+}$ and *Trpm4*$^{-/-}$

56

littermates to test whether TRPM4-dependent currents only significantly contribute to synaptic transmission in an inflamed state. Clinical scores and body weight were measured daily (Figure 4A, B). When a mouse reached the peak of the acute phase, i.e. a clinical score of at least 3 or a decreasing score, acute slices were prepared for electrophysiology recordings, again blinded to genotype (Figure 4A). There were no differences due to genotype in the clinical scores or body weight at time of sacrifice during the acute phase of EAE, as previously reported (Figure 4 A, B; Table 1) (Schattling et al. 2012).
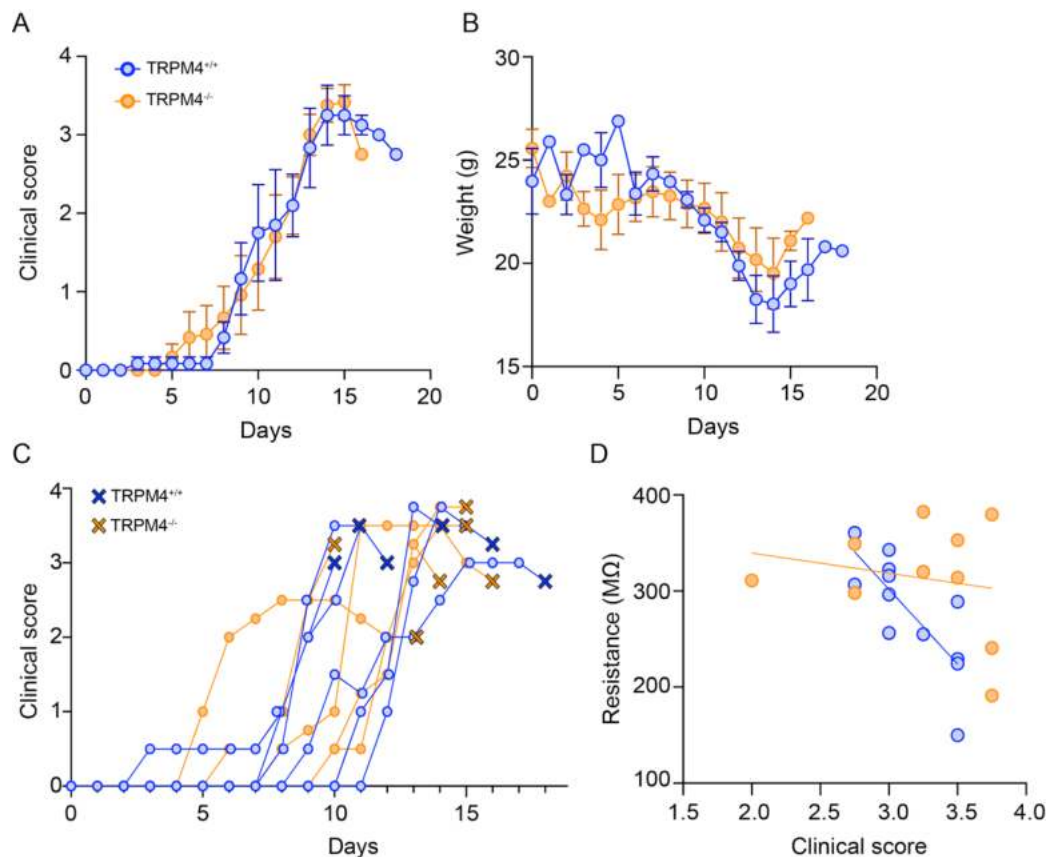
Figure 4: The induction and acute phase of EAE was not different in *Trpm4$^{-/-}$* and *Trpm4$^{+/+}$* littermates. (**A**) Daily clinical scores and (**B**) body weight of *Trpm4$^{-/-}$* (orange, n = 6 mice) and *Trpm4$^{+/+}$* (blue, n = 6 mice) littermates recorded daily after induction of experimental autoimmune encephalomyelitis (EAE) on day 0 (mean ± SEM). (**C**) EAE clinical progression of individual mice and score at time of sacrifice for electrophysiology (X's). (**D**) Cell resistance was calculated from 200 ms current injection in drug-free

ACSF. Cell resistance is negatively correlated with the final clinical score in *Trpm4$^{+/+}$* mice (Pearson's r = -0.77, p = 0.0035**) but not in *Trpm4$^{-/-}$* mice (Pearson's r = -0.2, p = 0.58).

We then recorded EPSPs from EAE mice following the same procedure as for the healthy mice. There were no differences in nearly all cell parameters, or EPSP amplitude or AUC at baseline. A two-way ANOVA for cell resistance showed a significant difference between genotypes (Table 1; $F_{(1, 42)}$ = 6.38, *p* = 0.015) and between healthy and EAE mice (Table 1; $F_{(1, 42)}$ = 11.54, *p* = 0.0015) and a post-hoc Sidak's test for multiple comparisons revealed a significant difference between healthy *Trpm4$^{+/+}$* and EAE *Trpm4$^{+/+}$* (Table 1; p = 0.046). Interestingly, in the EAE slices there was a significant negative correlation of cell resistance with clinical score in *Trpm4$^{+/+}$* neurons that was absent in *Trpm4$^{-/-}$* neurons (Figure 4D; *Trpm4$^{+/+}$*: R^2 = 0.57, *p* = 0.004; *Trpm4$^{-/-}$*: R^2 = 0.05, *p* = 0.58).

Cell parameters at baseline	Healthy *Trpm4$^{+/+}$*	Healthy *Trpm4$^{-/-}$*	EAE *Trpm4$^{+/+}$* (*p* vs healthy *Trpm4$^{+/+}$*)	EAE *Trpm4$^{-/-}$*	2-way ANOVA Genotype EAE
Number of cells	10	11	12	10	--
Peak amplitude (mV)	28.8 ± 7.6	38.6 ± 7.7	41.9 ± 9.1	41.5 ± 7.1	F= 0.20, *p=0.66* F= 0.75, *p=0.39*
Resting membrane potential (mV)	-72.0 ± 4.8	-78.3 ± 3.5	-69.6 ± 1.8	-70.5 ± 2.7	F= 1.10, *p=0.30* F= 3.07, *p=0.087*

Total resistance (MΩ)	221 ± 19	265 ± 12	279 ± 17 (*p=0.046**)	314 ± 19	F = 6.381, *p=0.0154** F =11.54, *p=0.0015$^{\$}$*
Area under the curve (mV*ms)	1945 ± 638	3110 ± 709	2966 ± 836	2700 ± 486	F = 0.368, *p=0.547* F = 0.153, *p= 0.698*
Half-width (ms)	47.2 ± 4.3	60.8 ± 3.8	53.0 ± 7.3	55.0 ± 5.1	F = 2.996, *p = 0.0908* F = 0.0596, *p = 0.808*
Rise slope (mV/ms)	3.6 ± 0.71	2.85 ± 0.21	4.53 ± 1.56	3.46 ± 0.96	F = 0.8503, *p = 3617* *F = 0.649, p = 0.452*
Rise time (ms)	4.8 ± 0.62	7.57 ± 1.37	7.52 ± 1.23	8.47 ± 1.30	F = 2.370, *p = 0.131* F = 2.240, *p = 0.142*
Clinical score	N/A	N/A	3.08 ± 0.11 *n* = 6 mice	3.00 ± 0.26 *n* = 6 mice	t(10) = 0.2988, *p = 0.77*
Body weight	N/A	N/A	19.88 ± 1.08 *n* = 6 mice	20.43 ± 1.24 *n* = 6 mice	t(10)= 0.3346, *p = 0.74*

Table 1: Only cell resistance significantly varies between genotype or health status at baseline All measurements are taken from the baseline prior to drug wash-in. Data are mean ± SEM. The degrees of freedom are (1, 42) for all parameters except clinical score and body weight. Upper pair of F and p

values are for genotype (*Trpm4*$^{+/+}$ vs *Trpm4*$^{-/-}$) comparisons and the lower pair are for treatment (EAE vs. healthy) comparisons. For clinical score and body weight, unpaired t-tests were used. *N*-size is indicated within each cell.

As in healthy animals, 9-phenanthrol had no apparent effect on EPSP amplitude or AUC in slices made from EAE *Trpm4*$^{+/+}$ mice (Figure 5 A–E, amplitude $p = 0.63$; AUC $p = 0.25$). The n-size for the *Trpm4*-deficient littermates is too small for statistics but given there was no drug effect in *Trpm4*$^{+/+}$ neurons, we had no need to eliminate off-target effects and elected not to treat additional animals. In contrast, the less-specific TRPM4 antagonist glibenclamide significantly reduced the EPSP amplitude (Figure 6 A, B, D; Wilcoxon test $p = 0.02$) but not the AUC (Figure 6 A, C, E; $p = 0.38$) in *Trpm4*$^{+/+}$ neurons. The reduction of EPSP amplitude by glibenclamide was absent in *Trpm4*$^{-/-}$ mice (Figure 6 D; $p = 0.16$), indicating the effect was TRPM4-specific. The AUC remained unchanged in CA1 neurons from both *Trpm4*$^{+/+}$ and *Trpm4*$^{-/-}$ mice (Figure 6 F; *Trpm4*$^{+/+}$ $p=0.38$; *Trpm4*$^{-/-}$ $p=0.56$).
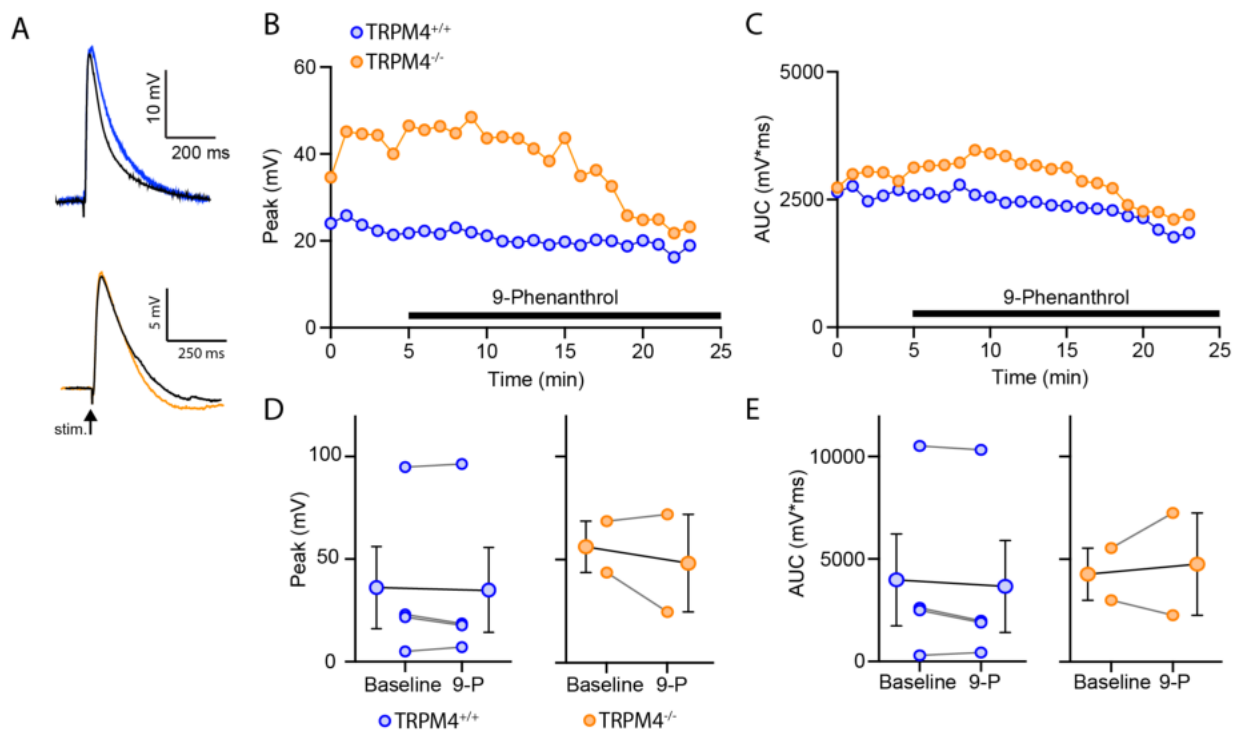
Figure 5: 9-phenanthrol does not reduce evoked excitatory postsynaptic potentials in CA1 pyramidal neurons in EAE mice. (**A**) EPSPs from representative CA1 pyramidal neurons in response to stimulation of stratum radiatum of acute slices from *Trpm4$^{+/+}$* (upper, blue/black) or *Trpm4$^{-/-}$* (lower orange/black) EAE mice. After establishing a stable baseline (blue/orange traces), 9-phenanthrol (30 µM) was washed into the bath for 20 min (black traces). Time course (**B**) and area under the curve (**C**) of the EPSPs in **A**. *Trpm4$^{+/+}$* neuron (blue triangles) and *Trpm4$^{-/-}$* neuron (orange triangles), black bar indicates time of glibenclamide in the bath. (**D**) EPSP peak amplitude at baseline (5 minute average) and after wash-in of 9-phenanthrol (average last 5 minutes) recorded from *Trpm4$^{+/+}$* (blue, n = 4) and *Trpm4$^{-/-}$* (orange, n = 2) neurons. Large filled circles are mean ± SEM and smaller circles are individual experiments. (**E**) As in **D** but area under the curve.
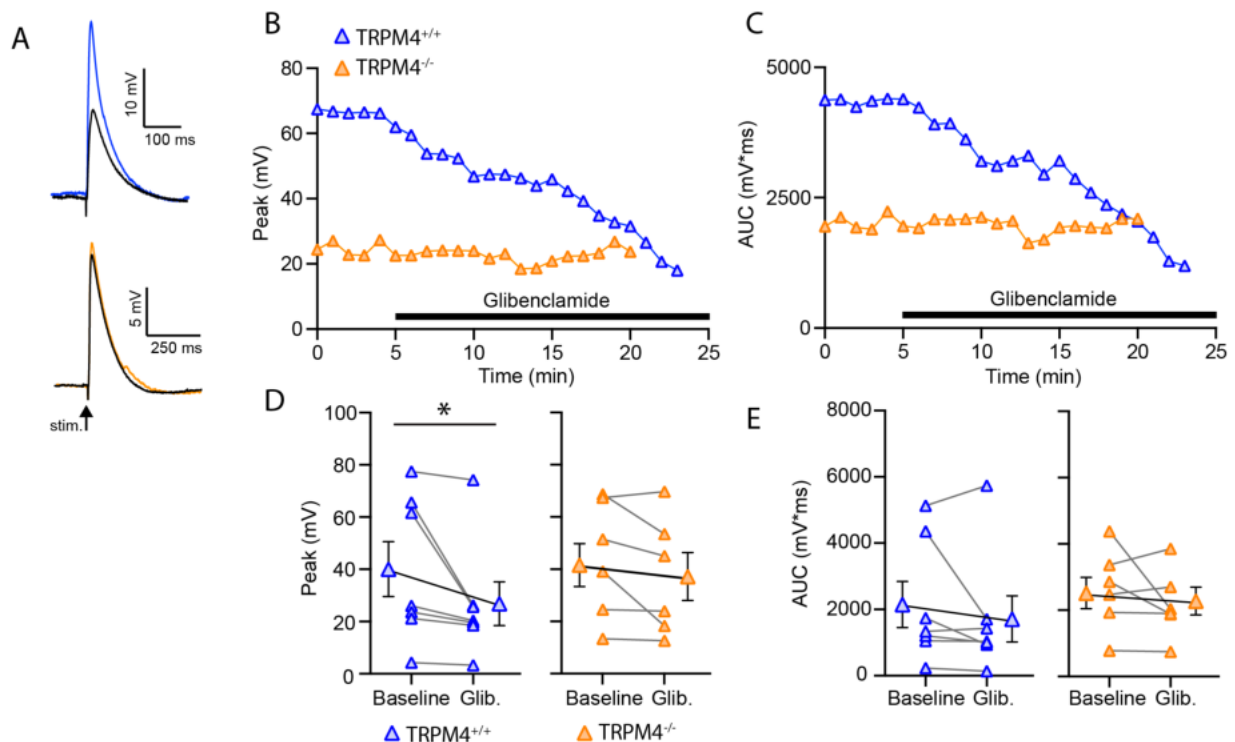
Figure 6: Glibenclamide reduces EPSPs peak amplitude in CA1 pyramidal neurons in EAE mice. (**A**) EPSPs from representative CA1 pyramidal neurons in response to stimulation of stratum radiatum of acute slices from *Trpm4$^{+/+}$* (upper, blue/black) or *Trpm4$^{-/-}$* (lower orange/black) EAE mice. After establishing a stable baseline (blue/orange traces), glibenclamide (20 µM) was washed into the bath for 20 min (black traces). Time course (**B**) and area under the curve (**C**) of the EPSPs in **A**. *Trpm4$^{+/+}$* neuron

(blue triangles) and *Trpm4*$^{-/-}$ neuron (orange triangles), black bar indicates time of glibenclamide in the bath. (**D**) EPSP peak amplitude at baseline (5 minute average) and after wash-in of glibenclamide (average last 5 minutes) recorded from *Trpm4*$^{+/+}$ (blue, n = 8) and *Trpm4*$^{-/-}$ (orange, n = 7) neurons. Large triangles are mean ± SEM and smaller triangles are individual experiments. **p* = 0.02 Wilcoxon test. (**E**) As in **D** but area under the curve.

Discussion

In this study, we have shown that TRPM4 is not involved in basal synaptic transmission at the CA3-CA1 Schaffer collateral synapse in organotypic hippocampal slice cultures or acute hippocampal slices made from healthy mice. In contrast, we obtained evidence that TRPM4 increases synaptic transmission in slices made from mice at the acute phase of EAE.

We undertook this study expecting to find that TRPM4 boosted synaptic calcium responses and EPSPs in the hippocampus particularly when synaptic stimulation was strong enough to cause dendritic calcium waves typical of NMDA spikes (Nevian and Sakmann 2004). We blocked postsynaptic action potentials, inhibitory GABA-A receptors and SK channels, which are also activated by calcium and hyperpolarize rather than depolarize spines and dendrites, and still did not see evidence of TRPM4 activation. 9-phenanthrol did not change the observed calcium influx at single spines and their parent dendrites. There are a few possible explanations for the lack of effect. Possibly, TRPM4-mediated depolarization at spines does not significantly contribute to the voltage changes driving calcium influx at the synapse. Using a voltage indicator rather than a calcium indicator may have shown such a change but the use of voltage indicators at single synapses to measure subthreshold voltage changes remains extremely challenging (M. Z. Lin and Schnitzer 2016). It is also possible that the synaptically-induced depolarization and calcium influx did not activate TRPM4. There is some evidence suggesting that ER-calcium release is required for TRPM4 activation (Mironov and Skorova 2011; Mathar et al. 2014). Previously we have demonstrated that ER-calcium release occurs at CA3-CA1 synapses but only at spines

with a spine apparatus (Holbro, Grunditz, and Oertner 2009). It is possible that we never examined such

a spine in this study but we think this is unlikely. As we observed no effect on EPSPs, it is unlikely that we

failed to image the correct spines and rather suggests that TRPM4 does not play an important role in

transmission at these synapses. It is possible that TRPM4 is not present at CA3-CA1 synapses or is not

expressed in CA1 pyramidal neurons in the healthy hippocampus. The Allen Brain Atlas indicates mRNA

expression in the cell body layer of CA1, which we accepted as evidence that TRPM4 protein was

present. However, we failed in our attempts to confirm expression at the protein level. The identical

staining patterns of all antibodies in the hippocampus of $Trpm4^{+/+}$ and $Trpm4^{-/-}$ mice indicate either that

the antibodies recognize a protein that is not TRPM4 or that there is undetectable TRPM4 in the

hippocampus of $Trpm4^{+/+}$ mice and we saw only background fluorescence. The antibody used in

Schattling et al. (2012) was unfortunately no longer available. Thus we cannot rule out the possibility

that the lack of TRPM4 contribution to synaptic transmission is due to the absence of TRPM4 at CA3-CA1

synapses in the healthy hippocampus.

As we did not observe a TRPM4-specific effect in healthy animals, we turned to synaptic

transmission in EAE. TRPM4 expression is known to be upregulated during EAE in the spinal cord and

cortex (Schattling et al., 2012). Moreover, cultured hippocampal neurons from $Trpm4^{-/-}$ mice and wild

type neurons in the presence of TRPM4 antagonists are protected from cell death in glutamate

excitotoxicity assays (Schattling et al. 2012; Bianchi, Smith, and Abriel 2018). Indeed, TRPM4 contributes

to EPSPs in slices from EAE mice. Surprisingly, the antagonist glibenclamide, but not the more specific 9-

phenanthrol, decreases EPSP amplitude in EAE TRPM4$^{+/+}$ mice. Importantly, this effect was not observed

in $Trpm4^{-/-}$ mice indicating a TRPM4 specific effect. Glibenclamide is considered less specific to TRPM4

than 9-phenanthrol (Grand et al. 2008) and glibenclamide is widely known for its ability to antagonize

SUR1-Kir6.2 (i.e. K$_{ATP}$) channels (Ashcroft 2005). It has been shown that SUR1-TRPM4 channels also co-

assemble and that glibenclamide has a 100-fold higher efficacy for SUR1-TRPM4 channels than for

TRPM4 homomeric channels (Woo et al. 2013). Therefore, glibenclamide may be antagonizing SUR1-TRPM4 channels in the slices from EAE mice. Indeed, SUR1 but not Kir6.2 is upregulated following middle cerebral artery stroke in rats (J. M. Simard et al. 2006) and we have shown that TRPM4 is upregulated in brain and spinal cord of EAE mice and multiple sclerosis patients (Schattling et al. 2012). Thus, one explanation consistent with our observation of glibenclamide rather than 9-phenanthrol decreasing EPSPs in EAE wild-type mice is due to an increased expression of SUR1-TRPM4 heteromeric channels at synapses in EAE.

In conclusion, TRPM4 does not significantly contribute to basal synaptic transmission at the Schaffer collateral synapse in the hippocampus of healthy animals but TRPM4 does boost EPSPs in EAE. Multiple sclerosis models often focus on the spinal cord but there are clear hippocampal-specific cognitive impairments, synaptic dysfunction and atrophy in both patients and animals models (Nistico et al. 2014; Di Filippo et al. 2018). Further study of the potential SUR1/TRPM4 channel in multiple sclerosis and what may trigger upregulation could lead to the discovery of important biomarkers and increase the possibility of early clinical interventions, as cognitive impairments often go undetected.
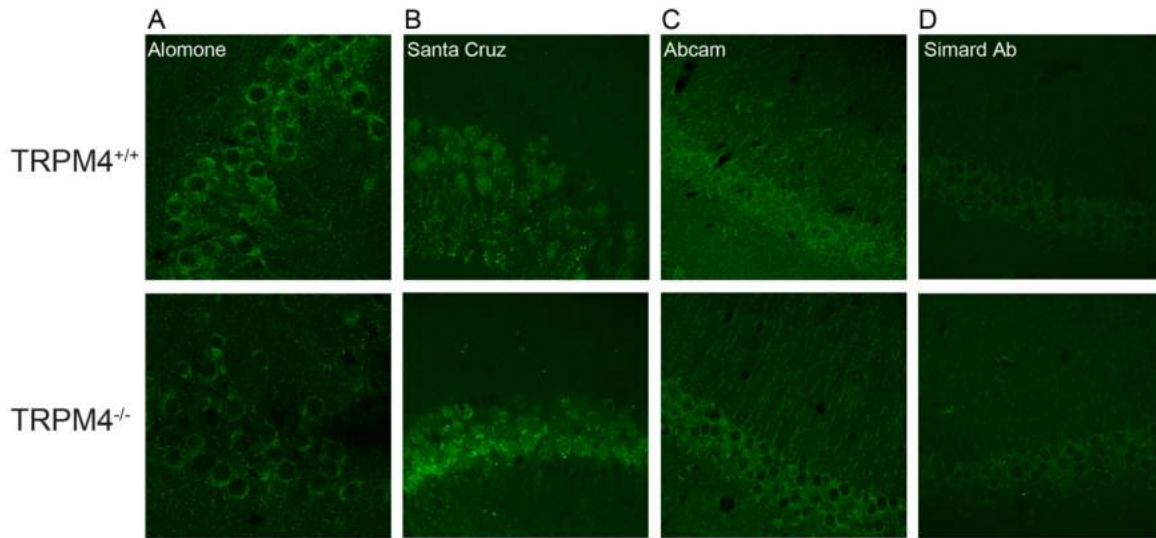
Supplementary Figure 1: Existing antibodies show no clear signal against TRPM4

Three commercial TRPM4 antibodies and one developed by the lab of J.M. Simard (A: Alomone, B: Santa Cruz, C: Abcam, D: Simard) were used in hippocampal sections from *Trpm4$^{+/+}$* and *Trpm4$^{-/-}$* mice. We found no clear difference in antibody reactivity between genotypes. All images were taken using a confocal microscope.

Materials & methods:

Animals

All mice were housed and bred at the University Medical Center Hamburg-Eppendorf (UKE) animal facility. All mice were housed with a 12-hour light/dark cycle and had water and food ad libitum. All procedures performed in mice were in compliance with German law and according to the guidelines of Directive 2010/63/EU. Protocols were approved by the local ethics committee (Behörde für Gesundheit und Verbraucherschutz of the City of Hamburg).

Mouse organotypic hippocampal slice cultures

Hippocampi were prepared from P4-P7 mice as described previously (Gee et al. 2017). Briefly, pups were anesthetized with 80% CO_2/20% O_2 and decapitated. Hippocampi were dissected in cold slice culture dissection medium containing (in mM): 248 sucrose, 26 NaHCO3, 10 glucose, 4 KCl, 5 $MgCl_2$, 1 $CaCl_2$, 2 kynurenic acid and 0.001% phenol red. The solution was saturated with 95% O_2, 5% CO_2, pH 7.4, 310-320 mOsm kg^{-1}. Tissue was cut into 400 μM thick sections on a tissue chopper and cultured on porous membranes (Millipore PICMORG50) at 37° C in 5% CO_2. No antibiotics were added to the slice culture medium which was partially exchanged (60-70%) twice per week and contained (for 500 ml): 394 ml Minimal Essential Medium (Sigma M7278), 100 ml heat inactivated donor horse serum (H1138 Sigma), 1 mM L-glutamine (Gibco 25030-024), 0.01 mg ml^{-1} insulin (Sigma I6634), 1.45 ml 5M NaCl (S5150 Sigma), 2 mM $MgSO_4$ (Fluka 63126), 1.44 mM $CaCl_2$ (Fluka 21114), 0.00125% ascorbic acid (Fluka 11140), 13 mM D-glucose (Fluka 49152).

Gold particles (1.6 μm, 2.75 μg DNA per mg gold) were coated with an 8:3 mixture of expression vectors encoding GCaMP6f and tdimer2 (respectively), each driven by the human synapsin-1 promoter. At DIV 7-9, slice cultures were ballistically transduced using a Helios gene gun (Bio-Rad). Experiments were conducted between DIV14-21.

Experimental autoimmune encephalomyelitis (EAE) induction

Mice used for EAE induction were 3-5 months old. As previously described (Schattling et al. 2012), we immunized mice subcutaneously with 200 μg MOG_{35-55} (NeoMPS) in complete Freund's adjuvant (Difco) containing 4 mg ml^{-1} *Mycobacterium tuberculosis* (H37Ra, Difco). We injected 200 ng pertussis toxin (Calbiochem) intravenously on the day of immunization and 48 h later. We scored the mice daily for clinical signs by the following system: 0, no clinical deficits; 1, tail weakness; 2, hind limb paresis; 3, partial hind limb paralysis; 3.5, full hind limb paralysis; 4, full hind limb paralysis and forelimb paresis; 5,

premorbid or dead. Mice with a score of ≥4, were immediately sacrificed to prevent undue harm.

Hippocampal slices were prepared at scores ≥3 or shortly after the score began to decrease 11-18 days after EAE induction (see Electrophysiology, below).

Two-photon microscopy

The two-photon imaging setup was custom built based on an Olympus BX51WI microscope. An Olympus LUMPlan W-IR2 60× 0.9 NA objective was used and image acquisition was controlled by the open-source software package ScanImage 3.7 (Pologruto, Sabatini, and Svoboda 2003), which we modified to allow user-defined arbitrary line scans. A pulsed Ti:Sapphire laser (Chameleon, Coherent) was used to excite GCaMP6f and tdimer2 at 980 nm. Emitted photons were collected through the objective and oil-immersion condenser (1.4 NA, Olympus) with two pairs of photomultiplier tubes (H7422P-40, Hamamatsu). 560 DXCR dichroic mirrors and 525/50 and 607/70 emission filters (Chroma) were used to separate green and red fluorescence. Excitation light was blocked by short-pass filters (ET700SP-2P, Chroma).

Calcium imaging

An organotypic hippocampal slice culture was transferred to the chamber at the two-photon microscope and bathed in oxygenated ACSF containing (in mM): 135 NaCl, 2.5 KCl, 4 $CaCl_2$, 4 $MgCl_2$, 10 Na-HEPES, 12.5 D-glucose, 1.25 NaH_2PO_4. To identify spines and dendrites responding to electrical stimulation of schaffer collateral axons (two 0.2 ms paired pulses with an interpulse interval of 40 ms), frame scans (at 15.625 Hz) of oblique dendrites were acquired. After finding a responding spine, user-defined arbitrary line scans (500 Hz) that crossed the responding spines and dendrite to improve time resolution and signal to noise. Responses to stimulation were acquired once per minute. A stable

baseline was acquired for at least twenty minutes. After baseline, 9-phenanthrol (30 µM) was washed

into the chamber and responses were acquired for another twenty minutes, once per minute. Finally,

fresh ACSF containing no drugs was washed into the chamber and responses were acquired for a final

twenty minutes. For analysis, regions of interest (ROI) were drawn over spines and dendrites in ImageJ

and the relative % change in GCaMP6f green fluorescence was calculated as $100 * (F-F_0) / F_0$ where F is

the fluorescence intensity and F_0 is the average fluorescence intensity prior to stimulation. Peak

amplitude and area under the curve (AUC) were extracted from within the response time-window.

Electrophysiology

Mice were sacrificed between 2-6 months of age. Mice were briefly anesthetized with 80% CO_2 /20%

O_2 prior to decapitation. The brain was dissected and immersed in ice-cold solution containing (in mM):

110 choline chloride, 25 $NaHCO_3$, 25 D-glucose, 11.6 sodium L-ascorbate, 7 $MgSO_4$, 1.25 NaH_2PO_4, 2.5

KCl, 0.5 $CaCl_2$, continuously bubbled with 95% O_2 and 5% CO_2, pH 7.4. Coronal slices (300 µm thick) were

cut using a vibratome and were allowed to recover at 34 °C for 30 minutes in oxygenated artificial

cerebrospinal fluid (ACSF) containing (in mM): 125 NaCl, 26.2 $NaHCO_3$, 11 D-glucose, 1 NaH_2PO_4, 2.5 KCl,

1.3 $MgCl_2$, 2.5 $CaCl_2$. Slices were then kept in the same solution at room temperature until used. After at

least 1 hour at room-temperature, a slice was placed in the recording chamber and continuously

perfused with oxygenated ACSF supplemented with D-Serine (30 µM) to occupy the second agonist

binding site of NMDA receptors, bicuculline-methochloride (10 µM) to block GABA-A receptors and SK-

channels (Khawaled et al. 1999) and 0.1% DMSO (see below). Current-clamp recordings from CA1

pyramidal cells were performed at 23-25 °C (Figures 1-3) or at 30-32 C° (slices from EAE treated mice,

Figures 5-6). Recordings were performed using either a Multiclamp 700B or an Axopatch 200B amplifier

(Molecular Devices). Recordings were controlled and digitized using National Instruments A/D boards

and Ephus software in the Matlab environment (Suter et al. 2010). Patch pipettes with a tip resistance of

3-5 MΩ were filled with (in mM): 135 K-gluconate, 10 HEPES, 4 MgCl$_2$, 4 Na$_2$-ATP, 0.4 Na-GTP, 10 Na$_2$-phosphocreatine, 3 L-ascorbic acid and 3 QX-314 chloride (to block voltage-gated sodium channels). To evoke excitatory postsynaptic potentials (EPSPs), a monopolar electrode was placed in the *stratum radiatum* and 0.2 ms pulses were delivered using an ISO-Flex stimulator (A.M.P.I.). The stimulation intensity was set to produce an EPSP of approximately 40 mV. After a stable baseline was achieved (at least five minutes), a TRPM4 antagonist, either 9-phenanthrol (30 µM) or glibenclamide (20 µM), was washed into the bath. Both 9-phenanthrol and glibenclamide were dissolved in DMSO and resulted in a final 0.1% DMSO total concentration in the ACSF. An equivalent concentration of DMSO was included in the drug-free ACSF.

Immunohistochemistry

We anesthetized TRPM4$^{+/+}$ and TRPM4$^{-/-}$ mice with an intraperitoneal injection of a solution of 100 µl (10 mg ml−1 esketamine hydrochloride (Pfizer), 1.6 mg ml−1 xylazine hydrochloride (Bayer) and water) per 10 g of body weight. Afterward we perfused the mice with 0.1 M phosphate buffer and fixed them with 4% paraformaldehyde (PFA). For immunohistochemistry, 40 micron thick free floating sections were washed 3 x 5 mins in 1x PBS followed by 10 mins in 0.5% sodium borohydride in 1x PBS. Slices were incubated in blocking solution for 1 hour (0.3% BSA Sigma #A-4503, 10% horse serum Invitrogen #16050-130, 0.3% Triton X-100). Slices were then incubated overnight with primary antibody against TRPM4 (Rabbit polyclonal, 1:200, Alomone ACC-044; goat polyclonal, 1:500, Santa-cruz SC-27540; rabbit polyclonal, 1:100, Abcam ab104572). Anti-serum as a gift from Dr. J M Simard was reconstituted in water and used at a concentration of 1:200. As secondary antibodies, I used Alexa-488 rabbit or goat antibodies (1:1000) incubated with slices for 2-5 hours. Slices were then mounted and acquired on a Leica confocal microscope using a 488 laser line. Acquisitions were taken with the same laser intensity and PMT voltages for samples acquired within the same batch of stainings.

Analysis & Statistics

Calcium imaging experiments were analyzed using ImageJ and repeated-measures ANOVA was used for statistical analysis. Electrophysiology analysis was completed in Matlab. All statistics were performed using Graphpad Prism (version 8). For paired analyses, the Wilcoxon matched pairs signed rank test was used. For analysis of the role of genotype and clinical score a two-way ANOVA was used for each parameter. A p-value below 0.05 was considered significant.

References

Aittoniemi, Jussi, Constantina Fotinou, Tim J. Craig, Heidi de Wet, Peter Proks, and Frances M. Ashcroft. 2009. "SUR1: A Unique ATP-Binding Cassette Protein That Functions as an Ion Channel Regulator." *Philosophical Transactions of the Royal Society of London. Series B, Biological Sciences* 364 (1514): 257–67.

Ashcroft, Frances M. 2005. "ATP-Sensitive Potassium Channelopathies: Focus on Insulin Secretion." *The Journal of Clinical Investigation* 115 (8): 2047–58.

Bianchi, Beatrice, Paul A. Smith, and Hugues Abriel. 2018. "The Ion Channel TRPM4 in Murine Experimental Autoimmune Encephalomyelitis and in a Model of Glutamate-Induced Neuronal Degeneration." *Molecular Brain* 11 (1): 41.

Chen, Bo, Gandi Ng, Yahui Gao, See Wee Low, Edwin Sandanaraj, Boominathan Ramasamy, Sakthivel Sekar, et al. 2019. "Non-Invasive Multimodality Imaging Directly Shows TRPM4 Inhibition Ameliorates Stroke Reperfusion Injury." *Translational Stroke Research* 10 (1): 91–103.

Di Filippo, Massimiliano, Emilio Portaccio, Andrea Mancini, and Paolo Calabresi. 2018. "Multiple Sclerosis and Cognition: Synaptic Failure and Network Dysfunction." *Nature Reviews. Neuroscience* 19 (10): 599–609.

Eckstein, Eugenia, Martina Pyrski, Silvia Pinto, Marc Freichel, Rudi Vennekens, and Frank Zufall. 2020. "Cyclic Regulation of Trpm4 Expression in Female Vomeronasal Neurons Driven by Ovarian Sex Hormones." *Molecular and Cellular Neurosciences* 105 (April): 103495.

Gee, Christine E., Iris Ohmert, J. Simon Wiegert, and Thomas G. Oertner. 2017. "Preparation of Slice Cultures from Rodent Hippocampus." *Cold Spring Harbor Protocols* 2017 (2). https://doi.org/10.1101/pdb.prot094888.

Gerzanich, Volodymyr, S. Kyoon Woo, Rudi Vennekens, Orest Tsymbalyuk, Svetlana Ivanova, Alexander Ivanov, Zhihua Geng, et al. 2009. "De Novo Expression of Trpm4 Initiates Secondary Hemorrhage in Spinal Cord Injury." *Nature Medicine*. https://doi.org/10.1038/nm.1899.

Gerzanich, Volodymyr, Tapas K. Makar, Poornachander Reddy Guda, Min Seong Kwon, Jesse A. Stokum, Seung Kyoon Woo, Svetlana Ivanova, et al. 2017. "Salutary Effects of Glibenclamide during the Chronic Phase of Murine Experimental Autoimmune Encephalomyelitis." *Journal of Neuroinflammation* 14 (1): 177.

Gonzales, Albert L., Zarine I. Garcia, Gregory C. Amberg, and Scott Earley. 2010. "Pharmacological Inhibition of TRPM4 Hyperpolarizes Vascular Smooth Muscle." *American Journal of Physiology. Cell Physiology* 299 (5): C1195–1202.

Grand, T., M. Demion, C. Norez, Y. Mettey, P. Launay, F. Becq, P. Bois, and R. Guinamard. 2008. "9-Phenanthrol Inhibits Human TRPM4 but Not TRPM5 Cationic Channels." *British Journal of Pharmacology*. https://doi.org/10.1038/bjp.2008.38.

Guinamard, Romain, Laurent Sallé, and Christophe Simard. 2011. "The Non-Selective Monovalent Cationic Channels TRPM4 and TRPM5." In *Transient Receptor Potential Channels*, edited by Md Shahidul Islam, 704:147–71. Advances in Experimental Medicine and Biology. Dordrecht: Springer Netherlands.

Holbro, N., A. Grunditz, and T. G. Oertner. 2009. "Differential Distribution of Endoplasmic Reticulum Controls Metabotropic Signaling and Plasticity at Hippocampal Synapses." *Proceedings of the National Academy of Sciences*. https://doi.org/10.1073/pnas.0905110106.

Jha, Ruchira M., Josh Bell, Giuseppe Citerio, J. Claude Hemphill, W. Taylor Kimberly, Raj K. Narayan, Juan Sahuquillo, Kevin N. Sheth, and J. Marc Simard. 2020. "Role of Sulfonylurea Receptor 1 and Glibenclamide in Traumatic Brain Injury: A Review of the Evidence." *International Journal of Molecular Sciences* 21 (2). https://doi.org/10.3390/ijms21020409.

Jiang, Bing, Lin Li, Qianwei Chen, Yihao Tao, Liming Yang, Bo Zhang, John H. Zhang, et al. 2017. "Role of Glibenclamide in Brain Injury After Intracerebral Hemorrhage." *Translational Stroke Research* 8 (2): 183–93.

Khawaled, R., A. Bruening-Wright, J. P. Adelman, and J. Maylie. 1999. "Bicuculline Block of Small-Conductance Calcium-Activated Potassium Channels." *Pflugers Archiv: European Journal of Physiology* 438 (3): 314–21.

Kim, Yu Shin, Eunchai Kang, Yuichi Makino, Sungjin Park, Jung Hoon Shin, Hongjun Song, Pierre Launay, and David J. Linden. 2013. "Characterizing the Conductance Underlying Depolarization-Induced Slow Current in Cerebellar Purkinje Cells." *Journal of Neurophysiology* 109 (4): 1174–81.

Koizumi, Hidehiko, Tibin T. John, Justine X. Chia, Mohammad F. Tariq, Ryan S. Phillips, Bryan Mosher, Yonghua Chen, et al. 2018. "Transient Receptor Potential Channels TRPM4 and TRPC3 Critically Contribute to Respiratory Motor Pattern Formation but Not Rhythmogenesis in Rodent Brainstem Circuits." *eNeuro* 5 (1). https://doi.org/10.1523/ENEURO.0332-17.2018.

Kurland, David B., Volodymyr Gerzanich, Jason K. Karimy, Seung Kyoon Woo, Rudi Vennekens, Marc Freichel, Bernd Nilius, Joseph Bryan, and J. Marc Simard. 2016. "The Sur1-Trpm4 Channel Regulates NOS2 Transcription in TLR4-Activated Microglia." *Journal of Neuroinflammation* 13 (1): 130.

Kwon, M. S., A. Ivanov, V. Gerzanich, and J. M. Simard. 2013. "The Sulfonylurea Receptor 1 (Sur1)-

Transient Receptor Potential Melastatin 4 (Trpm4) Channel." *Journal of Biological*. http://www.jbc.org/content/288/5/3655.short.

Launay, Pierre, Henrique Cheng, Subhashini Srivatsan, Reinhold Penner, Andrea Fleig, and Jean-Pierre Kinet. 2004. "TRPM4 Regulates Calcium Oscillations after T Cell Activation." *Science* 306 (5700): 1374–77.

Launay, Pierre, Andrea Fleig, Anne Laure Perraud, Andrew M. Scharenberg, Reinhold Penner, and Jean Pierre Kinet. 2002. "TRPM4 Is a Ca2+-Activated Nonselective Cation Channel Mediating Cell Membrane Depolarization." *Cell* 109 (3): 397–407.

Leiva-Salcedo, Elías, Denise Riquelme, Oscar Cerda, and Andrés Stutzin. 2017. "TRPM4 Activation by Chemically- and Oxygen Deprivation-Induced Ischemia and Reperfusion Triggers Neuronal Death." *Channels* 11 (6): 624–35.

Lin, Eric C., Crescent L. Combe, and Sonia Gasparini. 2017. "Differential Contribution of Ca2+-Dependent Mechanisms to Hyperexcitability in Layer V Neurons of the Medial Entorhinal Cortex." *Frontiers in Cellular Neuroscience* 11 (June): 182.

Lin, Michael Z., and Mark J. Schnitzer. 2016. "Genetically Encoded Indicators of Neuronal Activity." *Nature Neuroscience* 19 (9): 1142–53.

Makar, Tapas K., Volodymyr Gerzanich, Vamshi K. C. Nimmagadda, Rupal Jain, Kristal Lam, Fahad Mubariz, David Trisler, et al. 2015. "Silencing of Abcc8 or Inhibition of Newly Upregulated Sur1-Trpm4 Reduce Inflammation and Disease Progression in Experimental Autoimmune Encephalomyelitis." *Journal of Neuroinflammation* 12 (1): 210.

Masoli, Stefano, Marialuisa Tognolina, Umberto Laforenza, Francesco Moccia, and Egidio D'Angelo. 2020. "Parameter Tuning Differentiates Granule Cell Subtypes Enriching Transmission Properties at the Cerebellum Input Stage." *Communications Biology*. https://doi.org/10.1038/s42003-020-0953-x.

Mathar, Ilka, Miklos Kecskes, Gerry Van der Mieren, Griet Jacobs, Juan E. Camacho Londoño, Sebastian Uhl, Veit Flockerzi, et al. 2014. "Increased β-Adrenergic Inotropy in Ventricular Myocardium From Trpm4 −/− Mice." *Circulation Research*. https://doi.org/10.1161/circresaha.114.302835.

Mehta, Rupal I., Cigdem Tosun, Svetlana Ivanova, Natalia Tsymbalyuk, Bolanle M. Famakin, Min Seong Kwon, Rudy J. Castellani, Volodymyr Gerzanich, and J. Marc Simard. 2015. "Sur1-Trpm4 Cation Channel Expression in Human Cerebral Infarcts." *Journal of Neuropathology and Experimental Neurology* 74 (8): 835–49.

Menigoz, A., T. Ahmed, V. Sabanov, K. Vinken, S. Pinto, S. Kerselaers, A. Segal, et al. 2015. "TRPM4 Is a Key Mediator for NMDA-Receptor Dependent Hippocampal LTP but Not LTD." In *Front. Neurosci. Conference Abstract: 11th National Congress of the Belgian Society for Neuroscience. Doi: 10.3389/conf. Fnins*. Vol. 80. https://www.frontiersin.org/10.3389/conf.fnins.2015.89.00080/event_abstract.

Mironov, Sergej L., and Ekaterina Y. Skorova. 2011. "Stimulation of Bursting in Pre-Bötzinger Neurons by Epac through Calcium Release and Modulation of TRPM4 and K-ATP Channels." *Journal of*

Neurochemistry 117 (2): 295–308.

Mrejeru, Ana, Aguan Wei, and Jan Marino Ramirez. 2011. "Calcium-Activated Non-Selective Cation Currents Are Involved in Generation of Tonic and Bursting Activity in Dopamine Neurons of the Substantia Nigra Pars Compacta." *The Journal of Physiology* 589 (10): 2497–2514.

Nevian, Thomas, and Bert Sakmann. 2004. "Single Spine Ca2+ Signals Evoked by Coincident EPSPs and Backpropagating Action Potentials in Spiny Stellate Cells of Layer 4 in the Juvenile Rat Somatosensory Barrel Cortex." *The Journal of Neuroscience: The Official Journal of the Society for Neuroscience* 24 (7): 1689–99.

Nilius, Bernd, Jean Prenen, Jisen Tang, Chunbo Wang, Grzegorz Owsianik, Annelies Janssens, Thomas Voets, and Michael X. Zhu. 2005. "Regulation of the Ca2+ Sensitivity of the Nonselective Cation Channel TRPM4." *The Journal of Biological Chemistry* 280 (8): 6423–33.

Nilius, Bernd, Jean Prenen, Thomas Voets, and Guy Droogmans. 2004. "Intracellular Nucleotides and Polyamines Inhibit the Ca2+-Activated Cation Channel TRPM4b." *Pflugers Archiv: European Journal of Physiology* 448 (1): 70–75.

Nistico, Robert, Francesco Mori, Marco Feligioni, Ferdinando Nicoletti, and Diego Centonze. 2014. "Synaptic Plasticity in Multiple Sclerosis and in Experimental Autoimmune Encephalomyelitis." *Philosophical Transactions of the Royal Society of London. Series B, Biological Sciences* 369 (1633): 20130162.

O'Malley, John J., Frederik Seibt, Jeannie Chin, and Michael Beierlein. 2020. "TRPM4 Conductances in Thalamic Reticular Nucleus Neurons Generate Persistent Firing during Slow Oscillations." *The Journal of Neuroscience: The Official Journal of the Society for Neuroscience*, May. https://doi.org/10.1523/JNEUROSCI.0324-20.2020.

Picardo, Maria Cristina D., Yae K. Sugimura, Kaitlyn E. Dorst, Prajkta S. Kallurkar, Victoria T. Akins, Xingru Ma, Ryoichi Teruyama, et al. 2019. "Trpm4 Ion Channels in Pre-Bötzinger Complex Interneurons Are Essential for Breathing Motor Pattern but Not Rhythm." *PLoS Biology* 17 (2): e2006094.

Pologruto, Thomas A., Bernardo L. Sabatini, and Karel Svoboda. 2003. "ScanImage: Flexible Software for Operating Laser Scanning Microscopes." *Biomedical Engineering Online* 2 (May): 13.

Riquelme, Denise, Ian Silva, Ashleigh M. Philp, Juan P. Huidobro-Toro, Oscar Cerda, James S. Trimmer, and Elias Leiva-Salcedo. 2018. "Subcellular Localization and Activity of TRPM4 in Medial Prefrontal Cortex Layer 2/3." *Frontiers in Cellular Neuroscience* 12 (January): 12.

Schattling, Benjamin, Karin Steinbach, Edda Thies, Martin Kruse, Aurélie Menigoz, Friederike Ufer, Veit Flockerzi, et al. 2012. "TRPM4 Cation Channel Mediates Axonal and Neuronal Degeneration in Experimental Autoimmune Encephalomyelitis and Multiple Sclerosis." *Nature Medicine* 18 (12): 1805–11.

Simard, Christophe, Thomas Hof, Zakia Keddache, Pierre Launay, and Romain Guinamard. 2013. "The TRPM4 Non-Selective Cation Channel Contributes to the Mammalian Atrial Action Potential." *Journal of Molecular and Cellular Cardiology* 59 (June): 11–19.

Simard, J. Marc, Mingkui Chen, Kirill V. Tarasov, Sergei Bhatta, Svetlana Ivanova, Ludmila Melnitchenko, Natalya Tsymbalyuk, G. Alexander West, and Volodymyr Gerzanich. 2006. "Newly Expressed SUR1-Regulated NC(Ca-ATP) Channel Mediates Cerebral Edema after Ischemic Stroke." *Nature Medicine* 12 (4): 433–40.

Simard, J. Marc, Orest Tsymbalyuk, Alexander Ivanov, Svetlana Ivanova, Sergei Bhatta, Zhihua Geng, S. Kyoon Woo, and Volodymyr Gerzanich. 2007. "Endothelial Sulfonylurea Receptor 1--Regulated NC Ca-ATP Channels Mediate Progressive Hemorrhagic Necrosis Following Spinal Cord Injury." *The Journal of Clinical Investigation* 117 (8): 2105–13.

Simard, J. Marc, Seung Kyoon Woo, Bizhan Aarabi, and Volodymyr Gerzanich. 2013. "The Sur1-Trpm4 Channel in Spinal Cord Injury." *Journal of Spine* Suppl 4 (August). https://doi.org/10.4172/2165-7939.S4-002.

Simard, J. Marc, S. Kyoon Woo, and Volodymyr Gerzanich. 2012. "Transient Receptor Potential Melastatin 4 and Cell Death." *Pflugers Archiv: European Journal of Physiology* 464 (6): 573–82.

Simon, Felipe, Elías Leiva-Salcedo, Ricardo Armisén, Ana Riveros, Oscar Cerda, Diego Varela, Ana Luisa Eguiguren, Pablo Olivero, and Andrés Stutzin. 2010. "Hydrogen Peroxide Removes TRPM4 Current Desensitization Conferring Increased Vulnerability to Necrotic Cell Death." *The Journal of Biological Chemistry* 285 (48): 37150–58.

Suter, Benjamin A., Timothy O'Connor, Vijay Iyer, Leopoldo T. Petreanu, Bryan M. Hooks, Taro Kiritani, Karel Svoboda, and Gordon M. G. Shepherd. 2010. "Ephus: Multipurpose Data Acquisition Software for Neuroscience Experiments." *Frontiers in Neural Circuits* 4 (August): 100.

Tosun, Cigdem, David B. Kurland, Rupal Mehta, Rudy J. Castellani, Joyce L. deJong, Min Seong Kwon, Seung Kyoon Woo, Volodymyr Gerzanich, and J. Marc Simard. 2013. "Inhibition of the Sur1-Trpm4 Channel Reduces Neuroinflammation and Cognitive Impairment in Subarachnoid Hemorrhage." *Stroke; a Journal of Cerebral Circulation* 44 (12): 3522–28.

Woo, Seung Kyoon, Min Seong Kwon, Alexander Ivanov, Volodymyr Gerzanich, and J. Marc Simard. 2013. "The Sulfonylurea Receptor 1 (Sur1)-Transient Receptor Potential Melastatin 4 (Trpm4) Channel." *The Journal of Biological Chemistry* 288 (5): 3655–67.

Zhang, Zheng, Haruhisa Okawa, Yuanyuan Wang, and Emily R. Liman. 2005. "Phosphatidylinositol 4,5-Bisphosphate Rescues TRPM4 Channels from Desensitization." *The Journal of Biological Chemistry* 280 (47): 39185–92.

Ziehn, Marina O., Andrea A. Avedisian, Seema Tiwari-Woodruff, and Rhonda R. Voskuhl. 2010. "Hippocampal CA1 Atrophy and Synaptic Loss during Experimental Autoimmune Encephalomyelitis, EAE." *Laboratory Investigation; a Journal of Technical Methods and Pathology* 90 (5): 774–86.

Publication #2: Nature Communications 2018

Improved methods for marking active neuron populations

Benjamien Moeyaert [1], Graham Holt[1,8], Rajtarun Madangopal [2], Alberto Perez-Alvarez [3], Brenna C. Fearey [3], Nicholas F. Trojanowski [4], Julia Ledderose[5], Timothy A. Zolnik[6], Aniruddha Das[7], Davina Patel[7], Timothy A. Brown[1], Robert N.S. Sachdev[6], Britta J. Eickholt[5,6], Matthew E. Larkum[6], Gina G. Turrigiano[4], Hod Dana [1,7], Christine E. Gee [3], Thomas G. Oertner[3], Bruce T. Hope[2] &, Eric R. Schreiter[1]

[1]Howard Hughes Medical Institute, Janelia Research Campus, 19700 Helix Drive, Ashburn, VA 20147, USA.
[2]Neuronal Ensembles in Addiction Section, Behavioral Neuroscience Research Branch, Intramural Research Program, National Institute on Drug Abuse, National Institutes of Health, Baltimore, MD 21224, USA.
[3]Institute for Synaptic Physiology, University Medical Center Hamburg-Eppendorf, 20251 Hamburg, Germany.
[4]Department of Biology, Brandeis University, Waltham, MA 02454, USA.
[5]Institute of Biochemistry, Charité - Universitätsmedizin Berlin, 10117 Berlin, Germany.
[6]NeuroCure Cluster of Excellence, Department of Biology, Humboldt University, 10117 Berlin, Germany
[7]Department of Neurosciences, Lerner Research Institute Foundation, Cleveland, OH 44195, USA.
[8]Present address: Program in Computational Biology and Bioinformatics, Duke University, Durham, NC 27708, USA.
Correspondence and requests for materials should be addressed to E.R.S. (email: schreitere@janelia.hhmi.org)

Specific contributions

The following paper has been published in Nature Communications. In our collaboration with the corresponding authors, I contributed to intellectual discussion, particularly relating to the timing of photoconversion light to the sensor calcium binding. I also actively participated in the editing of the manuscript prior to first submission and during revisions. However, the main authors chose to include their own timing and photoconversion data, which reflected the same results as my own (Supplementary figure 7). I am including my own data specifically demonstrating the change in fluorescence upon calcium binding and characterization of photoconversion timing (Supplementary figures 18 & 19).

I, _____, agree with the above statements as the direct supervisor.

_____, Date & Place_____

ARTICLE

Improved methods for marking active neuron populations

Benjamien Moeyaert [1], Graham Holt[1,8], Rajtarun Madangopal [2], Alberto Perez-Alvarez [3], Brenna C. Fearey [3], Nicholas F. Trojanowski [4], Julia Ledderose[5], Timothy A. Zolnik[6], Aniruddha Das[7], Davina Patel[7], Timothy A. Brown[1], Robert N.S. Sachdev[6], Britta J. Eickholt[5,6], Matthew E. Larkum[6], Gina G. Turrigiano[4], Hod Dana [1,7], Christine E. Gee [3], Thomas G. Oertner [3], Bruce T. Hope[2] & Eric R. Schreiter[1]

Marking functionally distinct neuronal ensembles with high spatiotemporal resolution is a key challenge in systems neuroscience. We recently introduced CaMPARI, an engineered fluorescent protein whose green-to-red photoconversion depends on simultaneous light exposure and elevated calcium, which enabled marking active neuronal populations with single-cell and subsecond resolution. However, CaMPARI (CaMPARI1) has several drawbacks, including background photoconversion in low calcium, slow kinetics and reduced fluorescence after chemical fixation. In this work, we develop CaMPARI2, an improved sensor with brighter green and red fluorescence, faster calcium unbinding kinetics and decreased photoconversion in low calcium conditions. We demonstrate the improved performance of CaMPARI2 in mammalian neurons and in vivo in larval zebrafish brain and mouse visual cortex. Additionally, we herein develop an immunohistochemical detection method for specific labeling of the photoconverted red form of CaMPARI. The anti-CaMPARI-red antibody provides strong labeling that is selective for photoconverted CaMPARI in activated neurons in rodent brain tissue.

[1] Howard Hughes Medical Institute, Janelia Research Campus, 19700 Helix Drive, Ashburn, VA 20147, USA. [2] Neuronal Ensembles in Addiction Section, Behavioral Neuroscience Research Branch, Intramural Research Program, National Institute on Drug Abuse, National Institutes of Health, Baltimore, MD 21224, USA. [3] Institute for Synaptic Physiology, University Medical Center Hamburg-Eppendorf, 20251 Hamburg, Germany. [4] Department of Biology, Brandeis University, Waltham, MA 02454, USA. [5] Institute of Biochemistry, Charité - Universitätsmedizin Berlin, 10117 Berlin, Germany. [6] NeuroCure Cluster of Excellence, Department of Biology, Humboldt University, 10117 Berlin, Germany. [7] Department of Neurosciences, Lerner Research Institute, Cleveland Clinic Foundation, Cleveland, OH 44195, USA. [8] Present address: Program in Computational Biology and Bioinformatics, Duke University, Durham, NC 27708, USA. Correspondence and requests for materials should be addressed to E.R.S. (email: schreitere@janelia.hhmi.org)

The coordinated activity of neurons that are spatially distributed throughout complex tissues like the brain are thought to mediate critical functions such as the selection and generation of actions in response to stimuli, learning from the outcomes of those actions, and the storage and recall of memories of those actions and outcomes. Methods to identify these neuronal ensembles based on their activity over various time and spatial scales are critical to furthering our understanding of brain function.

Activity-dependent genes such as the immediate early genes (IEGs) Fos and Arc[1] have been extensively used to mark and manipulate recently activated neuronal ensembles[2–5]. However, IEG-based methods suffer from poor temporal resolution (minutes to hours)[6,7] and the relationship between neuronal activity and IEG expression is indirect. Some of these issues can be circumvented by imaging neuronal calcium transients in vivo in behaving animals, for instance, using head-fixed two-photon microscopy through cranial windows[8] or epifluorescent microscopy through microendoscopic lenses[9,10]. Calcium has a direct and quantifiable relationship with electrical spiking in neurons[11]. However, live calcium signals can only be imaged with limited fields of view, and it is challenging to correlate these signals with post hoc in vitro analyses, such as immunohistochemistry or gene expression profiling.

As a new approach to examining active neuronal ensembles, we recently introduced CaMPARI, a photoconvertible green fluorescent protein whose irreversible photoconversion (PC) to a red form is not only dependent on the presence of light but also on the concentration of free calcium ions[12]. However, this early version of CaMPARI (CaMPARI1) had some shortcomings, including a modest PC contrast, slow calcium unbinding, and sensitivity to chemical fixatives such as formaldehyde[13].

In this work, we present CaMPARI2, an improved variant of CaMPARI1. Using site-directed amino acid mutagenesis combined with functional screening and selection, we significantly increase the contrast of green-to-red PC between the calcium-bound and calcium-free states. This effect is further enhanced by a higher brightness of the red form of the protein. CaMPARI2 also has a higher rate of calcium unbinding compared to CaMPARI1. To accommodate different cell types and calcium levels, we develop a range of affinity variants, with dissociation constants (K_d) for calcium binding ranging from 100 nM to 1 μM. We demonstrate the functionality of CaMPARI2 in vitro and in vivo. Additionally, we develop a monoclonal antibody that specifically recognizes the photoconverted red form, allowing immunohistochemical detection and selective amplification of the red CaMPARI2 signal in fixed cells or tissue.

Results

Engineering CaMPARI2. We sought to improve the brightness of the green and red forms of CaMPARI1 and improve the difference in PC rate between high and low calcium conditions to enhance the visible contrast between active and non-active cells in a neuronal population. We targeted site-saturation mutagenesis to amino acid positions around the fluorescent protein chromophore and at the protein interface between the fluorescent protein and the calcium-sensitive domains of CaMPARI, as defined by the crystal structures of CaMPARI and other genetically encoded calcium inhibitors[12,14,15]. We assayed fluorescence and PC contrast (extent of PC in high-calcium vs. low-calcium conditions) of ~950 unique single amino acid substitutions at 50 separate positions of CaMPARI1_W391F-V398L in a medium-throughput assay in bacterial lysates[12]. CaMPARI1_W391F-V398L was chosen as a template for optimization due to its four times faster calcium release kinetics and reasonable K_d for Ca^{2+} (~ 200 nM).

Several single amino acid variants improved CaMPARI brightness, PC contrast, or both (Supplementary Table 1). A library of combinations of these single amino acid variants was then screened in the same way, which revealed variants with further improved brightness and PC contrast (Supplementary Table 2).

One variant with five amino acid substitutions was selected that showed significantly higher fluorescence in both the green and red form, nearly four-fold higher PC contrast, and exhibited a K_d for calcium of 285 nM (CaMPARI1_W391F-V398L-Q142V-F198Y-C202T-L217I-N345S (Fig. 1a, Supplementary Fig. 1, Supplementary Table 2)). To enable a wide range of applications in different cell types and organisms with various baseline calcium levels, we mutated key residues in the calmodulin-binding peptide at positions that were previously identified to alter the calcium affinity of CaMPARI[12]. We generated 15 variants with K_d values between 145 nM and 2.1 μM (Supplementary Table 3) and selected four that spanned this affinity range (Supplementary Table 4) to characterize further. Three consecutive epitope tags (FLAG–HA–myc) were added to the C-terminus of the optimized CaMPARI and its affinity variants, enabling flexible immunohistochemical detection in tissue. CaMPARI1_W391F-V398L-Q142V-F198Y-C202T-L217I-N345S_FLAG-HA-myc is hereafter referred to as CaMPARI2 (Supplementary Fig. 1). Addition of the C-terminal epitope tags led to increased calcium affinity (Supplementary Fig. 2), although the reasons for this observation are unclear.

Characterization of CaMPARI2. We characterized purified CaMPARI2 protein in vitro (Table 1, Fig. 1, Supplementary Fig. 3 and 4) and found that the green and red forms were 60% and 130% brighter, respectively, compared with CaMPARI1 and that calcium unbinding occurred several times faster. Although the rate of PC in high calcium conditions is similar for CaMPARI1 and CaMPARI2 (0.020 s^{-1} vs. 0.026 s^{-1}), CaMPARI2 has a markedly lower PC rate in its calcium-free state (0.00022 s^{-1}) compared to CaMPARI1 (0.0010 s^{-1}) (Fig. 1 and Supplementary Table 5). Thus CaMPARI2 exhibits a six-fold larger PC rate contrast (PC rate with calcium/PC rate without calcium) compared to CaMPARI1. We screened a CaMPARI2 library with site-saturated mutations at ~50 positions for higher PC rate when saturated with calcium but did not identify significantly improved variants.

Next, CaMPARI1 and CaMPARI2 were compared in dissociated primary rat hippocampal neurons in culture. To compare PC rates, we shined 405 nm light through a widefield microscope objective while driving action potential firing at 80 Hz and followed the PC over time (Fig. 1c, right). As we saw with purified proteins, the rates of PC of CaMPARI1 and CaMPARI2 during action potential firing (high calcium) were similar (0.22 s^{-1} vs. 0.14 s^{-1}, respectively), but the rate of PC in resting neurons (low calcium) was five times lower for CaMPARI2, resulting in a three-fold higher PC rate contrast (Supplementary Fig. 5 and Supplementary Table 5). We next measured the extent of PC of CaMPARI1, CaMPARI2, and four affinity variants following different frequencies of action potential firing during a 2 s light pulse. As expected, the highest affinity variant (CaMPARI2_F391W) reached maximum PC at lower stimulation frequencies, while the lowest affinity variant (CaMPARI2_L398T) required higher stimulation frequencies (Fig. 1d). CaMPARI1 exhibited relatively high amounts of PC in resting neurons, resulting in a low PC contrast at all stimulation frequencies. Finally, we saw that CaMPARI2 has faster calcium unbinding kinetics in neuron cultures (Supplementary Fig. 6). The relative rates of calcium unbinding between the different affinity mutants depended on the number of evoked action
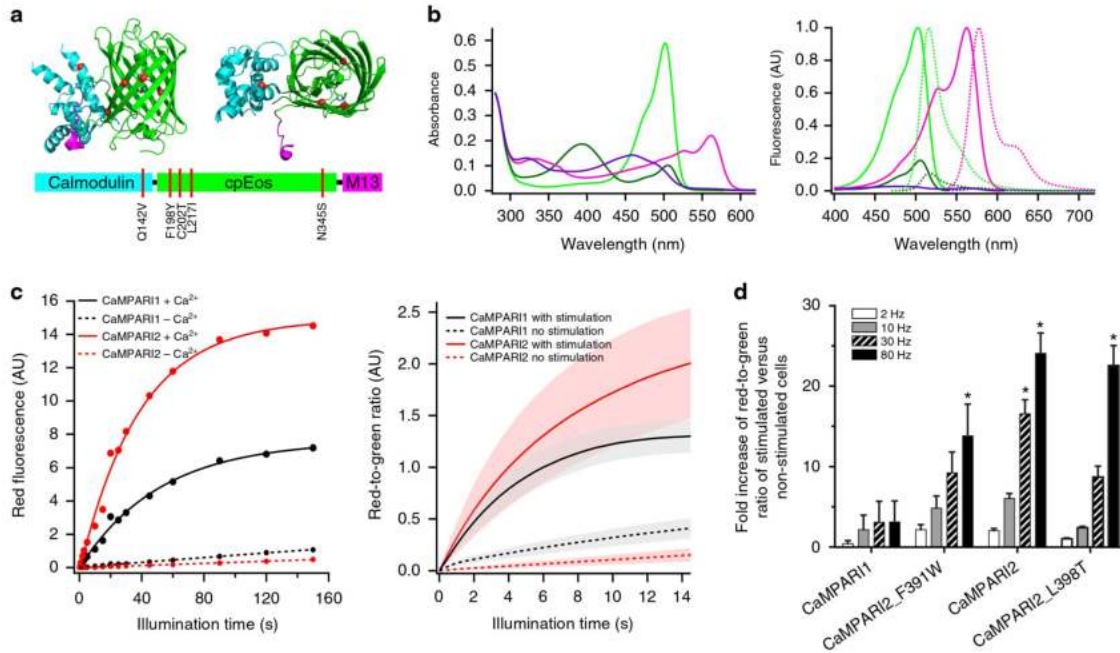
Fig. 1 In vitro characterization of CaMPARI2. **a** Primary (bottom) and tertiary (top) structures of CaMPARI2. Mutations relative to CaMPARI1_W391F-V398L are shown in red. Two orthogonal views of the same CaMPARI crystal structure (PDB ID 4OY4 [https://doi.org/10.2210/pdb4OY4/pdb] are shown. **b** Absorption (left) and fluorescence (right) excitation (full line) and emission (dotted line) spectra of CaMPARI2. Green and magenta spectra represent the green and red forms of CaMPARI; bright and dark lines represent the calcium-free and calcium-saturated states. **c** Photoconversion timecourse showing the red fluorescence of CaMPARI1 (black) and CaMPARI2 (red) as a function of exposure to 405 nm light. Left: photoconversion of purified CaMPARI protein in the presence (solid lines) or absence (dashed lines) of calcium. Right: photoconversion of primary rat hippocampal neurons with (solid lines) or without (dashed lines) 80 Hz stimulation. **d** Fold increase of the red-to-green ratio of CaMPARI variant-expressing neurons after 2 s of photoconversion during different electrical stimulation frequencies relative to no stimulation. Error bars are standard deviation, $n = 3$, asterisks denote values significantly differing from the corresponding CaMPARI1 value ($p < 0.001$, Dunnett's multiple comparisons test)

Table 1 Photophysical properties of CaMPARI1, CaMPARI2, CaMPARI2_F391W, and CaMPARI2_L398T

	λ_{ex}, G (nm)	λ_{em}, G (nm)	λ_{ex}, R (nm)	λ_{em}, R (nm)	ε, G (mM^{-1} cm^{-1})	ε, R (mM^{-1} cm^{-1})	QY, G (%)	QY, R (%)	Brightness[a], G	Brightness[a], R	K_d Ca^{2+} (nM)	$\Delta F/F$	k_{off} (s^{-1})
CaMPARI1	498	514	560	576	73.5 ± 5.8	32	78	58	1.0	1.0	134.7 ± 10.8	5.9 ± 0.2	0.29 ± 0.017
CaMPARI2	502	516	562	577	111.3 ± 2.2	65	81	65	1.6	2.3	199.2 ± 11.8	7.8 ± 1.8	1.43 ± 0.020
CaMPARI2_F391W	502	516	562	577	114.8 ± 1.7	60	81	62	1.6	2.0	109.7 ± 2.7	6.8 ± 0.3	0.59 ± 0.082
CaMPARI2_L398T	502	516	562	577	114.2 ± 3.6	58	80	66	1.6	2.1	824.6 ± 26.2	5.4 ± 0.8	2.50 ± 0.063

ε is the extinction coefficient in mM^{-1} cm^{-1}
[a]Brightness is expressed as molecular brightness (extinction coefficient × quantum yield) normalized to CaMPARI1 in the corresponding state. Full table can be found as Supplementary Table 4. ± values are SD from $n = 3$ or 4 ($n = 15$ for k_{off})

potentials and were different from the stopped flow experiments with purified proteins (Table 1, Supplementary Table 4). Nevertheless, CaMPARI2 and its variants generally exhibited faster calcium unbinding kinetics than CaMPARI1, and tighter calcium binding correlated with slower calcium unbinding. We also confirmed that the extent of PC depended on the timing between the stimulus and the light pulse in a way that reflected calcium unbinding kinetics (Supplementary Fig. 7).

We next compared CaMPARI1 to CaMPARI2 (CaMPARI2_F391W-L398V without epitope tags, see Supplementary Table 4) in CA1 neurons of organotypic rat hippocampal slice cultures during whole-cell patch clamp electrophysiology (Fig. 2).

Similar to our findings in dissociated neuron cultures, we found that CaMPARI2 is brighter and has a 2.5-fold higher PC rate contrast compared to CaMPARI1 (Supplementary Table 5). After photoconverting during synaptic stimulation, the red signal is strongly visible for at least 24 h, but the R/G ratio falls to ~20% of its maximum value after 72 h, allowing re-labeling by repeating the stimulation and PC (Supplementary Fig. 8).

The PC signal was then compared in vivo in larval transgenic zebrafish expressing either CaMPARI1 or CaMPARI2 from a neuron-specific promoter. When neuronal activity was blocked with the sodium channel blocker tricaine during a PC light pulse, the red-to-green (R/G) ratios were slightly lower with

78
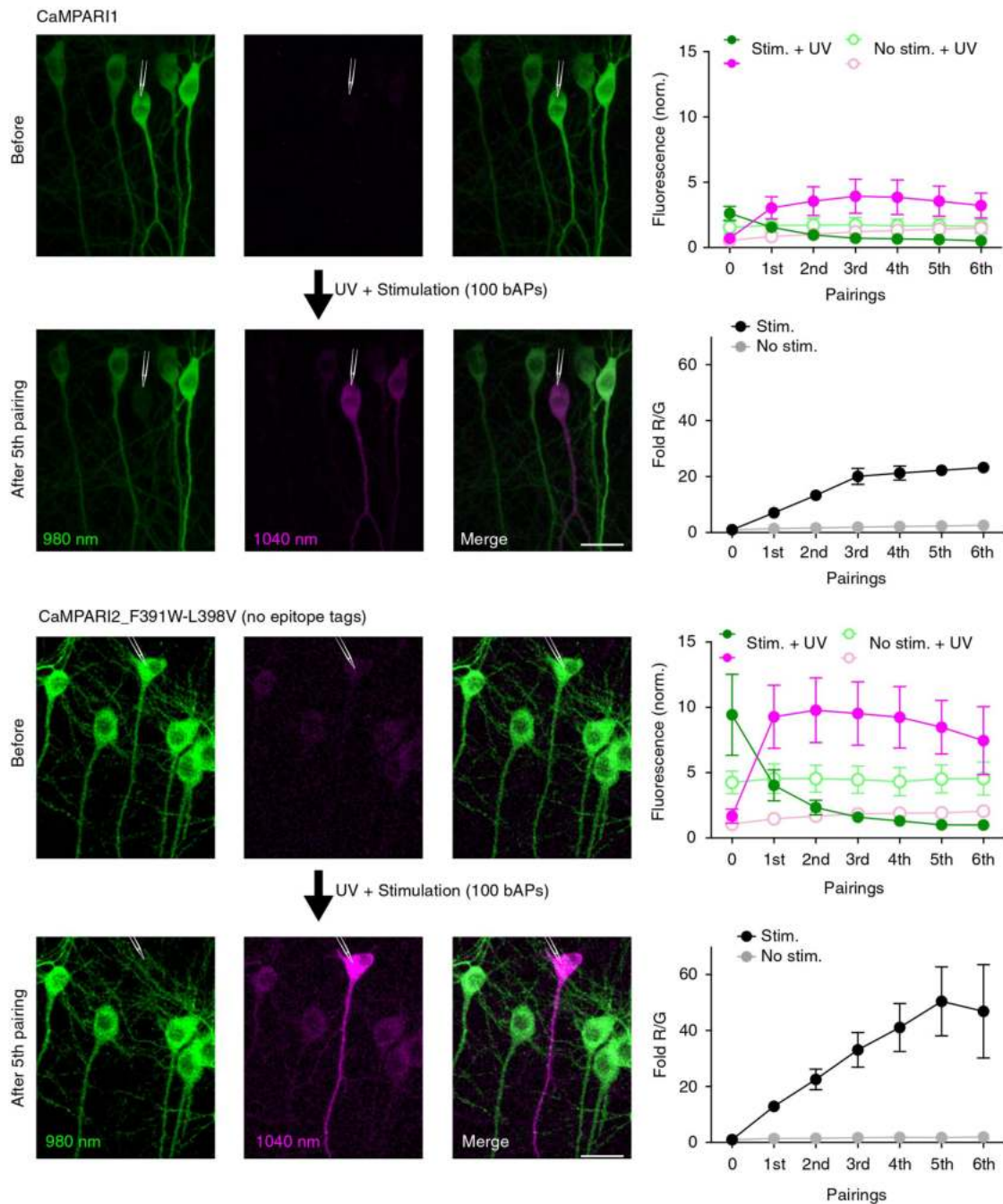
Fig. 2 Brightness and photoconversion of CaMPARI1 and CaMPARI2. Two-photon images of CaMPARI1 and CaMPARI2_F391W-L398V (no epitope tags) expressed in CA1 neurons of rat hippocampal slice cultures before and after pairing of stimulation (100 bAPs at 100 Hz) with UV light (2 s, 16 mW mm^{-2}). Two lasers were simultaneously employed to acquire images of the green (980 nm) and red species (1040 nm) of the CaMPARI variants. A single cell, denoted by a pipette drawing, is patched and stimulated during the UV illumination. Green and red fluorescence is quantified along with the fold R/G in both stimulated (CaMPARI1 $n = 5$; CaMPARI2 $n = 6$) and unstimulated neighboring neurons (CaMPARI1 $n = 5$; CaMPARI2 $n = 14$) as a function of the number of pairings. Error bars are SEM. Note that fluorescence intensity is normalized to the laser power (see Methods), showing the increased brightness of CaMPARI2. Scale bars are 25 μm

CaMPARI2, in agreement with a lower baseline PC rate for CaMPARI2 (Fig. 3, Supplementary Fig. 9, 10). After PC of freely swimming fish to mark neurons with ongoing spontaneous activity, we measured many neurons with higher red/green ratios and a larger range of red/green ratios with CaMPARI2 (Supplementary Fig. 9 and 10), suggesting that it is possible to mark activity on a fine scale in the CaMPARI2 transgenic zebrafish.

Finally, to demonstrate the ability of CaMPARI2 to mark neurons in response to specific stimuli in vivo, we expressed CaMPARI2 and CaMPARI2-F391W in the mouse visual cortex and measured CaMPARI2 PC as well as traditional calcium indicator fluorescence in response to specific visual stimuli. Bright CaMPARI2 labeling was evident 15 days after adeno-associated virus (AAV) injection and individual layer 2/3 neurons could be easily identified (Fig. 4a). Lightly anesthetized mice were presented with upward drifting gratings while illuminated with PC light. Following the PC, the calcium response of individual neurons was recorded in response to the presentation of drifting gratings in eight different directions (Fig. 4b, Methods).

We identified neurons with significant calcium responses (analysis of variance (ANOVA) test, $p < 0.01$) during presentation of any of the visual stimuli and grouped them as neurons with a significant calcium response during the upward drifting gratings displayed during PC (PC-tuned) and with no significant response to the upward drifting grating but with significant responses to other directions of motion (responsive but not PC-tuned). In addition, we calculated the orientation selectivity index (OSI)[16] of each neuron. We grouped together all responsive neurons with OSI < 0.5 (broadly tuned, Fig. 4c). This group of cells with broad-tuning to grating orientation contains most of the inhibitory cells[16–18]. It was previously shown that inhibitory neurons have lower response amplitudes during calcium imaging[17] and lower OSI for responding to drifting grating stimuli than excitatory neurons[16,18], allowing us to categorize them separately based on their response profile.

Of all the segmented neurons, 11.5% were identified as responsive (48/359 and 18/203 and 41/525, 48/366, and 63/419 for two CaMPARI2 and three CaMPARI2-F391W mice, respectively) and 3.2% was PC-tuned (10 and 1 and 17, 26, and 6 for two CaMPARI2 and three CaMPARI2-F391W mice, respectively). The R/G ratio of the responsive cells was correlated to the peak change in fluorescence for the northward moving grating stimulus (Fig. 4c, Supplementary Fig. 11 top) but not to the orthogonal direction stimulus (Supplementary Fig. 11 middle). The R/G ratio was significantly higher for PC-tuned cells than both responsive and not PC-tuned cells and cells that had no significant change to the visual stimuli (Fig. 4d, Supplementary Fig. 11 bottom, Wilcoxon Rank-Sum Test), demonstrating that CaMPARI2 can mark neurons that are responsive to specific stimuli in vivo. We note that the PC of CaMPARI2 yielded better separation among these groups than CaMPARI2-F391W (Supplementary Fig. 11), presumably because the higher calcium affinity of CaMPARI2-F391W led to partial saturation in the absence of stimuli that resulted in higher baseline PC and lower contrast between responsive and non-responsive neurons.

Development of an anti-CaMPARI-red antibody. Although the red form of CaMPARI2 is bright and easily detectable in live cells and tissue with conventional fluorescence microscopy, chemical tissue fixation using formaldehyde, for example, generally results in loss of fluorescent signal due to changes in protein conformation following chemical modification by formaldehyde. To
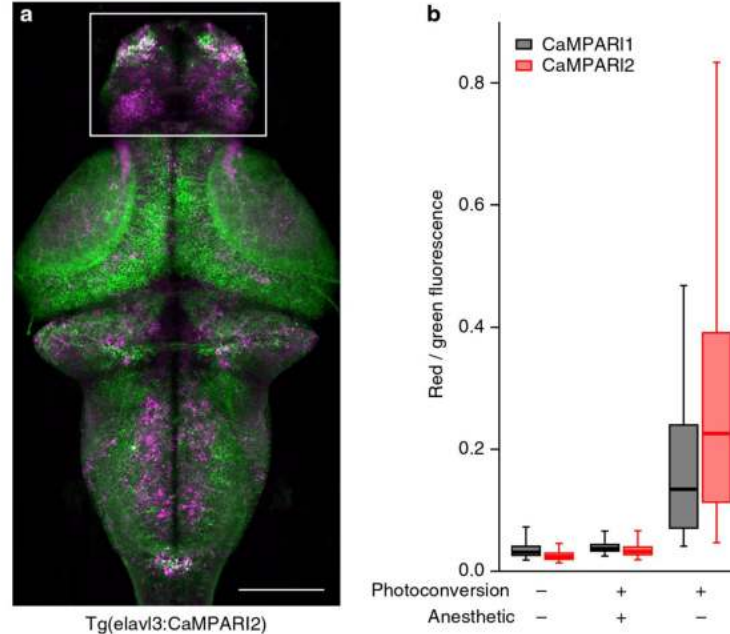
Fig. 3 In vivo characterization of CaMPARI2 in zebrafish. **a** Representative z-projection from a confocal stack from a 6-dpf larval transgenic pan-neuronal CaMPARI2 zebrafish brain photoconverted for 30 s during free swimming. **b** Boxplots represent the distribution of red-to-green fluorescence signals from individual neurons (between 1800 and 6000 cells per condition, representing 2–4 fish (Supplementary Fig. 9, 10). Data are measured from neurons in the forebrain (white box in **a**) following photoconversion of either freely swimming or tricaine-anesthetized larval zebrafish. Box represents 1st, 2nd, and 3rd quartile, while whiskers represent the 5th and 95th percentile. Scale bar is 100 μm
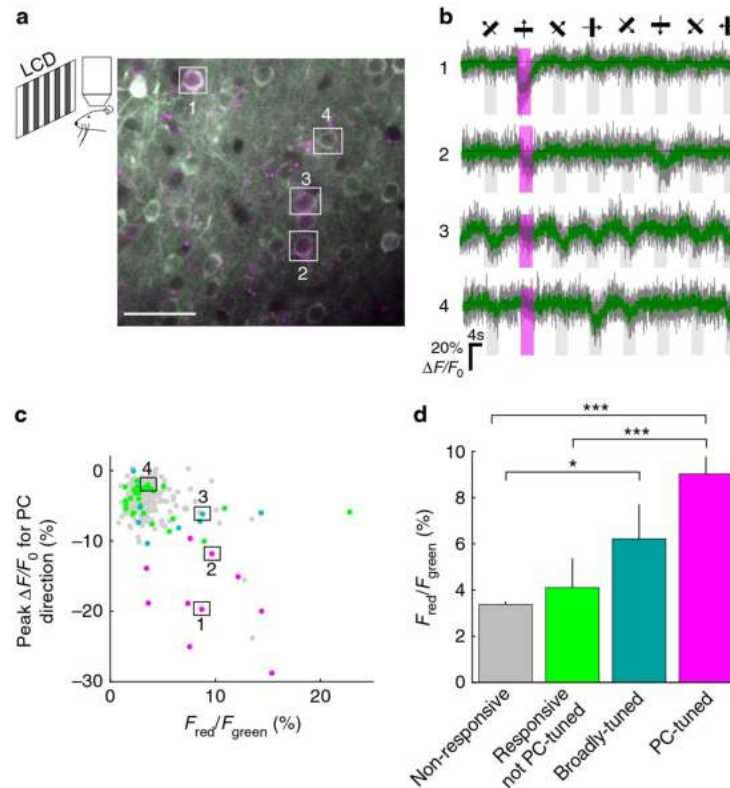
Fig. 4 CaMPARI2 activity and PC in mouse primary visual cortex. **a** Schematic of the experimental setup (left). Two-photon fluorescence signal from cortical layer 2/3 neurons in V1 after PC (right). **b** Changes in fluorescence signal from four example cells marked in **a**. Cell numbers 1–2 are PC-tuned and have high OSI (0.8 and 0.92, respectively), cell number 3 is responsive and broadly tuned (OSI = 0.22), and cell number 4 is responsive and not PC-tuned (OSI = 0.96). **c** Correlation between peak $\Delta F/F_0$ for the northward moving grating stimulus and the red-to-green ratio for individual responsive cells expressing CaMPARI2. Cells were grouped into four categories: non-responsive (not significantly responsive cells, gray dots), broadly tuned (significantly responsive and OSI < 0.5, cyan), PC-tuned (OSI > 0.5 and significant response to northward moving grating stimulus, magenta), and not PC-tuned (OSI > 0.5 and no significant response to northward moving grating stimulus, green). **d** Comparison of red-to-green ratio distribution of the four groups mentioned in **c**. PC efficiency was higher for PC-tuned cells, leading to a significant increase in red-to-green ratio. *$p < 0.05$, ***$p < 0.001$ (Wilcoxon Rank-Sum Test). Error bars indicate the standard error. Scale bar is 40 μm

improve the signal-to-noise ratio when imaging CaMPARI in fixed tissue, we sought to develop a monoclonal antibody that specifically targets the photoconverted form of CaMPARI and allows recovery or amplification of the red signal.

To do so, we purified and photoconverted EosFP protein, subjected it to proteolysis, and further purified the proteolytic fragment containing the red chromophore (Fig. 5a and Supplementary Fig. 12). This proteolytic fragment, which is identical to the equivalent region of CaMPARI1 and CaMPARI2, was used as an antigen to generate a mouse monoclonal antibody ("anti-CaMPARI-red") using standard protocols. Western blots containing several fluorescent proteins demonstrate the specificity of the anti-CaMPARI-red antibody for the photoconverted red forms of green-to-red photoconvertible fluorescent proteins, but not the green form (Supplementary Fig. 13). Other commonly used red fluorescent proteins (such as mCherry, mNeptune, mRuby) with different chromophore structures were not recognized by anti-CaMPARI-red. The antibody amino acid sequence was determined and is given in Supplementary Fig. 14.

Following PC in vivo, we performed immunohistochemistry on mouse and rat brain slices expressing CaMPARI2 to confirm the

functionality and specificity of anti-CaMPARI-red antibody labeling in complex tissue. Similar to cell culture experiments, the endogenous green and especially red CaMPARI fluorescence decreased significantly after fixation but could be recovered with antibody staining (Figs. 5b, 6 and Supplementary Fig. 15, 16 and 17).

In both cultured cells and rodent brain tissue, the anti-CaMPARI-red antibody specifically recognizes the photoconverted form of CaMPARI and the stained images are reflective of the endogenous red CaMPARI2 signal in vivo (Figs. 5b, 6 and Supplementary Fig. 16, 17), although staining of dissected larval zebrafish brains with anti-CaMPARI-red antibody was unsuccessful in our hands. The immunohistochemical labeling correlates with the endogenous red fluorescent signal of the photoconverted CaMPARI2 molecules (Fig. 6) and the ratio of the intensity of the anti-CaMPARI-red signal to the anti-FLAG epitope tag signal (total CaMPARI) correlates with the endogenous R/G fluorescence ratio of CaMPARI. In other words, the immunohistochemical labeling reflects the relative extent of PC and the endogenous R/G fluorescence intensity ratio of CaMPARI in multiple cell types (Fig. 6).
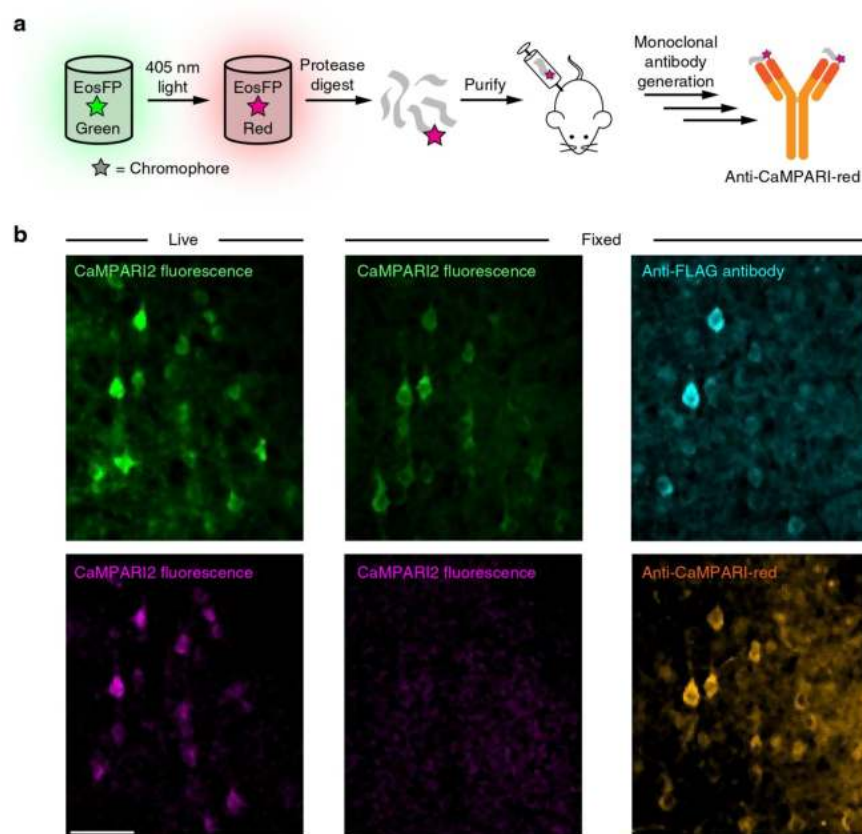
Fig. 5 Anti-CaMPARI-red antibody. **a** Schematic representation of the protocol used to generate the anti-CaMPARI-red monoclonal antibody. **b** Green (top) and red (bottom) endogenous CaMPARI2 fluorescence (left and middle columns) in mouse brain tissue imaged before (left column) and after (middle column) chemical fixation with paraformaldehyde. The right column shows the same region of fixed tissue after antibody staining with anti-FLAG antibody for total CaMPARI (top, cyan) and anti-CaMPARI-red antibody (bottom, orange). Note that following chemical fixation much of the red CaMPARI fluorescence was lost but was recovered with the anti-CaMPARI-red antibody staining. Scale bar is 50 μm

Discussion

As a complement to existing techniques for marking active neuronal populations, we recently introduced CaMPARI, a fluorescent protein whose green-to-red PC is calcium-dependent. CaMPARI allows marking of active neurons with finer time resolution than activity-dependent gene expression and provides a more permanent signal than transient calcium indicators like GCaMP. In this work, we have developed CaMPARI2, with higher molecular brightness, faster calcium unbinding kinetics, and less background PC in the absence of calcium compared to CaMPARI1, leading to a higher contrast between high-calcium and low-calcium cells. CaMPARI2 is therefore an improved tool for a range of applications. For instance, the reduced background PC is useful for integrating sparse neuronal activity, which calls for long illumination times. Second, the 130% higher brightness of the red form of CaMPARI2 compared to the red form of CaMPARI1 facilitates imaging and image processing. This should allow for detection of smaller amounts of photoconverted CaMPARI from smaller structures within complex tissue. The slow CaMPARI turnover dramatically increases the potential field of view for live imaging experiments. Distant neurons that are active at an instant of time can be marked by PC and then mapped at high resolution post hoc without time constraints. Relabeling will allow chronic imaging of active neuronal ensembles.

Additionally, the faster calcium unbinding kinetics increases the temporal resolution of calcium activity integration, allowing for more precise PC of neurons active during a short epoch of animal behavior. A corollary to faster calcium release kinetics of CaMPARI2 is that, during each calcium transient, less time is spent in the state that photoconverts at a high rate. This leads to less absolute PC of CaMPARI2 relative to CaMPARI1 for an equivalent number of calcium transients and equivalent light exposure. This is largely offset by the brighter red fluorescence per molecule of CaMPARI2 but could be limiting under some circumstances. Our experiments in larval zebrafish brain showed a similar amount of red fluorescence with CaMPARI1 and CaMPARI2 and a wide distribution of red/green values among CaMPARI2-expressing neurons, indicating that it can delineate fine gradations of activity. In vivo calcium imaging and PC in mouse visual cortex confirms that CaMPARI2 is able to selectively label neurons that are active during a specific stimulus. We identified variants of CaMPARI2 with higher or lower calcium affinity and variable calcium release kinetics (Supplementary Table 4) that might be preferable in other tissues or cell types.

Many conditions for chemical fixation and preservation of tissue lead to unfolding of proteins, which results in a loss of fluorescent signal from fluorescent proteins. To circumvent this problem and to amplify the signal from the red photoconverted
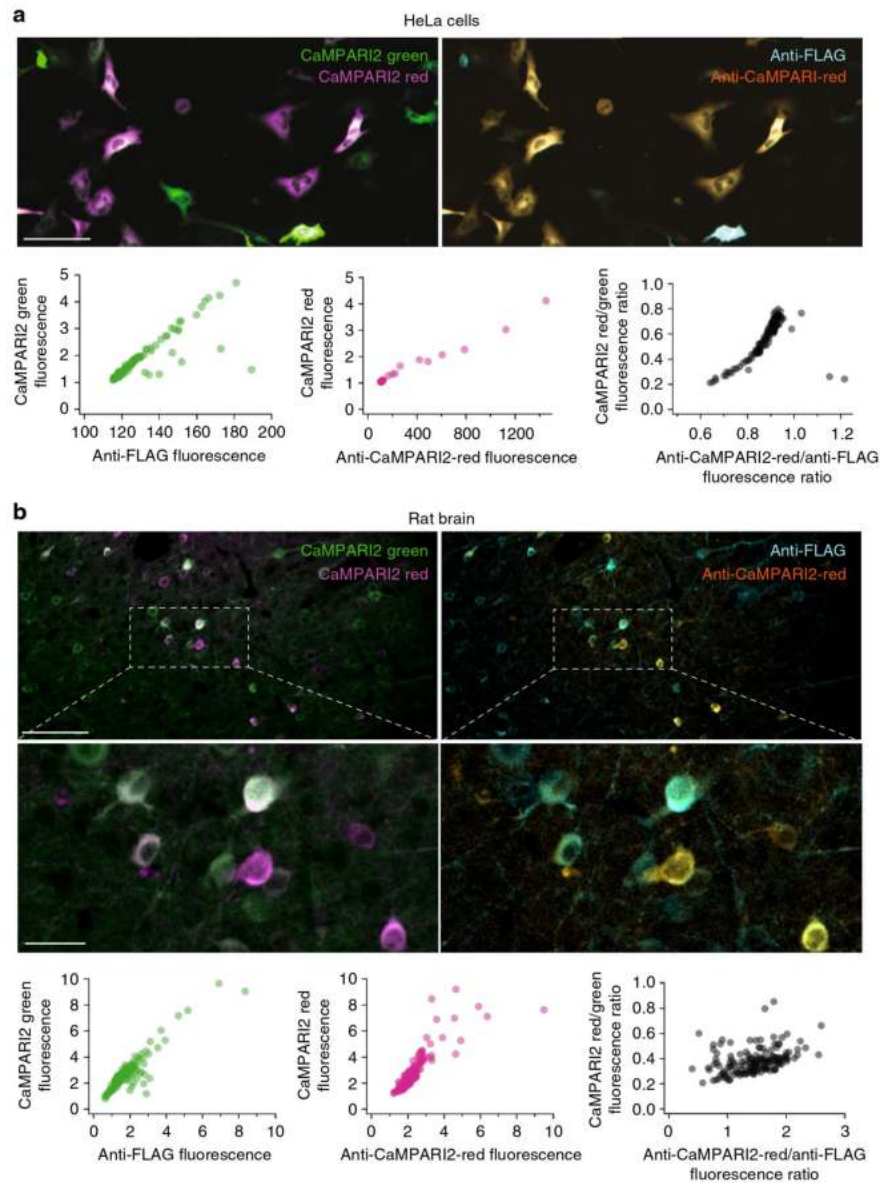
Fig. 6 Comparison between endogenous fluorescence and anti-CaMPARI-red antibody stain. HeLa cells (**a**) and rat brain (**b**) were immunostained with anti-CaMPARI2-red and anti-FLAG antibody as described in Supplementary Methods. Plots of endogenous fluorescence vs. the antibody signal show a linear relationship (green and magenta scatterplots). The black scatterplots show the correlation between the endogenous red-to-green ratio and the anti-CaMPARI-red-to-anti-FLAG ratio. Scale bars are 100 or 25 μm (insets)

form of CaMPARI, we developed a mouse monoclonal antibody that specifically detects the red, but not green, CaMPARI chromophore. It also recognizes the red chromophores of other common green-to-red photoconvertible fluorescent proteins (such as EosFP, Kaede, and mMaple) but does not recognize conventional red fluorescent proteins (such as mCherry), which have a different chromophore structure. Although the chromophore of CaMPARI and other fluorescent proteins is normally buried within the folded structure of the protein and is thus not accessible for antibody recognition, we hypothesize that protein unfolding during chemical fixation exposes the chromophore for binding by the antibody.

In summary, our current work expands and improves the toolkit for marking active neuronal populations in behaving animals. CaMPARI2 offers improved brightness and contrast over CaMPARI1, and we recommend its adoption for most preparations. Additionally, the anti-CaMPARI-red antibody offers additional flexibility by enabling immunohistochemical detection of CaMPARI PC, bringing back the signal when endogenous fluorescence is lost during chemical fixation of tissue.

Methods

Directed evolution of CaMPARI2 and in vitro characterization. We conducted multiple rounds of site-saturation mutagenesis, functional screening, and selection to improve the properties of CaMPARI. Site-saturation mutagenesis at individual amino acid positions was done using the QuikChange Multi protocol (Agilent). Generally, 90 colonies were picked from a site-saturation mutagenesis library at each amino acid position, along with controls, into deep-well 96-well blocks. The T7 Express *Escherichia coli* bacteria (New England Biolabs) were grown at 30 °C for 36 h and pelleted by centrifugation. Soluble lysate was prepared from the pellets by incubation with Bacterial Protein Extraction Reagent (Thermo Fisher) followed by centrifugation. Functional screening included measurement of green and red fluorescence of bacterial lysates using a fluorescence plate reader (Tecan) after addition of 0.5 mM $CaCl_2$ or 1 mM EGTA to separate lysate aliquots. Fluorescence was measured again after irradiation with 405 nm light using a light-emitting diode (LED) array (Loctite; 1 min, ~200 mW cm^{-2}) and again after addition of 10 mM EGTA and 5 mM $CaCl_2$, respectively. From these fluorescence reads, we selected mutants with the highest difference in extent of PC with calcium compared to without calcium. Secondary preference was given to variants that also appeared brighter in the green and red forms. Multiple beneficial amino acid substitutions were combined in small libraries and additional screening and selection was conducted in the same way. Details of the in vitro characterization of CaMPARI variants are provided in Supplementary Methods.

PC and electrophysiology in rat slice cultures. Rats were housed and bred at the University Medical Center Hamburg animal facility. All procedures were performed in compliance with German law and according to protocols approved by the Behörde für Gesundheit und Verbraucherschutz of the City of Hamburg.

CaMPARI1 (Addgene #604021) or CaMPARI2 (without C-terminal epitope tags) were subcloned into a pAAV vector under the control of a human synapsin1 promoter. Mutations F391W and L398V were introduced in CaMPARI2, resulting in CaMPARI2_notags_F391W-L398V.

Hippocampal slice cultures from Wistar rats were prepared at postnatal days 4–7 as described[19]. No antibiotics were added to the culture medium. At days in vitro (DIV) 13–17, single-cell electroporation was used to transfect CA1 pyramidal neurons with CaMPARI1 or CaMPARI2_notags_F391W-L398V. Thin-walled pipettes were filled with intracellular K-gluconate based solution into which plasmid DNA was diluted to 20 ng μl^{-1}. The intracellular solution contained in (mM): 135 K-gluconate, 4 $MgCl_2$, 4 Na_2-ATP, 0.4 Na-GTP, 10 Na_2-phosphocreatine, 3 ascorbate, 0.02 Alexa Fluor 594, and 10 HEPES (pH 7.2). Pipettes were positioned against neurons and DNA was ejected using an Axoporator 800A (Molecular Devices) with 50 hyperpolarizing pulses (−12 V, 0.5 ms) at 50 Hz[20].

Experiments were performed 3–4 days after electroporation (DIV 16–20). The custom-built two-photon imaging set-up was based on an Olympus BX51WI microscope equipped with a LUMPlan W-IR2 ×60/0.9 NA objective (Olympus), controlled by the open-source software package ScanImage[21]. Two pulsed Ti: Sapphire lasers (MaiTai DeepSee, Spectra Physics) controlled by electro-optic modulators (350–80, Conoptics) were used to excite CaMPARI green (980 nm) and red species (1040 nm), respectively. z-Stacks of CaMPARI-expressing neurons were acquired by sequentially scanning each z-plane at 980 and 1040 nm. Emitted photons were collected through objective and oil-immersion condenser (1.4 NA, Olympus) with two pairs of photomultiplier tubes (PMTs, H7422P-40, Hamamatsu). 560 DXCR dichroic mirrors and 525/50 and 607/70 emission filters (Chroma Technology) were used to separate green and red fluorescence. Excitation light was blocked by short-pass filters (ET700SP-2P, Chroma).

Hippocampal slice cultures were placed in the recording chamber of the microscope and continuously perfused with artificial cerebrospinal fluid saturated with 95% O_2 and 5% CO_2 and consisting of (in mM): 119 NaCl, 26.2 $NaHCO_3$, 11 D-glucose, 1 NaH_2PO_4, 2.5 KCl, 4 $CaCl_2$, and 4 $MgCl_2$ (pH 7.4, 308 mOsm) at room temperature (21–23 °C). Whole-cell recordings from CaMPARI-expressing CA1 pyramidal cells were made at room temperature (21–23 °C) with a Multiclamp 700B amplifier (Molecular Devices) under the control of Ephus software written in Matlab (The MathWorks)[22]. Patch pipettes with a tip resistance of 3–4 MΩ were filled with (in mM): 135 K-gluconate, 4 $MgCl_2$, 4 Na_2-ATP, 0.4 Na-GTP, 10 Na_2-phosphocreatine, 3 ascorbate, and 10 HEPES (pH 7.2, 295 mOsm). Series resistance was <20 MΩ. In current clamp mode, somatic current injections of 1 ms duration and 3.5 nA current amplitude triggered back-propagating action potentials (bAPs) at the resting membrane potential.

Two brief ultraviolet (UV) light pulses (395 nm, 100 ms, 16 mW mm^{-2}, 0.1 Hz) were delivered through the objective using a Spectra X Light Engine (Lumencor) just before imaging to photoswitch CaMPARI into its bright state[12]. The PMTs were protected by shutters (Uniblitz) during the UV pulses. To compare brightness and PC of CaMPARI variants, CaMPARI-expressing neurons were patched and stimulated to fire 100 bAPs at 100 Hz, while simultaneously delivering PC light (395 nm, 2 s, 16 mW mm^{-2}). After PC, another z-stack was taken to quantify the change in green and red fluorescence. This procedure was repeated 5–6 times. In experiments designed to monitor turnover of photoconverted CaMPARI, a monopolar electrode was placed in *stratum radiatum* to strongly stimulate synapses onto CA1 CaMPARI-expressing neurons (100 pulses of 0.2 ms duration, at 100 Hz). PC was achieved by delivery of UV light (395 nm, 2 s, 16 mW mm^{-2})

with a 1 s delay from stimulus onset. Slices were returned to the incubator between imaging sessions and CaMPARI fluorescence was monitored for up to 72 h.

For the CaMPARI2 turnover experiments, CA1 neurons in rat organotypic hippocampal slice cultures were electroporated at DIV 15 with DNA (20 ng μl^{-1}) encoding CaMPARI2_F391W-L398V (no epitope tags). Four days later, two-photon z-stacks were collected using two MaiTai Deep See lasers. For each z-plane, two frames (images) were acquired, exciting at 980 nm (2–5 mW measured at the back-focal plane of the objective) and 1040 nm (3–8 mW), respectively. The procedure was repeated several times (up to 3 days). Between imaging sessions, slices were put back in the incubator. To increase intracellular calcium in response to synaptic activity, a monopolar electrode was placed in the stratum radiatum and 0.2 ms electrical pulses were delivered 100 times at 100 Hz at an intensity that induced postsynaptic spiking in a neighboring nontransfected CA1 neuron. UV light (395 nm, 16 mW mm^{-2}) was applied for 2 s with a 1 s delay relative to the start of stimulation (24 neurons, 4 slices). Images were taken at time points t = −0.5, 0, 6, 12, 24, 30, 48, 60, 72, and 72.5 h with t = 0 immediately after stimulation +UV light or UV light alone. To compare intensity between imaging sessions, images were normalized to a calibration solution containing 200 μg ml^{-1} fluorescein and 100 μg ml^{-1} sulforhodamine 101. These higher dye concentrations were selected to closely match the intensity of the CaMPAR2 green species prior to PC and the red species after PC. Fluorescence values of the CaMPARI green and red channels were divided by the corresponding calibration values. R/G is the normalized red fluorescence divided by the normalized green fluorescence.

A macro written in Fiji[23] was used for image analysis (see Supplementary Methods). Image stacks taken with 2P excitation at 980 nm and 1040 nm were *xyz*-aligned to correct for chromatic aberration[24]. After median filtering and rolling ball background subtraction, fluorescence values were obtained from regions of interest (ROIs) drawn onto maximum intensity projections. As the brightness of CaMPARI versions varies, higher laser power is required to image neurons expressing CaMPARI1 than CaMPARI2_F391W-L398V (no epitope tags) (980 nm: 4–10 vs. 3–5 mW; 1040 nm: 10–15 vs. 4–8 mW, respectively), when measured at the back-focal plane of the objective). To allow comparison between imaging sessions, 1 ml of an aqueous solution containing 2 μg ml^{-1} fluorescein (Alcon) and 0.2 μg ml^{-1} sulforhodamine 101 (Tocris) was placed in the imaging chamber after each session and fluorescence intensity was measured with identical acquisition settings used to collect the CaMPARI images in that session. The green and red CaMPARI fluorescence values were normalized by dividing by the values from the calibration solution. The R/G ratio is the normalized red fluorescence divided by the normalized green fluorescence. Fold R/G is (R/G)$_{post}$ divided by (R/G)$_{pre}$.

CaMPARI2 in larval zebrafish. All zebrafish experiments were conducted in accordance with the animal research guidelines from the National Institutes of Health and were approved by the Institutional Animal Care and Use Committee and Institutional Biosafety Committee of Janelia Research Campus.

Zebrafish (*Danio rerio, casper* background) embryos in the 1–2 cell stage were injected with Tol2 vector containing CaMPARI2 under control of the *elavl3* pan-neuronal promoter. At 6 days post-fertilization (dpf), fish were screened and founders were selected. Founders were crossed with *casper* background fish and offspring with bright fluorescence in the central nervous system were selected.

The freely swimming fish were photoconverted for 30 s with 400 nm LED array (Loctite, 200 mW cm^{-2}) in the presence or absence of 0.24 mg ml^{-1} tricaine methanesulfonate (MS-222, Sigma). Control fish were not illuminated. All fish were then transferred to 0.24 mg ml^{-1} tricaine and mounted in 1% agarose for imaging.

The forebrain of zebrafish larvae (white box in Fig. 3) was imaged using a Zeiss 710 confocal microscope using a ×20 water immersion objective. The imaged field of view was 250.1 × 250.1 μm^2 with a 4.1-μs dwell time. For the green channel, we excited with 5% 488 nm and 0.5% 405 nm light (to compensate for photoswitching effects), detecting at 495–554 nm with a detection gain of 600. For the red channel, the 561 nm laser was set at 7% and detection range was 566–700 nm at a detection gain of 700. z-Slices were acquired every 10 μm.

We imaged for each of the two transgenic lines, 2 control fish (not photoconverted), 4 (CaMPARI1) or 3 (CaMPARI2) fish that were photoconverted in the presence of 0.24 mg ml^{-1} tricaine and 4 fish each that were photoconverted in the absence of tricaine. Using an in-house developed MATLAB script, individual cells were segmented (between 1800 and 6000 cells per condition) and their red-to-green fluorescence signal was determined.

Note that the CaMPARI1 fish used in this study are Tg(elavl3:CaMPARI (W391F+V398L))^{jf9} fish, which we made and used in our previous study[12]. These fish express a CaMPARI1 variant with a K_d for Ca^{2+} of 200 nM.

CaMPARI2(-F391W) in mouse visual cortex. All experiments were conducted in accordance with the animal research guidelines from the National Institutes of Health and were approved by the Institutional Animal Care and Use Committee of Cleveland Clinic Lerner Research Institute. Mice were held in standard housing cages with ad libitum access to food and water. Adult mice were anesthetized using isoflurane (2.5% for induction and 1.5% during surgery) in oxygen and placed onto a heated pad (37 °C). A hole was drilled in the skull and AAV was injected into the cortex carrying the CaMPARI2 or CaMPARI2-F391W sequence under the human *synapsin1* promoter. The injections were targeted to the left primary visual cortex (V1) and centered around

coordinates 2.7 mm lateral and 0.2 mm anterior to Lambda (4 injections, 35 nl each of ~1 × 10^{12} gc ml^{-1} AAV solution). A cranial window (two glued layers of #1 glass, Warner Instruments) and a custom headbar were cemented to the skull. Mice were imaged 15–21 days (CaMPARI2) and 15–67 days (CaMPARI2-F391W) after the AAV injection. Prior to starting the imaging session, mice were injected with chlorprothixene hydrochloride (30 µl of 0.33 mg ml^{-1} solution, intramuscular, Santa Cruz) and kept lightly anesthetized during imaging (0.5% isoflurane). PC light was illuminated during presentation of a drifting grating moving upward (north direction) stimulus to the mouse right eye. We used an X-Cite Fire lamp (Excelitas) and 440 nm short-pass filter (Semrock FF01-440/SP) with up to 100 mW illumination in the sample plane. PC light was focused to a 7 mm diameter circle with up to ~260 mW cm^{-2} and was shined for total of 40 s, 40 cycles of 1 s illumination and 11 s break for tissue cooling, or 20 cycles of 2 s illumination and 10 s break. Imaging was performed using a Bergamo II two-photon microscope with a resonant scanner at 30 Hz acquisition rate and ThorImage software (Thorlabs) with 512 × 512 pixels covering 200 × 200 µm^2 of tissue. The light source for two-photon imaging was Insight X3 (Spectra-Physics). We used 950 nm excitation to image functional changes of the CaMPARI green fluorescence to drifting grating moving in 8 different directions (4 s of drifting grating movement followed by 8 s of blank display), and 1040 nm excitation to acquire red and green images to calculate the R/G ratio (without visual stimulus).

Data analysis was performed in Matlab (Mathworks) similar to previous published works[12,17,25]. Cells bodies were segmented using a semi-automatic algorithm[17], and neuropil contamination was corrected using $r = 0.6$. Only cells with baseline fluorescence >90% of their surrounding neuropil signal were included in the analysis. Responsive cells were identified using an ANOVA test with $p < 0.01$. Cells were identified as PC-tuned if they were both responsive and their response to the northward moving grating was significantly lower than their response to a blank display stimulus. We used the OSI as previously defined to describe the tuning level of individual cells to the drifting grating stimuli[16].

Anti-CaMPARI-red antibody. EosFP was purified from *E. coli* and photoconverted using 400 nm LED light (Loctite). The photoconverted red form was selectively precipitated at 69 °C and spun down; the green supernatant was further photoconverted and precipitated as well. The orange colored pellet of photoconverted, precipitated EosFP was resuspended in papain protease solution (Sigma) and digested at 37 °C for 5 h followed by 24 h at room temperature. The orange-brown colored digest supernatant was filtered and loaded on a size-exclusion column (Superdex 200, GE Healthcare) and fractionated by isocratic elution with 1 mM Tris, 5 mM NaCl, pH8. The small chromophore-containing fragment, absorbing at 450 nm, was retained longer on the column than other peptide fragments and was collected and verified by liquid chromatography/mass spectrometry (Agilent) to comprise the red chromophore and the next two amino acids (Asn, Arg). This antigen was used by Genscript (Piscataway, NJ, USA) for monoclonal antibody production in mice following standard protocols. Briefly, the antigen was linked to KLH and five immunizations each were given to Balb/c or C57 mice. After screening mouse bleeds for specific antigen recognition (enzyme-linked immunosorbent assay (ELISA) and western blot), three mice were selected and hybridoma libraries were prepared from each. Supernatants from individual hybridoma clones were screened by ELISA with both positive and negative selection using denatured full-length red and green CaMPARI, respectively. Hits were confirmed via ELISA and western blot for specific recognition of the red but not the green form of CaMPARI. Three promising hybridoma clones were scaled up for monoclonal antibody production. After testing them by western blot and immunofluorescence, the sequence of the variable regions of the best-performing antibody was determined by Genscript using rapid amplification of cDNA ends (Figure S13).

CaMPARI2 PC and histochemistry in HeLa cells. Hela cells were transfected with pCAG-CaMPARI2 and a vector expressing the ATP-gated Ca^{2+} channel P2X using the manufacturer's protocols (Lipofectamine 2000, Invitrogen). After 24 h, cells were washed with Hank's Balanced Salt Solution, and ATP was administered to a final concentration of 100 µM immediately followed by PC of one field of view (20 s of 400-nm light at 3 mW cm^{-2}) on a Nikon Ti Eclipse wide-field microscope equipped with an LED illuminator (SPECTRA-X, Lumencor), a ×20 objective and an sCMOS camera (Zyla, Andor). The cells were then fixed using formaldehyde (4% in phosphate-buffered saline (PBS) containing 10 mM EGTA, 10 min) and immunostained using standard protocols with anti-CaMPARI-red (1:10,000) and rabbit anti-FLAG (1:3000, F7425, Sigma-Aldrich) as primary and goat-anti-rabbit Alexa Fluor 405 (1:1000; A31556, Invitrogen) and goat-anti-mouse Alexa Fluor 647 (1:1000, A21236, Invitrogen) as secondary antibodies. Cells were then imaged on the same microscope using the 4,6-diamidino-2-phenylindole, fluorescein isothiocyanate, tetramethylrhodamine, and Cy5 imaging channel. In the resulting four-color image, individual cells were segmented in the green channel and four color intensities were calculated.

CaMPARI2 PC in mouse cortex and histochemistry. All experimental procedures were approved by the Institutional Animal Care and Use Committee at

Brandeis University and followed the guidelines of the National Institutes of Health.

Male B6.129-Camk4t^{m1Gsc}/Ieg mice (EMMA EM:02126) were subject to stereotactic injection of 100 nl of AAV2/1_hsyn1_CaMPARI2 at post-natal day (p) 15[26], then implanted with a fiberoptic cannula made in house (250-µm core diameter, 0.66 NA, ~0.5 mm length, 1.25 ferrule diameter) at p22. At p36, mice were subject to PC light (~50 mW cm^{-2} 390 nm LED connected to the cannula by a custom fiber with 500-µm core diameter, 0.63 NA, and 0.5 m length (Prizmatix)) for 1 h followed immediately by brain dissection. Coronal slices containing V1 were prepared as previously described[27,28], except at 150-µm thickness. Slices were then placed on a glass slide, coverslipped, and imaged on a Leica SP5 confocal microscope. Image stacks with 488 and 543 nm lasers were obtained using a ×20 objective, an optical section height (z-step) of 2 µm, and at 512 × 512 resolution.

Following this initial imaging session, the outline of each slice was traced onto the back of the microscope slide to allow subsequent re-imaging of the same ROIs. Slices were then fixed in 4% paraformaldehyde (PFA) in PBS containing 10 mM EGTA for 1 h. These were rinsed three times in PBS and then incubated in the following solutions (each made in PBS with 10 mM EGTA) for the indicated durations on a rotating shaker at room temperature: permeabilization buffer (0.5% TritonX-100, 20% dimethyl sulfoxide (DMSO), 0.3 M glycine, 2 h), blocking buffer (0.5% TritonX-100, 10% DMSO, 6% Normal Goat Serum (NGS), 1 h), primary antibody buffer (0.5% Tween20, 5% DMSO, 3% NGS, overnight), wash buffer (0.5% Tween20, 3 × 30 min), secondary antibody buffer (0.5% Tween20, 3% NGS, 4 h), and wash buffer (0.5% Tween20, 3 × 30 min). Primary antibodies consisted of rabbit anti-FLAG (1:500, F7425, Sigma-Aldrich) and mouse anti-CaMPARI-red (1:1000). Secondary antibodies consisted of anti-rabbit Alexa Fluor 405 (1:400; A31556, Invitrogen) and anti-mouse Alexa Fluor 647 (1:400; A21236, Invitrogen). Following the final wash, the slices were re-aligned to their previous positions on slides, then mounted with an anti-fade medium (Fluoromount-G; SouthernBiotech), coverslipped, and imaged as before, with the addition of 405 and 647 nm lasers. Images were subsequently analyzed in ImageJ.

CaMPARI2 in vivo PC and histochemistry in rats. All experiments followed the guidelines outlined in the Guide for the Care and Use of Laboratory Animals (Eighth edition; http://grants.nih.gov/grants/olaw/Guide-for-the-Care-and-Use-of-Laboratory-Animals.pdf) and were approved by the Institutional Animal Care and Use Committee and Institutional Biosafety Committee of the Intramural Research Program of the National Institute on Drug Abuse.

To demonstrate in vivo labeling of active neurons using CaMPARI2, we photoconverted neurons in the prelimbic cortex of rats during mild foot shock. We used male Long-Evans rats (Charles River Laboratories; total $n = 4$), weighing between 300 and 350 g at the time of surgery. Rats were housed individually before and after surgery under a reverse 12 h light/dark cycle (lights off at 8:00 a.m.). Food and water was available ad libitum throughout the experiment. Rats were injected bilaterally with AAV2/1-hSyn-CaMPARI2 in the prelimbic cortex (anterior–posterior (AP) +3.2, medial–lateral (ML) ±0.7, dorsal–ventral (DV) −3.45) and a 400 µm optical fiber was implanted unilaterally for PC in one hemisphere (AP +3.2, ML ±0.7, DV −3.2). The opposite hemisphere was used as the expression control. PC experiments were performed at least 10 days post-surgery to allow sufficient expression of CaMPARI2 in neurons. Rats were connected to the PC laser using custom fiber-optic patch cables and then housed in behavioral testing chambers overnight to minimize non-specific activation. In the morning, rats were presented with a train of mild foot shocks (0.5 mA shock, 12 shocks, 0.5 s ON, 4.5 s OFF, 60 s total presentation) and a 375 nm UV laser (10 mW, CW) was used to photoconvert neurons activated by this aversive stimulus. Rats were perfused for subsequent immunohistochemistry, 90 min after the first shock pulse.

Immediately following behavioral testing, rats were anesthetized with isofluorane and perfused transcardially with ~250 ml of 1× PBS with 10 mM EGTA at pH 7.4 (PBS-E), followed by ~250 ml of 4% PFA with 10 mM EGTA at pH 7.4 (PFA-E). Brains were extracted, post-fixed in PFA-EGTA for 2 h, and then transferred to 30% sucrose with 10 mM EGTA for 48 h at 4 °C. Equilibrated brains were frozen on dry ice and stored at −80 °C. Coronal sections (40 µm) containing prelimbic cortex were then cut using a Leica cryostat, collected in PBS-EGTA, and stored at 4 °C until further processing. Free-floating sections were first rinsed in PBS-E with 0.5% Tween20 and 10 µg ml^{-1} heparin (wash buffer, 3 × 10 min). Sections were incubated in PBS-E with 0.5% TritonX-100, 20% DMSO, and 23 mg ml^{-1} glycine for 3 h at 37 °C (permeabilization buffer) and then in PBS-E with 0.5% TritonX-100, 10% DMSO, and 6% normal donkey serum (NDS) for 3 h at 37 °C (blocking buffer) prior to antibody labeling. Primary antibody was diluted 1:2000 in PBS-E with 0.5% Tween20, 5% DMSO, 3% NDS, and 10 µg ml^{-1} heparin (1° Ab buffer) and sections were incubated overnight in this solution at 37 °C. Following, 1° antibody labeling, sections were rinsed in wash buffer (3 × 10 min) and then incubated in 2° antibody solution (2° antibody diluted 1:500 in PBS-E with 0.5% Tween20, 3% NDS, and 10 µg ml^{-1} heparin) overnight. Following, 2° antibody labeling, sections were rinsed again in wash buffer (3 × 10 min), mounted onto gelatin-coated slides, partially dried, coverslipped with MOWIOL mounting medium, and allowed to hard-set overnight prior to imaging on a Nikon C2 confocal microscope.

Confocal z-stacks of prelimbic cortex were acquired just below the optical fiber on a Nikon C2 confocal microscope using a ×20/0.75 NA air objective. The imaged field of view was 318.20 × 318.20 μm² (0.3107 μm/pixel) with a 5.3-μs dwell time. For native CaMPARI2 green fluorescence, tissue was excited with 4% laser power at 488 nm and emitted fluorescence was collected from 500 to 550 nm with a detection gain of 75 and an offset of −4. To image immunolabeled CaMPARI2 (epitope tag), tissue was excited with 2% laser power at 640 nm and emitted fluorescence collected from 670 to 1000 nm with a detection gain of 75 and an offset of 3. For native CaMPARI2 red fluorescence tissue was excited with 10% laser power at 561 nm and emitted fluorescence was collected from 570 to 1000 nm with a detection gain of 75 and an offset of 4. To image immunolabeled red CaMPARI2 (anti-red antibody), tissue was excited with 20% laser power at 405 nm and emitted fluorescence was collected from 417 to 477 nm with a detection gain of 100 and an offset of 7. All four channels were imaged sequentially (order: 488, then 567, then 647, and finally 405) to minimize overlap and prevent CaMPARI2 PC during image acquisition from confounding colocalization analysis. z-Slices containing all four channels were acquired every 2 μm and the maximum intensity projection for each channel over z was used for colocalization analysis.

Reagent availability. DNA constructs for pAAV_hsyn_CaMPARI2, pAAV_h-syn_CaMPARI2_F391W, pAAV_hsyn_CaMPARI2_H396K, pAAV_hsyn_CaM-PARI2_F391W-G395D, and pAAV_hsyn_CaMPARI2_L398T are available via Addgene (http://www.addgene #101060-#101064). AAV virus can be requested at the University of Pennsylvania Vector Core (http://www.med.upenn.edu/gtp/vectorcore). Tg(elavl3:CaMPARI2)^jf92 transgenic zebrafish are deposited to the ZIRC (https://zebrafish.org). Drosophila expressing CaMPARI2 and CaMPARI2-L398T under UAS and LexA promoter in chromosome 2 (su(Hw)attP5), 3 (VK00005), or X (su(Hw)attP8) are available from the Bloomington Drosophila Stock Center (https://bdsc.indiana.edu, #78316-#78326).

Data availability

Source data from experiments in this study are available from the authors upon reasonable request.

References

1. Guzowski, J. F., Setlow, B., Wagner, E. K. & McGaugh, J. L. Experience-dependent gene expression in the rat hippocampus after spatial learning: a comparison of the immediate-early genes Arc, c-fos, and zif268. *J. Neurosci.* **21**, 5089–5098 (2001).
2. Guenthner, C. J., Miyamichi, K., Yang, H. H., Heller, H. C. & Luo, L. Permanent genetic access to transiently active neurons via TRAP: targeted recombination in active populations. *Neuron* **78**, 773–784 (2013).
3. Koya, E. et al. Targeted disruption of cocaine-activated nucleus accumbens neurons prevents context-specific sensitization. *Nat. Neurosci.* **12**, 1069–1073 (2009).
4. Reijmers, L. G., Perkins, B. L., Matsuo, N. & Mayford, M. Localization of a stable neural correlate of associative memory. *Science* **317**, 1230–1233 (2007).
5. Denny, C. A. et al. Hippocampal memory traces are differentially modulated by experience, time, and adult neurogenesis. *Neuron* **83**, 189–201 (2014).
6. Sheng, M. & Greenberg, M. E. The regulation and function of c-fos and other immediate early genes in the nervous system. *Neuron* **4**, 477–485 (1990).
7. Cruz, F. C., Javier Rubio, F. & Hope, B. T. Using c-fos to study neuronal ensembles in corticostriatal circuitry of addiction. *Brain Res.* **1628**, 157–173 (2015).
8. Dana, H. et al. Thy1-GCaMP6 transgenic mice for neuronal population imaging in vivo. *PLoS ONE* **9**, e108697 (2014).
9. Jercog, P., Rogerson, T. & Schnitzer, M. J. Large-scale fluorescence calcium-imaging methods for studies of long-term memory in behaving mammals. *Cold Spring Harb. Perspect. Biol.* **8**, a021824 (2016).
10. Ghosh, K. K. et al. Miniaturized integration of a fluorescence microscope. *Nat. Methods* **8**, 871–878 (2011).
11. Lin, M. Z. & Schnitzer, M. J. Genetically encoded indicators of neuronal activity. *Nat. Neurosci.* **19**, 1142–1153 (2016).
12. Fosque, B. F. et al. Labeling of active neural circuits in vivo with designed calcium integrators. *Science* **347**, 755–760 (2015).
13. Zolnik, T. A. et al. All-optical functional synaptic connectivity mapping in acute brain slices using the calcium integrator CaMPARI. *J. Physiol.* **595**, 1465–1477 (2017).
14. Akerboom, J. et al. Crystal structures of the GCaMP calcium sensor reveal the mechanism of fluorescence signal change and aid rational design. *J. Biol. Chem.* **284**, 6455–6464 (2009).
15. Akerboom, J. et al. Optimization of a GCaMP calcium indicator for neural activity imaging. *J. Neurosci.* **32**, 13819–13840 (2012).
16. Niell, C. M. & Stryker, M. P. Highly selective receptive fields in mouse visual cortex. *J. Neurosci.* **28**, 7520–7536 (2008).
17. Chen, T.-W. et al. Ultrasensitive fluorescent proteins for imaging neuronal activity. *Nature* **499**, 295–300 (2013).
18. Kerlin, A. M., Andermann, M. L., Berezovskii, V. K. & Reid, R. C. Broadly tuned response properties of diverse inhibitory neuron subtypes in mouse visual cortex. *Neuron* **67**, 858–871 (2010).
19. Gee, C. E., Ohmert, I., Wiegert, J. S. & Oertner, T. G. Preparation of slice cultures from rodent hippocampus. *Cold Spring Harb. Protoc.* **2017**, 126–130 (2017).
20. Wiegert, J. S., Gee, C. E. & Oertner, T. G. Single-cell electroporation of neurons. *Cold Spring Harb. Protoc.* https://doi.org/10.1101.pdf.prot094904 (2017).
21. Pologruto, T. A., Sabatini, B. L. & Svoboda, K. ScanImage: flexible software for operating laser scanning microscopes. *Biomed. Eng. Online* **2**, 1–9 (2003).
22. Suter, B. A. et al. Ephus: multipurpose data acquisition software for neuroscience experiments. *Front. Neural Circuits* **4**, 100 (2010).
23. Schindelin, J. et al. Fiji: an open-source platform for biological-image analysis. *Nat. Methods* **9**, 676–682 (2012).
24. Preibisch, S., Saalfeld, S. & Tomancak, P. Globally optimal stitching of tiled 3D microscopic image acquisitions. *Bioinformatics* **25**, 1463–1465 (2009).
25. Dana, H. et al. Sensitive red protein calcium indicators for imaging neural activity. *eLife* **5**, e12727 (2016).
26. Lambo, M. E. & Turrigiano, G. G. Synaptic and intrinsic homeostatic mechanisms cooperate to increase L2/3 pyramidal neuron excitability during a late phase of critical period plasticity. *J. Neurosci.* **33**, 8810–8819 (2013).
27. Nahmani, M. & Turrigiano, G. G. Deprivation-induced strengthening of presynaptic and postsynaptic inhibitory transmission in layer 4 of visual cortex during the critical period. *J. Neurosci.* **34**, 2571–2582 (2014).
28. Maffei, A., Nelson, S. B. & Turrigiano, G. G. Selective reconfiguration of layer 4 visual cortical circuitry by visual deprivation. *Nat. Neurosci.* **7**, 1353–1359 (2004).

Author contributions

B.M., G.H., and E.R.S. performed in vitro screening and characterization. B.M. generated and characterized transgenic zebrafish lines. B.M. and T.A.B. generated and characterized transgenic fly lines. A.P.-A. and B.C.F. performed electrophysiology on rat slices. N.F.T. did in vivo photoconversion and immunohistochemistry in mouse tissue, while R.M. performed in vivo photoconversion and immunohistochemistry in the rat brain. H.D. and A.D. performed the experiments involving functional imaging and photoconversion in mouse visual cortex. J.L. and T.A.Z. performed immunohistochemistry on ex vivo photoconverted mouse slices with R.N.S.S. B.M., G.H., R.M., A.P.-A., B.C.F., N.F.T., A.D., D.P., H.D., and E.R.S. analyzed data. H.D., B.J.E., M.E.L., G.G.T., C.E.G., T.G.O., B.T.H., and E.R.S. supervised the work. The manuscript was written by B.M. and E.R.S. with help from R.M., A.P.-A., N.F.T., H.D., and R.N.S.S. All authors reviewed and approved the manuscript.

Supplementary Figures

```
CaMPARI1    1     DQLTEEQIAEFKEAFSLFDKDGDGTITTKELGTVMRSLGQNPTEAELQDMINEVDADGDG    60
CaMPARI2    1     DQLTEEQIAEFKEAFSLFDKDGDGTITTKELGTVMRSLGQNPTEAELQDMINEVDADGDG    60

CaMPARI1    61    TIDFPEFLTMMARKMKDTDSEEEIREAFRVFDKDGNGYISAAELRHVMTNLGEKLTDEEV    120
CaMPARI2    61    TIDFPEFLTMMARKMKDTDSEEEIREAFRVFDKDGNGYISAAELRHVMTNLGEKLTDEEV    120

CaMPARI1    121   DEMIREADIDGDGQVNYEEFVQMMTAKLECEKIYVRDGVLTGDIHMILLLEGNAHYRCDF    180
CaMPARI2    121   DEMIREADIDGDGQVNYEEFVVMMTAKLECEKIYVRDGVLTGDIHMILLLEGNAHYRCDF    180

CaMPARI1    181   RTTYKAKEKGVKLPGVHFVDHCIEILSHDKDYNKVKLYEYAVAHSGLPDNARRGGTGGSM    240
CaMPARI2    181   RTTYKAKEKGVKLPGVHYVDHTIEILSHDKDYNKVKIYEYAVAHSGLPDNARRGGTGGSM    240

CaMPARI1    241   VSAIKPDMKIKLRMEGNVNGHHFVIDGDGTGKPYEGKQTMDLEVKEGGPLPFAFDILTTA    300
CaMPARI2    241   VSAIKPDMKIKLRMEGNVNGHHFVIDGDGTGKPYEGKQTMDLEVKEGGPLPFAFDILTTA    300

CaMPARI1    301   FHYGNRVFVKYPDNIQDYFKQSFPKGYSWERSMTFEDGGICYARNDITMEGDTFYNKVRF    360
CaMPARI2    301   FHYGNRVFVKYPDNIQDYFKQSFPKGYSWERSMTFEDGGICYARSDITMEGDTFYNKVRF    360

CaMPARI1    361   YGTNFPANGPVMQKKTLKWMPSWTRSSRRKWNKTGHAVRAIGRLSS*                406
CaMPARI2    361   YGTNFPANGPVMQKKTLKWMPSWTRSSRRKFNKTGHALRAIGRLSSGGSGGSDYKDDDDK   420
CaMPARI2          (F391W)            ...SSRRKWNKTGHALRAIGRLSS...
CaMPARI2          (H396K)            ...SSRRKWNKTGKALRAIGRLSS...
CaMPARI2          (F391W-G395D)      ...SSRRKWNKTDHALRAIGRLSS...
CaMPARI2          (L398T)            ...SSRRKWNKTGHATRAIGRLSS...

CaMPARI2    421   GGSGGSYPYDVPDYAGGSGGSEQKLISEEDLRT*                             453
```

Supplementary Figure 1: Sequence alignment of CaMPARI1, CaMPARI2 and the 4 different affinity variants of CaMPARI2. The calmodulin domain is shaded grey, while the calmodulin-interacting peptide is underlined; the chromophore is shaded black. The yellow residues are the mutations between CaMPARI1 and CaMPARI2 outside of the calmodulin-interacting peptide. The cyan residues are the affinity mutations described in Table 1 and Table S3. Epitope tags (FLAG – HA – myc) are in bold.

1
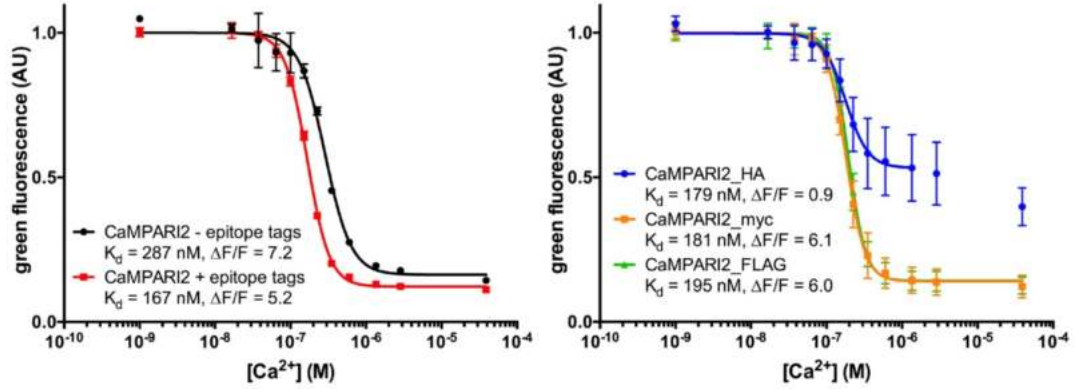
Supplementary Figure 2: Effect of adding epitope tags on the calcium affinity of CaMPARI2.
Titration curves for calcium of CaMPARI2 with (*n* = 2) or without (*n* = 2) epitope tags attached
(left) or CaMPARI2 with a single epitope attached (HA: *n* = 6, myc: *n* = 8, FLAG: *n* = 6) (right). The
ΔF/F is the difference in green fluorescence intensity between high and low calcium conditions,
divided by the green fluorescence intensity in high calcium conditions. Error bars are standard
deviation.

2
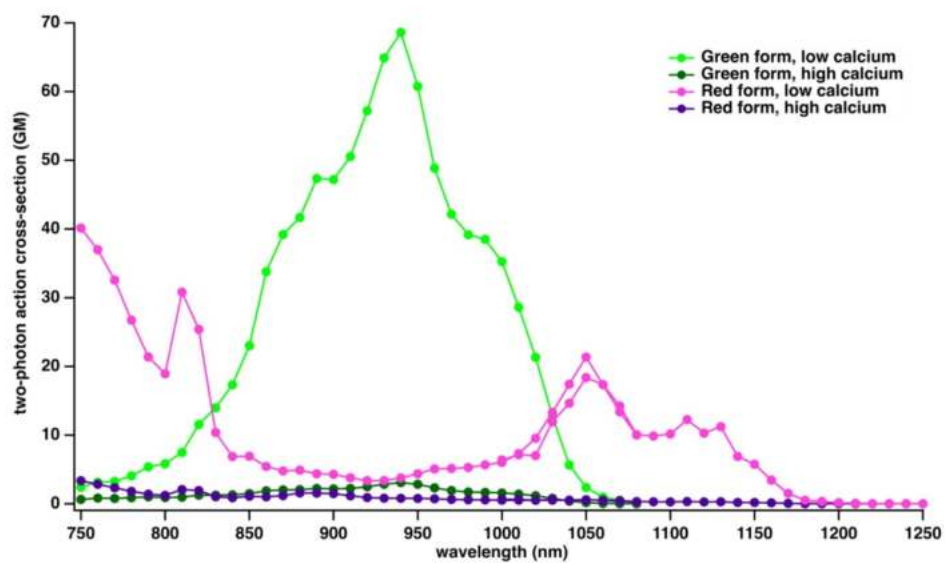
Supplementary Figure 3: Two-photon action cross-section of CaMPARI2. Spectra of the green and red state of CaMPARI2 in high and low calcium conditions are plotted. The peak at 810 nm that appears in the red species was not seen in the raw data and is probably an artifact of the reference spectrum[1] used to normalized for instrumental variation in the data acquisition.

3
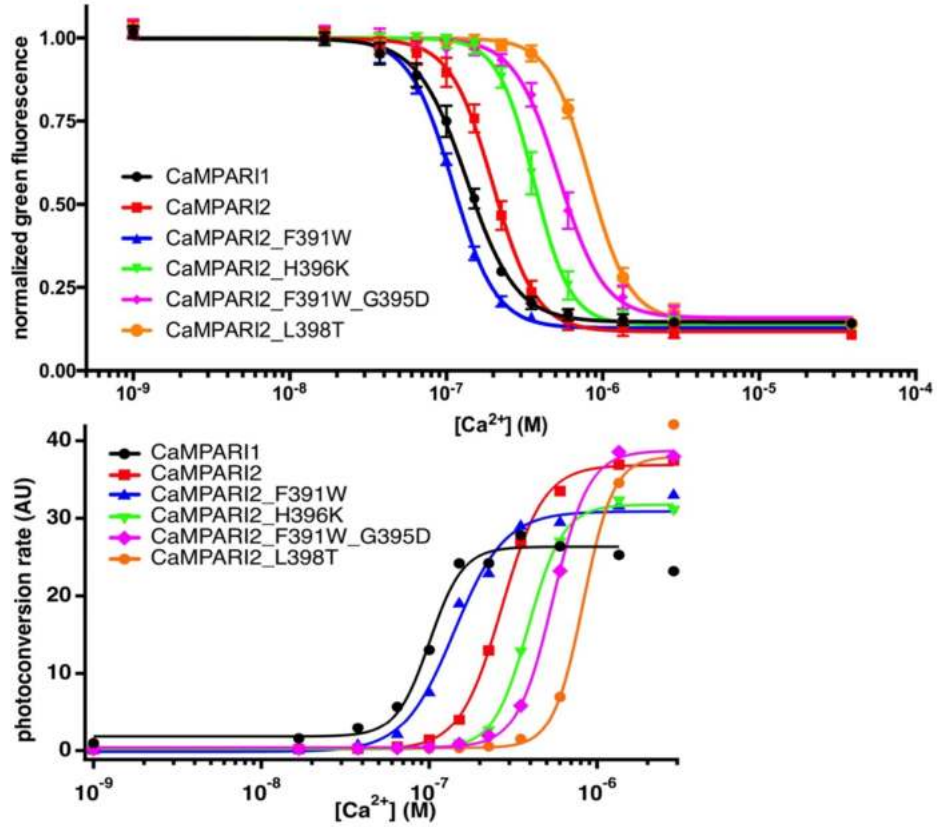
Supplementary Figure 4: Calcium titration of green fluorescence and photoconversion rate.
The top graph represents the titration curves for Ca^{2+} of several CaMPARI variants, measuring the green fluorescence and normalized to 1 for low Ca^{2+} concentrations ($n = 8$, error bars are standard error). The bottom graph represents the rate of photoconversion for CaMPARI variants in different concentrations of Ca^{2+}.

4
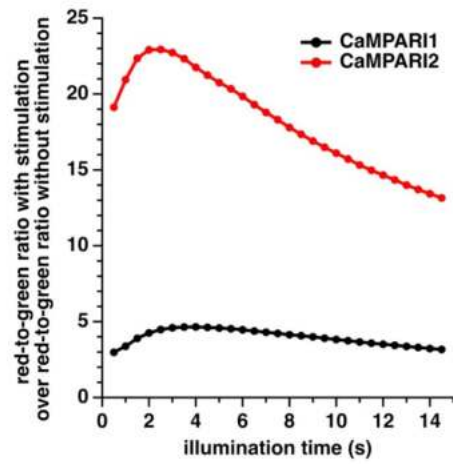
Supplementary Figure 5: Red-to-green contrast between high and low calcium photoconversion in neurons. The amount of photoconversion (as measured by the ratio between red and green CaMPARI) in high Ca^{2+} conditions (during field stimulation) versus low Ca^{2+} conditions (no field stimulation) is plotted against the cumulative time of 405 nm light delivered. Data derived from the data presented in Figure 1C, right panel.

5
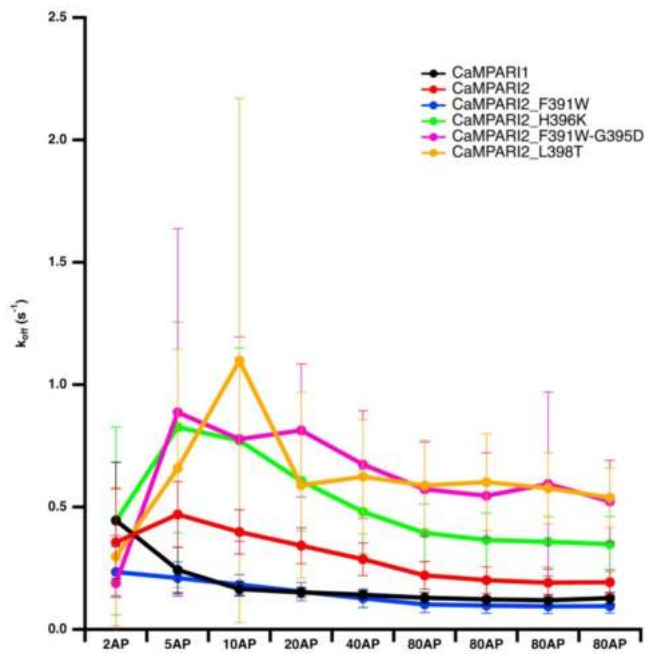
Supplementary Figure 6: Rate constant of calcium unbinding of CaMPARI2 in primary rat hippocampal neurons. The fitted rate constant of fluorescence change following cessation of stimulation (k_{off}, average of 6 trials) is plotted for each number of field stimulations. Error bars are standard deviation.

6
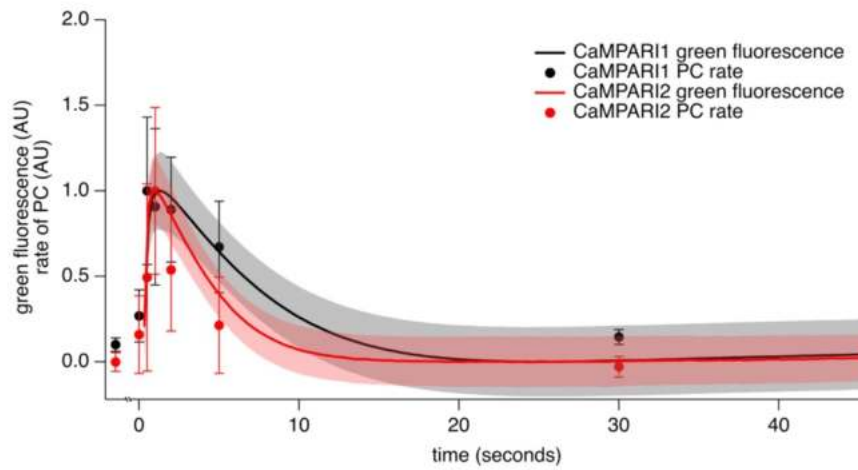
Supplementary Figure 7: Delay between stimulation and photoconversion light. The extent of photoconversion of CaMPARI1 and CaMPARI2 in cultured neurons are plotted as a function of the delay between field stimulation (20 AP at 80 Hz) and photoconversion light (395 nm, 250 ms at ~3 W/cm^2). Control measurements without stimulation are shown left of the t = 0 timepoint. Solid lines represent the normalized inverse of the green fluorescence during the imaging session, shaded areas represent standard deviation from between 220 and 408 cells, depending on the timepoint.

7
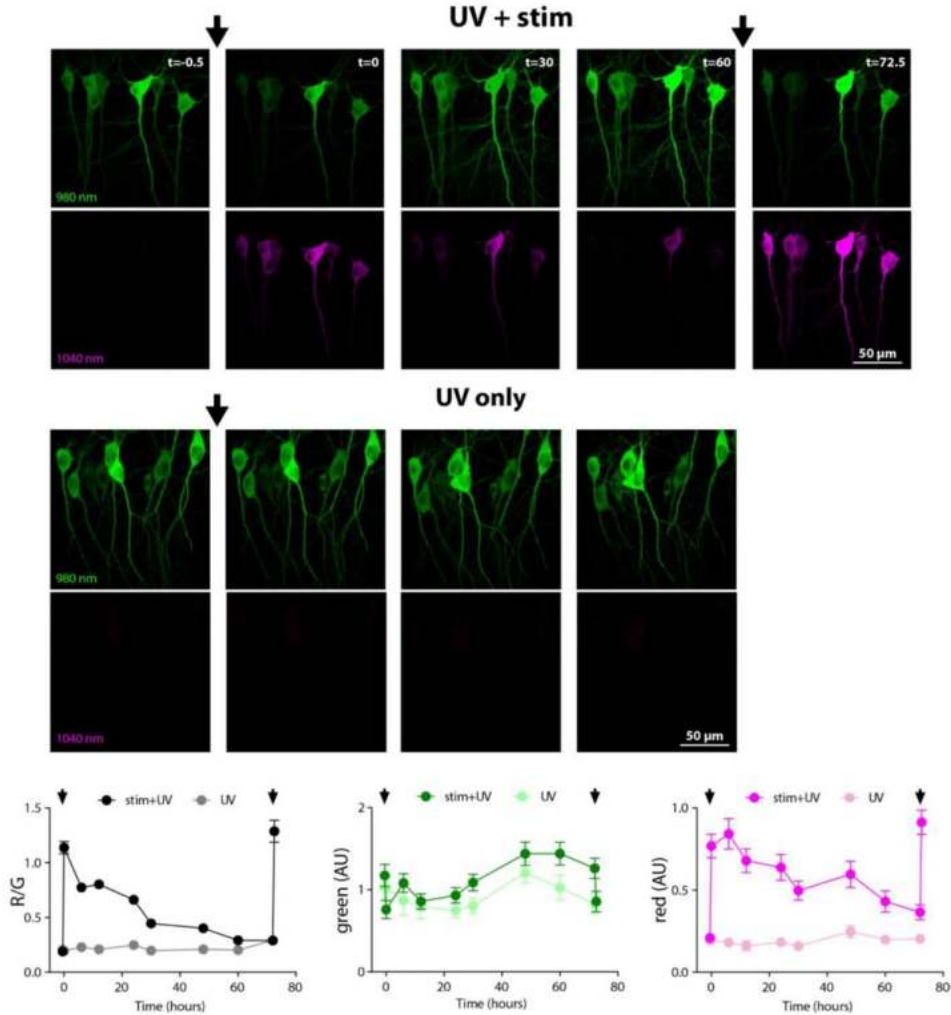
Supplementary Figure 8: Three day turnover of CaMPARI2 and re-conversion. Two-photon image stacks of CA1 neurons from rat hippocampal slice cultures starting 4 days after electroporation at DIV15 with DNA encoding CaMPARI2_F391W-L398V (no epitope tags) at the time points indicated (hours, t = 0 immediately after photoconversion). Arrows indicate when CaMPARI2 photoconversion was induced by combining strong electrical stimulation of synaptic inputs in the stratum radiatum (100 times at 100 Hz) with UV light (2 seconds, 395 nm, 16 mW mm^{-2}) applied with a 1 s delay from the start of stimulation (UV + stim; 24 neurons, 4 slices). Controls received the same UV without electrical stimulation (UV only; 21 neurons, 3 slices). Values are mean ± standard error of the mean.

8
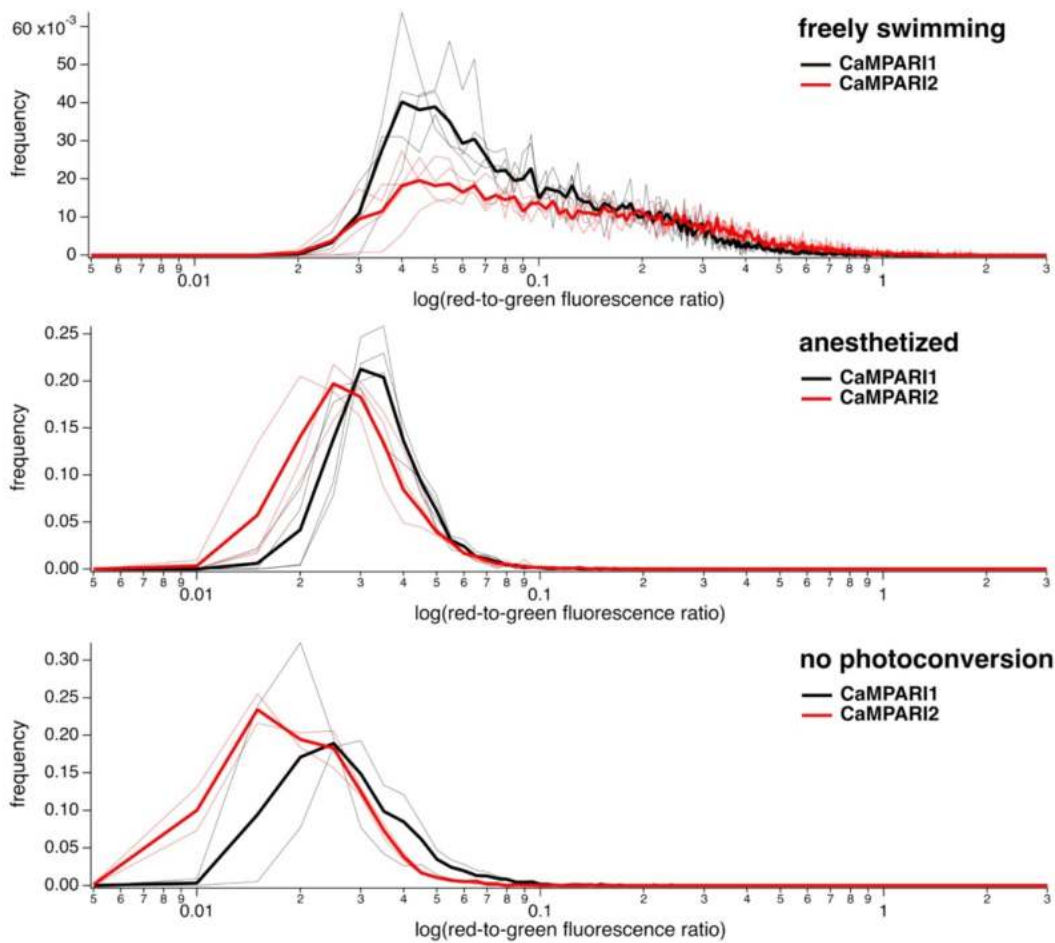
Supplementary Figure 9: Histograms of the red-to-green fluorescence ratio in zebrafish. Fish were photoconverted in the absence (top graph) or presence (middle graph) of the anesthetic tricaine or not photoconverted (bottom graph). Thin lines represent histograms of the red-to-green ratio of all cells from individual fish, thick lines are the histogram of all measured cells of all fish for the given condition. Note the log scale on the x-axis, intended to draw the focus on the low red-to-green ratios, but thereby obscuring the difference between CaMPARI1 and CaMPARI2 at higher red-to-green fluorescence ratios.

9
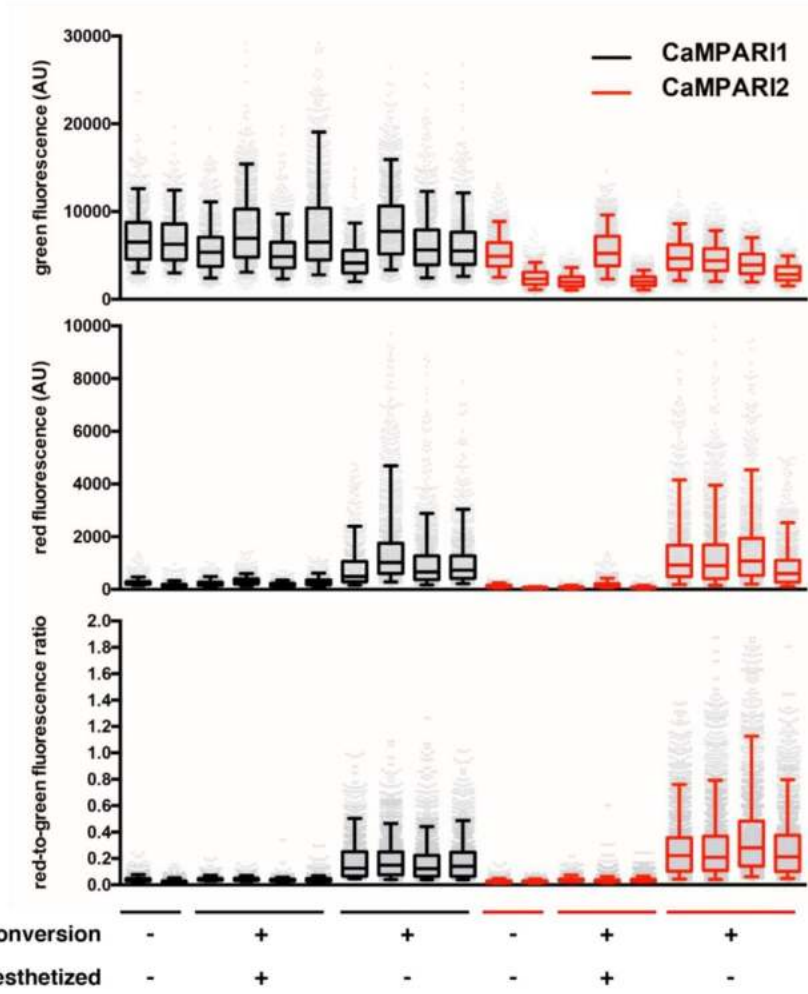
Supplementary Figure 10: Boxplots representing the per-cell green and red fluorescence and red-to-green fluorescence ratio in individual zebrafish. Each boxplot represents one fish. Grey dots are individual cells. Box represents 1st, 2nd and 3rd quartile while whiskers indicate 5th and 95th percentile.
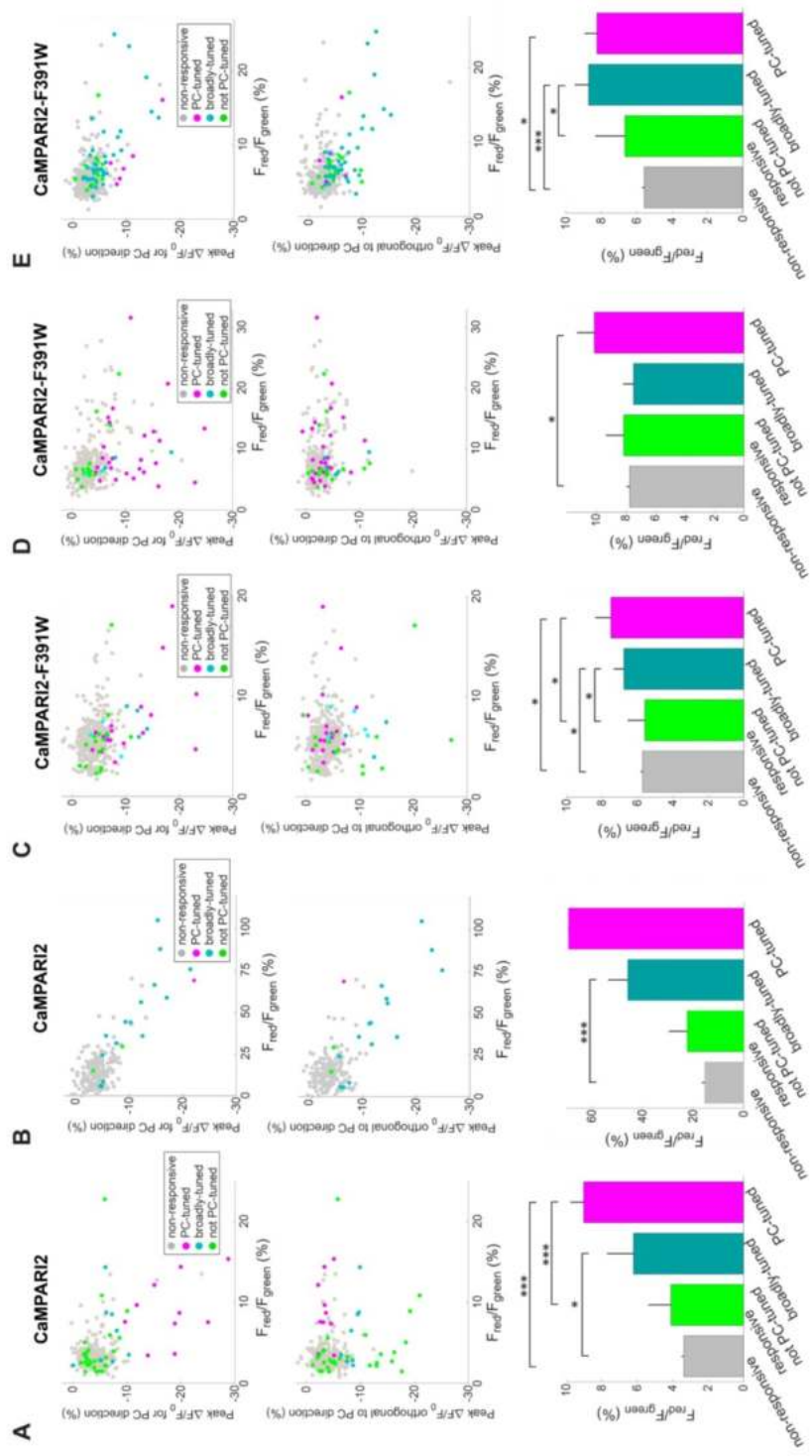
Supplementary Figure 11: Comparison of CaMPARI2 and CaMPARI2-F391W activity and PC in the mouse primary visual cortex. (A-B) Summary of CaMPARI2 performance in the mouse visual cortex. Upper panel: Correlation between peak $\Delta F/F_0$ response for the northward moving grating stimulus and the red-to-green ratio for individual cells. Middle panel: Similar comparison for the eastward moving grating stimulus (orthogonal to the PC direction shown in the upper panel). Lower panel: comparison of red-to-green ratio of PC-tuned cells, not PC-tuned cells, broadly-tuned cells and cells that were not identified as responsive. (C-E) Summary of CaMPARI2-F391W performance in the mouse visual cortex, panels show the same comparison as in panel **A-B.** For both constructs, PC efficiency was higher for PC-tuned cells, leading to a significant increase in red-to-green ratio. Note that differences between PC-tuned and non-responsive cells are larger for CaMPARI2 than CaMPARI2-F391W. * $p<0.05$, ** $p<0.01$, *** $p<0.001$ (Wilcoxon Ranksum Test). Error bars indicate the standard error.

12
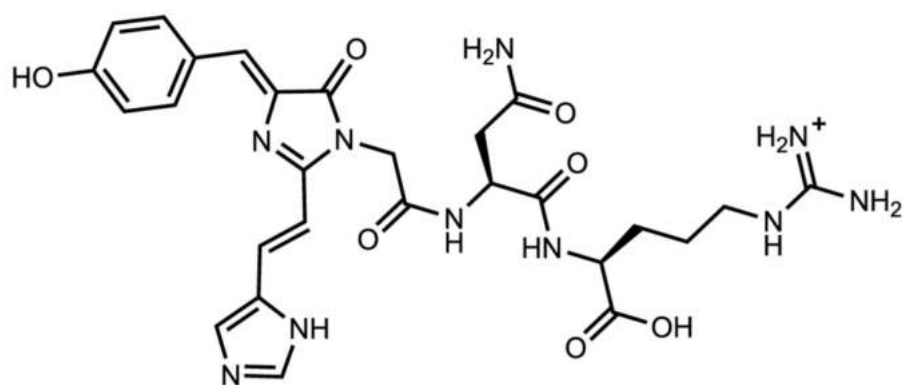
Supplementary Figure 12: Epitope structure. Structure of the proteolytic fragment used to raise the anti-CaMPARI-red antibody, consisting of the red EosFP chromophore and two downstream amino acids (Asn – Arg).

13
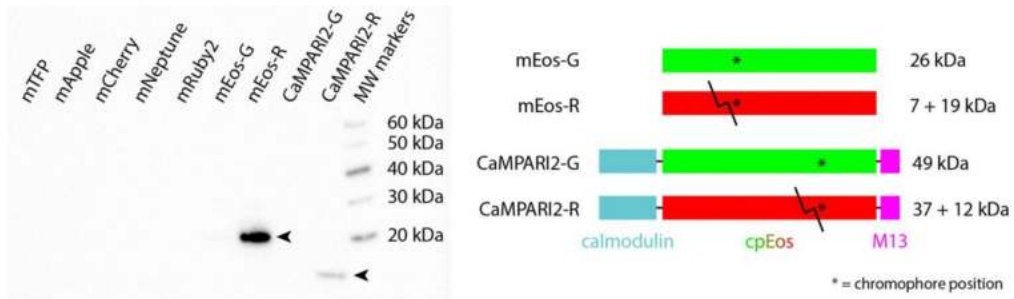
Supplementary Figure 13: Western blot. Western blot of a range of red fluorescent proteins with different chromophore structures, as well as EosFP and CaMPARI2 in the green and red state, probed with the anti-CaMPARI-red monoclonal antibody. All red fluorescent proteins are ±26 kDa and the expected molecular masses of EosFP and CaMPARI2 in the green and red state are shown in the right-hand panel. Each well was loaded with 0.5 μg of protein.

14

Heavy chain (DNA)

```
  1 ATGGCTGTCC TGGGGCTGCT TCTCTGCCTG GTGACGTTCC CAAGCTGTGT
051 CCTGTCCCAG GTGCAGCTGA AGGAGTCAGG ACCTGGCCTG GTGGCACCCT
101 CACAGAGCCT GTCCATCACA TGCACTGTCT CTGGGTTCTC ATTATCCAGA
151 TATAGTGTAC ACTGGGTTCG CCAGCCTCCA GGAAAGGGTC TGGAATGGCT
201 GGGATTCATA TGGGGTGTTG GATCCACAGA CTATAATTCA GCTCTCAGGT
251 CCAGACTGAC CATCACCAAG GACAACTCCA AGAGCCAGGT TTTCTTAAAA
301 ATGAACAGTC TGCAAACTGA TGACACAGCC ATGTACTACT GTGCCAGAAG
351 CCCGATCTAC TATGATTACG ACGCCTCCTA TGCTATGGAC TACTGGGGTC
401 AAGGAACCTC AGTCACCGTC TCCTCA
```

Heavy chain (protein)

Leader sequence-FR1-CDR1-FR2-CDR2-FR3-CDR3-FR4

```
  1 MAVLGLLLCL VTFPSCVLSQ VQLKESGPGL VAPSQSLSIT CTVSGFSLSR
 51 YSVHWVRQPP GKGLEWLGFI WGVGSTDYNS ALRSRLTITK DNSKSQVFLK
101 MNSLQTDDTA MYYCARSPIY YDYDASYAMD YWGQGTSVTV SS
```

Light chain (DNA)

```
  1 ATGAAGTTGC CTGTTAGGCT GTTGGTGCTG ATGTTCTGGA TTCCTGCTTC
 51 CAGCAGTGAA GTTTTGATGA CCCAAACTCC ACTCTCCCTG CCTGTCAGTC
101 TTGGAGATCA AGCCTCCATC TCTTGCAGGT CTAGTCAGAG CATTGTACAT
151 AGTAATGGAA ACACCTATTT AGAGTGGTAT CTGCAGAAAC AGGCCAGTC
201 TCCAAAGCTC CTGATCTACA AAGTTTCCAA CCGATTTTCT GGGGTCCCAG
251 ACAGGTTCAG TGGCAGTGGA TCAGGGACAG ATTTCACACT CAAGATCAGT
301 AGAGTGGAGG CTGAGGATCT GGGAGTTTAT TACTGCTTTC AAGGTTCACA
351 TGATCCGTGG ACGTTCGGTG GAGGCACCAA GCTGGAAATC AAA
```

Light chain (protein)

Leader sequence-FR1-CDR1-FR2-CDR2-FR3-CDR3-FR4

```
  1 MKLPVRLLVL MFWIPASSSE VLMTQTPLSL PVSLGDQASI SCRSSQSIVH
051 SNGNTYLEWY LQKPGQSPKL LIYKVSNRFS GVPDRFSGSG SGTDFTLKIS
101 RVEAEDLGVY YCFQGSHDPW TFGGGTKLEI K
```

Supplementary Figure 14: Anti-CaMPARI-red antibody sequence. Sequence analysis of the variable regions of the anti-CaMPARI-red antibody.

15
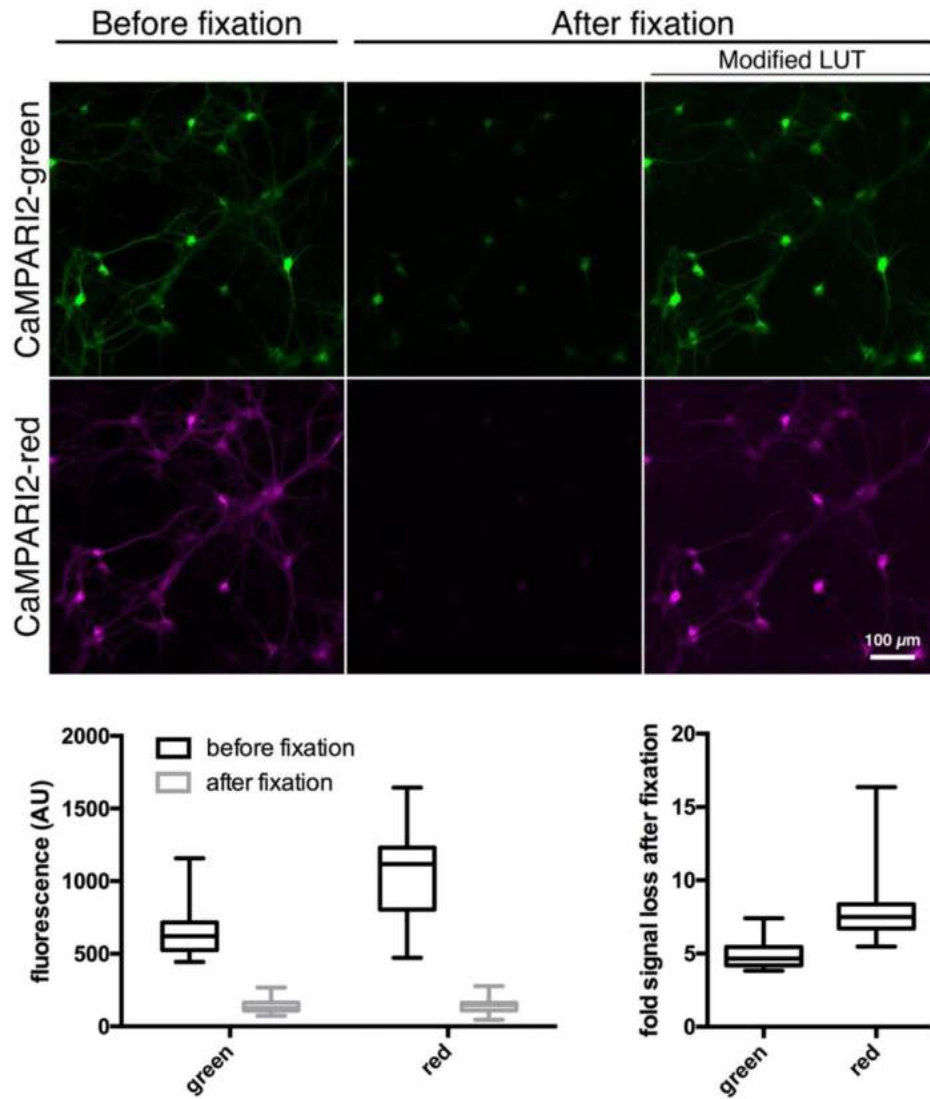
Supplementary Figure 15: Decrease of per-image green and red fluorescence signal of CaMPARI2 in primary neurons after formaldehyde fixation. Representative images of CaMPARI2-expressing primary rat hippocampal neurons after photoconversion. Left, before fixation; middle and right; after fixation (10 min with 4% PFA in PBS-EGTA at room temperature). The right column has a modified color lookup table (LUT) to show the preserved overall structure of the neurons after fixation. Boxplots represent the decrease in green and red fluorescence of 31 images (each containing >20 neurons) before and after fixation. Box represents 1st, 2nd and 3rd quartile while whiskers represent the minimum and maximum value.

16
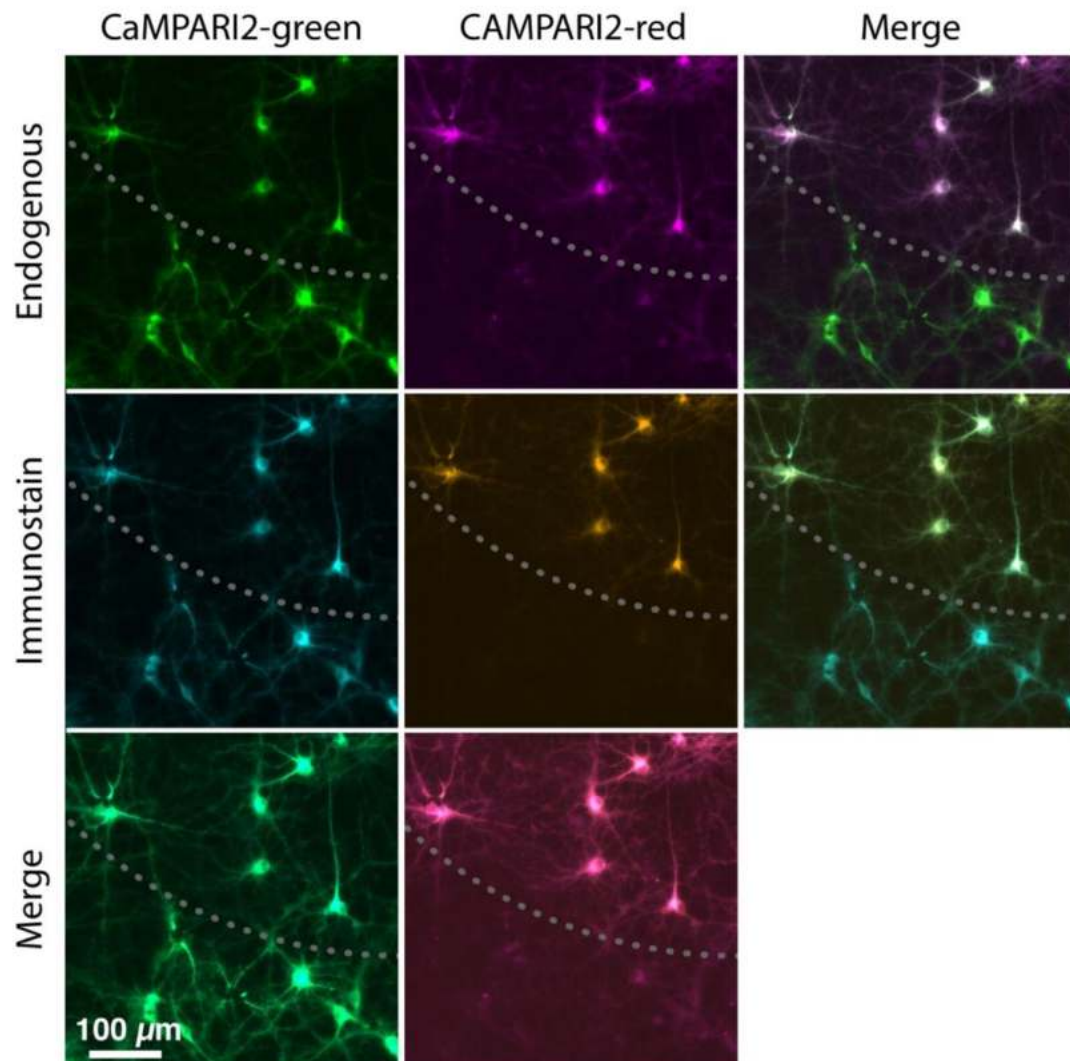
Supplementary Figure 16: Immunohistochemical staining of cultured neurons with anti-CaMPARI-red antibody. The green and red fluorescence of CaMPARI2 after fixation are shown in green and magenta, respectively, while the anti-FLAG antibody signal is shown in cyan and the anti-CaMPARI-red antibody signal is shown in orange. The dotted line represents the edge of the illumination spot for photoconversion (photoconversion above, no photoconversion below). Right and bottom panels show composites of the images to the left or above.

17
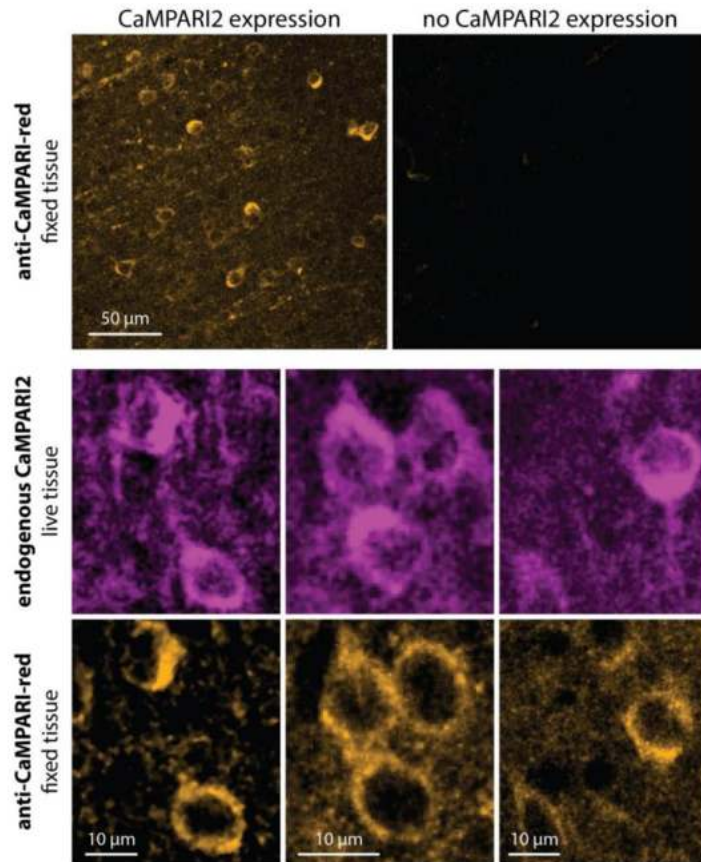
Supplementary Figure 17: Mouse tissue immunostain. Mouse brain tissue expressing CaMPARI2 was photoconverted in the presence of KCl, fixed with paraformaldehyde and immunostained. The anti-CaMPARI-red antibody did not stain the hemisphere contralateral to the injection side (top). The anti-CaMPARI-red antibody signal overlaps well with the endogenous CaMPARI2 signal, imaged before fixation (bottom).

18
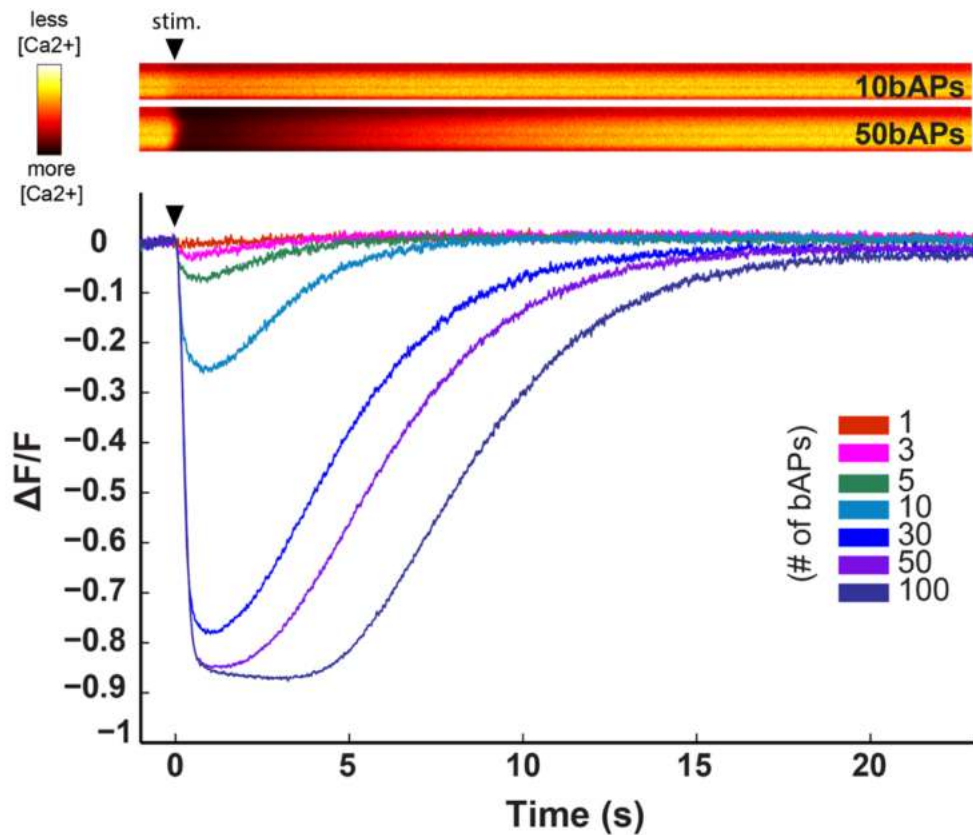
Supplementary Figure 18: Calcium-dependent dimming of CaMPARI2

Top: Example linescans at the soma of a CaMPARI2 expressing neuron during either 10 or 50 bAPs. Signal closer to black indicates higher calcium. Bottom: The $\Delta F/F_0$ for CaMPARI2 without epitope tags for increasing numbers of bAPs. Note that the scale is negative as CaMPARI2 is a reverse calcium indicator.
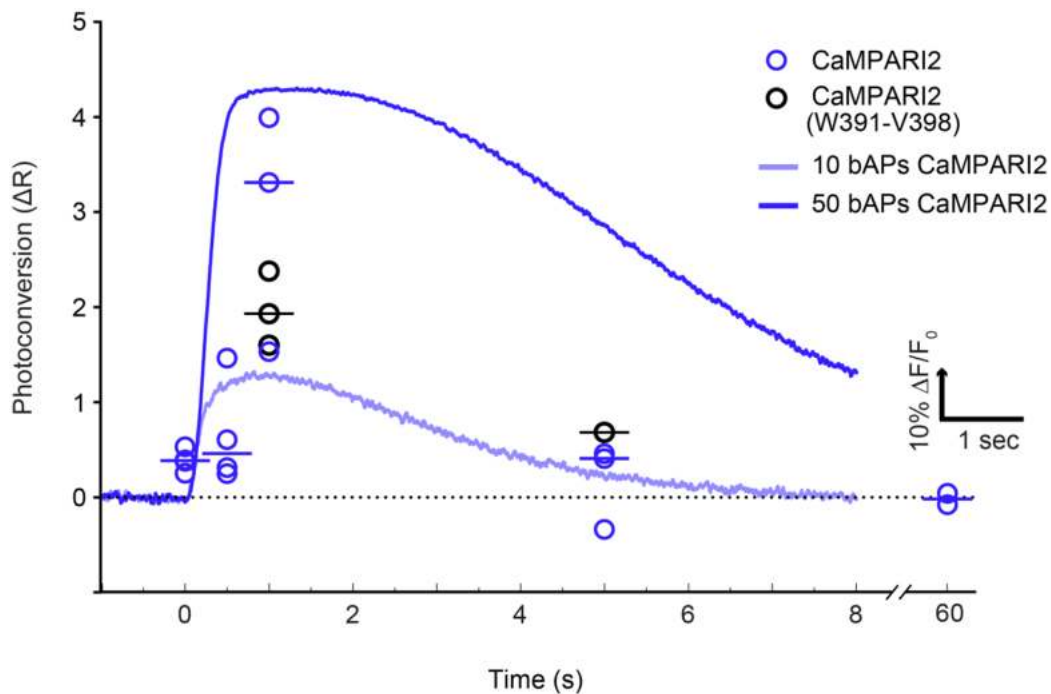
Supplementary Figure 19: Amount of photoconversion relative to timing of violet light to stimulus

All points represent photoconversion (change in red fluorescence, R_1-R_0) from 50 bAPs paired with 100 ms of violet light (395 nm, 16 mW*mm^{-2}). Blue points are from experiments using CaMPARI2 without epitope tags and black points are from CaMPARI2 (W391-V398). The violet light was timed at different intervals relative to bAP onset. Example traces of calcium-dependent dimming of CaMPARI2 to 10 (light blue) and 50 bAPs (dark blue). Note that the time scale is matched to violet light timing and the highest photoconversion corresponds with the peak of CaMPARI2 dimming.

Supplementary Tables

mutation	ΔF/F	Max green (AU)	Max red (AU)	ΔP/P	K_d (nM)
CaMPARI1 (control)	4.27± 0.57	165± 46	276± 90	23.16± 3.10	212
Q142V	4.90	186	367	36.29	207
M143L	4.20	164	307	32.55	283
A146L	2.78	103	170	40.49	372
F198Y	3.63	219	455	30.74	219
C202T	8.86	169	298	27.67	268
C202A	4.63	185	290	31.12	243
L217I	4.33	241	485	34.08	240
L252V	3.65	224	433	36.26	232
N345S	3.61	253	266	36.05	235

Supplementary Table 1: *In vitro* **characteristics of the CaMPARI1_W391F-V398L single amino acid mutation library hits.** The 9 most interesting hits from the CaMPARI1_W391F-V398L single amino acid site saturation mutagenesis libraries are shown. **ΔF/F** is the difference in green fluorescence intensity between the calcium-bound and calcium-free state divided by the fluorescence of the calcium-bound state of CaMPARI. **Max green / max red** is the green/red fluorescence intensity of the calcium-free state of CaMPARI. **ΔP/P** is the difference in extent of photoconversion between the calcium-bound and calcium-free state of CaMPARI divided by the extent of photoconversion of the calcium-bound state. Higher numbers thus reflect a higher photoconversion contrast ratio. **K_d** is the equilibrium constant of calcium binding determined by measuring the green fluorescence in different Ca^{2+} buffers. CaMPARI1 was used as a control in each 96-well block of the library and the average value of those recordings are reported here with standard deviation. Color coding is such that the more desirable values are darker.

19

Q142	M143	A146	F198	C202	L217	L252	N345	ΔF/F	Normalized max green (AU)	Normalized max red (AU)	ΔP/P	Kd (nM)
CaMPARI1 (control)								2.98 ± 0.27	1 ± 0.056	1 ± 0.10	1 ± 0.12	200
V	L		Y	T	I		S	2.75	1.67	1.72	4.97	414
V	L		Y	T			S	2.00	1.83	1.93	4.11	415
V			Y	T	I		S	2.82	1.51	1.73	3.86	285
	L		Y	T	I		S	2.11	1.79	1.80	4.17	440
V	L		Y		I		S	3.09	1.40	1.55	4.45	325
V	L		Y	A	I			3.37	1.24	1.90	3.99	329

Supplementary Table 2: *In vitro* characteristics of the CaMPARI1_W391F-V398L combinatorial library hits. The 6 most interesting hits from the CaMPARI1_W391F-V398L combinatorial library lysate screens are shown. **ΔF/F** is the difference in green fluorescence intensity between the calcium-bound and calcium-free state divided by the fluorescence of the calcium-bound state of CaMPARI. **Normalized max green / max red** is the green/red fluorescence intensity of the calcium-free state of CaMPARI normalized to the EBFP signal relative to CaMPARI1. **ΔP/P** is the difference in extent of photoconversion between the calcium-bound and calcium-free state of CaMPARI divided by the extent of photoconversion of the calcium-bound state relative to CaMPARI1. Higher numbers thus reflect a higher photoconversion contrast ratio relative to CaMPARI1. **K_d** is the equilibrium constant of calcium binding determined by measuring the green fluorescence of purified protein in different Ca^{2+} buffers. CaMPARI1 was used as a control in each 96-well block of the library and the average value of those recordings are reported here with standard deviation. Color coding is such that the more desirable values are darker. CaMPARI2 (without epitope tags) is in a red box.

20

	ΔF/F	K_d (nM)	Hill coefficient
CaMPARI2 no tags	8.0	267	2.8
F391W	6.2	145	3.3
G395A	7.0	173	3.2
F391W-L398V	6.7	174	3.2
T394A	10.4	196	3.0
S387L	5.0	346	2.9
L398V	5.9	376	3.4
F391L	6.2	525	2.9
H396K	9.1	548	2.6
F391M	5.2	671	3.1
F391W-L398T	5.9	720	2.9
F391Y	4.6	801	2.6
F391V	4.5	806	3.2
F391W-G395D	4.9	865	2.8
L398T	5.4	1404	2.8
T394D	3.5	2107	2.1

Supplementary Table 3: Full list of CaMPARI2 (without tags) affinity mutants designed.
CaMPARI2 (no tags) was used as template for 15 affinity mutants. Shaded mutants were selected and further characterized (see Table S4). Note that the mutations mentioned here are relative to CaMPARI2, which contains the W391F-V398L mutations compared to CaMPARI1.

21

	λ_{ex}, G (nm)	λ_{em}, G (nm)	λ_{ex}, R (nm)	λ_{em}, R (nm)	ε, G (mM^{-1} cm^{-1})	ε, R (mM^{-1} cm^{-1})	QY, G (%)	QY, R (%)	Brightness, G[a]	Brightness, R[a]	K_d Ca^{2+} (nM) (fluorescence)	$\Delta F/F$[b]	K_d Ca^{2+} (nM) (photoconversion)	k_{off} (s^{-1})	k_{on} (s^{-1})
CaMPARI1	498	514	560	576	73.5 ± 5.8	32	78	58	1.0	1.0	134.7 ± 10.8	5.9 ± 0.2	100	0.29 ± 0.0044	57.5 ± 1.6
CaMPARI2	502	516	562	577	111.3 ± 2.2	65	81	65	1.6	2.3	199.2 ± 11.8	7.8 ± 1.8	224	0.91 ± 0.067	53 ± 0.98
CaMPARI2 _F391W	502	516	562	577	114.8 ± 1.7	60	81	62	1.6	2.0	109.7 ± 2.7	6.8 ± 0.3	141	0.48 ± 0.0029	85 ± 1.1
CaMPARI2 _H396K	502	516	562	577	117.9 ± 10.1	58	85	65	1.7	2.0	356.7 ± 26.1	6.4 ± 1.1	389	1.8 ± 0.019	27 ± 4.5
CaMPARI2 _F391W-G395D	502	516	562	577	122.1 ± 6.1	61	86	64	1.8	2.1	530.0 ± 39.6	5.7 ± 0.6	546	1.3 ± 0.075	31 ± 0.25
CaMPARI2 _L398T	502	516	562	577	114.2 ± 3.6	58	80	66	1.6	2.1	824.6 ± 26.2	5.4 ± 0.8	828	2.1 ± 0.012	75 ± 1.1
CaMPARI2 _F391W-L398V no epitope tags	503	515	562	577	91.8	44	81	67	1.3	1.6	174.2 ± 29.3	6.2 ± 1.4	NM	0.37 ± 0.0028	66 ± 1.3

Supplementary Table 4: Photophysical properties of CaMPARI1, CaMPARI2 and 4 affinity variants of CaMPARI2. ε is the extinction coefficient in mM^{-1}cm^{-1}. [a]Brightness is expressed as molecular brightness (extinction coefficient × quantum yield) relative to the molecular brightness of CaMPARI1 in the corresponding state. [b]$\Delta F/F$ is the difference in green fluorescence intensity between the calcium-bound and calcium-free state divided by the fluorescence of the calcium-free state of CaMPARI. NM = not measured. Errors represent the standard deviation of repeated measurements.

22

	CaMPARI1			CaMPARI2			ratio
	+ Ca^{2+} / + stimulation (s^{-1})	- Ca^{2+} / - stimulation (s^{-1})	Rate contrast	+ Ca^{2+} / + stimulation (s^{-1})	- Ca^{2+} / - stimulation (s^{-1})	Rate contrast	
Protein	0.020	0.0010	20	0.026	0.00022	120	6.0
Neurons	0.22	0.023	10	0.14	0.0046	30	3.0
Slices†	0.40	0.0097	41	0.22	0.0021	105	2.6

Supplementary Table 5: Rate contrast of CaMPARI1 and CaMPARI2 in different *in vitro* and *ex vivo* settings. The apparent rate of photoconversion in purified protein, cultured rat hippocampal neurons and rat hippocampal slice cultures is given for high calcium / stimulated and low calcium / unstimulated (protein / neurons and cultured slice, respectively) conditions. The rate contrast is calculated as the ratio of photoconversion in high calcium / with stimulation to photoconversion in low calcium / without stimulation. The final column "ratio" is rate contrast of CaMPARI2 divided by the rate contrast of CaMPARI1 for each preparation. †The slice culture experiments (data shown in Figure 2) used CaMPARI2_F391W-L398V (no epitope tags) instead of CaMPARI2.

23

Supplementary Methods

Characterization of purified CaMPARI proteins

- Protein expression and purification

pRSet-NES-His$_6$-CaMPARI was transformed in T7express cells and grown in auto-induction medium[2] at 30°C for 40 h and kept at 4°C for 32 h before harvesting. The pellet was lysed through two freeze-thaw cycles, the lysate was next diluted in 10 ml B-PER (Thermo Scientific), incubated for 1 h at 30°C and finally sonicated for 1 minute on ice. The lysate was cleared by spinning it for 30 minutes at 5000 g and NiNTA agarose resin (Qiagen) was added to the supernatant. The resin was loaded on a column, washed with 10 column volumes of TBS buffer (19.98 mM Tris, 136 mM NaCl, pH 7.4) and 10 column volumes TBS with 10 mM imidazole. Finally, the protein was eluted in TBS buffer containing 200 mM imidazole. Proteins were stored at 4°C.

- Steady-state spectroscopic characterization

Absorption spectra were measured using a Cary 100 UV-VIS spectrophotometer (Agilent). Excitation and emission spectra of the green and red form were acquired using a Cary Eclipse fluorimeter (Agilent). For the green form, excitation/emission wavelength was set at 460/550 nm and the emission/excitation scanned from 470-720/250-540 nm. For the red form, excitation/emission wavelength was set at 530/620 nm and the emission/excitation scanned from 540-720/250-610 nm.

The extinction coefficients of the green form (at 500 nm) were determined using Ward's method,[3] comparing the absorption of identical dilutions of protein in TBS buffer at pH 7.4 and phosphate buffer at pH 13, assuming an extinction coefficient of 44000 cm^{-1}M^{-1} at 440 nm for the base-denatured protein. For the red form, a sample of protein was split in two, one of which was (partially) photoconverted to the red form. From the green extinction coefficient at 500 nm and the difference in green absorption (at 500 nm) and red absorption (at 560 nm), the extinction coefficient of the red species was determined. These measurements all took place in the absence of free Ca^{2+}.

The quantum yield of both the green and red form, in the absence of free Ca^{2+}, was measured using an absolute quantum yield spectrometer (Quantarus-QY C11347, Hamamatsu) set at an excitation wavelength of 480/560 nm for the green/red species.

- Dissociation constant and photoconversion rate

To measure the K$_d$ of calcium binding and free Ca^{2+}-dependent photoconversion efficiency, we diluted protein in 12 different MOPS-KCl buffers (50 mM MOPS, 100 mM KCl, pH 7.2) with EGTA-buffered free Ca^{2+} concentrations between 1 nM and 39 μM. The green fluorescence emission (excitation 495 nm, emission at 520 nm) was measured on an Infinity M1000 fluorescence plate reader (Tecan) to obtain a titration curve which was fitted to Supplementary Equation (1) (Prism, Graphpad) to obtain the K$_d$.

24

To assess the photoconversion efficiency, the protein was similarly diluted in 12 Ca^{2+} buffers, split into 18 identical aliquots and irradiated with 405 nm LED light (200 mW/cm^2, Loctite) for 0-1-2-3-5-10-15-20-25-30-45-60-90-120-150-180-240-300 s. Before measuring red fluorescence emission, all free Ca^{2+} was chelated by adding a saturating amount of EGTA to all samples. The red fluorescence emission (excitation 555 nm, emission at 580 nm) was measured on an Infinity M1000 fluorescence plate reader (Tecan). For each calcium concentration, the red fluorescent signal was fitted to an exponential function to extract the apparent rate constant of photoconversion. At higher photoconversion times, and most notably at and above 150 s of photoconversion, the curves started to show a downward trend, which we attribute to photobleaching. To avoid this artifact from influencing the fits, we left out the last few data points for each curve. From these fits, we determined a global plateau value by averaging the plateau value of the three highest calcium concentrations and repeated, for each sample, the fits with the plateau value fixed to this value. The rate constants were then plotted against the calcium concentrations. We noticed that at the higher calcium concentrations, the rate constants dropped from the maximum value, especially for the CaMPARI1 samples. We therefore left out these values before fitting the data to Supplementary Equation (2) (IgorPro, Wavemetrics) to extract an apparent K_d.

Supplementary Equation (1)	$y = \Delta F \cdot \left(1 - \frac{x^h}{K_d{}^h + x^h}\right) + F_{min}$
Supplementary Equation (2)	$y = \Delta F \cdot \left(\frac{x^h}{K_d{}^h + x^h}\right) + F_{min}$
with	$y =$ fluorescent signal (AU)
	$K_d =$ dissociation constant in M
	$h =$ Hill coefficient
	$x = [Ca^{2+}]$ in M

- Kinetics

The rates of calcium binding (k_{on}) and unbinding (k_{off}) were determined by stopped flow. Proteins were diluted in TBS buffer with 10 µM EGTA / $CaCl_2$. Using a SX-20 (Applied Photophysics) with 490 nm LED, the protein solution was quickly mixed with a 10 mM $CaCl_2$ / EGTA solution in TBS and green fluorescence was followed in time. The decrease / increase in fluorescence was fitted with a bi-exponential curve to retrieve the rate constants using IgorPro (Wavemetrics).

- Two photon action cross-sections

CaMPARI2 two-photon action cross-sections were measured in the green and red state and in saturating EGTA and saturating Ca^{2+} conditions. The protein samples were placed on an inverted microscope equipped with a 60× 1.2NA objective and excited with Ti:Sapphire (1 mW, 735-1075 nm) or OPO laser (2 mW, 1000-1250 nm). Emission was collected through a 720SP

25

and 550/88 filter (green form) or a 720SP and 607/70BP filter (red form). The CaMPARI2 two-photon excitation spectra (average of 2 (high Ca^{2+}) or 4 (low Ca^{2+}) runs) were measured side-by-side with fluorescein (in borate buffer, pH 9.7) and rhodamine B (in methanol) as references for the action cross-section.[1] Emission in the red state was corrected for differential detection efficiency between rhodamine B and CaMPARI2-red due to the emission filters used and the respective emission spectra.

CaMPARI characterization in primary neuron cultures

Primary rat hippocampal neurons were prepared as described previously[4] and infected with AAV2/1 virus encoding CaMPARI under control of the human synapsin promoter 3 days after isolation. 6 days after infection, the coverslips with neurons were transferred to a 24-well plate with neuron imaging medium containing spontaneous synaptic activity-blocking drugs (described previously[5]). A custom-built electrode, controlled by a high current isolator (A385, World Precision Instruments) set at 90 mA was inserted into the medium for field stimulation. The neurons were imaged on a wide-field microscope (Nikon Ti Eclipse) equipped with a LED illuminator (SPECTRA-X, Lumencor), a 20× objective and an sCMOS camera (Zyla, Andor).

- Photoconversion in cultured primary neurons

To follow photoconversion in time, we irradiated the CaMPARI-expressing neurons with 0.5 s of 395 nm light (~3 W/cm^2) accompanied by 40 field pulses of 1 ms at 80 Hz or in the absence of field stimulation. After 30 s in the dark (to allow the calcium to fully unbind from CaMPARI), the cells were imaged in the green and red channels. This procedure was repeated 30 times, to result in 15 s of accumulated 395-nm light irradiation. The resulting red fluorescence was plotted in time, and fitted with an exponential function to extract the rate constant of photoconversion.

- Calcium unbinding kinetics in cultured primary neurons

To measure the rate of calcium unbinding in CaMPARI-expressing neurons, we continuously imaged the green channel at relatively low light power (270 $\mu W/cm^2$) to avoid photobleaching and field stimulated the neurons (1 ms pulses at 80 Hz), followed by 30 s of recovery. We delivered first 1 pulse, then 2, 5, 10, 20, 40 and 80 pulses. The fluorescence recovery was fitted with an exponential function and averaged over the 150-200 cells in total (from 3 trials in 2 independent culture dishes) to extract the rate constant of calcium unbinding. Generally, the traces resulting from one field pulse could not be fitted, and the two and five pulse traces could only be fitted in 20-50% of neurons.

- Photoconversion in primary neurons at different stimulation frequencies

To observe the effect of the affinity tuning on the photoconversion in CaMPARI-expressing neurons, we imaged the pre-green and pre-red signal, field stimulated the neurons for 2 s at 0 (no stimulation), 2, 10, 30 or 80 Hz while photoconverting using ~3 W/cm^2 of 395 nm light, and measured a post-green and post-red image again. From the post-red image, the pre-red image

26

was subtracted. An image mask was calculated based on the pre-green and the background-corrected red image was divided by the pre-green signal in the masked area. The ratio between the stimulated samples and non-stimulated sample was calculated, resulting in a fold increase in red-to-green ratio upon stimulation.

- Delay between stimulation and photoconversion light

We stimulated several fields of view of neuron cultures expressing CaMPARI variants with 20 field pulses at 80 Hz and 250 ms of photoconversion light. 45 s later, green and red fluorescence images were acquired. This stimulation and photoconversion was repeated for 10 cycles. This protocol was performed with 0, 0.5, 1, 2, 5 and 30 s delay between stimulation and photoconversion as well as a negative control without stimulation. For each, the rate of photoconversion was measured as the slope of the increase of red/green signal vs cumulative photoconversion time. This was normalized to 1 at the highest rate. For comparison, calcium binding and fluorescence change kinetics were measured by continuous imaging of the green CaMPARI fluorescence during an equivalent stimulation of 20 field pulses at 80Hz.

CaMPARI2-red signal turnover experiments:

CA1 neurons in rat organotypic hippocampal slice cultures were electroporated at DIV15 with DNA ($20ng\ \mu l^{-1}$) encoding CaMPARI2_F391W-L398V (no epitope tags). Four days later, two-photon z-stacks were collected using two MaiTai Deep See lasers. For each z-plane, two frames (images) were acquired, exciting at 980 nm (2-5 mW measured at the back-focal plane of the objective) and 1040 nm (3-8 mW), respectively. The procedure was repeated several times (up to 3 days). Between imaging sessions slices were put back in the incubator. To increase intracellular calcium in response to synaptic activity, a monopolar electrode was placed in the stratum radiatum and 0.2 ms electrical pulses were delivered 100 times at 100 Hz at an intensity that induced postsynaptic spiking in a neighboring nontransfected CA1 neuron. UV light (395 nm, 16 mW mm^{-2}) was applied for 2 s with a 1 s delay relative to the start of stimulation (24 neurons, 4 slices). Images were taken at time points t = -0.5, 0, 6, 12, 24, 30, 48, 60, 72 and 72.5 hours with t = 0 immediately after stimulation + UV light or UV light alone. To compare intensity between imaging sessions, images were normalized to a calibration solution containing 200 μg ml^{-1} fluorescein and 100 μg ml^{-1} sulforhodamine 101. These higher dye concentrations were selected to closely match the intensity of the CaMPAR2 green species prior to photoconversion, and the red species after photoconversion. Fluorescence values of the CaMPARI green and red channels were divided by the corresponding calibration values. R/G is the normalized red fluorescence divided by the normalized green fluorescence.

Macro for 2P image analysis of CaMPARI conversion in neurons

We stablished a workflow to analyze 3D images generated in ScanImage[6] employing alternate-frame 2P 980/1040nm wavelength acquisition. We used Fiji[7], an image processing package distribution of ImageJ. Channels corresponding to 980 nm or 1040 nm acquisition were deinterleaved and 3D stitched using the Pairwise Stitching plugin[8]. For further analysis, we used

27

the green fluorescence collected at 980 nm excitation and red fluorescence collected at 1040 nm excitation. After median filtering and rolling ball background subtraction[9], a maximum intensity projection image was generated and saved. Maximum pixel values from ROIs drawn at neuronal somata were saved in Excel and divided from fluorescence values obtained from median-filtered fluorescein/SR101 solutions. Code of the Fiji/ImageJ macro is reproduced below.

```
//This is a macro for analysis of CaMPARI 4ch images acquired with alternate-frame 2P
980/1040nm wv acquisition in ScanImage
//It deinterleaves, corrects for chromatic aberration, filters image, makes maximum
projection, subtracts background and finally
//saves the image containing the relevant channels for analysis (ch1/ch4) APA 26.3.18

run("Bio-Formats Windowless Importer", "view=Hyperstack stack_order=XYCZT");
imageTitle=getTitle();
run("Deinterleave", "how=4");
run("Merge Channels...", "c1=["+imageTitle +" #1] c2=["+imageTitle +" #2] create");
rename("Composite 980.tif");
run("Merge Channels...", "c3=["+imageTitle +" #3] c4=["+imageTitle +" #4] create");
rename("Composite 1040.tif");
wait(100);
run("Pairwise stitching", "first_image=[Composite 980.tif] second_image=[Composite
1040.tif] fusion_method=[Overlay into composite image] fused_image=[Composite
980.tif<->Composite 1040.tif] check_peaks=5 compute_overlap x=0 y=0.0000 z=0.0000
registration_channel_image_1=[ Average all channels] registration_channel_image_2=[
Average all channels]");
selectWindow("Composite 980.tif");
close();
selectWindow("Composite 1040.tif");
close();
imageTitle=getTitle();
run("Split Channels");
run("Merge Channels...", "c1=[C1-Composite 980.tif<->Composite 1040.tif] c4=[C4-
Composite 980.tif<->Composite 1040.tif] create");
selectWindow("C3-Composite 980.tif<->Composite 1040.tif");
close();
selectWindow("C2-Composite 980.tif<->Composite 1040.tif");
close();
Stack.setChannel(1);
run("Green");
run("Enhance Contrast", "saturated=0.35");
Stack.setChannel(2);
run("Red");
run("Enhance Contrast", "saturated=0.35");
imageTitle=getTitle();
run("Median...", "radius=0.5");
run("Z Project...", "projection=[Max Intensity]");
run("Subtract Background...", "rolling=100");
saveAs("Tiff");
selectWindow("Composite 980.tif<->Composite 1040.tif");
close();
```

Western blots with anti-CaMPARI-red antibody

Western blots were prepared by loading 0.5 µg of protein in each well of a bis-tris PAGE gel (Novex, Invitrogen). The gel was blotted onto a PVDF membrane (Invitrolon, Invitrogen) and

28

117

blocked for 1 h at room temperature in TBS with 0.1% Tween (TBST) and 5% dry non-fat milk powder (TBST-milk). We diluted mouse bleeds (1:1000), hybridoma supernatant (1:10) or primary antibody (1:10 000), in TBST-milk and incubated for 16 h at 4°C. Then, the membrane was washed three times in TBST and labeled with a HRP-conjugated horse-anti-mouse (Cell Signaling, 7076) diluted 1:3000 in TBST-milk for 1 h at room temperature. The blot was again washed three times with TBST and 3 times with TBS before bioluminescent substrate was added (SuperSignal West Pico, Thermo Scientific) and the blot imaged.

Immunohistochemistry in neuron cultures

For immunostaining, we used neurons 11 days after infection. One focal area was photoconverted with 5 s of 400-nm light (3 mW/cm^2) using the microscope's 20× objective while the whole dish was stimulated at 80 Hz for 2 s concurrent with the illumination. The neurons were then fixed in 4% paraformaldehyde for 10 minutes at room temperature and washed 3 times with PBS-EGTA. To image at this point, we changed the buffer to PBS-EGTA.

For immunohistochemical staining we applied perm/block1 solution (10% normal goat serum, 0.1% Triton X-100 in PBS) for 1 h at room temperature after the PBS-EGTA wash. Then, primary antibody was applied (mouse-anti-CaMPARI-red 1:10 000, rabbit-anti-flag 1:3000), diluted in perm/block1, and left shaking at 4°C overnight. The neurons were then washed 3 times with PBS-EGTA and secondary antibodies (goat-anti-rabbit-alexa405 and goat-anti-mouse-alexa647) were applied, diluted 1:1000 in perm/block1 solution. After 1 h at room temperature, they were washed 3 times with PBS-EGTA and imaged.

To measure the extent of endogenous fluorescent signal loss due to fixation, we aligned red and green images of a photoconverted field of view before and after fixation but before staining. The average pixel intensity in a region without neurons was subtracted from the average pixel intensity of the whole field of view. We did this for 30 images of 12 different wells of cultured neurons.

CaMPARI2 *ex vivo* photoconversion and immunostain in mouse acute brain slice

- Viral injections

P21–P25 mice (C57/BL6J, supplied by the Charité Universitätsmedizin Berlin FEM) were deeply anesthetized with ketamine/xylazine (7 mg kg^{-1}/1 mg kg^{-1}), and then injected with 100–200 nl of the adeno-associated virus AAV2/1-Syn-CaMPARI2 in the somatosensory cortex. We waited for > 14 days before use.

- Slice preparation

Coronal slices, 300 µm thick, were prepared from AAV2/1-Syn-CaMPARI2-injected mice (postnatal ages P36–P50). The artificial cerebrospinal fluid (ACSF) used for recordings and brain slicing contained (in mM): 125 NaCl, 2.5 KCl, 1.25 NaH$_2$PO$_4$, 25 NaHCO$_3$, 2 CaCl$_2$, 1 MgCl$_2$ and 25

29

d-glucose, pH ~7.4. Immediately following slice preparation, the slices were incubated at 32°C for 5 min in a solution containing (in mM): 110 choline chloride, 2.5 KCl, 1.25 NaH_2PO_4, 26 $NaHCO_3$, 11.6 sodium ascorbate, 3.1 sodium pyruvate, 7 $MgCl_2$, 0.5 $CaCl_2$ and 10 d-glucose, pH ~7.4, followed by 25 min at 32°C in ACSF and then at room temperature, before recording in a submersion chamber at 32°C. 5 mM KCl was added to the ACSF during CaMPARI2 conversion to depolarize the neurons in the brain slice. All solutions were saturated with 95% O_2/5% CO_2 and had pH ~7.4.

- Photoconversion and imaging

CaMPARI2 photoconversion was delivered using an X-cite 200 W mercury lamp (Excelitas Technologies, Mississauga, Ontario, Canada) and light guide through a 405/10 bandpass filter (Semrock, FF01-405/10-25). Conversion light intensity was ~ 200 mW cm^{-2}.

A Femto 2D two-photon laser scanning system (Femtonics Ltd, Budapest, Hungary) was equipped with a femtosecond pulsed Chameleon Ti:Sapphire laser (Coherent, Santa Clara, CA, USA). Imaging was controlled by the MATLAB-based MES software package (Femtonics). For CaMPARI red and green fluorescence measurements the laser was tuned to λ = 820 nm. Fluorescence was detected in epifluorescence mode with a water immersion objective (LUMPLFL 60×/1.0 NA, Olympus, Hamburg, Germany). Trans-fluorescence and transmitted infrared light were detected using an oil immersion condenser (Olympus; 1.4 NA). Fluorescence was divided by a dichroic mirror at ~590–600 nm, and green and red signals were filtered using 525/50 and 650/50 bandpass filters, respectively.

- CaMPARI immunohistochemistry

After imaging of the live brain slices, they were fixed in PFA (4 %) at 4°C overnight. Slices were washed in phosphate buffered solution (PBS) and then blocked in normal goat serum (NGS) and PBS (5 % NGS, 1% Triton in PBS) for two hours at room temperature. Brain slices were then incubated in primary antibody solution (anti-CaMPARI-red, 1:1000) at 4°C overnight. Slices were washed in PBS before incubation in the secondary antibody solution (Alexa 633, goat anti mouse, Invitrogen A21050, 1:500) for two hours at room temperature. Slices were then washed in PBS and mounted in Glycerol (80% in PBS + 2.5 % DAPCO).

- Confocal imaging

Slices were imaged on a confocal laser scanning microscope (Nikon A1Rsi+) using a 20× air objective (Plan Apo, 0.8 NA, 1.000 WD) and a 647 nm laser. Fluorescence was imaged through a 700/50 bandpass emission filter.

Data analysis

Images were processed in ImageJ / Fiji. Data was analyzed and graphs were plotted using IgorPro (Wavemetrics) or Prism (GraphPad). Figures were made using Illustrator (Adobe).

30

Reagents

DNA constructs for pAAV_hsyn_CaMPARI2, pAAV_hsyn_CaMPARI2_F391W, pAAV_hsyn_CaMPARI2_H396K, pAAV_hsyn_CaMPARI2_F391W-G395D and pAAV_hsyn_CaMPARI2_L398T are available via Addgene (http://www.addgene.org #101060-#101064). AAV virus can be requested at the University of Pennsylvania Vector Core (http://www.med.upenn.edu/gtp/vectorcore). Tg(elavl3:CaMPARI2)[jf92] transgenic zebrafish will be deposited to the ZIRC (https://zebrafish.org). Drosophila expressing CaMPARI2 and CaMPARI2-L398T under UAS and LexA promoter in chromosome 2 (su(Hw)attP5), 3 (VK00005) or X (su(Hw)attP8) are available from the authors and at the Bloomington Drosophila Stock Center (https://bdsc.indiana.edu, #78316-#78326).

Supplementary References

1. Makarov, N. S., Drobizhev, M. & Rebane, A. Two-photon absorption standards in the 550-1600 nm excitation wavelength range. *Opt. Express* **16,** 4029–4047 (2008).

2. Studier, F. W. Protein production by auto-induction in high density shaking cultures. *Protein Expr. Purif.* **41,** 207–34 (2005).

3. Ward, W. W. Properties of the Coelenterate green-fluorescent proteins. *Biolumin. Chemilumin. Basic Chem. Anal. Appl. Eds. DeLuca, M. McElroy, WD (Academic Press. Inc., NY)* 235–242 (1981).

4. Wardill, T. J. *et al.* A Neuron-Based Screening Platform for Optimizing Genetically-Encoded Calcium Indicators. *PLoS One* **8,** 1–12 (2013).

5. Chen, T.-W. *et al.* Ultrasensitive fluorescent proteins for imaging neuronal activity. *Nature* **499,** 295–300 (2013).

6. Pologruto, T. A., Sabatini, B. L. & Svoboda, K. ScanImage: Flexible software for operating laser scanning microscopes. *Biomed. Eng. Online* **2,** 1–9 (2003).

7. Schindelin, J. *et al.* Fiji: an open-source platform for biological-image analysis. *Nat. Methods* **9,** 676–682 (2012).

8. Preibisch, S., Saalfeld, S. & Tomancak, P. Globally optimal stitching of tiled 3D microscopic image acquisitions. *Bioinformatics* **25,** 1463–5 (2009).

9. Sternberg. Biomedical Image Processing. *Computer (Long. Beach. Calif).* **16,** 22–34 (1983).

31

Publication #3: Nature Communications 2020

Freeze-frame imaging of synaptic activity using SynTagMA

Alberto Perez-Alvarez [1]*, Brenna C. Fearey [1]*, Ryan J. O'Toole [2], Wei Yang [3], Ignacio Arganda-Carreras[4,5,6], Paul J. Lamothe-Molina [1], Benjamien Moeyaert [7], Manuel A. Mohr [7], Lauren C. Panzera [2], Christian Schulze [1], Eric R. Schreiter [7], J. Simon Wiegert [3], Christine E. Gee [1], Michael B. Hoppa [2] & Thomas G. Oertner [1]

[1] Institute for Synaptic Physiology, University Medical Center Hamburg-Eppendorf, Hamburg, D-20251 Germany
[2] Department of Biological Sciences, Dartmouth College, Hanover, NH, 03755 USA
[3] HHMI, Janelia Farm Research Campus, Ashburn VA, 20147 USA
[4] Ikerbasque, Basque Foundation for Science, Bilbao, Spain
[5] Dept. of Computer Science and Artificial Intelligence, Basque Country University, San Sebastian, Spain
[6] Donostia International Physics Center (DIPC), San Sebastian, Spain
[7] Research Group Synaptic Wiring and Information Processing, University Medical Center Hamburg-Eppendorf, Hamburg, D-20251 Germany
* These authors contributed equally to the study
§ Corresponding author: thomas.oertner@zmnh.uni-hamburg.de

Specific contribution

The following paper has been published in Nature Communications. I am shared first author. I contributed to the writing, editing, and figure creation/design of the entire paper. My work is explicitly displayed in Figures: 2e, 4, 5, 6j, S5a-c, S6, S7, S8, S9, S11. Although not shown in the paper, my original data demonstrated turnover of postSynTagMA (Appendix Fig. 1). I also spent a significant amount of time working on data that did not make it into the paper including simultaneous SynTagMA and Fluo5F imaging at single synapses (Appendix Fig. 2).

I, _____, agree with the above statements as the direct supervisor.

_____, Date & Place_____

Freeze-frame imaging of synaptic activity using SynTagMA

Alberto Perez-Alvarez [1,8], Brenna C. Fearey [1,8], Ryan J. O'Toole [2], Wei Yang [3], Ignacio Arganda-Carreras [4,5,6], Paul J. Lamothe-Molina [1], Benjamien Moeyaert [7], Manuel A. Mohr[7], Lauren C. Panzera [2], Christian Schulze[1], Eric R. Schreiter [7], J. Simon Wiegert [3], Christine E. Gee [1], Michael B. Hoppa[2] & Thomas G. Oertner [1✉]

Information within the brain travels from neuron to neuron across billions of synapses. At any given moment, only a small subset of neurons and synapses are active, but finding the active synapses in brain tissue has been a technical challenge. Here we introduce SynTagMA to tag active synapses in a user-defined time window. Upon 395–405 nm illumination, this genetically encoded marker of activity converts from green to red fluorescence if, and only if, it is bound to calcium. Targeted to presynaptic terminals, preSynTagMA allows discrimination between active and silent axons. Targeted to excitatory postsynapses, postSynTagMA creates a snapshot of synapses active just before photoconversion. To analyze large datasets, we show how to identify and track the fluorescence of thousands of individual synapses in an automated fashion. Together, these tools provide an efficient method for repeatedly mapping active neurons and synapses in cell culture, slice preparations, and in vivo during behavior.

[1] Institute for Synaptic Physiology, University Medical Center Hamburg-Eppendorf, Hamburg D-20251, Germany. [2] Department of Biological Sciences, Dartmouth College, Hanover, NH 03755, USA. [3] Research Group Synaptic Wiring and Information Processing, University Medical Center Hamburg-Eppendorf, Hamburg D-20251, Germany. [4] Ikerbasque, Basque Foundation for Science, Bilbao, Spain. [5] Dept. of Computer Science and Artificial Intelligence, Basque Country University, San Sebastian, Spain. [6] Donostia International Physics Center (DIPC), San Sebastian, Spain. [7] HHMI, Janelia Farm Research Campus, Ashburn, VA 20147, USA. [8] These authors contributed equally: Alberto Perez-Alvarez, Brenna C. Fearey. ✉email: thomas.oertner@zmnh.uni-hamburg.de

The physical changes underlying learning and memory likely involve alterations in the strength and/or number of synaptic connections. On the network level, neuroscience faces an extreme 'needle in the haystack' problem: it is thought to be impossible, in practice, to create a map of all synapses that are active during a specific sensory input or behavior. Excellent genetically-encoded sensors for calcium, glutamate and voltage have been developed[1–3], which when combined with two-photon laser-scanning microscopy can monitor the activity of neurons even down to the synaptic level in highly light-scattering brain tissue[4]. However, the tradeoff between spatial and temporal resolution makes it impossible with this technology to simultaneously measure fluorescence in the thousands of synapses of even a single pyramidal neuron. Most functional imaging experiments are therefore limited to cell bodies, i.e., low spatial resolution[5], or monitor the activity of a few synapses within a single focal plane[6]. Multi-beam scanning designs have been proposed, but due to scattering of emitted photons, they do not produce sharp images at depth[7,8]. Projection microscopy can be a very efficient approach[9], but only in situations where the fluorescent label is restricted to one or very few neurons. In general, the need to choose between high temporal or high spatial resolution limits the information we can extract from the brain with optical methods.

A strategy to overcome this limit is to rapidly 'freeze' activity in a defined time window and read it out at high resolution later. The Ca^{2+}-modulated photoactivatable ratiometric integrator CaMPARI undergoes an irreversible chromophore change from green to red when the Ca^{2+} bound form is irradiated with violet (390–405 nm) light[10,11]. CaMPARI has been successfully applied to map the activity of thousands of neurons in zebrafish, *Drosophila*, and in mouse[10,12–14]. As CaMPARI was designed to diffuse freely within the cytoplasm, it does not preserve subcellular details of Ca^{2+} signaling. By anchoring CaMPARI to either pre- or postsynaptic compartments, we are able to mark active synapses a in short time window defined by violet light illumination. Three steps were necessary to create a Synaptic Tag for Mapping Activity (SynTagMA): (1) We introduced point mutations in CaMPARI to generate a new probe, CaMPARI2, with improved brightness and conversion efficiency[11]; (2) We target CaMPARI2 (F391W_L398V) to either presynaptic boutons by fusing it to synaptophysin (preSynTagMA) or to the postsynaptic density by fusing it to an intrabody against PSD95[15] (postSynTagMA); (3) We present an analysis workflow that corrects for chromatic aberration, tissue displacement (warping) and automatically finds regions of interest (i.e., postsynapses or boutons) to quantify green and red fluorescence. Bouton-localized preSynTagMA allows us to distinguish active and inactive axons. We use spine-localized postSynTagMA to visualize the extent of action potential back-propagation into the large apical dendritic tree of hippocampal pyramidal cells. Following repeated sparse activation of Schaffer collateral axons, postSynTagMA marks a small subset of synapses on CA1 pyramidal cells as highly active. PostSynTagMA is not only useful to analyze the organization of inputs on spiny pyramidal cells, but works equally well for interneurons where most synapses are formed on the dendritic shaft. A fraction of postSynTagMA is sequestered to the nucleoplasm, generating a useful label to identify neurons that are active during a specific behavior. As an application example, we photoconvert active CA1 pyramidal cells during reward collection in a spatial memory task. In summary, the key advantage of SynTagMA compared to acute calcium sensors is the greatly extended read-out period, allowing three-dimensional scanning of relatively large tissue volumes at cellular or at synaptic resolution.

Results

Creating and characterizing a presynaptic marker of activity.
To visualize activated presynaptic boutons, we fused the Ca^{2+}-modulated photoactivatable ratiometric integrator CaMPARI[10] to the vesicular protein synaptophysin (sypCaMPARI). In cultured hippocampal neurons, sypCaMPARI showed a punctate expression pattern along the axon, indicating successful targeting to vesicle clusters in presynaptic boutons (Fig. 1a). SypCaMPARI fluorescence decreased after stimulating neurons to evoke trains of action potentials (APs), saturating at 50 APs and slowly returning to baseline (Fig. 1b–d). This Ca^{2+}-dependent dimming, which is a known property of CaMPARI[10], provides a low-pass-filtered read-out of ongoing neuronal activity. Indeed, the signal-to-noise ratio was sufficient for detecting single APs in single boutons when 30 sweeps were averaged, suggesting a high sensitivity of localized sypCaMPARI for Ca^{2+} influx (Fig. 1c). The Ca^{2+}-bound form of CaMPARI is irreversibly photoconverted from a green to a red fluorescent state by violet light irradiation[10]. Repeatedly pairing electrical field stimulation with 405 nm light flashes increased the red-to-green fluorescence ratio (R/G) of sypCaMPARI boutons in a stepwise fashion (Fig. 1e, f). Blocking action potential generation with tetrodotoxin (TTX) strongly reduced photoconversion, indicating that spike-induced Ca^{2+} influx through high-threshold voltage-activated Ca^{2+} channels was necessary for efficient conversion. Similar to the dimming response, the amount of sypCaMPARI photoconversion depended on the number of APs (Fig. 1g), suggesting that the R/G ratio can be interpreted as a lasting and quantitative record of axonal activity rather than just a binary signal.

Ca^{2+}-dependent dimming of sypCaMPARI peaked about 1 s after stimulation and returned to baseline after 3–15 s (Fig. 1b, c). To determine the photoconversion time window, multiple delays of violet light illumination were tested in single experiments using a digital mirror device (Fig. 2a). Photoconversion of sypCaMPARI was not efficient when light pulses (100 ms duration) were coincident with stimulation onset (Fig. 2b, c). Rather, maximal photoconversion occurred when violet light was applied 2–5 s after stimulation. The photoconversion window of sypCaMPARI extended to at least 10 s after stimulation, outlasting the dimming response to 5 APs (Fig. 1b). Some photoconversion also occurred in the absence of stimulation or in the presence of TTX (Fig. 1e, g and Fig. 2b, c). The long temporal window and activity-independent photoconversion are both undesirable traits that limit the utility of sypCaMPARI.

Parallel efforts to improve CaMPARI resulted in CaMPARI2, which contains a number of point mutations improving brightness, increasing kinetics, reducing activity-independent photoconversion and lowering the Ca^{2+} affinity[11]. We selected the variant CaMPARI2 (F391W_L398V) (K_d Ca^{2+} = 174 nM, k_{on} 66 s^{-1}, k_{off} 0.37 s^{-1}, photoconversion rate in slices 0.22 s^{-1} with Ca^{2+}, 0.0021 s^{-1} without Ca^{2+})[11] and fused it to synaptophysin to create preSynTagMA and expressed it in cultured hippocampal neurons. The temporal precision and dynamic range of preSynTagMA were both enhanced. PreSynTagMA showed no photoconversion in the absence of activity (Supplementary Fig. 1a–c). We could readily distinguish active from inactive axons by the differential preSynTagMA photoconversion in the presence of the GABA$_A$ antagonist bicuculline (Supplementary Fig. 1d–g). When the same axons were directly electrically stimulated via field electrodes, green preSynTagMA fluorescence dimmed in all axons, indicating that action potentials triggered calcium transients in all axons (Supplementary Fig. 1h). The rapid recovery from dimming corresponds to the short photoconversion time window (0.2–2 s post-stimulation) of preSynTagMA (Fig. 2d, e; Supplementary Fig. 1h). The photoconversion time windows of preSynTagMA and
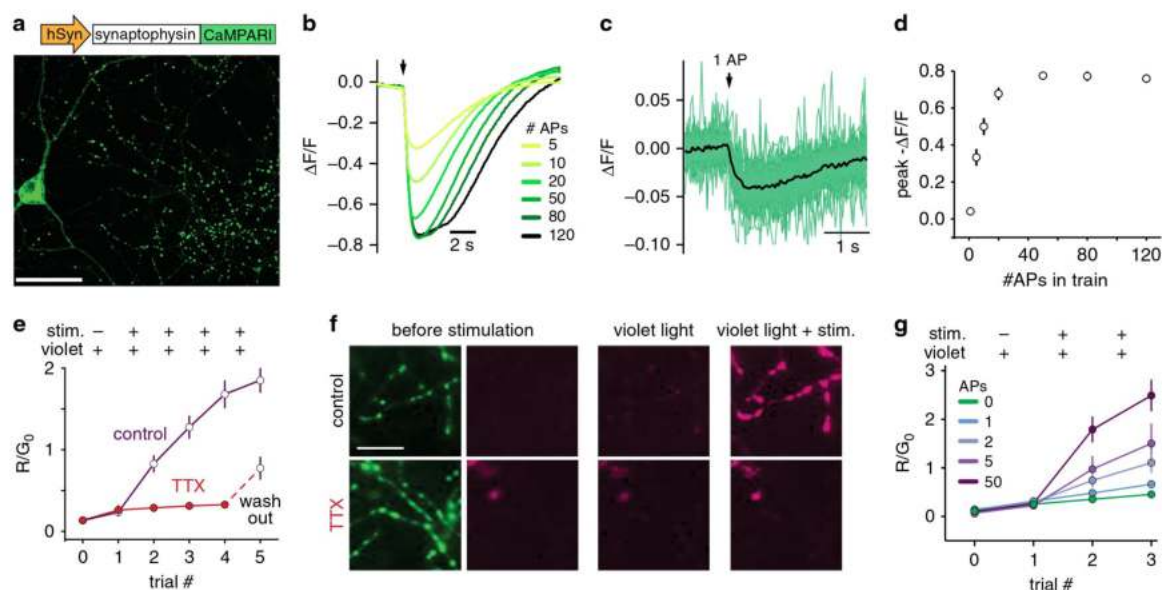
Fig. 1 Synaptophysin-fused CaMPARI marks active presynaptic terminals. a Representative image of cultured rat hippocampal neurons expressing sypCaMPARI. Note the clear punctate labeling of axonal boutons. **b** Average fluorescence response of sypCaMPARI boutons (green channel emission) to varying numbers of action potentials (APs) evoked at 50 Hz ($n = 6$ neurons, 317 synapses). **c** Trial-averaged responses to 30 single APs (green, $n = 57$ synapses). Black line is the average response of $n = 3$ neurons. **d** Plot of the maximum $\Delta F/F$ versus number of APs from the experiments in **b** and **c. e** Plot of initial red to green ratio of boutons expressing sypCaMPARI at baseline, after photoconverting violet light alone (20 light pulses of 1 s duration at 0.1 Hz, 405 nm, 10.8 mW cm^{-2}) and after simultaneous stimulation with trains of 50 APs at 50 Hz (trials 1–4). The experiment was performed in the absence or presence of 3 μM tetrodotoxin to block action potentials (control: $n = 8$ neurons; TTX: $n = 7$ neurons). Note that after washing out TTX, the R/G_0 ratio (trial 5) increased to the same amplitude as the first instance in control neurons (trial 2). **f** Representative red (magenta, trial 0, trial 1, trial 3) and green (green, trial 0) images of boutons from the experiment in **e. g** The amount of photoconversion (R/G_0) in a similar experiment as **e** but varying the number of APs in a 50 Hz train (20 light pulses of 1 s duration at 0.1 Hz, 405 nm, 54.1 mW cm^{-2}; Stim: 20 bursts at 50 Hz). AP fold increase was statistically different from all other stimulation conditions using a one-way ANOVA with Tukey's post-hoc comparison (*$p = 0.032$). Neurons per condition: 0 AP ($n = 4$), 1 AP ($n = 4$), 2 APs ($n = 5$), 5 APs ($n = 5$), 50 APs ($n = 7$). Data are presented as mean ± SEM in **d**, **e**, and **g**. Scale bar: 50 μm (**a**), 20 μm (**f**). Cultured neurons were 14–22 days old, expressing sypCaMPARI for 8–16 days.

CaMPARI2 (F391W_L398V) were near-identical (Fig. 2e), suggesting that synaptic targeting did not affect the kinetics of the indicator. Two hours after photoconversion, the R/G ratio was still 68% of the peak value, indicating photoconverted preSynTagMA marks activated boutons for several hours (Supplementary Fig. 1i). To quantify preSynTagMA localization, we co-expressed preSynTagMA together with cytosolic mCerulean in hippocampal slice cultures. In Schaffer collateral axons, preSynTagMA was 3.8-fold enriched in boutons vs. axonal shafts (Supplementary Fig. 2). For dense axonal labeling, we microinjected a viral vector (AAV2/9-syn-preSynTagMA) in CA3 and imaged Schaffer collateral boutons in CA1 *stratum radiatum*. Repeated electrical stimulation combined with violet light illumination induced photoconversion of preSynTagMA-expressing boutons while no photoconversion was induced by identical violet illumination when action potentials were suppressed by TTX (Supplementary Fig. 3).

Targeting SynTagMA to excitatory postsynapses. We chose to target SynTagMA to the postsynaptic protein PSD95, which has a higher retention time than most postsynaptic density proteins[16]. We decided against making a PSD95-CaMPARI fusion protein as overexpression of PSD95 is known to induce dramatic changes in function, size, and connectivity of dendritic spines[17]. Instead, we fused CaMPARI2 (F391W_L398V) (after deleting the nuclear export sequence) to a genetically encoded intrabody against PSD95 (PSD95.FingR)[15]. The resulting fusion protein, however, was not restricted to dendritic spines, where most excitatory

synapses are located, but labeled the entire dendrite of CA1 pyramidal neurons (Fig. 3a, d). We reasoned that the lack of spine enrichment was due to a large fraction of unbound cytoplasmic protein. An elegant method to reduce cytoplasmic fluorescence is to fuse a zinc finger (ZF) and the transcription repressor KRAB (A) to the targeted protein and include a ZF binding sequence near the promoter[15,18]. It is presumed that the ZF-KRAB domains direct excess unbound cytosolic protein into the nucleus where the ZF binds to the ZF binding sequence and KRAB(A) suppresses transcription of the exogenous genes. We added these additional regulatory elements to the PSD95.FingR-CaMPARI2 (F391W_L398V) construct, which has no additional nuclear export or localization sequences added, and co-expressed it with mCerulean. Punctate green fluorescence was now observed predominantly in spines and nuclei were fluorescent as expected for a ZF-KRAB(A) containing protein. The ratio of spine-to-dendrite green fluorescence was about 4 times higher than mCerulean spine-to-dendrite ratios, suggesting CaMPARI2 was now localized to postsynapses (Fig. 3b, e). Serendipitously, we discovered that the upstream ZF binding sequence was dispensable for autoregulation (Fig. 3c, f), which simplified swapping of promotors. We named this minimal construct postSynTagMA and characterized it further. To test for potential effects of postSynTagMA on neuronal physiology, we measured passive and active electrical properties, miniature excitatory postsynaptic currents and spine densities of postSynTagMA/mCerulean-expressing neurons and neurons expressing only mCerulean

124
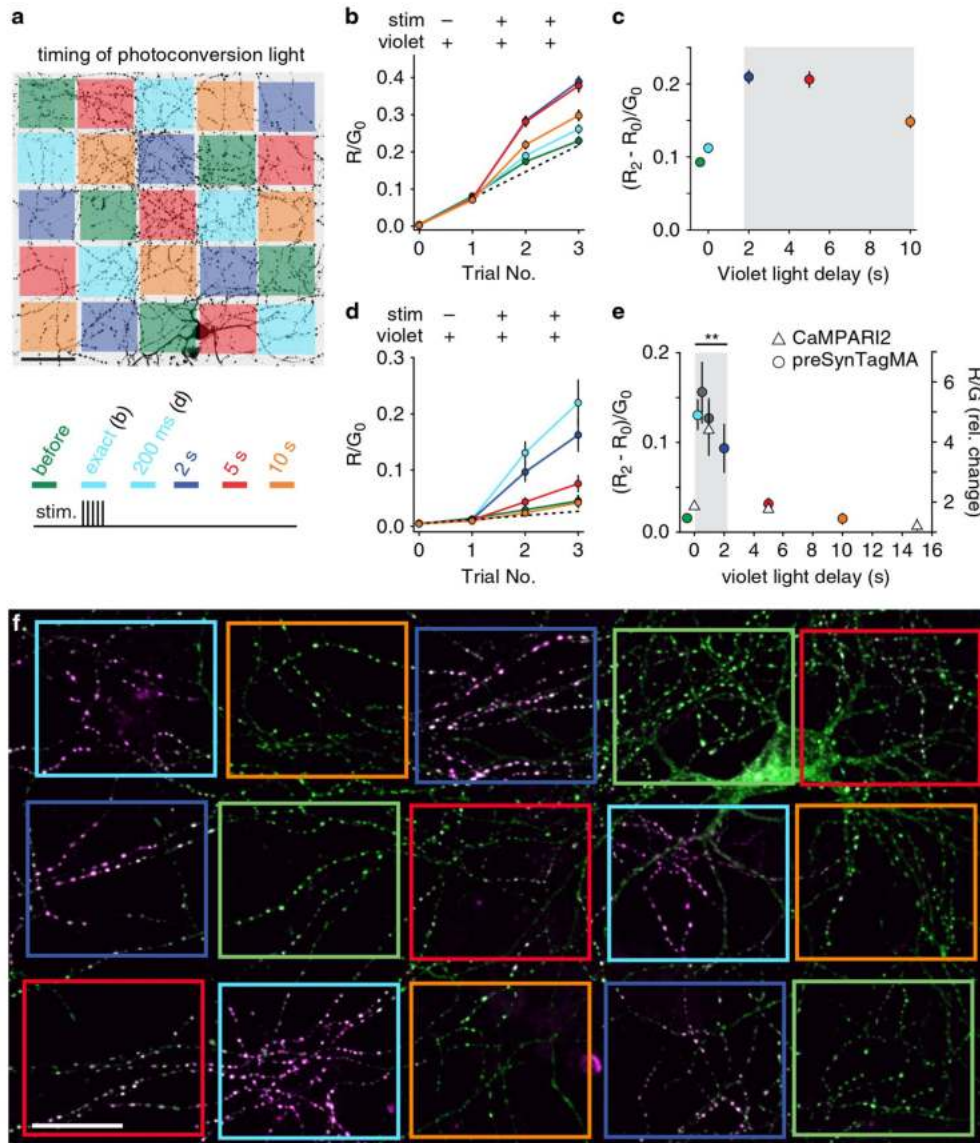
Fig. 2 Temporal resolution of preSynTagMA photoconversion. a A spatial light modulator was used to illuminate parts of the axonal arbor (405 nm, 50 mW cm^{-2}, 100 ms) at different times relative to a brief tetanic stimulation (5 APs). After each trial, new images were acquired. 'Exact' & '200 ms' timing share the same color code (cyan) as we used 'exact' timing in sypCaMPARI experiments and a 200 ms delay in preSynTagMA experiments. **b** Ratio of red to green fluorescence (R/G$_0$) from sypCaMPARI boutons illuminated at different times relative to the electrical stimulation. Trial 1 shows the effect of illumination without stimulation. Line color code as in **a**, $n = 6$ neurons. **c** Activity-dependent photoconversion ($\Delta R/G_0$) versus delay from start of stimulation to violet light from the same experiments in **b**. The gray box indicates the time window for efficient photoconversion of sypCaMPARI. **d** Neurons expressing preSynTagMA (synaptophysin-CaMPARI2 (F391W_ L398V)) were stimulated as in **a–c**. Note the greatly reduced increase in R/G$_0$ with violet light alone (Trial 1). $n = 6$ neurons. **e** Left axis: activity-dependent photoconversion ($\Delta R/ G_0$) versus delay of preSynTagMA expressing neurons (circles). $n = 12$ neurons for the before, 200 ms, and 2 s conditions and $n = 6$ neurons for the 500 ms, 1 s, 5 s and 10 s conditions. Right axis: photoconversion of CaMPARI2(F391W_L398V) after 50 bAPs and 100 ms violet light (triangles). $n = 5$ neurons. **f** Cultured rat hippocampal neuron expressing preSynTagMA, trial # 3 from **d**. Boxes indicate regions where photoconversion light was applied with different delays (color code as in **a**). All data are presented as mean ± SEM. In **e**, a Kruskal-Wallis test followed by the Benjamini-Hochberg FDR method was used. Timing conditions inside the gray box were not significantly different while the timing conditions outside the gray box were significantly different from those within the box ($p < 0.001$). Scale bars: 50 μm (**a**), 25 μm (**f**). Cultured neurons were 14–18 days old, expressing sypCaMPARI or preSynTagMA for 8–16 days.

125
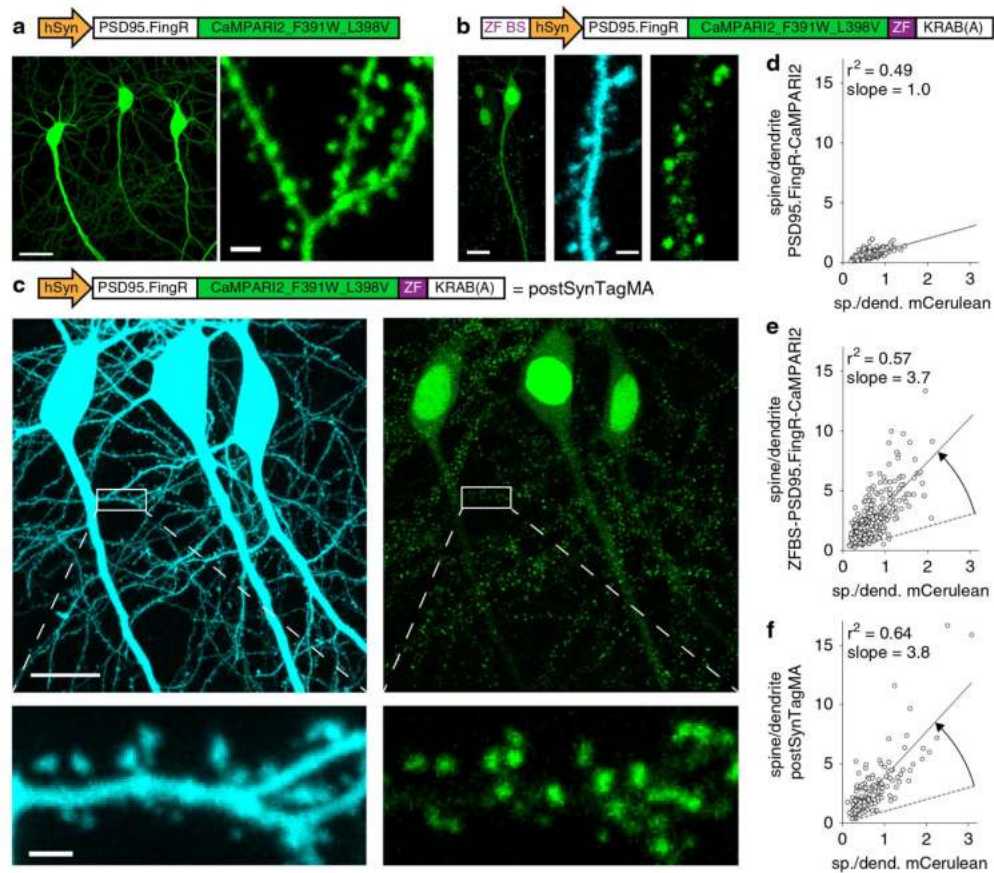
Fig. 3 Postsynaptic targeting of SynTagMA using a PSD95 intrabody. a CA1 neurons expressing the unregulated construct: a fusion protein of PSD95 fibronectin intrabody (PSD95.FingR) and CaMPARI2_F391W_L398V (without NES or epitope tags). Scale bars: 20 μm, 2 μm. **b** CA1 neurons expressing PSD95.FingR-CaMPARI2 with a zinc finger binding sequence (ZF BS) added upstream of the promoter and a zinc finger (ZF) fused to a transcriptional repressor domain (KRAB(A)) and mCerulean as a cytosolic filler (840 nm). Scale bars 12 μm (left panel) and 2 μm (center and right panels). **c** Postsynaptically targeted SynTagMA (postSynTagMA). As in **b**, with the ZF-KRAB(A) but no upstream ZF-BS. Note that postSynTagMA is still enriched in spines and the nucleus, leaving the cytoplasm almost free of SynTagMA. Scale bars: upper 20 μm, lower 2 μm. **d** The unregulated construct is expressed at high levels, leading to near-identical concentrations in dendrites and spines. For individual spines (circles), the spine-to-dendrite green fluorescence ratio was similar to the mCerulean spine-to-dendrite ratio ($n = 348$ spines, 4 neurons). **e** The construct with autoregulatory elements shuts off its own production, resulting in strong enrichment in spines ($n = 367$ spines, 3 neurons). **f** The construct without zinc finger binding sequence (postSynTagMA) is also auto-regulated, showing equally strong enrichment in spines ($n = 179$ spines, 3 neurons). All images are two-photon (2P) maximum intensity projections. In **d**, **e** and **f**, the black line is the linear fit to data points and the dotted line is the unity line.

(Supplementary Fig. 4). These control experiments, which were performed blind, yielded no significant differences between groups, indicating that expression of postSynTagMA did not alter neuronal physiology. For global labeling experiments, we generated a recombinant AAV2/9 encoding postSynTagMA, which produced dense punctate expression throughout the neuropil (Supplementary Fig. 5a–d). Viral expression of the construct without the autoregulatory elements (no ZF-KRAB(A)) flooded the neurons with fluorescent protein and was not usable for synaptic imaging (Supplementary Fig. 5e–g).

Calibration of postSynTagMA with trains of action potentials. We evoked backpropagating action potentials (bAPs) by brief somatic current injections to raise intracellular Ca^{2+} and applied 395 nm light pulses (500 ms) with a 1 s delay to characterize postSynTagMA photoconversion. In the absence of stimulation (0 bAPs), violet illumination did not change the R/G

ratio ($R_1/G_1 = R_0/G_0$). Pairing violet light with increasing bAP trains (15 repeats) lead to increased R_1/G_1 ratios (Fig. 4a). To determine the best metric for quantifying SynTagMA photoconversion, we plotted several against the initial green fluorescence, which indicates synapse size (Fig. 4b, Supplementary Fig. 6). Considering only the change in red fluorescence ($\Delta R = R_1 - R_0$), the apparent photoconversion positively correlated with synapse size and only large synapses in the 3 bAP and 50 bAP groups could be separated from the non-converted (0 bAP) synapses. The R_1/G_1 ratio, albeit showing better separation than ΔR, negatively correlated with size, and therefore would bias a classification of successful photoconversion towards small synapses. When strong photoconversion occurs, small synapses with few indicator molecules may lose all green fluorescence, which is problematic when one wishes to divide by this measure. Evidence of this is seen in the extremely high values (i.e., 20–200) for R_1/G_1 in small to medium-sized synapses (Fig. 4a). As

126
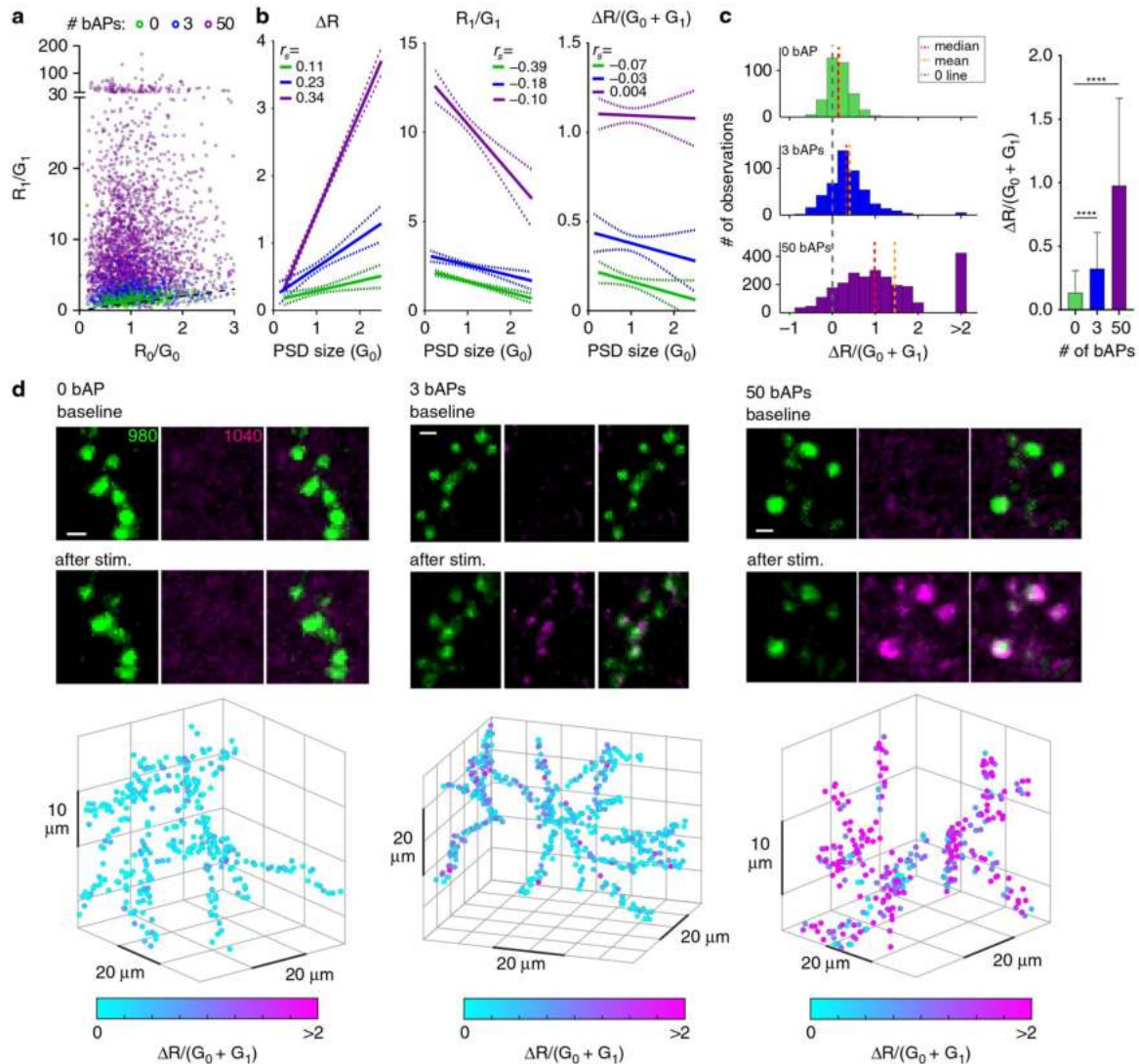
Fig. 4 PostSynTagMA photoconversion with back-propagating action potentials (bAPs). 2P image stacks of postSynTagMA expressing CA1 pyramidal neurons were taken before and after 15 pairings of trains of bAPs with photoconverting violet light (395 nm, 16 mW mm^{-2}, 500 ms duration, 1 s delay). Synaptic transmission was blocked. **a** R/G ratios of individual synapses before (R_0/G_0) vs after (R_1/G_1) photoconversion. Note the variability in photoconversion within conditions. Dotted black line is the unity line. Magenta: 50 bAPs. Blue: 3 bAPs. Green: 0 bAP. **b** Three different metrics vs. PSD size (linear regression lines with 95% confidence intervals, see Supplementary Fig. 6a-c for regressions). ΔR is positively correlated with PSD size (0 bAPs: $r_s = 0.11$, $p = 0.03$; 3 bAPs: $r_s = 0.23$, $p < 0.0001$; 50 bAPs: $r_s = 0.34$, $p < 0.0001$). Normalizing ΔR by $(G_0 + G_1)$ removes the correlation with PSD size (0 bAP: $r_s = -0.07$, $p = 0.164$; 3 bAPs: $r_s = -0.03$, $p = 0.583$; 50 bAPs: $r_s = 0.004$ $p = 0.876$). r_s is the correlation coefficient (Spearman's rho). **c** Histograms of photoconversion $\Delta R/(G_0 + G_1)$ for each condition (0 bAP: median = 0.139, mean = 0.164; 3 bAPs: median = 0.327, mean = 0.406; 50 bAPs: median = 0.984, mean = 1.452). Values above 2 are binned. Right bar graph: $\Delta R/(G_0 + G_1)$ vs the number of bAPs (data are median and interquartile range; Kruskal-Wallis test followed by Dunn's multiple comparsions: 0 bAP vs. 3 or 50 bAPs ****$p < 0.0001$, see Supplementary Fig. 6c for individual points). 0 bAP: $n = 356$ synapses, 1 neuron; 3 bAPs: $n = 472$ synapses, 1 neuron; 50 bAPs: $n = 2587$ synapses, 3 neurons. **d** Example green, red and merged images of SynTagMA-labeled synapses photoconverted with 0, 3 or 50 bAPs. 3D plots show the positions of individual synapses; markers are colored according to the calculated photoconversion value ($\Delta R/(G_0 + G_1)$). Scale bar: 1 μm.

photoconversion both increases red and decreases green fluorescence, we reasoned that using all channels before and after conversion would provide an optimal metric and avoid dividing by values close to 0. Indeed, $\Delta R/(G_0 + G_1)$ was not correlated with PSD size. Using this measure, we detected a significant

increase in photoconversion after 15×50 bAPs and even after 15×3 bAPs (Fig. 4c, d). The signal-to-noise ratio could be further improved by deconvolution of the image stacks (Supplementary Fig. 6d). To test whether violet light had adverse effects on cell health, we performed propidium iodide stainings of cultures

Fig. 5 Workflow for automated detection and analysis of SynTagMA photoconversion. a Green and red fluorescence is collected in alternate frames, switching between two Ti/Sapph lasers (980 nm/1040 nm). Images are registered in 3D to correct for chromatic aberration and laser alignment. **b** Median filtering and deconvolution is then applied to all images 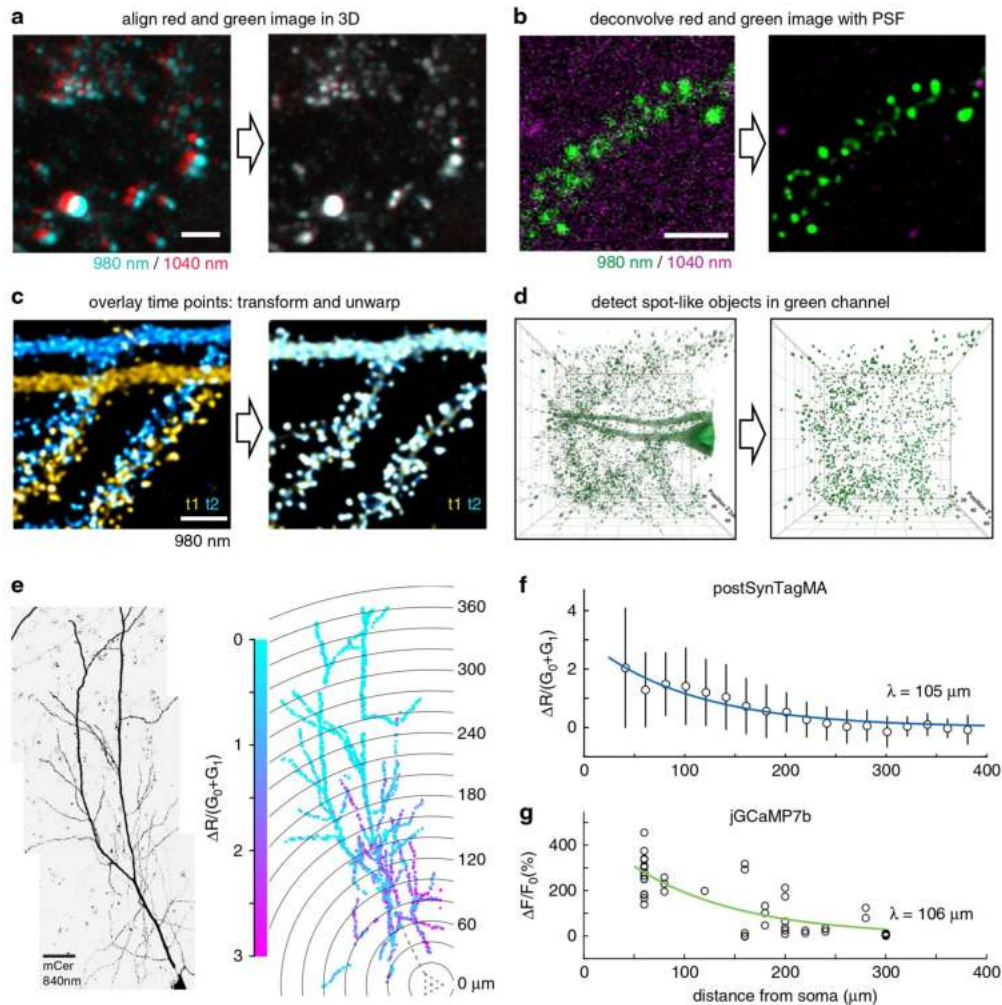(both green and red channels). **c** To superimpose multiple time points in 3D, translation, rotation and unwarping are applied. **d** Synapses (ROIs) are detected as spherical objects, i.e., 'spots' from which fluorescence values are extracted and analyzed. **e** Maximum intensity projection of a CA1 pyramidal cell expressing cytosolic mCerulean (inverted gray scale) and postSynTagMA. The cell was stimulated with 50 bAPs at 100 Hz and illuminated with 395 nm (as in Fig. 4). For each identified synapse, $\Delta R/(G_0 + G_1)$ was analyzed, color-coded, and plotted at its original location. Distance from soma is indicated as concentric rings. **f** Photoconversion decreased exponentially from the soma with a distance constant of $\lambda = 105\,\mu m$ (median ± interquartile range, $n = 1860$ synapses, 1 cell, $R^2 = 0.91$). This experiment was reproduced in 4 neurons. **g** Spine calcium transient amplitudes during 50 bAP trains (jGCaMP7b) decreased exponentially with distance from the soma with $\lambda = 106\,\mu m$ ($n = 55$ synapses, 5 neurons, $R^2 = 0.66$). Scale bar: 4 μm (**a**, **b**, **c**), 30 μm (**e**).

exposed to different doses of violet light (Supplementary Fig. 7). The violet light dose used for SynTagMA photoconversion was well below the threshold for photodamage.

Analysis workflow to quantify SynTagMA photoconversion. While the efficient targeting of SynTagMA allows simultaneous interrogation of a large population of synapses, it also presents an analysis challenge. To place regions of interest (ROIs) on individual synapses (Figs. 1 and 2), simple spot detection algorithms (e.g., Imaris, ImageJ) can be used, but matching of objects across several time points is not straightforward. When the number of synapses reaches into the thousands, a manually curated approach is no longer feasible. We developed an image analysis workflow to tackle this problem. Images acquired using two-photon excitation

at different wavelengths must first undergo correction for laser alignment and chromatic aberration (Fig. 5a). As synapses in tissue are quite motile even on short time scales[19,20], a non-rigid 3D transformation, termed 'unwarping', was applied to re-align and preserve synapse identity across time points. To achieve the highest quality transformation, images were first deconvolved and then underwent 'unwarping' (Fig. 5b–c). Synapses were then detected on transformed datasets using the Spot feature of Imaris (Oxford Instruments) (Fig. 5d). Although each of these steps can be performed using a combination of freely and commercially available software packages, it is a time-consuming process that generates several gigabytes of data in intermediate steps. We therefore developed SynapseLocator (available at GitHub), a Matlab-based program to streamline the aforementioned steps

using freely available ancillary software tools (Fiji[21], Deconvolu-tionLab2[22], FeatureJ, elastix[23]). A machine-learning approach[24] was implemented to generate synapse templates (boutons or postsynaptic sites) that were used to automatically detect and extract fluorescence values. Transformed images and fluorescence values from identified synapses (ROIs) were saved for statistical analysis and imported into ImageJ or Imaris for 3D visualization (Fig. 5d). A specific difficulty for automated analysis is the presence of spot-like autofluorescence with a broad emission spectrum, leading to detection of spurious objects outside the labeled neurons. Objects with elevated R_0 values (10–30% of all detected objects) were considered non-synaptic and therefore excluded from further analysis (Supplementary Fig. 8). Automation of the synapse identification process greatly reduced the analysis time (from days for ~500 hand-curated ROIs at several time points to minutes for ~4000 automatically detected ROIs from the same dataset, using a personal computer). Manual and automated analysis produced comparable results (Supplementary Fig. 9).

Back-propagating action potentials reach proximal synapses. For a given number of bAPs, the amount of photoconversion was quite variable between individual spines (Fig. 4a), likely reflecting spine Ca^{2+} transients of different amplitude. Whereas synapses close to the soma were strongly photoconverted, conversion decreased with distance, suggesting that bAP bursts do not increase $[Ca^{2+}]$ in distal branches of the apical dendrite (Fig. 5e, f). To test whether SynTagMA conversion is a linear reporter of local Ca^{2+} signal amplitude, we performed equivalent experiments on CA1 neurons expressing jGCaMP7b. Indeed, Ca^{2+} imaging during trains of bAPs yielded the same exponential decay of amplitude as a function of distance from the soma, validating our observation that bursts of bAPs do not invade distal dendrites (Fig. 5g). In contrast to imaging Ca^{2+} synapse-by-synapse, postSynTagMA photoconversion reliably reports the amplitude of bAP-induced Ca^{2+} elevations across the entire dendritic tree, resulting in higher coefficients of determination (R^2) in the statistical analysis ($R^2 = 0.91$ vs. 0.66).

Using postSynTagMA to map synaptic activity. Having established the linear Ca^{2+}-dependence of photoconversion in patch-clamped CA1 neurons, we wanted to assess how long converted postSynTagMA would persist in individual spines. We illuminated rectangular areas of cultured neurons while stimulating the culture at 50 Hz, limiting postSynTagMA photoconversion to the illuminated dendritic sections (Fig. 6a). We observed that $\Delta R/(G_0 + G_1)$ returned to baseline with a time constant of 29 min (Fig. 6b), in contrast to the much slower turnover of pre-SynTagMA (Supplementary Fig. 1i) and of photoconverted soluble CaMPARI[11]. This relatively fast decay of the spine signal, which is consistent with the short retention time of synaptic PSD95 in the neocortex of young mice[25], limits the post-photoconversion acquisition time to about 30 min.

We next tested whether presynaptic stimulation would raise spine Ca^{2+} sufficiently to trigger postSynTagMA photoconversion. In hippocampal slice culture, we activated Schaffer collateral axons and illuminated the dendrites of postSynTagMA-expressing CA1 pyramidal cells (100 ms violet light after 1 s delay, 50 repeats). Strong synaptic stimulation resulted in widespread photoconversion in dendritic spines (Fig. 6c). However, as postsynaptic neurons may have been driven to spike in these experiments, we could not distinguish spines that received direct synaptic input from spines that were passively flooded with Ca^{2+}. Weak stimulation resulted in a very sparse and distributed conversion pattern, suggesting active synapses (Fig. 6d). In the example, a $65 \times 65 \times 78\ \mu m^3$ volume contained

1500 postSynTagMA-labeled synapses, fourteen of which showed values above 3σ ($\Delta R/(G_0 + G_1) = 0.97$) and were therefore classified as active. Given the relatively low release probability of Schaffer collateral synapses, only a third of this 1% of activated synapses will release transmitter at any given stimulation pulse. This low number of synchronized inputs is not expected to generate APs or dendritic spikes in the postsynaptic neuron, which is consistent with the distributed pattern of photoconverted synapses.

To demonstrate that postSynTagMA indeed labels active synapses, it would be desirable to have an independent marker of synaptic activation. We turned to optogenetic stimulation to allow visualization of active presynaptic terminals. CA3 neurons expressing channelrhodopsin2 ET/TC (ChR2) and synaptophysin-mCerulean[26] were stimulated by blue light pulses (Fig. 6e). Light stimulation intensity was adjusted to be below the threshold for AP generation in a patch-clamped CA1 pyramidal cell ('reporter' neuron). Combining light stimulation of CA3 neurons with violet light illumination of postSynTagMA-expressing CA1 pyramidal cells resulted in very sparse photoconversion of Schaffer collateral synapses (Fig. 6f, g). Next to strongly photoconverted spines, cyan fluorescent boutons were observed, suggesting that these synapses were directly innervated and activated by ChR2-expressing presynaptic CA3 neurons (Fig. 6h). Non-photoconverted spines were also distant from activated terminals and thus represented 'true negatives' (Fig. 6i, Supplementary Movie 1). As red postSynTagMA has a relatively rapid turnover (Fig. 6b), it should be possible to generate multiple maps of active synapses over time. Indeed, using electrical stimulation of Schaffer collateral axons, we were able to convert (median $\Delta R/(G_0 + G_1) = 1.26$) and, 18 hours later, reconvert (median $\Delta R/(G_2 + G_3) = 1.25$) postSynTagMA expressing CA1 pyramidal cells (Fig. 6j). The remarkably similar degree of conversion on consecutive days suggests the possibility of repeated activity mapping with postSynTagMA.

PostSynTagMA maps active neurons and synapses in vivo. The nuclear sequestration of postSynTagMA prompted us to test whether it could be used to identify active neurons in vivo. After injection with AAV2/9-hSyn-postSynTagMA, and a chronic hippocampal imaging window was implanted, head-fixed mice were trained to run on a linear treadmill. While running, the hippocampus was illuminated with 405 nm light through the window; resulting in a small percentage of photoconverted CA1 neuronal nuclei (Fig. 7a). In the same mouse, there was no photoconversion during ketamine-xylazine anesthesia (Fig. 7b), consistent with the strongly reduced activity observed using GCaMP6f (Supplementary Movie 2). Next, we trained mice to stop and receive a water reward at a particular location (Fig. 7c, d). After reaching criterion, we imaged green fluorescence continuously during four laps (Fig. 7e, f), followed by 15 laps with reward-triggered 405 nm light illumination (sans imaging). The neurons that were photoconverted also showed dimming (i.e., increased $[Ca^{2+}]$) just prior to each reward (Fig. 7f, magenta) whereas a matched number of randomly selected non-converted neurons did not (Fig. 7f, green). Therefore, in awake behaving animals, postSynTagMA photoconversion selectively labels behaviorally relevant neurons with high calcium transients (Supplementary Movie 3). In contrast to analysis of cytoplasmic, nuclear-excluded calcium indicators (e.g., GCaMP), which require analysis packages such as Suite2P[27], we found automatic segmentation and analysis of the nuclear SynTagMA trivial.

The density of neuropil labeling in these mice (Supplementary Fig. 5a) prompted us to switch to expressing postSynTagMA in interneurons (Supplementary Fig. 10) in order to test whether postSynTagMA could be used to identify individual active

129
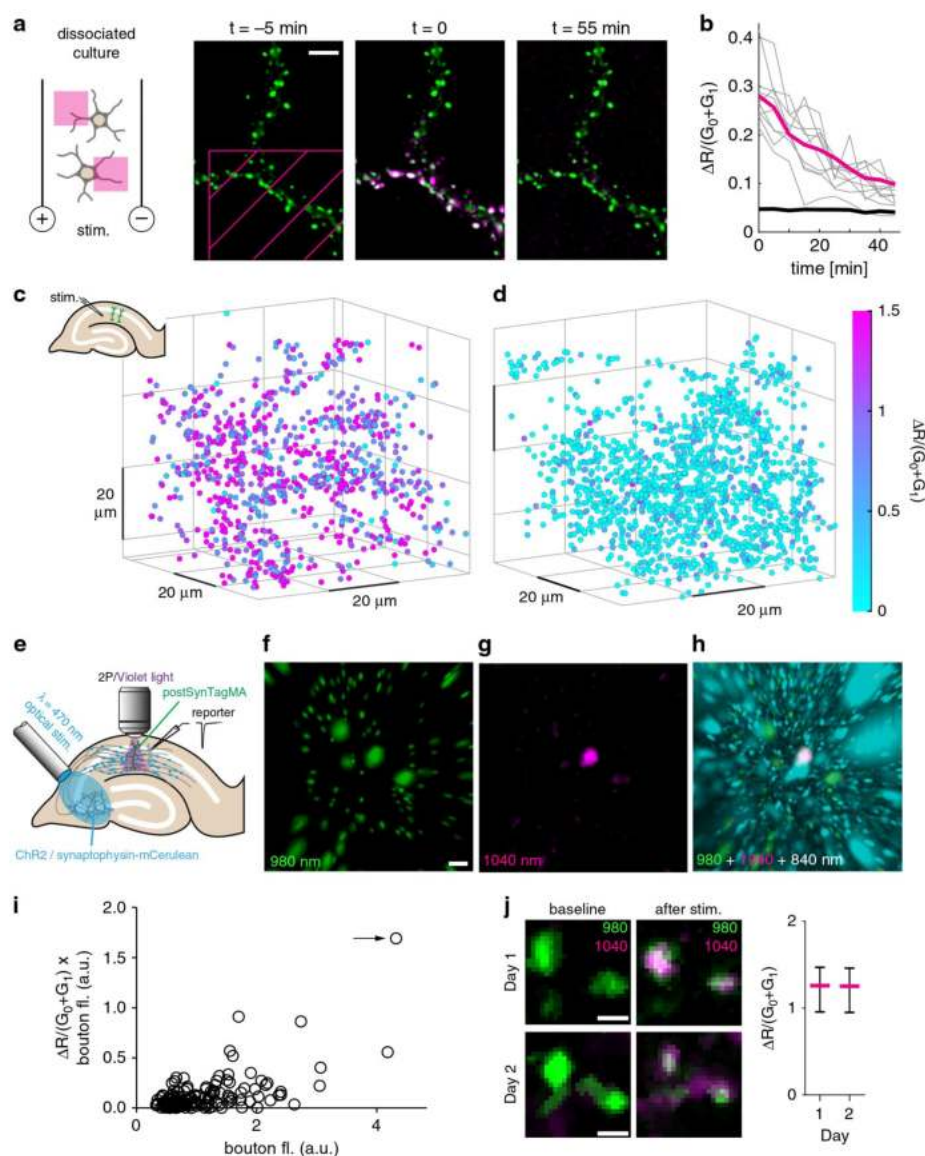
Fig. 6 Using postSynTagMA to map active synapses. a Time series from a postSynTagMA-expressing neuron in culture. At $t = 0$, one violet light pulse was applied via DMD inside the magenta hatched area (405 nm, 18.6 mW mm^{-2}, 0.5 s) while stimulating with a single train of action potentials delivered at 50 Hz for one second. **b** Inside the illuminated area, red fluorescence generated by photoconversion of postSynTagMA decayed exponentially with $\tau = 29.4$ min ($R^2 = 0.99$, $n = 138$ synapses, 2 experiments). Gray lines show individual synapses. For objects outside the illuminated square, $\Delta R/(G_0 + G_1)$ was constant (black line, $n = 712$ synapses, 2 experiments). **c** Photoconversion after Schaffer collateral stimulation in organotypic slice culture. Color-coded $\Delta R/(G_0 + G_1)$ of synapses plotted at their locations in the $65 \times 65 \times 78$ μm volume of tissue. Strong stimulation of synaptic inputs was paired with violet light (100 ms, 395 nm, 16 mW mm^{-2}, 50 repeats). Note that $\Delta R/(G_0 + G_1)$ is equal or greater than 1.5 for most of the synapses ($n = 897$ synapses). **d** As in **c**, but with weak stimulation, below the threshold for postsynaptic APs ($n = 1502$ synapses). **e** CA3 neurons expressing ChR2-ET/TC and synaptophysin-mCerulean were stimulated with 470 nm flashes to evoke subthreshold (~500 pA) excitatory synaptic responses in a patch-clamped CA1 neuron (reporter). Simultaneously, an adjacent postSyntagMA-expressing CA1 neuron was illuminated with violet light (same illumination as **c–d**). **f** Green spots ($G_0 + G_1$) segmented with Imaris™. **g** Red fluorescence after photoconversion (R1), masked by the green channel. Note the strongly photoconverted synapse (spot #1). **h** Spot #1 (magenta) is in close contact with a presynaptic ChR2-expressing terminal (cyan). Non-converted (green) spots are not in direct contact with cyan terminals. **i** Quantification of panels **f–h** ($n = 167$ spots). Arrow indicates spot #1. **j** Red/green overlay before and after photoconversion of the same synapses on successive days. Strong extracellular stimulation was paired with 395 nm light (500 ms, 1 s delay, 15×). Photoconversion of postSynTagMA was near-identical on day 1 and day 2 ($p = 0.386$, paired two-tailed t-test, $n = 37$ synapses, data presented as median ± interquartile range). All experiments were reproduced in at least twice independent experiments. Scale bars: 5 μm (**a**), 3 μm (**f–h**), 1 μm (**j**).

130

synapses/dendrites in sparsely labeled neurons in vivo. We photoconverted sparsely labeled interneurons in *stratum oriens* under isoflurane anesthesia, which retains neuronal activity close to awake levels but reduces motion artifacts (Fig. 7g, h, Supplementary Movie 2). Photoconversion of clusters of synapses was observed; consistent with local dendritic calcium events that have been described in interneurons in vivo[28]. Thus, under conditions of sparse SynTagMA expression, it is possible to resolve individual photoconverted synapses in vivo. During photoconversion, movement of the brain is not problematic as imaging is not concurrent and SynTagMA can be used to tag active neurons and synapses during behavior. To resolve SynTagMA at the level of individual synapses, minimizing tissue movement with anesthesia may improve data quality.

Discussion

To create a synaptically localized, photoconvertible calcium sensor, we fused CaMPARI2 to the vesicle protein synaptophysin (preSynTagMA) for presynaptic targeting or to an intrabody against the postsynaptic scaffold of excitatory synapses (postSynTagMA). Both targeting strategies have previously been used to label synapses with fluorescent proteins[15,29], and we verified that SynTagMA-expressing neurons are physiologically normal. When SynTagMA is combined with a second fluorescent protein, here mCerulean, postSynTagMA puncta can be assigned to particular dendrites or neurons. PreSynTagMA should prove useful for identifying active axons in tissue and may also prove useful for distinguishing high from low release probability boutons based on the graded photoconversion. PostSynTagMA should likewise facilitate identification and mapping of active synapses, but on the postsynaptic side.

Identifying active synapses is a long-standing quest in neuroscience and many approaches have been put forward. In two-dimensional neuronal cultures, it is relatively straightforward to monitor the activity of a large number of synapses with a high speed camera, e.g. by employing genetically encoded sensors of vesicular pH[30,31]. In intact brain tissue, however, monitoring more than one synapse with high temporal resolution becomes very challenging[6,32]. To create a more permanent tag of active synapses, Ca^{2+} precipitation in active spines was used to create an electron-dense label that can be detected by electron microscopy[33]. As this method requires tissue fixation, it does not allow monitoring changes in synaptic activity over time. Expressing the two halves of split-GFP on the extracellular surface of pre- and postsynaptic neurons (mGRASP) labels contact points between the neurons as green fluorescent puncta[34]. Refined transsynaptic labeling methods with multiple colors have led to remarkable insights about network connectivity[35,36]. Whereas mGRASP and eGRASP just report anatomical proximity, SynTagMA photoconversion is Ca^{2+}-dependent and therefore sensitive to synaptic activity.

One of the many interesting applications of postSynTagMA will be to create extensively detailed input maps of individual neurons at single synapse resolution. The question of whether inputs carrying similar information segregate to branches of the dendritic tree is currently being investigated using spine-by-spine Ca^{2+} imaging[6,37,38]. By freezing the activity status of all spines during a particular labeling protocol, SynTagMA may simplify such experiments by reading out fluorescence ratios in thousands of spines in a single high-resolution stack. Importantly, postSynTagMA maps can be repeated, opening the possibility to study the functional dynamics of excitatory connections rather than just morphology and turnover of dendritic spines. In addition to synapses on mushroom-shaped spines, postSynTagMA provides access to synapses on structures that are difficult to probe with

Ca^{2+} dyes or diffusible GECIs, such as stubby spines or shaft synapses[39]. Thus, postSynTagMA may open the possibility to study the long-term dynamics of interneuron excitation, a key homeostatic mechanism that involves Ca^{2+}-induced-Ca^{2+} release from intracellular stores[40]. In addition to Ca^{2+} influx though voltage- or ligand-gated channels, Ca^{2+} release is thought to be important in both presynaptic[41] and postsynaptic compartments[42–44], and SynTagMA may help investigating the sources of Ca^{2+} in individual synapses.

To test the linearity of calcium-dependent photoconversion, we used bursts of action potentials (APs) which are known to be strongly attenuated on their way into the dendrite[45,46]. Indeed, postSynTagMA photoconversion was greatest in spines relatively close to the soma while distal synapses were not converted at all. The distance constant estimated from a Sholl analysis of postSynTagMA conversion ($\lambda = 105\ \mu m$, Fig. 5f) was the same as that determined by calcium imaging of individual spines ($\lambda = 106\ \mu m$, Fig. 5g). Previous studies[45,46] have measured back-propagation along the apical dendrite, but not along thin oblique dendrites or into individual spines. Studies with single-spine resolution[47,48] have not included large-scale spatial information, as only few synapses per cell can be investigated. In future SynTagMA studies, reconstructions of the neuronal morphology in 3D would allow accurate measurements of the dendritic path length to every synapse and combine that data with functional information. We observed that even close to the soma, conversion of spines was not very uniform and the same was true for boutons. Understanding the sources of this heterogeneity, and whether these correspond to particular classes of synapses, may lead to important insights into synapse-specific calcium regulation.

An unexpected application arose from the nuclear localization of postSynTagMA. As we show, nuclear SynTagMA conversion can be used to visualize the location of the most active neurons in behaving animals. As the cytoplasm is almost free of label, automatic segmentation is very easy. Nuclear calcium elevations may be of particular relevance during learning, as they are driven by burst firing and trigger transcription of plasticity-related genes[49]. There are several existing strategies for labeling active neurons[50], but their time resolution is in the hours timescale in contrast to the 2 s photoconversion time window of SynTagMA. SynTagMA might serve as an intermediate between acute calcium imaging and labeling methods based on immediate early gene expression.

There are some caveats to working with SynTagMA. Before or during imaging, it is important to photoswitch the protein to the bright state using low intensity violet light[10,11]. The quite rapid turnover of postSynTagMA means that after photoconversion, images should be collected within about 30 min. SynTagMA analysis is complicated by endogenous red fluorescence which can be mistaken for photoconverted SynTagMA. We found that depending on the age of the tissue, 0.4-4% of the total imaged volume was red fluorescent at baseline. Green objects detected inside these autofluorescent areas were typically non-synaptic (Supplementary Fig. 8). For automatic exclusion, SynapseLocator sets a dynamic threshold based on the histogram of the red channel at baseline (R_0, before photoconversion) and rejects objects with elevated R_0. This process effectively prevents false-positive errors, but requires acquisition of at least two time points (before and after photoconversion). If for experimental reasons only a single time point can be acquired, we strongly recommend excluding objects that have high red fluorescence in the voxels surrounding green puncta. When acquiring two-photon image stacks, we collected each optical section twice, exciting either the green or the red form of SynTagMA by rapidly switching the power of two different Ti:Sapph lasers. Near-simultaneous acquisition of red and green fluorescence prevented movement
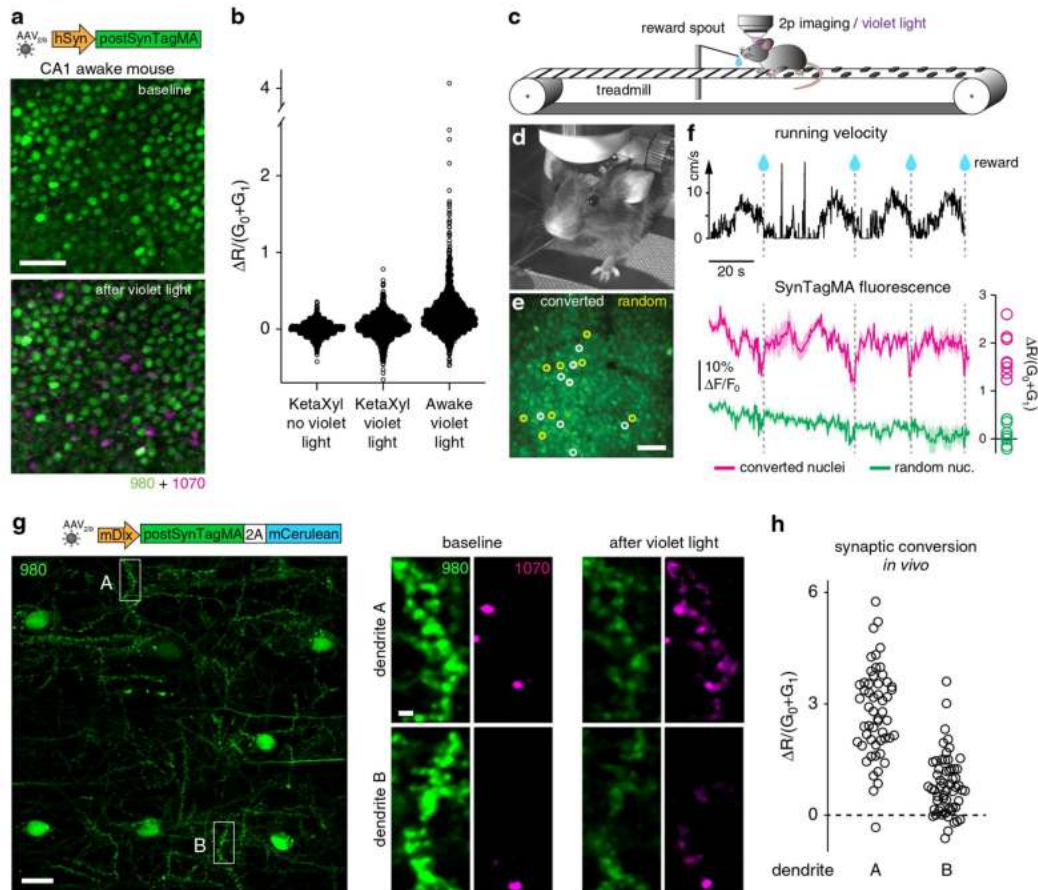
131

Fig. 7 SynTagMA identifies active neurons during behavior. a Nuclei of CA1 neurons expressing AAV2/9-hSyn-postSynTagMA imaged in vivo through a chronic cranial window using 980 nm and 1070 nm to excite green and red SynTagMA fluorescence, respectively. Ten 2 s, 405 nm, 12.1 mW mm^{-2} light pulses were applied in an awake mouse after which a small percentage of nuclei became photoconverted (magenta). **b** Photoconversion relative to baseline under ketamine-xylazine anesthesia ($n = 1105$ nuclei), after violet light ($n = 1105$ nuclei) and under awake conditions ($n = 1576$ nuclei). **c** Closed loop paradigm: a head-fixed mouse was trained to stop at a certain position on the running belt to receive a water reward (teardrop). Nuclear fluorescence in CA1 was continuously monitored during 4 laps, followed by 15 laps where 405 nm, 12.1 mW mm^{-2}, 2 s light pulses were triggered during water reward. **d** Mouse engaged in the task. Note spout for water delivery. **e** 2P image of CA1 cell body layer during running. Eight nuclei that later became photoconverted are marked by white circles. Yellow circles are eight randomly selected non-converted nuclei used for comparison of calcium signals. **f** Black trace is running speed during the first 4 laps with times of reward delivery (teardrop/dashed line). Magenta and green traces are the average green SynTagMA fluorescence of the 8 photoconverted nuclei and the 8 non-converted nuclei indicated in **e**, respectively. At right is the photoconversion of the individual nuclei. Note the consistent dips in the magenta trace (i.e., high calcium) just before the water reward/photoconversion light would be triggered. **g** Interneurons expressing AAV2/9-mDlx-postSynTagMA-2A-mCerulean imaged through a chronic cranial window under isoflurane anesthesia (mCerulean fluorescence not shown). At high magnification, green fluorescence reveals PSD spots on the dendrite. Red spots at baseline are autofluorescent material, unrelated to SynTagMA. Violet light (20 flashes, 0.2 Hz, 3 s duration, 0.42 mW mm^{-2}) was applied to photoconvert postSynTagMA. **h** Photoconversion of synapses on dendrite A ($n = 54$ synapses) and B ($n = 58$ synapses) indicate higher activity levels in dendrite A. Scale bars: 50 μm (**a**, **e**); 20 μm and 2 μm (**g**). All experiments were performed in at least two mice and found to be reproducible.

artefacts and made it straightforward to correct for chromatic aberration. When the two color channels are collected in successive stacks, Ca^{2+}-dependent dimming driven by spontaneous activity may affect one and not the other channel. Particularly when imaging in vivo, the time required to re-tune a single laser to the different excitation wavelengths might render analysis of individual synapses impossible.

For in vivo experiments, depth-dependent attenuation of the violet photoconversion light by scattering and absorption has to be considered. We found that photoconversion efficiency was a linear function of violet light intensity (Supplementary Fig. 11). Using published modeling software[51], we compared cranial window

illumination (405 nm) to illumination via implanted optical fiber. While the relatively homogenous illumination through a cranial window leads to uniform light intensity (and thus, photoconversion) within a field of view (Fig. 7a, Supplementary Fig. 11), photoconversion via fiber would be expected to be rather inhomogeneous in all spatial directions and results therefore difficult to interpret. Similar to CaMPARI experiments, it is safest to compare cells or synapses imaged at similar depths[52].

If the postsynaptic neuron fires APs during strong (suprathreshold) synaptic activation, the resulting global calcium elevation could interfere with SynTagMA-based input mapping at proximal synapses. As we show (Fig. 5e), this is much less of a

problem in the distal dendritic tree. For input-mapping experiments, it is advisable to repeat weak, subthreshold stimuli many times, each time paired with a (delayed) pulse of violet light. To avoid phototoxicity, it is important to keep track of the total light dose applied during each protocol, using shorter pulses (or lower light intensities) for protocols with many repetitions.

Finally, SynTagMA is amenable for viral delivery using recombinant AAVs. Using different promoters, we demonstrate pan-neuronal expression for network analysis (Fig. 7a–f, Supplementary Fig. 3, Supplementary Fig. 5) and sparse viral expression of Syn-TagMA in hippocampal interneurons (Fig. 7g, Supplementary Fig. 10). To achieve sparse expression of SynTagMA in pyramidal cells, dual-AAV labeling systems could be employed[53].

Methods

Dissociated rat hippocampal cell cultures. Neurons from P1 Sprague-Dawley rats of either sex were isolated from hippocampal CA1-CA3 regions with dentate gyrus removed, dissociated (bovine pancreas trypsin; 5 min at room temperature), and plated on polyornithine-coated coverslips inside a 6 mm diameter cloning cylinder. Calcium phosphate-mediated gene transfer was used to transfect 5-7 day old cultures. All measurements unless otherwise noted, are from mature 13–21 day old neurons. Procedures with Sprague-Dawley rats were approved by Dartmouth College's Institutional Animal Care and Use Committee (IACUC). Cells were maintained in culture media consisting of Earle's MEM (Thermofisher 51200038), 0.6% glucose, 0.1 g l^{-1} bovine transferrin, 0.25 g l^{-1} insulin, 0.3 g l^{-1} glutamine, 5% fetal calf serum (Atlanta Biologicals), 2% B-27 (Life Technologies), and 4 μM cytosine β-D-arabinofuranoside added 48 h after plating in 6 mm diameter cloning cylinders (Ace Glass).

Rat hippocampal slice cultures. Hippocampal slice cultures from Wistar rats of either sex were prepared at postnatal day 4–7[54]. Briefly, rats were anesthetized with 80% CO$_2$ 20% O$_2$ and decapitated. Hippocampi were dissected in cold slice culture dissection medium containing (in mM): 248 sucrose, 26 NaHCO$_3$, 10 glucose, 4 KCl, 5 MgCl$_2$, 1 CaCl$_2$, 2 kynurenic acid, 0.001% phenol red (310–320 mOsm kg^{-1}, saturated with 95% O$_2$, 5% CO$_2$, pH 7.4). Tissue was cut into 400 μM thick sections on a tissue chopper and cultured at the medium/air interface on membranes (Millipore PICMORG50) at 37 °C in 5% CO$_2$. No antibiotics were added to the slice culture medium which was partially exchanged (60–70%) twice per week and contained (for 500 ml): 394 ml Minimal Essential Medium (Sigma M7278), 100 ml heat inactivated donor horse serum (H1138 Sigma), 1 mM L-glutamine (Gibco 25030-024), 0.01 mg ml^{-1} insulin (Sigma I6634), 1.45 ml 5 M NaCl (S5150 Sigma)), 2 mM MgSO$_4$ (Fluka 63126), 1.44 mM CaCl$_2$ (Fluka 21114), 0.00125% ascorbic acid (Fluka 11140), 13 mM D-glucose (Fluka 49152). Wistar rats were housed and bred at the University Medical Center Hamburg-Eppendorf. All procedures were performed in compliance with German law and according to the guidelines of Directive 2010/63/EU. Protocols were approved by the Behörde für Gesundheit und Verbraucherschutz of the City of Hamburg.

Mouse acute hippocampal slices. Male, adult (4-6 months old) C57BL/6J mice were housed and bred in pathogen-free conditions at the University Medical Center Hamburg-Eppendorf. The light/dark cycle was 12/12 h and the humidity and temperature were kept constant (40% relative humidity; 22 °C). All procedures were performed in compliance with German law and according to the guidelines of Directive 2010/63/EU. Protocols were approved by the Behörde für Gesundheit und Verbraucherschutz of the City of Hamburg. A bilateral intrahippocampal injection with AAV2/9 encoding syn-postSyntagMA (3.4 × 10^{13} vg ml^{-1}) was administered 7–15 days before acute slice preparation. Mice were anesthetized by CO$_2$ inhalation, decapitated and brains rapidly removed. Coronal slices (300 um) were cut on a vibratome (Leica VT1000S) in ice cold solution containing (in mM): 110 choline chloride, 25 NaHCO$_3$, 25 D-Glucose, 11.6 sodium-L-ascorbate, 7 MgSO$_4$, 1.25 NaH$_2$PO$_4$, 2.5 KCl, and 0.5 CaCl$_2$. Slices were then incubated at 34 °C for 30–45 min in oxygenated slice culture artificial cerebrospinal fluid (ACSF), containing (in mM): 125 NaCl, 26.2 NaHCO$_3$, 11 D-Glucose, 1 NaH$_2$PO$_4$, 2.5 KCl, 1.3 MgCl$_2$, and 2.5 CaCl$_2$. Slices were kept in the same solution at room temperature until use.

Anesthetized and awake mice. Male, adult (4–6 months old) C57BL/6J mice were housed and bred in pathogen-free conditions at the University Medical Center Hamburg-Eppendorf. The light/dark cycle was 12/12 h and the humidity and temperature were kept constant (40% relative humidity; 22 °C). An AAV2/9 encoding mDlx-postSynTagMA (2.0 × 10^{12} vg ml^{-1}), syn-postSynTagMA (3.4 × 10^{13} vg ml^{-1}) or syn-GCaMP6f (1.45 × 10^{13} vg ml^{-1}) was injected unilaterally in the hippocampus. All procedures performed in mice were in compliance with German law and according to the guidelines of Directive 2010/63/EU. Protocols were approved by the Behörde für Gesundheit und Verbraucherschutz of the City of Hamburg.

Plasmid construction. To create preSynTagMA, synaptophysin-GCaMP3 was, as previously described[55], digested by HindIII and BamHI to remove GCaMP3, and CaMPARI was fused to synaptophysin using the In-Fusion® HD Cloning method and kit (Takara Bio USA) after amplifying variants of CaMPARI with PCR using custom primers with base pair overhangs homologous to the synaptophysin plasmid (3' Primer [CGATAAGCTTTTATGAGCTCAGCCGACC], 5' Primer [CAGATGAAGCTTATGCTGCAGAACGAGCTTG]).

Developing postSynTagMA involved the creation of several intermediate constructs. After removal of restriction site XbaI from pCAG_PSD95.FingR-eGFP-CCR5TC, PSD95.FingR-eGFP-CCR5TC was inserted into a pAAV-hsyn1 backbone without the CAG promoter or upstream zinc finger binding site, to produce pAAV-syn-PSD95.FingR-eGFP-CCR5TC (available upon request). The eGFP was then replaced with CaMPARI1[10], from which we had deleted the nuclear export signal (NES), to produce pAAV-syn-PSD95.FingR-dNES-CaMPARI1-CCR5TC, a fusion construct of the fibronectin intrabody and a CaMPARI variant that is not restricted to the cytosol and can enter the nucleus. To finally generate pAAV-syn-postSynTagMA, CaMPARI1 was then replaced by CaMPARI2 (without NES and epitope tags) and the point mutations F391W and L398V were using QuickChange PCR to increase calcium affinity[11]. The left-handed zinc finger (aka CCR5TC) fused to the KRAB(A) transcriptional repressor[18] was removed to produce pAAV-syn-PSD95.FingR-dNES-CaMPARI2_F391W_L398V, the unregulated variant. A sequence including the zinc finger binding sequence[15,56] (5'-GTCATCCTCATC-3') upstream of the hsyn1 promoter was synthesized (ThermoFisher) and inserted using the MluI and EcoRI restriction sites to generate pAAV-ZFBS-syn-PSD95.FingR-dNES-CaMPARI2_F391W_L398V-CCR5TC. PostSynTagMA (ID: 119736) and preSynTagMA (ID: 119738) are available on www.addgene.org. Other plasmids such as the lower affinity pAAV-syn-PSD95. FingR-dNES-CaMPARI2-CCR5TC, pAAV-syn-synaptophysin-CaMPARI2 and the variants with zinc finger binding sequence are available upon request.

mDlx-postSynTagMA-2A-mCerulean was created by first removing the stop codon from postSynTagMA and inserting a 3'-BsiWI restriction site via PCR. 2A-mCerulean was then inserted 3'of postSynTagMA via Acc65 (5') and HindIII (3') to create postSynTagMA-2A-mCerulean. This construct was subsequently cloned via NheI (5') and BsrGI (3') into the mDlx-GFP-Fishell1 backbone by replacing the GFP with postSynTagMA-2A-mCerulean to generate mDlx-postSynTagMA-2A-mCerulean.

Cell culture imaging. SypCaMPARI experiments (Fig. 1) were performed at 34 °C using a custom-built objective heater. Coverslips were mounted in a rapid-switching, laminar-flow perfusion and stimulation chamber on the stage of a custom-built mixer microscope. The volume of the chamber was maintained at ~75 μl and was perfused at a rate of 400 μl min^{-1}. Neurons were perfused continuously during imaging with a standard saline solution containing the following in mM: 119 NaCl, 2.5 KCl, 2 CaCl$_2$, 2 MgCl$_2$, 25 HEPES, 30 D-Glucose, 10 μM CNQX, and 50 μM D-APV. When noted, 3 μM Tetrodotoxin (TTX) and 20 μM Bicuculline were added to the saline solution.

Neurons were imaged through a EC Plan-Neofluar 40×1.3 NA objective (Zeiss) or an UAPON40XO340-2 40×1.35 NA objective (Olympus), using an IXON Ultra 897 EMCCD camera (Andor) at a frame rate of 25 Hz (exposure time: 39.72 ms). Green fluorescence was excited at 488 nm (Coherent OBIS laser, ~ 3 mW) through a ZET488/10x filter and ZT488rdc dichroic (Chroma). Red fluorescence was excited at 561 nm (Coherent OBIS) through a ZET561/10x filter and ZT561rdc dichroic (Chroma). Green and red fluorescence was collected via ET 525/50 m and ET600/50 m emission filters (Chroma), respectively.

Cell culture stimulation and photoconversion. Field stimulation-evoked action potentials were generated by passing 1 ms current pulses, yielding fields of ~12 V cm^{-2} through the recording chamber bracketed by platinum/iridium electrodes. Electrical stimuli were locked to start according to defined frame number intervals using a custom-built board named "Neurosync" powered by an Arduino Duo chip (Arduino) manufactured by an engineering firm (Sensostar)[57]. A collimated 405 nm LED light source (Thorlabs) was set on top of the microscope stage with a custom-built plastic case (Bob Robertson, Dartmouth College). This light source was coupled to a T-Cube LED Driver (Thorlabs) and a Pulse Pal (Open Ephys) was used to trigger light flashes of specific duration and delay. The light source trigger was set relative to a TTL input from Neurosync. Power density of the 405 nm light was measured using a digital handheld optical power and energy meter with an attached photodiode power sensor (Thorlabs). The power densities used were either 10.8 mW cm^{-2} or 54.1 mW cm^{-2}.

For incubator photoconversion experiments (Supplementary Fig. 1), custom-built circular 51-diode 405 nm LED arrays (Ultrafire) were wired up to a custom dual programmable relay board to flash light for 100 ms every 10 s, inside a cell culture incubator (New Brunswick; Eppendorf) set to ~37° C and ~5% CO$_2$. Neurons were then mounted on the microscope with perfusion, and green fluorescence was imaged during 50 stimulations @ 50 Hz (as above) to measure calcium-dependent dimming. Only neurons responsive to stimulation were then analyzed (over 90% of cells measured).

Experimental setup for variably timed photoconversion. Variably timed photoconversion experiments (Fig. 2) were performed on a Nikon Ti-E microscope

133

fitted with an Andor W1 Dual Camera (Andor CMOS ZYLA), dual spinning disk, Coherent Lasers (OBIS 405, 488 and 561 nm) and the Andor Mosaic 3 micro-mirror system, controlled by Andor iQ software, and Nikon elements for image acquisition. PulsePal software was used to time lock the stimulus with the mosaic sequence start. A custom 5×5, 250 μm^2 square grid was drawn to illuminate different areas (squares) at different times relative to the electrical stimulation. Photoconversion was induced using a train of 5 action potentials (50 Hz) paired with a 100 ms violet light pulse (405 nm, 50 mW cm^{-2}) at different delays. The protocol was repeated 5 times at 30 s intervals.

Cell culture image analysis. EMCCD camera images or confocal image stacks were imported into Fiji. A maximum intensity projection was made from the confocal stacks. Ten-pixel diameter circular ROIs were placed over boutons identified by eye using an ImageJ plugin (https://imagej.nih.gov/ij/plugins/time-series.html) to localize them over the brightest pixel in the green channel. Boutons were identified as punctate spots that showed a dimming response to AP stimulation (>98% of punctate spots). ROIs were centered on the brightest green pixel in the green channel and average intensity was measured for red and green channels. Average background fluorescence was determined from several larger ROIs placed across the imaging field where there were no transfected axons. The average green and red background fluorescence was subtracted from the respective values before calculating R/G ratios or ΔF/F.

Electrophysiology in slice cultures. Hippocampal slice cultures were placed in the recording chamber of the two-photon laser scanning microscope and continuously perfused with an artificial cerebrospinal fluid (ACSF) saturated with 95% O_2 and 5% CO_2 consisting of (in mM): 119 NaCl, 26.2 NaHCO$_3$, 11 D-glucose, 1 NaH$_2$PO$_4$, 2.5 KCl, 4 CaCl$_2$, 4 MgCl$_2$. (pH 7.4, 308 mOsm) at room temperature (21-23 °C) or with a HEPES-buffered solution (in mM): 135 NaCl, 2.5 KCl, 10 Na-HEPES, 12.5 D-glucose, 1.25 NaH$_2$PO$_4$, 2 CaCl$_2$, 4 MgCl$_2$ (pH 7.4). Whole-cell recordings from CA1 pyramidal neurons were made with patch pipettes (3–4 MΩ) filled with (in mM): 135 K-gluconate, 4 MgCl$_2$, 4 Na$_2$-ATP, 0.4 Na-GTP, 10 Na$_2$-phosphocreatine, 3 sodium-L-ascorbate, and 10 HEPES (pH 7.2, 295 mOsm kg^{-1}). In Supplementary Fig. 4f, patch pipettes contained (in mM): 135 Cs-MeSO$_4$, 4 MgCl$_2$, 4 Na$_2$-ATP, 0.4 Na-GTP, 10 Na$_2$-phosphocreatine, 3 sodium-L-ascorbate, 10 HEPES (pH 7.2, 295 mOsm kg^{-1}). Series resistance was below 20 MΩ. A Multiclamp 700B amplifier (Molecular Devices) was used under the control of Ephus[58] or Wavesurfer software written in Matlab (The MathWorks). When using somatic current injection to evoke action potentials in CaMPARI2_F391W_L398V or SynTagMA expressing neurons, the antagonists CPPene (10 μM) and NBQX (10 μM) were added to the extracellular recording solution to block synaptic transmission.

Single cell electroporation. At DIV 13-17, CA1 neurons in rat organotypic hip-pocampal slice culture were transfected by single-cell electroporation[59]. Thin-walled pipettes (~10 MΩ) were filled with intracellular K-gluconate based solution into which SynTagMA variants or CaMPARI2_ F391W_L398V, or jGCaMP7b plasmid DNA was diluted to 20 ng μl^{-1}. In some experiments, a plasmid encoding mCer-ulean was also included in the pipette at 20 ng μl^{-1}. All experiments were conducted 3-6 days after electroporation. For blind analysis of neurons with and without SynTagMA, the electroporation mixes were coded by a second lab member and only after all recordings and analysis were completed was the investigator unblinded. Pipettes were positioned against neurons and DNA was ejected using an Axoporator 800 A (Molecular Devices) with 50 hyperpolarizing pulses (−12 V, 0.5 ms) at 50 Hz.

Two-photon microscopy in hippocampal slices. Two-photon imaging was performed in rat organotypic hippocampal slice cultures and mouse acute hippocampal slices. The custom-built two-photon imaging setup was based on an Olympus BX51WI microscope equipped with LUMPlan W-IR2 60× 0.9 NA (Olympus), W Plan-Apochromat 40× 1.0 NA (Zeiss) or IRAPO 25×1.0 NA (Leica) objectives controlled by the open-source software package ScanImage[60]. Two pulsed Ti:Sapphire lasers (MaiTai DeepSee, Spectra Physics) controlled by electro-optic modulators (350-80, Conoptics) were used to excite SynTagMA green (980 nm) and red species (1040 nm), respectively. When Z-stacks of SynTagMA-expressing neurons were acquired, each plane was scanned twice, using 980 nm and 1040 nm excitation, respectively. For quantification of pre- or postsynaptic targeting, axons of CA3 cells or oblique dendrites of CA1 neurons expressing mCerulean and SynTagMA were imaged at 840 nm and 980 nm. For three-color experiments, separate stacks were taken to image mCerulean (840 nm) and Syn-TagMA (980 nm & 1040 nm). Emitted photons were collected through the objective and oil-immersion condenser (1.4 NA, Olympus) with two pairs of photomultiplier tubes (H7422P-40, Hamamatsu). 560 DXCR dichroic mirrors and 525/50 and 607/70 emission filters (Chroma) were used to separate green and red fluorescence. Excitation light was blocked by short-pass filters (ET700SP-2P, Chroma). Two brief violet light pulses (395 nm, 100 ms, 16 mW mm^{-2}, 0.1 Hz) were delivered through the objective using a Spectra X Light Engine (Lumencor) just before imaging to photoswitch the CaMPARI moiety into its bright state[10].

Viral transduction of hippocampal slices. Organotypic hippocampal slices were microinjected at DIV 7-11 with a viral vector containing preSynTagMA under the

control of the synapsin promoter (AAV2/9-syn-preSynTagMA), or AAV2/9 synapsin-ChR2(ET/TC)−2A-synaptophysin-mCerulean. Both viruses were prepared at the UKE vector facility. Briefly, working in a laminar air flow hood, a glass pipette was backfilled with 1 μl of the viral vector and the tip inserted in hippocampal CA3 area. A picospritzer (Science Products) coupled to the pipette was used to deliver 3–4 short (50 ms) low pressure puffs of viral vector into the tissue. Injected slices were taken back to the incubator and imaged in the multi-photon microscope 3–4 weeks later.

Photoconversion in hippocampal slices. Photoconversion was achieved by delivery of violet light (395 nm, 16 mW mm^{-2}, duration 100 ms–2 s as indicated in figure legends) using a Spectra X Light Engine (Lumencor) coupled with a liquid light guide to the epifluorescence port of the two-photon microscope. During the violet light pulses, shutters (Uniblitz) protected the photomultiplier tubes. We typically used 100–500 ms violet light pulses repeated 15–50 times with a 1 s delay from stimulus onset to photoconvert SynTagMA (see figure legends for protocol details). Image stacks were acquired prior to and following photoconversion.

Recording and analysis of EPSCs and cellular parameters. CA1 pyramidal neurons expressing mCerulean or mCerulean plus SynTagMA were patched using only the mCerulean fluorescence to identify them. TTX 1 μM, CPPene 1–10 μM, and picrotoxin 50 μM were added to oxygenated ACSF (see above). For miniature EPSC (mEPSC) measurements, recording electrodes (3–4 MΩ) contained Cs-gluconate intracellular solution (see above). After the slice rested at least 15 min in the bath, cells were patched and held at −70 mV in the whole-cell voltage clamp configuration (no liquid junction potential correction). EPSCs were recorded 5–15 min after break-in. The Event Detection feature of Clampfit 10 (Molecular Devices) was used to detect and measure mEPSC amplitudes and inter-event intervals. For cell parameter measurements, recording electrodes contained K-gluconate solution (see above). Membrane resistance (R_m) and capacitance (C_m) was calculated by Ephus using −5 mV voltage steps (50 ms) from a holding potential of −70 mV. Resting membrane voltage was measured in current clamp mode. A 1 s current ramp (0 to +600 pA) was injected to measure the rheobase and the voltage threshold for action potentials. Firing rates were calculated from 1 s current steps (−400 pA to +600 pA).

Spine density measurement and analysis. Two-photon microscopy at 840 nm was used to excite cells expressing mCerulean or mCerulean plus SyntagMA. An Olympus LUMFL N 60×1.1NA objective (PSF: 0.35 × 0.35 × 1.5 μm) was used to collect Z-stacks (0.3 μm z-step) of stratum radiatum proximal oblique dendrites (~100 μm from soma). Image stacks were deconvolved using a blind deconvolution algorithm in Autoquant X3 (Media cybernetics). Spines and dendrites were semi-automatically detected using the Filament tracer feature of Imaris (Oxford Instruments). For each neuron, spine density was determined from 1–3 dendrites of 30–100 μm length (Supplementary Fig. 4g).

Quantification of pre- and postSynTagMA localization. A macro written in Fiji[21] was used for two-photon 3D image analysis at 840, 980 and/or 1040 nm wavelengths. When z-stacks contained alternating images collected at different excitation wavelengths, they were first separated and then xyz-aligned to correct for chromatic aberration using green and/or red channels and the pairwise stitching plugin[61]. mCerulean and SynTagMA fluorescence values were obtained from images after median filtering and rolling ball background subtraction[62]. Regions of interest (ROI) were drawn onto maximum intensity projections and compared to axonal or dendrite shafts, respectively. Only spines projecting laterally from the dendrite were analyzed.

Photoconversion after back-propagating action potentials. The first image stack was acquired before patching the SynTagMA-expressing neuron (Figs. 4–5). The cell was then whole-cell patch-clamped and bAPs (100 Hz) were evoked by somatic current injection and paired with 500 ms of 395 nm light (1 s delay) in the presence of CPPene (10 μM) and NBQX (10 μM) to block synaptic transmission. This pairing was repeated 15 times. For experiments with CaMPARI2 (Fig. 2e), 50 bAPs at 100 Hz were evoked and paired with 100 ms of 395 nm light. This pairing was repeated 10 times. While acquiring the second image stack, the cell was held in voltage clamp at −65 mV to prevent depolarization. The field of violet light illumination for these experiments was 557 um in diameter and therefore large enough to illuminate the entire dendritic arbor.

Propidium iodide staining. Organotypic hippocampal slices aged between DIV 18-28 were used. 2-4 days before staining, CA1 neurons were electroporated with mCerulean (20 ng μl^{-1}) and postSynTagMA (20 ng μl^{-1}). Slices were placed in the two-photon imaging chamber in HEPES-buffered solution containing 3 μM propi-dium iodide (PI). The objective was then placed above the CA1 region of the slice and illuminated with violet light (395 nm, 16 mW mm^{-2}). Following illumination, slices were kept in the PI solution for 30-45 minutes and subsequently imaged (840 nm excitation). PI fluorescence was collected through 607/70 filters and mCerulean fluorescence was collected through 525/50 filters. NMDA excitotoxicity was used as a

134

positive control. Slices were exposed to 1 mM NMDA in HEPES-buffered solution for 1.5 h and then labeled with PI for 30–45 min before imaging as above. To quantify violet light toxicity, PI-positive nuclei were counted in each 2P image stack (background subtracted, median filtered) and normalized to the tissue volume.

Semi-automatic segmentation and analysis of SynTagMA. For the initial characterization of postSynTagMA (Figs. 1–3), quantification of green to red conversion was performed manually in a small set of synapses (<50) in Matlab and/or Fiji. Covering relative larger areas of the dendritic tree gave rise to larger data sets (>1000 synapses) that made a semi-automated analysis approach necessary (Figs. 4–6). Rigid registration was performed using the Pairwise stitching plugin[61] in Fiji. The broad emission spectrum of autofluorescent objects proved useful to align the red emission from the 980 nm stack to the green channel from the 1040 nm stack. Image stacks were further processed using a blind deconvolution algorithm in AutoQuant X3. Particularly critical was to correct for position change of synapses in 3D due to tissue deformation ("warping") between acquisitions of image stacks (pre- and post-stimulation). To correct for tissue warping, synapse voxels were reassigned to their initial position using either elastix[23] or ANTs (Advanced Normalization Tools[63]). To detect synapses, we used Imaris 3D spot detection on the deconvolved G_0 signal. Prior to data extraction, spots that were not due to SynTagMA but autofluorescence were filtered out based on their red fluorescence at baseline (R_0, see Supplementary Fig. 8). Approximately 10-30% of originally detected spots were rejected using this filter. Spots (volumetric ROIs) were used to extract fluorescence intensities from green and red channels (maximum pixel values from non-deconvolved, median-filtered images) at every time point. To quantify photoconversion, green (G_0 and G_1) and red (R_0 and R_1) values were normalized to the population mean of G_0 and R_0, respectively.

Automated segmentation and analysis of SynTagMA. To analyze thousands of synapses in large 3D datasets, we developed a pipeline to automatically identify spots in 3D and define volumes (ROIs) for accurate measurements of fluorescence changes (Supplementary Fig. 3, Supplementary Fig. 9). After two microscope-specific pre-processing steps (de-interleaving of 980/1040 nm image stacks to separate green and red channels, rigid registration to correct for chromatic aberration and beam misalignment), the data is processed by SynapseLocator, a GUI-controlled software package written in Matlab, which calls specific subroutines (Fiji, elastix, Weka) to perform the analysis:

1. Deconvolution and transformation of post-image to pre-image using elastix
2. Random forest model, built with machine learning
3. Spot identification and ROI creation
4. User interactive visualization of fluorescent values and calculations of SynTagMA photoconversion in ROIs

The detailed workflow in SynapseLocator consists of an initial deconvolution step (Fiji, DeconvolutionLab2 plugin[22]) in which diffraction-induced blurring of the images was reduced. We used elastix[23] to register image stacks across time points (using only the green channel; G_0 and G_1). Registration proceeds in four steps (rigid transformation, rotation transformation, affine transformation, and non-rigid registration) for which we provide optimized parameter sets. The transformation was then applied to both red and green channel data (deconvolved and raw). Synapse detection involved a machine learning process accessed via Fiji (Weka, Trainable Weka Segmentation plugin[24]). Two classes are manually (by the user) identified as "spot" and "no spot" to train a random forest model considering a set of scale-invariant image features (Hessian and Laplacian, each calculated at three scales, Fiji, FeatureJ plugin). Typically, the model was robust enough to allow for analysis of all experiments from a series. A synapse is identified as a region in which a group of voxels with spot class properties shows minimal connectivity (26-connected neighborhood). For each region, an ellipsoid enclosing the identified connected voxels is calculated in Matlab and stored as ROI. To exclude spots that are not related to SynTagMA fluorescence, all ROIs with high red fluorescence at baseline are automatically excluded from analysis. After spot identification, the user can interactively examine the data using a table and apply additional filters. Spot intensities are extracted in parallel from raw imaging data, median-filtered data, and from filtered and deconvolved data, allowing the user to compare the effects of image processing. Please see Github documentation for further details.

Distance-dependence of bAP-induced calcium transients. CA1 neurons expressing mCerulean and postSynTagMA were used for these experiments. Prior to patching, z-stacks (as described above) were acquired along the apical dendritic tree to image postSynTagMA. Two to three stacks were required to image the apical dendritic tree. The time taken to image all stacks was 30–40 min. The cell was then whole-cell patch-clamped and 50 bAPs were paired with 500 ms violet light (1 s delay). This pairing was repeated 15 times (0.1 Hz). Immediately after, all image stacks were acquired followed by complementary stacks of mCerulean at 840 nm for morphology.

In CA1 neurons expressing jGCaMP7b, frame scans (6×6 μm) of oblique dendrites along the entire dendritic arbor were acquired (980 nm) while evoking 50 bAPs. In each trial, 50 frames (64×64 pixels) were acquired at 5.9 Hz. At least 3 trials were recorded from each section of dendrite. Following calcium imaging, the

morphology of the entire cell was imaged using jGCaMP7b baseline fluorescence. The fluorescence time course was measured by placing ROIs on individual spines in Fiji. We calculated $\Delta F/F_0$; F_0 was determined 300 ms prior to bAP onset.

To analyze photoconversion (postSynTagMA) or calcium transients (jGCaMP7b) in synapses as a function of distance from the soma, we created a series of 20 μm wide concentric rings around the soma using a custom-written MATLAB script. For the synapses located in each ring, we calculated the median photoconversion or median calcium transient amplitude and the interquartile range.

postSynTagMA turnover measurements. postSynTagMA turnover experiments were performed on dissociated hippocampal neurons (DIV 14-16, 9-11 days post-transfection). Cells were imaged at ~21°C in a modified Tyrode's solution containing the following (in mM): 119 NaCl, 2.5 KCl, 3 CaCl2, 1 MgCl2, 25 HEPES, and 30 D-Glucose with 10 μM CNQX. PostSynTagMA photoconversion was induced using a train of 50 action potentials (50 Hz) paired with a 500 ms photoconverting light pulse in custom-drawn rectangular regions (18.6 mW mm^{-2}, 500-750 ms delay). Z-stacks with 0.25 μm step size were collected over the course of an hour every 5–6 min. Cells were illuminated at each step by 405 nm (1% intensity), 488 (25% intensity) and 561 (20% intensity) lasers.

Photoconverting sub- and suprathreshold responses. For extracellular synaptic stimulation, a monopolar electrode was placed in *stratum radiatum* and two 0.2 ms pulses, 40 ms apart, were delivered using an ISO-Flex stimulator (A.M.P.I.). Stimulation intensity was adjusted to be subthreshold for action potentials (i.e., to evoke ~15 mV EPSPs or ~−500 pA EPSCs) or suprathreshold (i.e. evoking action potentials) by patching a nearby neuron in CA1. Stimulation was paired with 100 ms violet light (1 s delay) 50 times.

Subthreshold optogenetic stimulation and photoconversion. CA3 neurons expressing AAV2/9 synapsin-ChR2(ET/TC)−2A-synaptophysin-mCerulean were stimulated with blue light pulses (470 nm, 2 pulses, 2-5 ms duration, 40 ms apart) applied through a light fiber placed above the CA3. The light intensity and pulse width were set to evoke EPSCs (0.5–1.0 nA) in a neighboring CA1 neuron. Stimulation was paired with 100 ms violet light (1 s delay) and repeated 50 times at 0.1 Hz to photoconvert postSynTagMA in active spines. Z-stacks were acquired before and after photoconversion as described above. A third z-stack at 840 nm was acquired immediately after the post-photoconversion stack to image mCerulean-labeled boutons.

Relabeling postSynTagMA. For relabeling experiments, paired-pulse extracellular stimulation (0.2 ms pulses, 40 ms apart) was combined with 250 ms of violet light. This was repeated 25 times (0.1 Hz) and a second image stack was acquired immediately thereafter. After imaging, the slice was returned to the incubator. Approximately 18 h later, the procedure was repeated.

Virus injection and hippocampal window surgery. Mice were anesthetized with an intraperitoneal injection of Ketamine/Xylazine (0.13/0.01 mg g^{-1} bodyweight) and placed on a heating blanket to maintain the body temperature. In addition, mice received a subcutaneous dose of Carprofen (4 mg kg^{-1}) for post-surgery analgesia. Eyes were covered with eye ointment (Vidisic, Bausch + Lomb) to prevent drying. Prior to surgery, the depth of anesthesia and analgesia was evaluated with a toe-pinch to test the paw-withdrawal reflex. Subsequently, mice were fixed in a stereotactic frame, the fur was removed with a fine trimmer and the skin of the head was disinfected with Betaisodona solution using sterile cotton swabs. The skin was removed by a midline scalp incision (1–3 cm), the skull was cleaned using a bone scraper (Fine Science Tools) and a small hole was drilled with a dental drill (Foredom) above the injection site. AAV2/9-mDlx-SynTagMA-2A-mCerulean or AAV2/9-syn-GCaMP6f was targeted unilaterally to the dorsal CA1 area (−2.0 mm AP, ± 1.3 mm ML, −1.5 mm DV relative to Bregma. 0.6 μl of virus suspension was injected. All injections were done at 100 nl min^{-1} using a glass micropipette. After the injection, the pipette stayed in place for at least 5 min after virus delivery before it was withdrawn and the scalp was closed with sutures. During the two days following surgery animals were provided with Meloxicam mixed into soft food.

Two weeks after virus injection, mice were anesthetized as described above to implant the hippocampal window. After fur removal, skin above the frontal and parietal bones of the skull was removed by one horizontal cut along basis of skull and two rostral cuts. The skull was cleaned after removal of the periosteum, roughened with a bone scraper and covered with a thin layer of cyanoacrylate glue (Cyano Veneer). After polymerization a 3-mm circle was marked on the right parietal bone (anteroposterior, −2.2 mm; mediolateral, +1.8 mm relative to bregma) with a biopsy punch and the bone was removed with a dental drill (Foredom). The bone fragment and dura were carefully removed with fine surgical forceps. The cortex above the hippocampus was aspirated with a 0.8 mm blunt needle connected to a water jet pump. When the first layer of fibers running orthogonal to midline became visible, a 0.4 mm blunt needle was used to carefully remove the upper two of three fiber layers of the external capsule. The craniotomy was washed with sterile PBS and a custom-built imaging window was inserted over

the dorsal hippocampus. The window consisted of a hollow glass cylinder (diameter: 3 mm, wall thickness: 0.1 mm, height: 1.5 mm) glued to a No. 1 coverslip (diameter: 3 mm, thickness: 0.17 mm) on the bottom and to a stainless-steel rim on the top with UV-curable glass glue (Norland NOA61). The steel rim and a head holder plate (Luigs & Neumann) were fixed to the skull with cyanoacrylate gel (Pattex). After polymerization, cranial window and head holder plate were covered with dental cement (Super Bond C&B, Sun Medical) to provide strong bonding to the skull bone. During the two days following surgery animals were provided with Meloxicam mixed into soft food.

Hippocampal imaging and photoconversion in vivo. SynTagMA imaging in vivo was performed in head-fixed animals during a behavioral task or under anesthesia (isoflurane or ketamine/xylazine). During anesthesia, mice were kept on a heated blanket to maintain body temperature and eyes were covered with eye ointment (Vidisic, Bausch + Lomb) to prevent drying. The window was centered under the two-photon microscope (MOM-scope, Sutter Instruments, modified by Rapp Optoelectronics) using a low-magnification objective (4× Nikon Plan Fluorite) and reporter expression (postSynTagMA or GCaMP6f) was verified in the hippocampus using epi-fluorescence. The cranial window was then filled with water to image in two-photon mode through a 40× (40X Nikon CFI APO NIR, 0.80 NA, 3.5 mm WD) or a 16× (16X Nikon CFI LWD Plan Fluorite Objective, 0.80 NA, 3.0 mm WD) objective. The green species of SynTagMA or GCaMP6f was excited with a Ti:Sa laser (Chameleon Vision-S, Coherent) tuned to 980 nm. The red species of SynTagMA was excited with an ytterbium-doped 1070-nm fiber laser (Fidelity-2, Coherent). Single planes (512×512 pixels) were acquired at 30 Hz with a resonant-galvanometric scanner at 29–60 mW (980 nm) and 41–60 mW (1070 nm) using ScanImage 2017b (Vidrio). Emitted photons were detected by a pair of photo-multiplier tubes (H7422P-40, Hamamatsu). A 560 DXCR dichroic mirror and 525/50 and 607/70 emission filters (Chroma Technology) were used to separate green and red fluorescence. Excitation light was blocked by a short-pass filter (ET700SP-2P, Chroma).

For identification of active CA1 neurons (Fig. 7a–c), the conversion protocol consisted of 2 s violet light pulses (405 nm, 12.1 mW mm^{-2}) repeated 10 or 15 times in awake and ketamine/xylazine (130/10 mg/kg) anesthetized mice. In awake behaving mice, photoconversion light was triggered upon water reward delivery. Acute imaging of calcium-dependent dimming of the green SynTagMA species was performed continuously while the animals were running multiple laps on the treadmill receiving a water reward upon completion of each lap. Running speed was simultaneously recorded.

For synaptic imaging of SynTagMA in hippocampal interneurons mice were anesthetized with isoflurane at a concentration ranging between 2.0% and 2.5% in 100% O$_2$ Since SynTagMA fluorescence was relatively low, 450–1800 frames per optical plane were acquired and averaged. Under isoflurane anesthesia (Fig. 7g), conversion of active synapses in interneurons was achieved with 20 flashes of 3 s violet light pulses (405 nm, 0.42 mW mm^{-2}). Motion artefacts were corrected with a custom-modified Lucas-Kanade-based alignment algorithm in Matlab. Quantification of nuclear and synaptic SynTagMA photoconversion was performed as described for slice cultures. Raw movies from acute SynTagMA imaging experiments were analyzed with suite2p, which performs image registration (motion correction), automatic region-of-interest detection, activity extraction and neuropil correction.

Quantification and statistical analysis. Quantification was done using automatic (i.e., blind) analyses using either Imaris or SynapseLocator, or quantification was done manually. Figures 1 and 2 were quantified manually (see Supplementary Fig. 9 for comparison of manual versus automatic analysis). The n-size for Figs. 1 and 2 is neuron number (all independent replications). However, some experiments use number of synapses as the n-size. For all in vitro postSynTagMA experiments (Figs. 3–6), the n-size is synapse number. We consider every synapse a unique biological entity. In vivo experiments use nuclei or synapses as the n-size (Fig. 7). The definition and the exact value for n is given in the figure and/or figure legend. Replication of experiments is reported in figure legends. Statistical analysis was performed using GraphPad Prism (v8) or Matlab. For data with normal distributions, Student's t-test or one-way ANOVA followed by Tukey's post-hoc comparison were used. Data considered non-normal (according to a D'Agostino-Pearson test) underwent non-parametric tests (Kruskal-Wallis followed by Benjamini-Hochberg FDR method, Mann-Whitney test Dunn's multiple comparisons test). Curve fitting was done in GraphPad Prism or in Matlab using the curve-fitting toolbox. Data are shown as either mean ± SEM or median with interquartile range. The specific test used is reported in the corresponding figure legend.

Reporting summary. Further information on research design is available in the Nature Research Reporting Summary linked to this article.

Data availability
The datasets generated and/or analyzed during the study are available from the corresponding author TGO on request. An example preSynTagMA and postSynTagMA dataset is deposited on Github with SynapseLocator.

Code availability
We deposited our analysis software, instructions and test data on GitHub (https://github.com/drchrisch/SynapseLocator).

References
1. Adam, Y. et al. Voltage imaging and optogenetics reveal behaviour-dependent changes in hippocampal dynamics. Nature 569, 413–417 (2019).
2. Dana, H. et al. High-performance calcium sensors for imaging activity in neuronal populations and microcompartments. Nat. Methods 16, 649–657 (2019).
3. Marvin, J. S. et al. Stability, affinity, and chromatic variants of the glutamate sensor iGluSnFR. Nat. Methods 15, 936–939 (2018).
4. Svoboda, K., Denk, W., Kleinfeld, D. & Tank, D. W. In vivo dendritic calcium dynamics in neocortical pyramidal neurons. Nature 385, 161–165 (1997).
5. Grewe, B. F., Langer, D., Kasper, H., Kampa, B. M. & Helmchen, F. High-speed in vivo calcium imaging reveals neuronal network activity with near-millisecond precision. Nat. Methods 7, 399–405 (2010).
6. Iacaruso, M. F., Gasler, I. T. & Hofer, S. B. Synaptic organization of visual space in primary visual cortex. Nature 547, 449–452 (2017).
7. Andresen, V. et al. High-resolution intravital microscopy. PLoS ONE 7, e50915 (2012).
8. Bewersdorf, J., Pick, R. & Hell, S. W. Multifocal multiphoton microscopy. Opt. Lett. 23, 655 (1998).
9. Kazemipour, A. et al. Kilohertz frame-rate two-photon tomography. Nat. Methods 16, 778–786 (2019).
10. Fosque, B. F. et al. Labeling of active neural circuits in vivo with designed calcium integrators. Science 347, 755–760 (2015).
11. Moeyaert, B. et al. Improved methods for marking active neuron populations. Nat. Commun. 9, 4440 (2018).
12. Patel, A. & Cox, D. Behavioral and functional assays for investigating mechanisms of noxious cold detection and multimodal sensory processing in Drosophila larvae. Bio. Protoc. 7, e2388 (2017).
13. Bohra, A. A., Kallman, B. R., Reichert, H. & VijayRaghavan, K. Identification of a single pair of interneurons for bitter taste processing in the Drosophila brain. Curr. Biol. 28, 847–858.e3 (2018).
14. Zolnik, T. A. et al. All-optical functional synaptic connectivity mapping in acute brain slices using the calcium integrator CaMPARI. J. Physiol. 595, 1465–1477 (2017).
15. Gross, G. G. et al. Recombinant probes for visualizing endogenous synaptic proteins in living neurons. Neuron 78, 971–985 (2013).
16. Sturgill, J. F., Steiner, P., Czervionke, B. L. & Sabatini, B. L. Distinct domains within PSD-95 mediate synaptic incorporation, stabilization, and activity-dependent trafficking. J. Neurosci. 29, 12845–12854 (2009).
17. Nikonenko, I. et al. PSD-95 promotes synaptogenesis and multiinnervated spine formation through nitric oxide signaling. J. Cell Biol. 183, 1115–1127 (2008).
18. Margolin, J. F. et al. Krüppel-associated boxes are potent transcriptional repression domains. Proc. Natl. Acad. Sci. USA 91, 4509–4513 (1994).
19. Bonhoeffer, T. & Yuste, R. Spine motility. Phenomenology, mechanisms, and function. Neuron 35, 1019–1027 (2002).
20. Fischer, M., Kaech, S., Knutti, D. & Matus, A. Rapid actin-based plasticity in dendritic spines. Neuron 20, 847–854 (1998).
21. Schindelin, J. et al. Fiji: an open-source platform for biological-image analysis. Nat. Methods 9, 676–682 (2012).
22. Sage, D. et al. DeconvolutionLab2: An open-source software for deconvolution microscopy. Methods 115, 28–41 (2017).
23. Klein, S., Staring, M., Murphy, K., Viergever, M. A. & Pluim, J. elastix: A Toolbox for Intensity-Based Medical Image Registration. IEEE Trans. Med. Imaging 29, 196–205 (2010).
24. Arganda-Carreras, I. et al. Trainable Weka segmentation: a machine learning tool for microscopy pixel classification. Bioinformatics 33, 2424–2426 (2017).
25. Gray, N. W., Weimer, R. M., Bureau, I. & Svoboda, K. Rapid redistribution of synaptic PSD-95 in the neocortex in vivo. PLoS Biol. 4, e370 (2006).
26. Berndt, A. et al. High-efficiency channelrhodopsins for fast neuronal stimulation at low light levels. Proc. Natl. Acad. Sci. USA 108, 7595–7600 (2011).
27. Pachitariu, M. et al. Suite2p: beyond 10,000 neurons with standard two-photon microscopy. Preprint at https://www.biorxiv.org/content/10.1101/061507v2 (2016)
28. Francavilla, R., Villette, V., Martel, O. & Topolnik, L. Calcium dynamics in dendrites of hippocampal CA1 interneurons in awake mice. Front. Cell. Neurosci. 13, 98 (2019).

136

29. Li, Z. & Murthy, V. N. Visualizing postendocytic traffic of synaptic vesicles at hippocampal synapses. *Neuron* **31**, 593–605 (2001).

30. Miesenbock, G., De Angelis, D. A. & Rothman, J. E. Visualizing secretion and synaptic transmission with pH-sensitive green fluorescent proteins. *Nature* **394**, 192–195 (1998).

31. Ariel, P. & Ryan, T. A. Optical mapping of release properties in synapses. *Front. Neural Circuits* **4**, 18 (2010).

32. Dürst, C. D. et al. High-speed imaging of glutamate release with genetically encoded sensors. *Nat. Protoc.* **14**, 1401–1424 (2019).

33. Toni, N., Buchs, P. A., Nikonenko, I., Bron, C. R. & Muller, D. LTP promotes formation of multiple spine synapses between a single axon terminal and a dendrite. *Nature* **402**, 421–425 (1999).

34. Feinberg, E. H. et al. GFP Reconstitution Across Synaptic Partners (GRASP) defines cell contacts and synapses in living nervous systems. *Neuron* **57**, 353–363 (2008).

35. Choi, J.-H. et al. Interregional synaptic maps among engram cells underlie memory formation. *Science* **360**, 430–435 (2018).

36. Macpherson, L. J. et al. Dynamic labelling of neural connections in multiple colours by trans-synaptic fluorescence complementation. *Nat. Commun.* **6**, 10024 (2015).

37. Scholl, B., Wilson, D. E. & Fitzpatrick, D. Local order within global disorder: synaptic architecture of visual space. *Neuron* **96**, 1127–1138.e4 (2017).

38. Chen, X., Leischner, U., Rochefort, N. L., Nelken, I. & Konnerth, A. Functional mapping of single spines in cortical neurons in vivo. *Nature* **475**, 501–505 (2011).

39. Soler-Llavina, G. J. & Sabatini, B. L. Synapse-specific plasticity and compartmentalized signaling in cerebellar stellate cells. *Nat. Neurosci.* **9**, 798–806 (2006).

40. Topolnik, L. & Camiré, O. Non-linear calcium signalling and synaptic plasticity in interneurons. *Curr. Opin. Neurobiol.* **54**, 98–103 (2019).

41. de Juan-Sanz, J. et al. Axonal endoplasmic reticulum Ca2+content controls release probability in CNS nerve terminals. *Neuron* **93**, 867–881.e6 (2017).

42. Sabatini, B. L., Oertner, T. G. & Svoboda, K. The life cycle of Ca(2+) ions in dendritic spines. *Neuron* **33**, 439–452 (2002).

43. Holbro, N., Grunditz, A. & Oertner, T. G. Differential distribution of endoplasmic reticulum controls metabotropic signaling and plasticity at hippocampal synapses. *Proc. Natl Acad. Sci. USA* **106**, 15055–15060 (2009).

44. Emptage, N., Bliss, T. V. & Fine, A. Single synaptic events evoke NMDA receptor-mediated release of calcium from internal stores in hippocampal dendritic spines. *Neuron* **22**, 115–124 (1999).

45. Spruston, N., Schiller, Y., Stuart, G. & Sakmann, B. Activity-dependent action potential invasion and calcium influx into hippocampal CA1 dendrites. *Science* **268**, 297–300 (1995).

46. Golding, N. L., Kath, W. L. & Spruston, N. Dichotomy of action-potential backpropagation in CA1 pyramidal neuron dendrites. *J. Neurophysiol.* **86**, 2998–3010 (2001).

47. Yasuda, R., Sabatini, B. L. & Svoboda, K. Plasticity of calcium channels in dendritic spines. *Nat. Neurosci.* **6**, 948–955 (2003).

48. Holbro, N., Grunditz, A., Wiegert, J. S. & Oertner, T. G. AMPA receptors gate spine Ca(2+) transients and spike-timing-dependent potentiation. *Proc. Natl. Acad. Sci. USA* **107**, 15975–15980 (2010).

49. Yu, Y., Oberlaender, K., Bengtson, C. P. & Bading, H. One nuclear calcium transient induced by a single burst of action potentials represents the minimum signal strength in activity-dependent transcription in hippocampal neurons. *Cell Calcium* **65**, 14–21 (2017).

50. DeNardo, L. & Luo, L. Genetic strategies to access activated neurons. *Curr. Opin. Neurobiol.* **45**, 121–129 (2017).

51. Stujenske, J. M., Spellman, T. & Gordon, J. A. Modeling the spatiotemporal dynamics of light and heat propagation for invivo optogenetics. *Cell Rep.* **12**, 525–534 (2015).

52. Trojanowski, N. F. & Turrigiano, G. Activity labeling in vivo using CaMPARI2 reveals electrophysiological differences between neurons with high and low firing rate set points. Preprint at https://www.biorxiv.org/content/10.1101/795252v2 (2019).

53. Lin, R. et al. Cell-type-specific and projection-specific brain-wide reconstruction of single neurons. *Nat. Methods* **15**, 1033–1036 (2018).

54. Gee, C. E., Ohmert, I., Wiegert, J. S. & Oertner, T. G. Preparation of slice cultures from rodent hippocampus. *Cold Spring Harb. Protoc.* **2017**, pdb.prot094888 (2017).

55. Hoppa, M. B., Lana, B., Margas, W., Dolphin, A. C. & Ryan, T. A. α2δ expression sets presynaptic calcium channel abundance and release probability. *Nature* **486**, 122–125 (2012).

56. Perez, E. E. et al. Establishment of HIV-1 resistance in CD4+ T cells by genome editing using zinc-finger nucleases. *Nat. Biotechnol.* **26**, 808–816 (2008).

57. Cho, I. H., Panzera, L. C., Chin, M. & Hoppa, M. B. Sodium channel β2 subunits prevent action potential propagation failures at axonal branch points. *J. Neurosci.* **37**, 9519–9533 (2017).

58. Suter, B. A. et al. Ephus: multipurpose data acquisition software for neuroscience experiments. *Front. Neural Circuits* **4**, 1–12 (2010).

59. Wiegert, J. S., Gee, C. E. & Oertner, T. G. Single-cell electroporation of neurons. *Cold Spring Harb. Protoc.* **2017**, 135–138 (2017).

60. Pologruto, T. A., Sabatini, B. L. & Svoboda, K. ScanImage: flexible software for operating laser scanning microscopes. *Biomed. Eng. Online* **2**, 13 (2003).

61. Preibisch, S., Saalfeld, S. & Tomancak, P. Globally optimal stitching of tiled 3D microscopic image acquisitions. *Bioinformatics* **25**, 1463–1465 (2009).

62. Sternberg. Biomedical Image Processing. *Computer (Long. Beach. Calif.)* **16**, 22–34 (1983).

63. Avants, B. B. et al. A reproducible evaluation of ANTs similarity metric performance in brain image registration. *Neuroimage* **54**, 2033–2044 (2011).

Acknowledgements

Author contributions

Conceptualization, T.G.O., C.E.G., M.B.H. and J.S.W.; Software, A.P.A., C.S. and I.A.C.; Investigation, A.P.A., B.C.F., R.J.O., W.Y., P.L.M., B.M., M.A.M., L.C.P., J.S.W. and M.B.H; Resources, E.R.S.; Writing – Original Draft, C.E.G., T.G.O., M.B.H., J.S.W., B.C.F., A.P.A., C.S.; Writing – Review & Editing, A.P.A., B.C.F., R.J.O., W.Y., I.A.C., P.L.M., B.M., M.A.M., L.C.P., C.S., E.R.S., J.S.W., C.E.G., M.B.H., T.G.O.; Visualization, B.C.F., A.P.A., C.S., T.G.O., M.B.H.; Supervision, E.R.S., J.S.W., C.E.G., M.B.H., T.G.O.; Project administration, C.E.G.; Funding acquisition, E.R.S., J.S.W., C.E.G., M.B.H., T.G.O.

Competing interests

E.R.S. is an inventor on US patent number 9,518,996 and US patent application 15/335,707, which may cover CaMPARI sequences described in this paper. The remaining authors declare no competing interests.

Additional information

137

Supplementary information
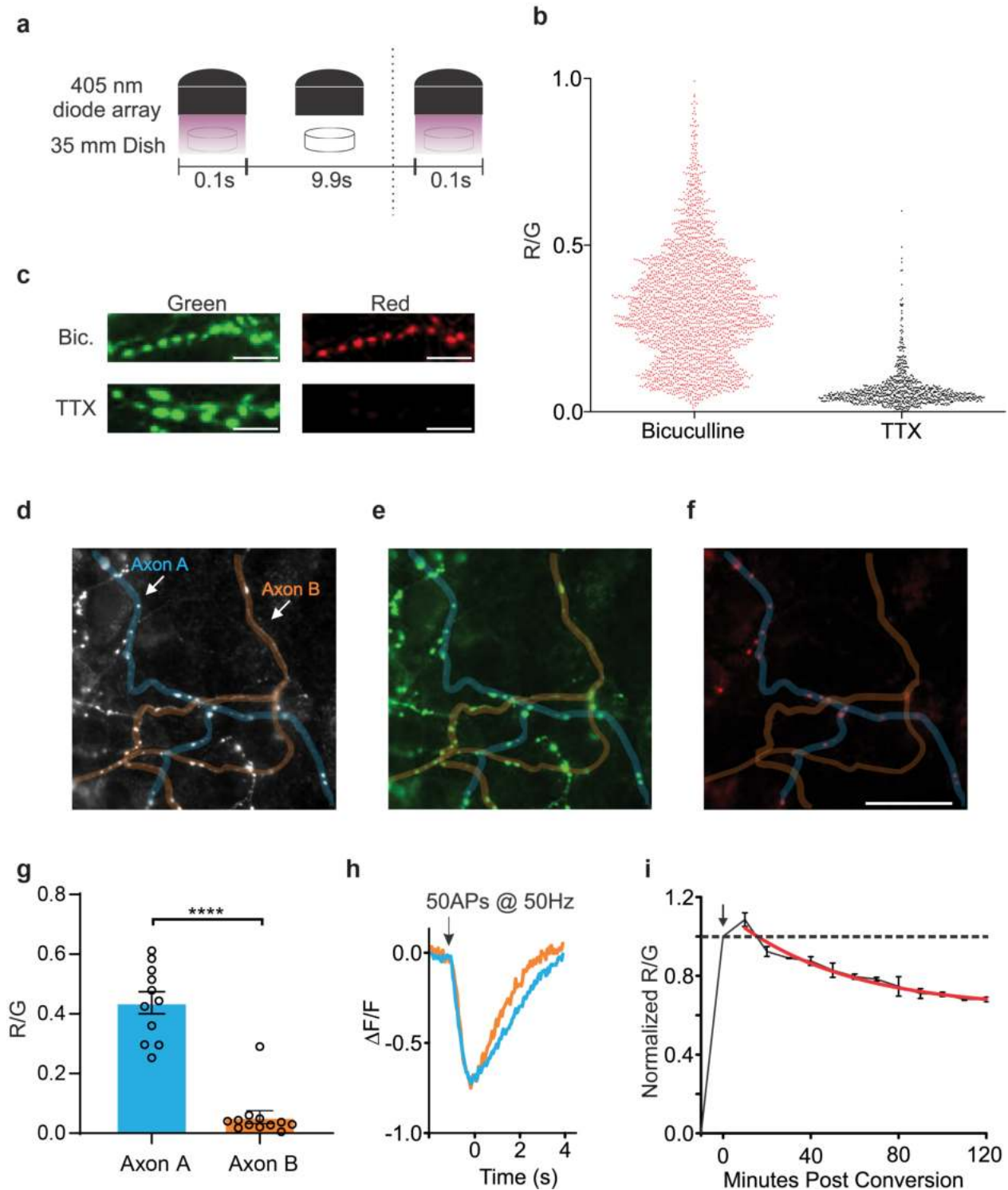
Supplementary Figure 1: Spontaneous circuit activity of cultured primary hippocampal neurons drives photoconversion of preSynTagMA.(a) LED arrays (51 diodes, 405 nm) were placed in an incubator (5% CO_2, 37°C) and set to flash for 100 ms every 10 s for 4 hours. LED arrays were placed on top of 35 mm dishes containing cultured

primary hippocampal neurons. **(b)** Example green and red raw fluorescence of boutons when incubated with bicuculline to increase activity or TTX to block activity while illuminating with violet light as shown in **a**.**(c)** R/G ratio of individual boutons with bicuculline (n = 2456 synapses, 3 experiments) or TTX (n = 866 synapses, 4 experiments) **(d)** Axons from two neurons in bicuculline condition (axon A, blue overlay; axon B, orange overlay). **(e)** Raw green fluorescence. **(f)** Raw red fluorescence. Note that photoconversion (red fluorescence) was restricted to boutons of axon A. **(g)** Mean R/G ± SE from boutons of axon A (n = 11 boutons, R/G = 0.44 ± 0.04) and axon B (n = 12 boutons, R/G = 0.05 ± 0.02) (****$p < 0.0001$, Student's t-test, unpaired), indicating differential activity. **(h)** Dimming of green fluorescence from axons A (blue) and B (orange) during a 50 AP, 50 Hz stimulus train. Similar dimming indicates both axons could fire action potentials and had similar calcium influx during induced spiking. Therefore, the lack of photoconversion in bicuculline was most likely due to a lack of spiking in axon B. **(i)** Slow decay of R/G ratio following strong photoconversion (40 x 1 s light, 405 nm, paired exactly with 20 APs @ 50Hz). Images were acquired every ten minutes for two hours (n = 4 cells). Data are shown as mean ± SEM. Scale bars: 5 µm (c), 50 µm (d-f)**.**
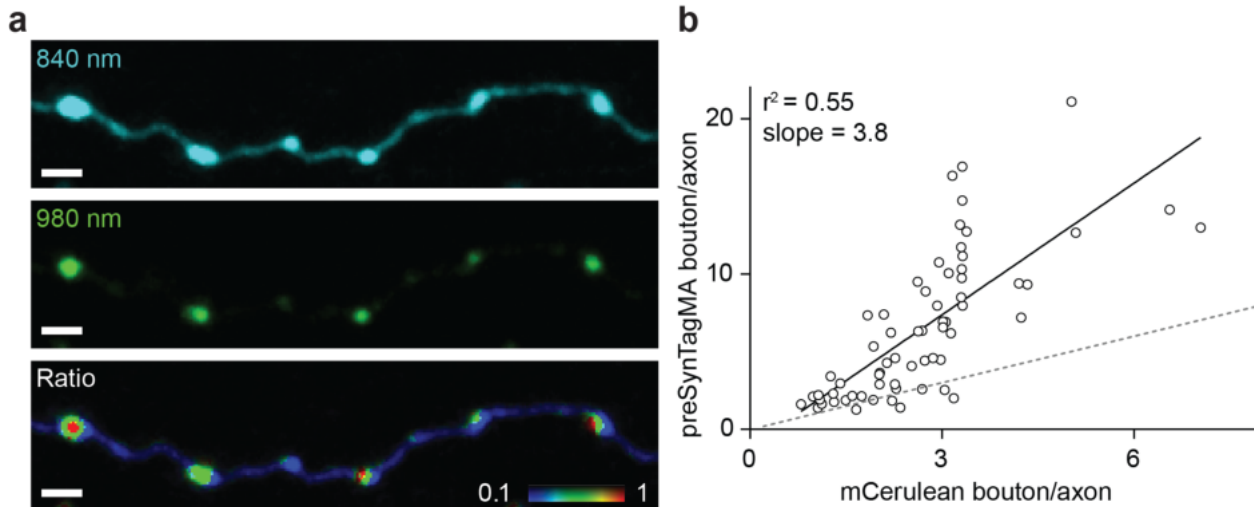
Supplementary Figure 2: Enrichment of preSynTagMA in Schaffer collateral boutons. (a) Two-photon image of

hippocampal slice culture showing axonal boutons in *stratum radiatum*, originating from CA3 neurons expressing

preSynTagMA and mCerulean as cytosolic filler. Upper panel: mCerulean (840 nm), middle panel: preSynTagMA (980

nm), lower panel: green/cyan ratio image, indicating labeled vesicle clusters. Scale bars: 2 μm. **(b)** The ratio of

preSynTagMA bouton to axonal shaft fluorescence vs the ratio of mCerulean bouton to axon fluorescence for n = 64

boutons. Solid line: linear fit. Dashed line (slope = 1) indicates the expected location of boutons without synaptic vesicles.

Experiment was reproduced in two slices.

a

b

c

2P/Violet light

preSynTagMA

Stim.
elect.

d

$(R_1-R_0)/G_0$

20

10

0

****

Stim. TTX

e

baseline

after stim. + violet light

980 nm

1040 nm

f Rejected spots

g preSynTagMA spots

20

0
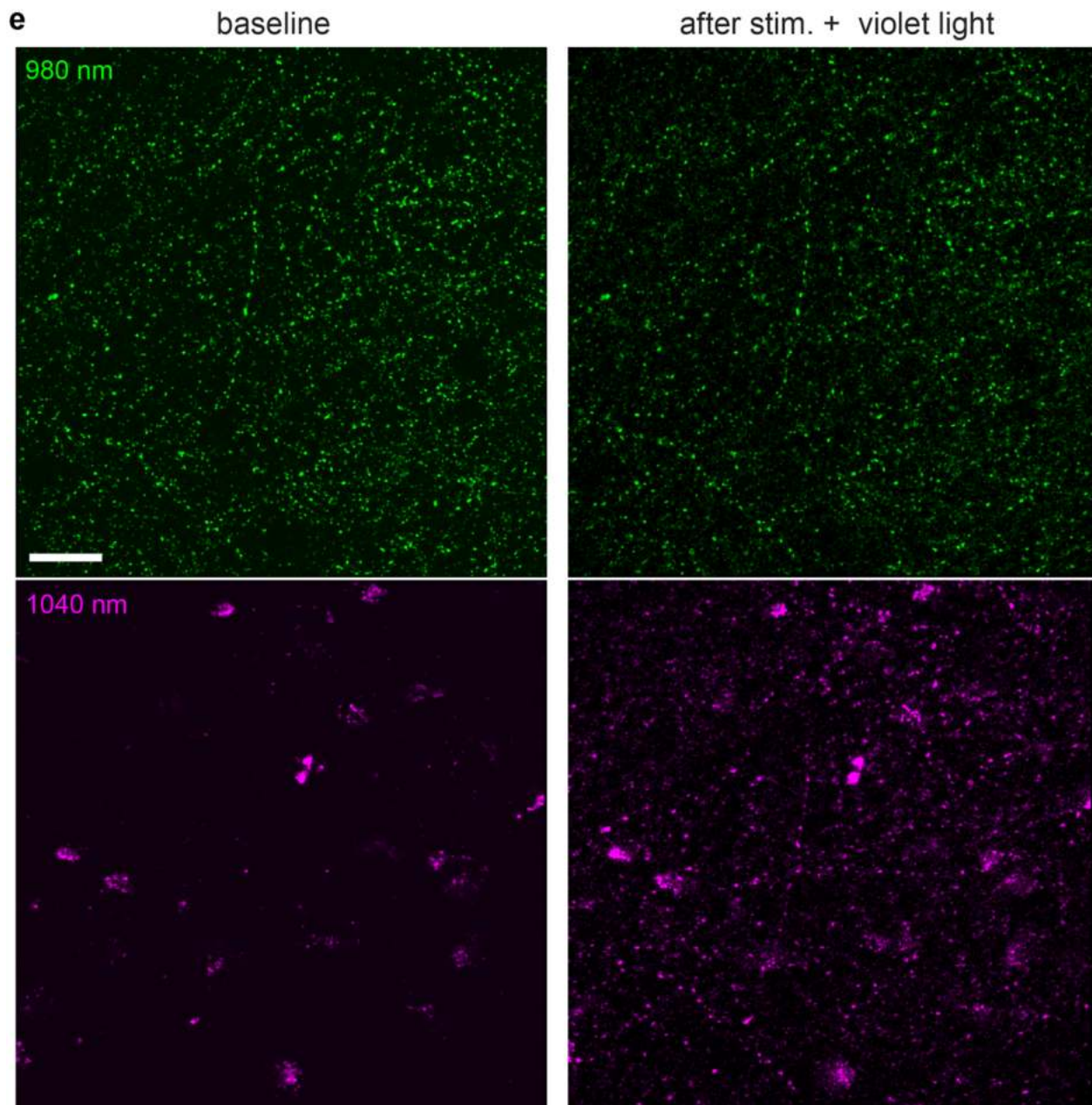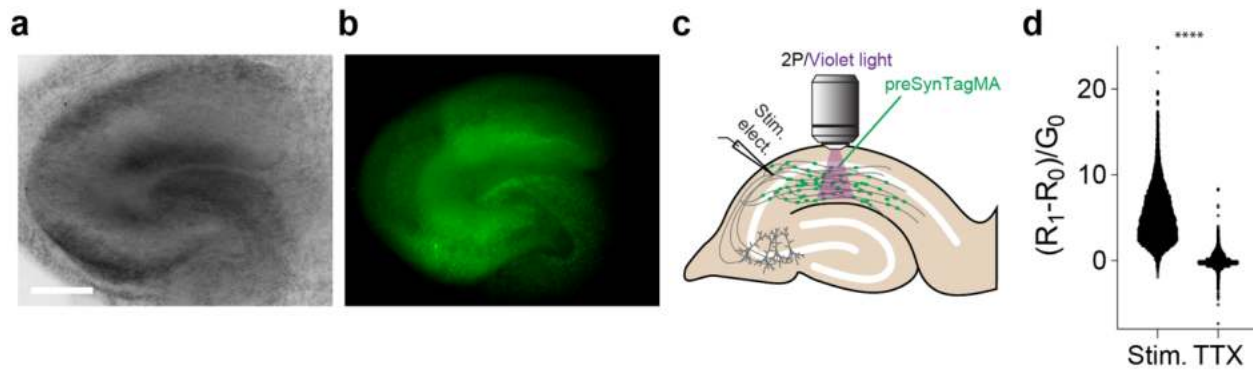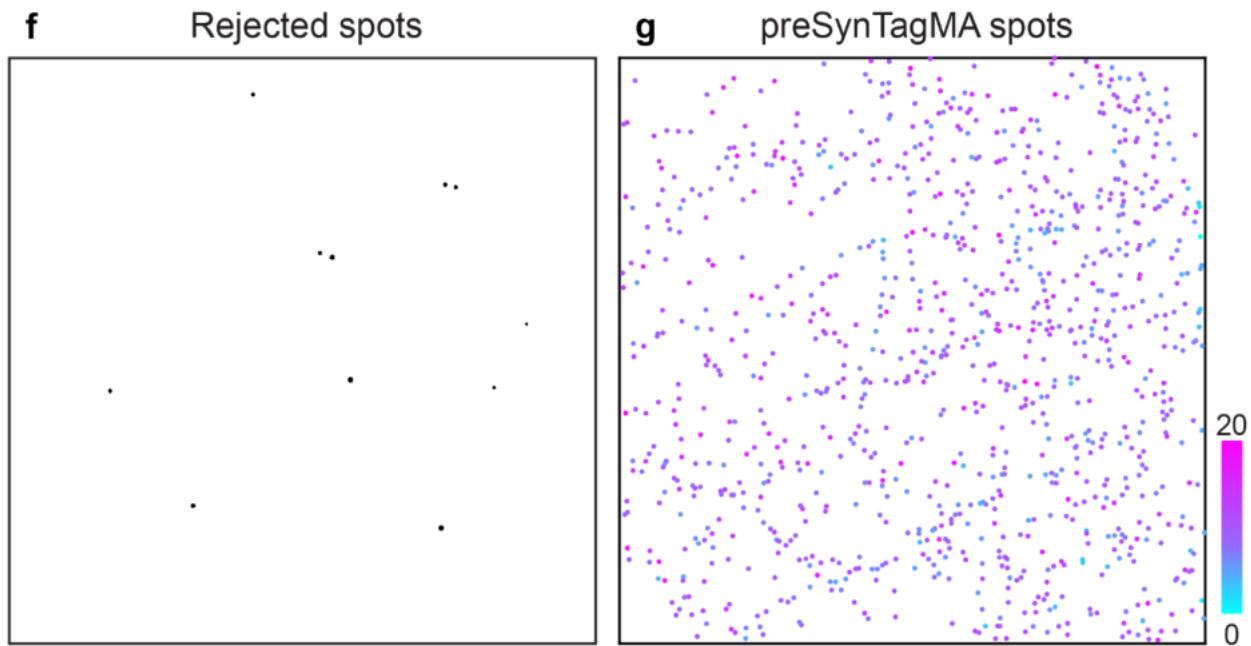
Supplementary Figure 3: Detection of active boutons in rat hippocampal slices. (a) Bright field image of a rat organotypic hippocampal slice microinjected with AAV2/9-syn-preSynTagMA in the CA3 area. **(b)** Wide-field fluorescent image showing preSynTagMA signal. **(c)** Scheme showing stimulus electrode and imaging area in *stratum radiatum*. Axon fibers were either stimulated with a glass monopolar electrode or silenced with TTX (1 μM). The electrode tip was placed in *stratum radiatum* to deliver an electrical stimulus to Schaffer collateral axons (0.2 ms pulses at 50Hz during 500 ms). Violet light (200 ms, 16 mW mm^{-2}) was delivered with a 1 s delay relative to stimulus. This paired protocol was repeated 25 times at 0.1 Hz. **(d)** Violin plot of bouton conversion [$(R_1 - R_0/G_0)$] in stimulated (5.13 ± 0.02; n= 12887 boutons, 5 slices) vs TTX groups (0.02 ± 0.01; n = 10193 boutons, 3 slices). A Mann Whitney test showed stimulated vs. TTX groups were significantly different (****p<0.0001). **(e)** Two-photon z-stacks before (green, acquired at 980 nm) and after (red, acquired at 1040 nm) the electrical stimulus protocol paired with violet light was repeatedly applied. **(f)** Automated analysis using SynapseLocator. Green spots with high red fluorescence at baseline (R_0) were rejected. **(g)** Analysis of all spots with low R_0. Scale bars: 500 μm (a,b), 25 μm (e-g).

142
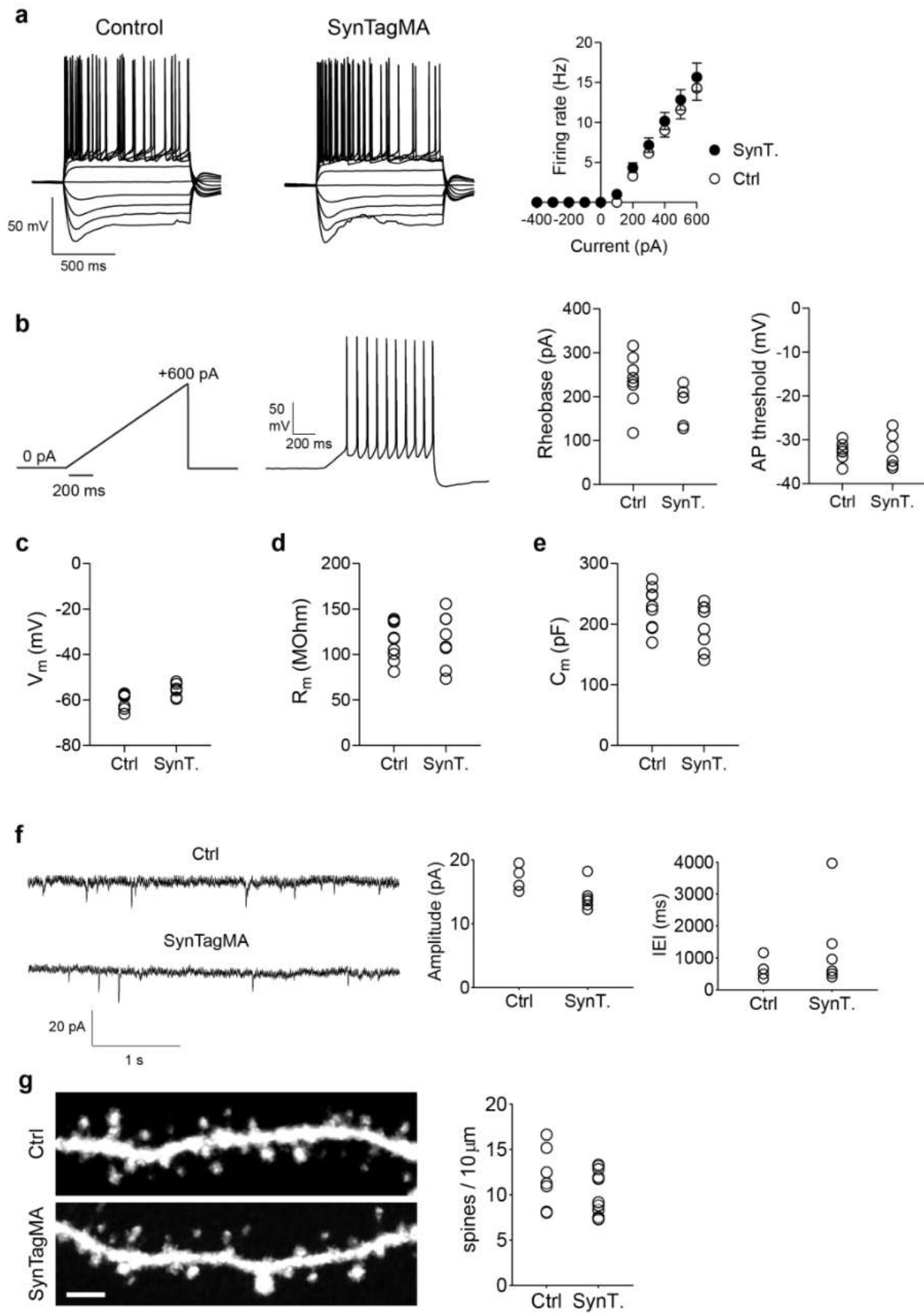
Supplementary Figure 4: Properties of SynTagMA-expressing neurons. **(a)** *Left,* example of voltage responses of

CA1 pyramidal neurons expressing either mCerulean (Ctrl, n = 6 neurons, 6 slices) or mCerulean and postSynTagMA

(SynT., n = 7 neurons, 7 slices) elicited by current steps from -400 pA to +600 pA (1 s duration, 0.067 Hz). *Right,* plot showing mean firing rate during voltage steps (mean ± SEM). **(b)** Current ramp (1 s duration from 0 to +600 pA) and example response of a SynTagMA-expressing neuron used to determine the rheobase and action potential (AP) threshold. Rheobase of SynTagMA-expressing neurons was not different from mCerulean controls (Ctrl: 235.2 ± 21.4 pA, n = 8 neurons; SynT: 183.2 ± 17.4 pA, n = 6; p = 0.108, Mann-Whitney test). AP threshold of SynTagMA-expressing neurons was not different from mCerulean controls (Ctrl: -32.8 ± 0.74 mV, n = 8 neurons; SynT: -32.4 ± 1.6 mV, n = 6, p = 0.80, two-tailed Student's t test). **(c)** Resting membrane potential (Vm, Ctrl: -59.9 ± 1.1 mV, n = 9 neurons; SynT: -55.7 ± 1.3 mV, n = 6; p = 0.088, Mann-Whitney test). **(d)** Membrane resistance (Rm) (Ctrl: 114.2 ± 6.9 MΩ, n = 9 neurons; SynT: 115.8 ± 10.2 MΩ; n = 8, p = 0.90, two-tailed Student's t test). **(e)** Membrane capacitance (Cm) (Ctrl: 227 ± 12 pF, n = 9 neurons; SynT: 197 ± 13 pF, n = 8; p = 0.105, two-tailed Student's t test). **(f)** Representative miniature AMPA receptor-mediated postsynaptic currents (mEPSCs) from CA1 pyramidal cells voltage clamped at -70 mV in the presence of CPPene, picrotoxin and tetrodotoxin. Mean mEPSC amplitude was 17.1 ± 1.0 pA for control neurons (n = 4) and 14.2 ± 0.9 pA (n = 6) for SynTagMA-expressing neurons (p = 0.067, Mann Whitney test). Inter-event intervals were 667 ± 176 ms for control neurons (n = 4) and 1314 ± 553 ms (n = 6) for SynTagMA-expressing neurons (p = 0.48, Mann-Whitney test). **(g)** Sections of CA1 oblique dendrites expressing mCerulean alone (above) or mCerulean and SynTagMA (below). Scale bar is 5 µm. Mean spine density per 10 microns (± SEM) was 11.8 ± 1.2 for mCerulean-expressing neurons (7 neurons, 3 slices, 2896 spines) and 10.1 ± 0.7 for mCerulean and SynTagMA-expressing neurons (11 neurons, 5 slices, 3946 spines; p = 0.42, Mann-Whitney test).

a | hSyn | PSD95.FingR | CaMPARI2_F391W_L398V | ZF | KRAB(A)

b acute slice — 488nm

c acute slice — 980nm

d organotypic slice culture

e | hSyn | PSD95.FingR | CaMPARI2_F391W_L398V

f organotypic slice culture

g 6x shorter exposure
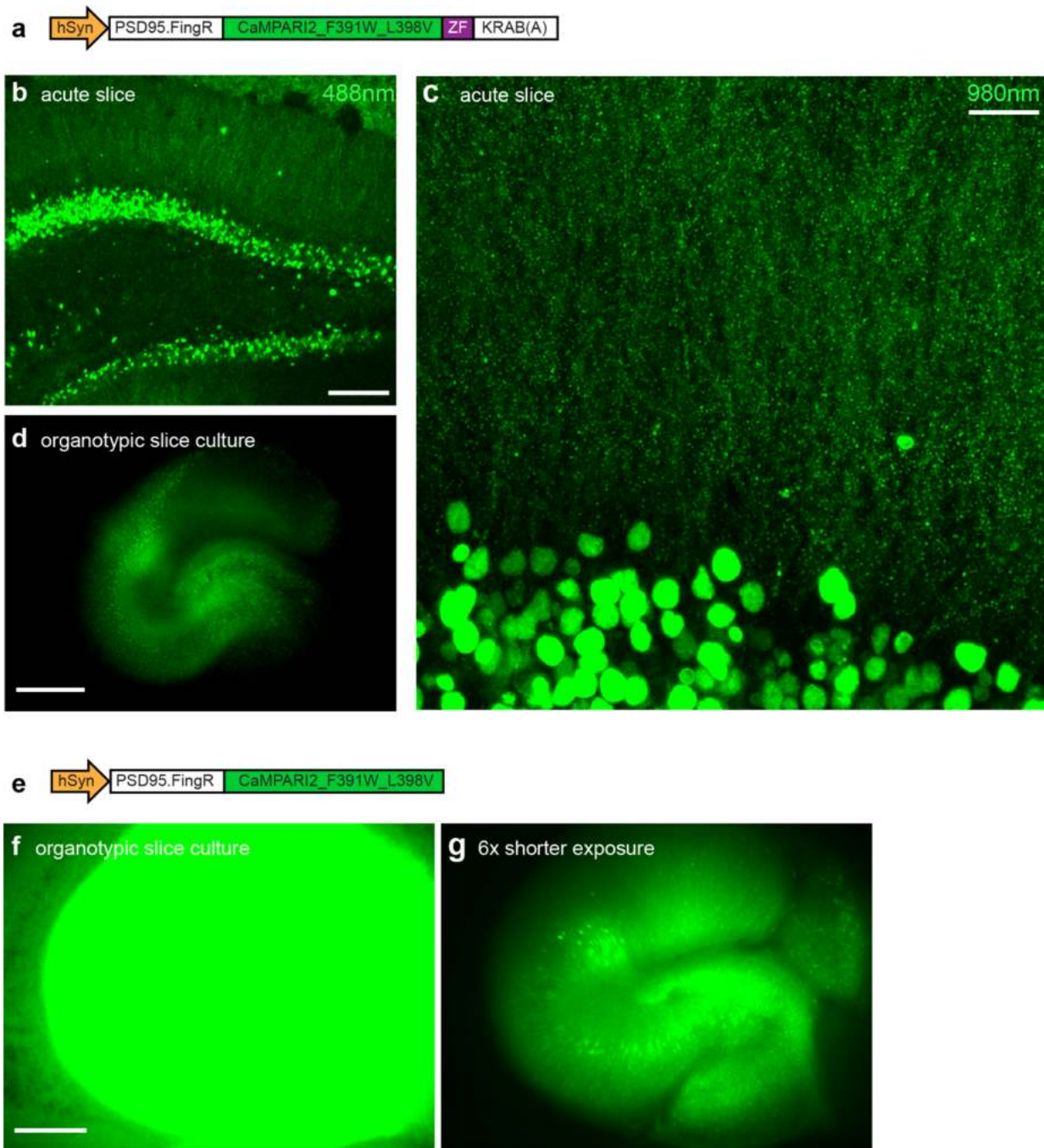
Supplementary Figure 5: Effect of autoregulatory elements on postSynTagMA expression level. (a) Scheme of postSynTagMA containing autoregulatory elements. **(b)** Confocal image of acute hippocampal slice from mouse expressing AAV9-postSynTagMA for two weeks. **(c)** Two-photon image (980 nm excitation) of dentate granule neurons expressing AAV9-postSynTagMA in an acute slice. Note dense, punctate expression in the molecular layers**. (d)** Organotypic rat hippocampal slice culture 4 days after AAV9-mediated transduction with postSynTagMA. **(e)** Scheme of postSynTagMA without autoregulatory elements. **(f)** Organotypic rat hippocampal slice culture 4 days after AAV9-

mediated transduction with PSD.95-FingR_CaMPARI2_F391W_L398V (no ZF-KRAB). Virus titer and applied volume were matched to d). **(g)** Same culture, image was de-saturated by six-fold reduction in exposure time. Scale bars: 100 (b), 20 (c), 500 microns (d, f, g).
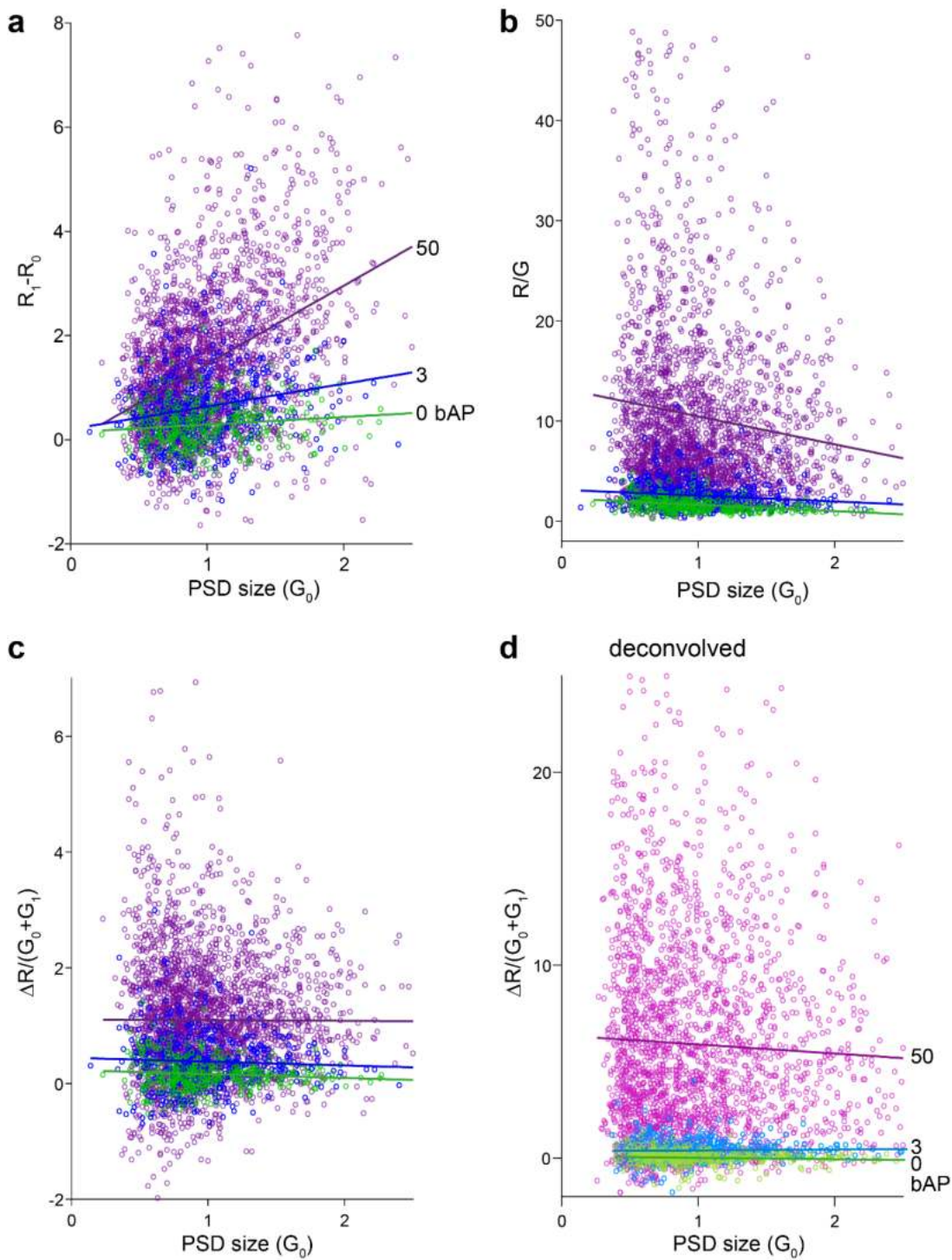
Supplementary Figure 6: Comparison of conversion metrics vs synapse size (a) Absolute change in red fluorescence ($\Delta R = R_1 - R_0$) plotted against PSD size (G_0). Slope of linear regression: 0.146 (0 bAP); 0.435 (3 bAP); 1.50

(50 bAP). Magenta: 50 bAPs. Blue: 3 bAPs. Green: 0 bAP. **(b)** Ratio after photoconversion (R_1/G_1) versus PSD size.

Slope of linear regression: -0.63 (0 bAP); -0.59 (3 bAP); -2.8 (50 bAP). **(c)** $\Delta R/(G_1 + G_0)$ versus PSD size. Slope of linear

regression: -0.068 (0 bAP); -0.066 (3 bAP); -0.011 (50 bAP). **(d)** Same analysis as in **c**), but on deconvolved data

(AutoQuant X3). Note improved separation between stimulated and non-stimulated synapses. Pink: 50 bAPs. Light blue: 3

bAPs. Light green: 0 bAP.
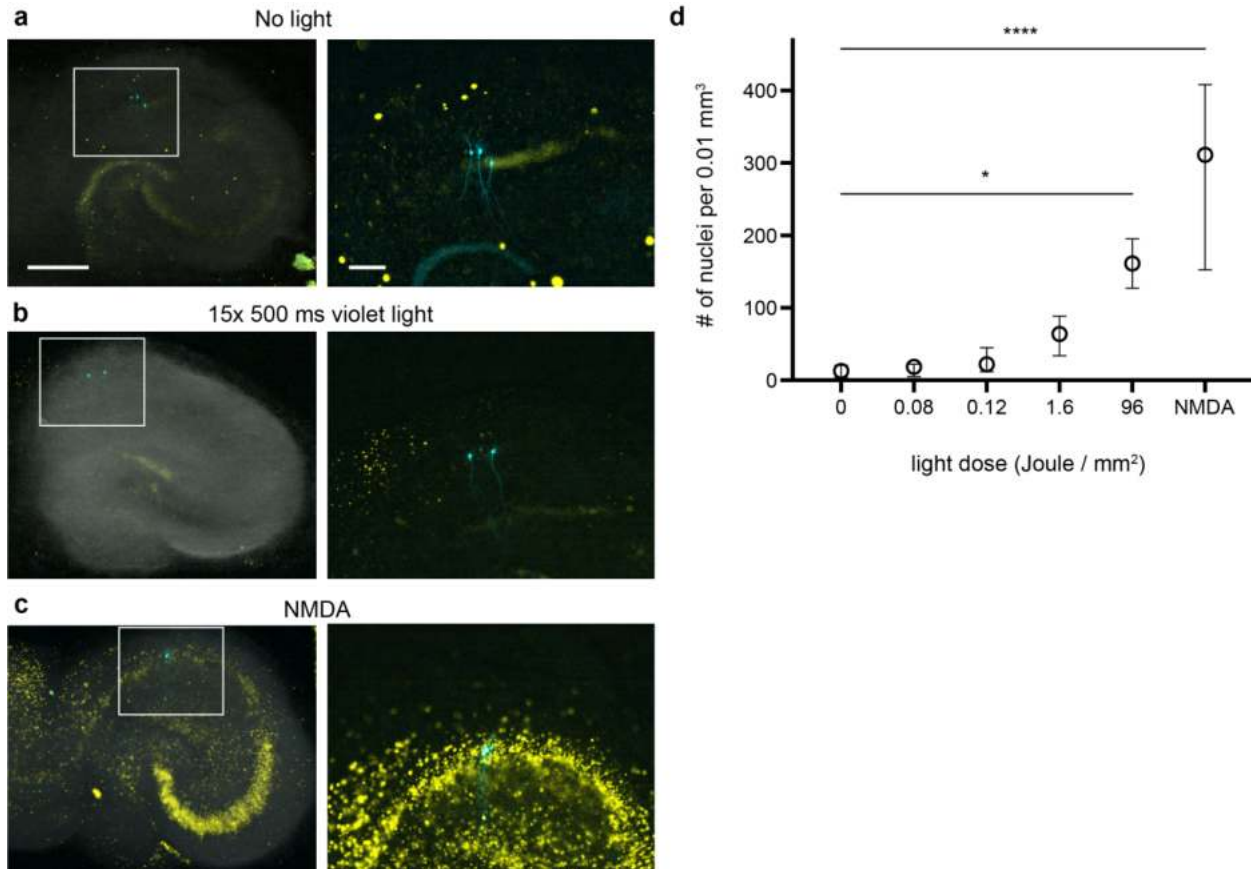
Supplementary Figure 7: Assessing photodamage caused by violet light and NMDA in organotypic cultures by propidium iodide (PI) staining. **(a-c)** Representative images of hippocampal slice cultures following incubation with propidium iodide, which enters and stains damaged cells. Overlay of Dodt-contrast image (grayscale), propidium iodide fluorescence (yellow) and cerulean-expressing CA1 pyramidal cells (cyan). Scale bars 500 µm and 200 µm, respectively. **(a)** Slice culture kept in the dark. **(b)** After exposure to our typical photoconversion protocol (15 x 500 ms light pulses, 395 nm, 16 mW mm^{-2}) resulting in a cumulative light dose of 0.12 J mm^{-2}. **(c)** After exposure to 1 mM NMDA for 1 hour. **(d)** Quantification of results vs light dose. Data are plotted as median and interquartile range. A one-way ANOVA followed by

Dunnett's multiple comparisons to the no light condition was used. No light (n = 5 slices) vs 0.08 J mm^{-2} (n = 3 slices, p > 0.999); No light vs 0.12 J mm^{-2} (n = 5 slices, p = 0.99); No light vs 1.6 J mm^{-2} (p = 0.74, n = 3 slices); No light vs 96 J mm^{-2} (*p < 0.0461, n = 2 slices); No light vs NMDA (**** p < 0.0001, n = 4 slices).

a G_0 fluorescence
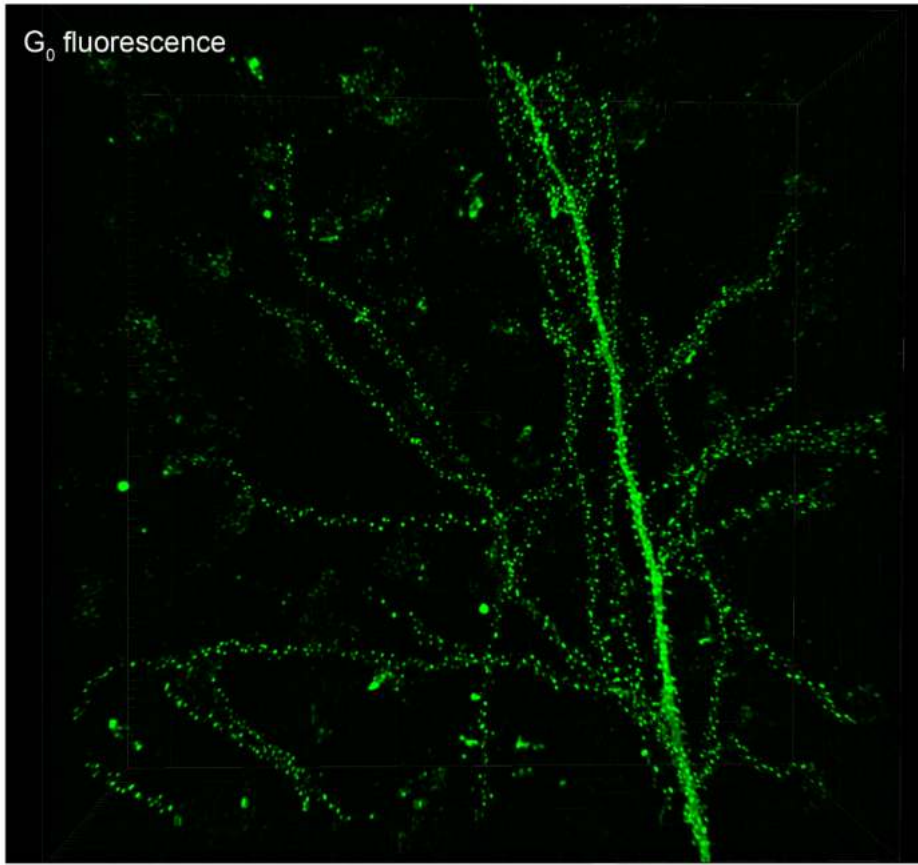
b R_0 fluorescence
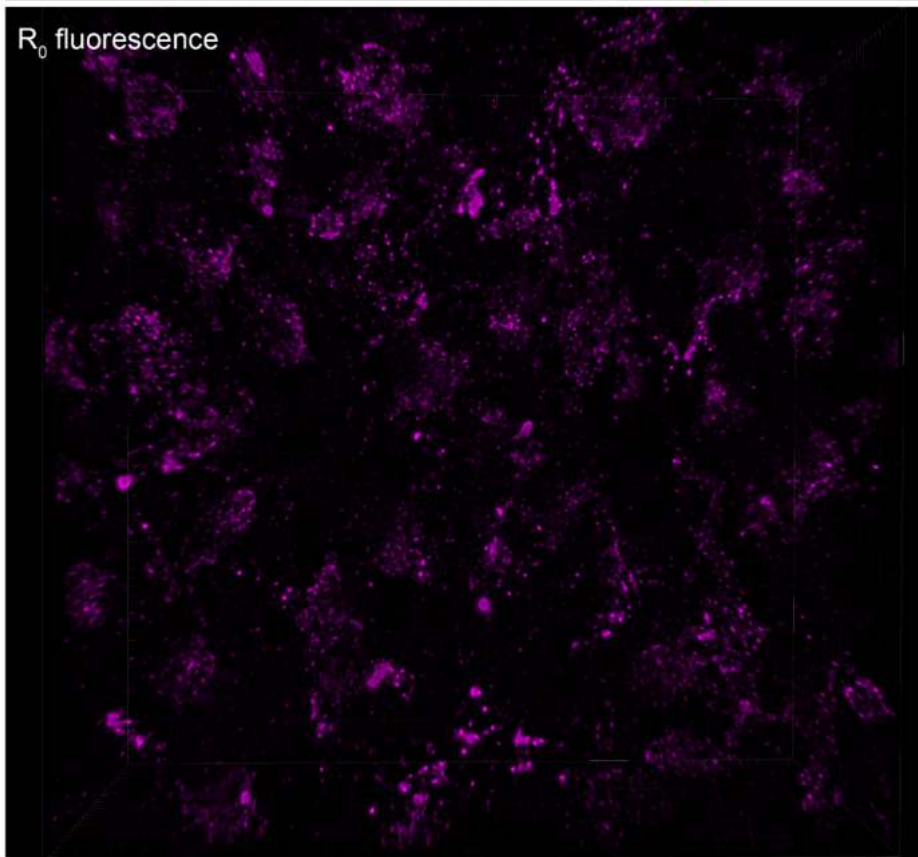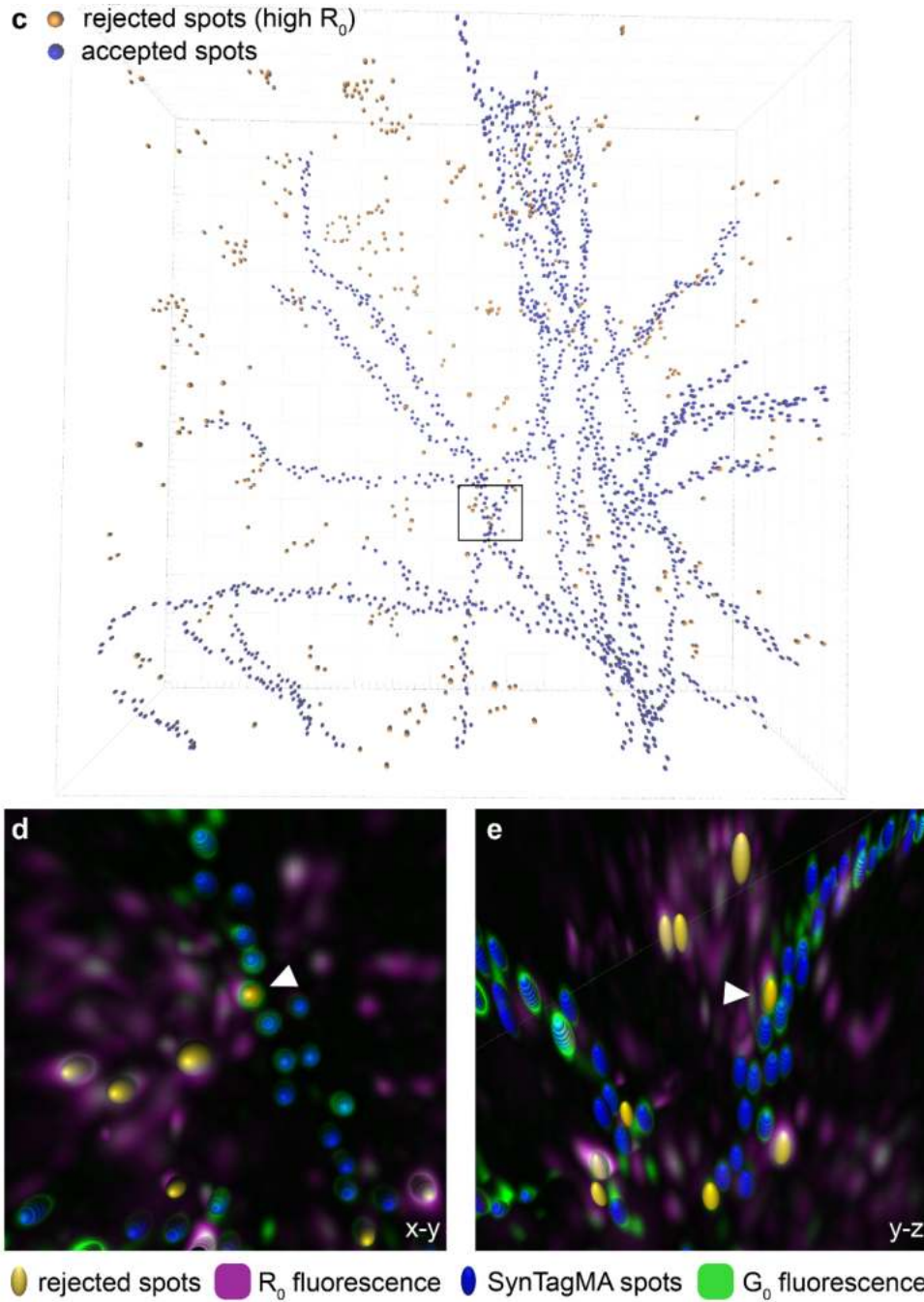
Supplementary Figure 8: Exclusion of non-SynTagMA objects (spots) by their red fluorescence. **(a)** SynTagMA-expressing pyramidal neuron before stimulation (G_0). Dendritic branches in *stratum lacunosum-moleculare*, 980 nm excitation, 150 x 150 x 60 μm volume. **(b)** Corresponding view of red autofluorescence (R_0) at 1040 nm excitation. **(c)** Spot detection in Imaris based on G_0. Spots were subsequently classified according to their red fluorescence before simulation (R_0). Spots with low R_0 are SynTagMA-labeled spines (blue) while spots with high R_0 (orange) were primarily detected in autofluorescent patches outside the labeled neuron. High R_0 spots were rejected from further analysis. 3D images in Imaris (**a-b**), scale in **c**. **(d, e)** Zoomed-in views (rotated) of the area denoted by black square in a). White arrow

points to a likely SynTagMA signal (green fluorescence) that due to its proximity to red autofluorescence has been rejected (yellow spot). Even in this problematic region, the large majority of auto-detected spots were sufficiently distant from autofluorescence to be analyzed (blue spots). Some small green spots escaped detection by the algorithm (no blue/yellow marker).
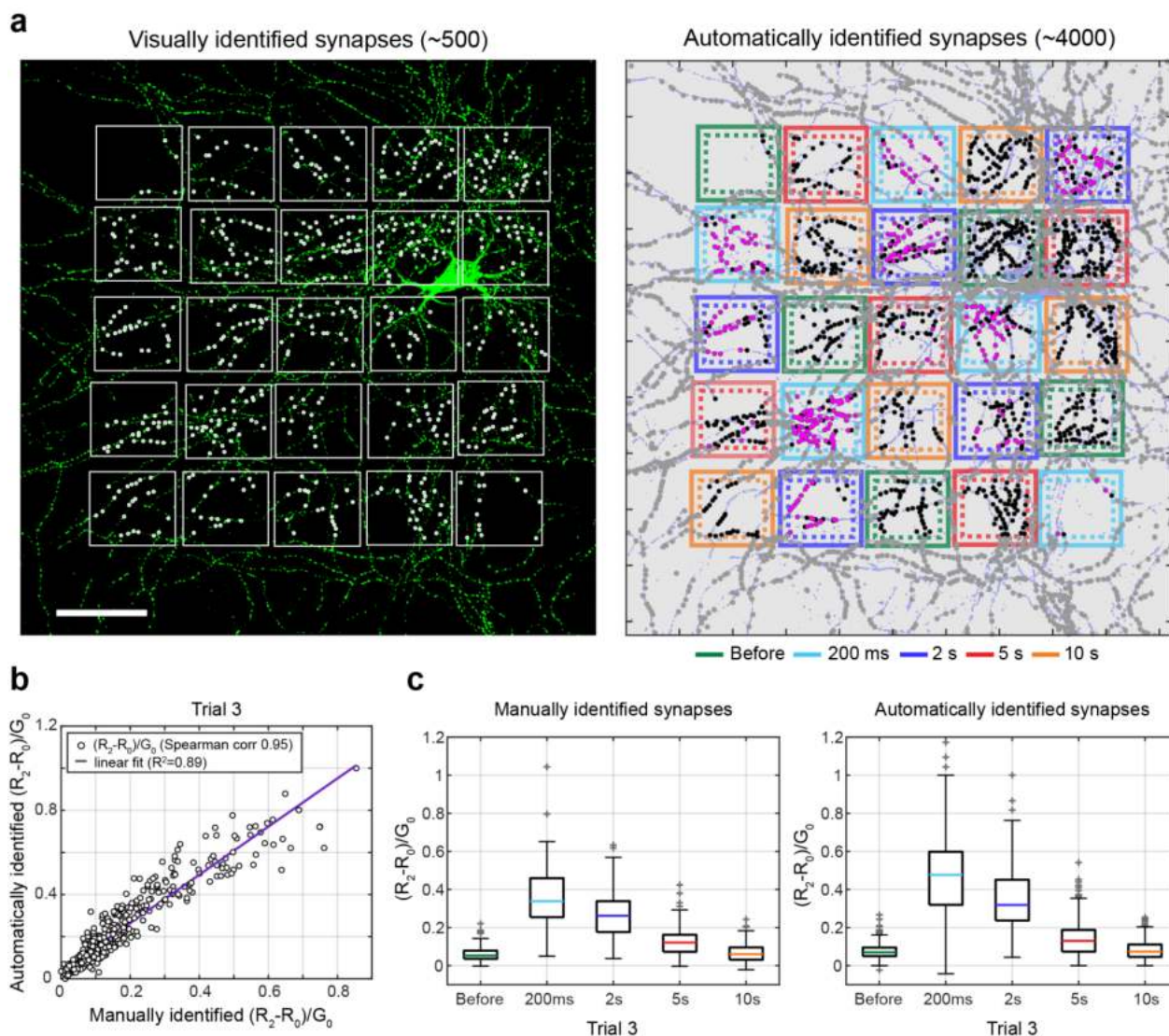
Supplementary Figure 9: Comparison of analysis results with manual identification of ROIs vs analysis performed with SynapseLocator. **(a)** Full-field view (maximum projection) of the same cultured hippocampal neuron expressing preSynTagMA as shown in Fig. 2 with overlaid photoconversion grid. Dashed lines are borders set for including automatically identified boutons in a group. Left: Regions of interest (~500 ROIs) were selected and manually curated using Fiji (white dots are ROIs). Right: Colored and grey dots indicate (ROIs) identified and analyzed by SynapseLocator. Grey spots were outside the illuminated fields and not quantified. Magenta spots: $(R_2 - R_0)/G_0 > 0.25$. Black spots: $(R_2 - R_0)/G_0 < 0.25$. Scale bar is 50 μm. **(b)** The photoconversion values from Trial 3 (see Fig. 2) from the

group of boutons that were both manually and automatically identified plotted against each other (n = 413 boutons). **(c)**

Photoconversion $(R_2 - R_0)/G_0$ vs timing delay for the same data manually identified (right, n = 583 boutons) or identified

and analyzed using SynapseLocator (left, n = 1059 boutons). Boxes: Median, 25% and 75% percentiles and whiskers the

1.5 interquartile interval. Grey + are outliers. The data distribution was not normal within any group (D'Agostino & Pearson

test, $P < 0.0001$). A non-parametric Kruskal-Wallis test followed by Dunn's multiple comparisons was used. Before manual

vs before automatic (p = 0.46), 200 ms manual vs 200 ms automatic (p = 0.1184), 2 s manual vs 2 s automatic (p =

0.0503), 5 s manual vs 5 s automatic (p > 0.999), 10 s manual vs 10 s automatic (p = 0.3644).
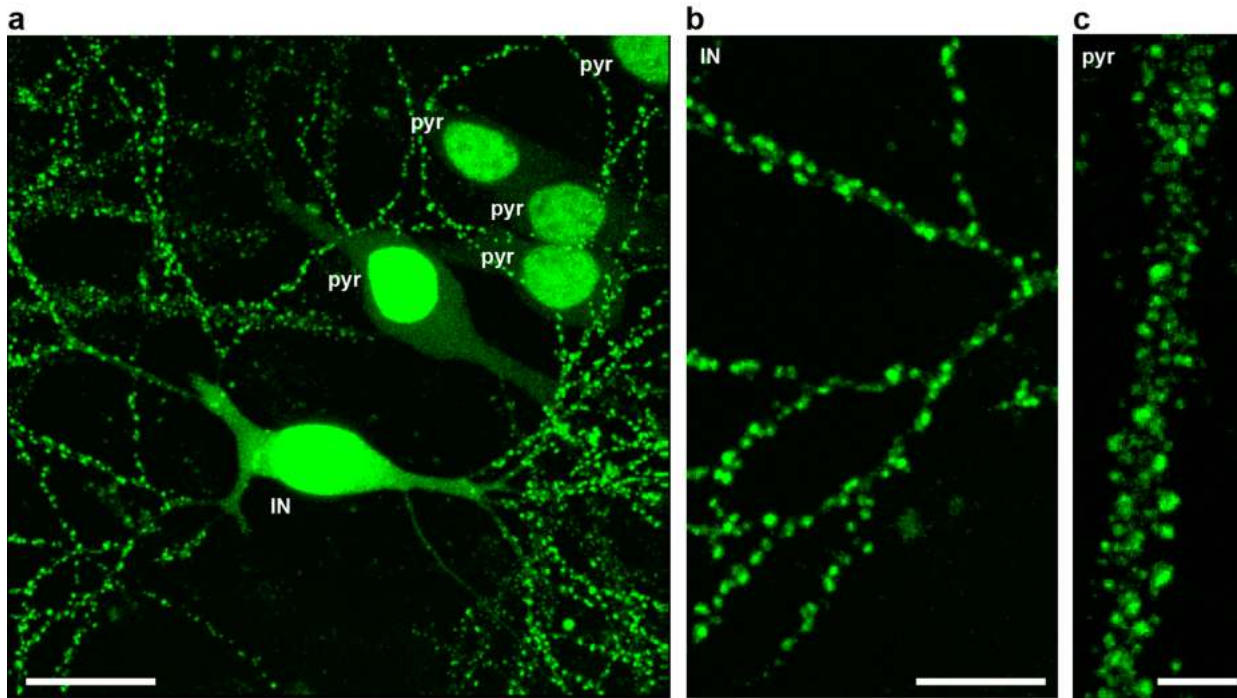
Supplementary Figure 10. PostSynTagMA identifies excitatory synapses on interneurons. **(a)** Two-photon

image (maximum intensity projection) showing expression of postSynTagMA in an interneuron (IN) next to five pyramidal

CA1 cells (pyr). Scale bar 20 μm. **(b)** Detail of postSynTagMA puncta in smooth interneuron dendrite (IN) and **(c)** spiny

pyramidal neuron dendrite (pyr). Scale bars a) 20 μm b) 10 μm c) 5 μm.
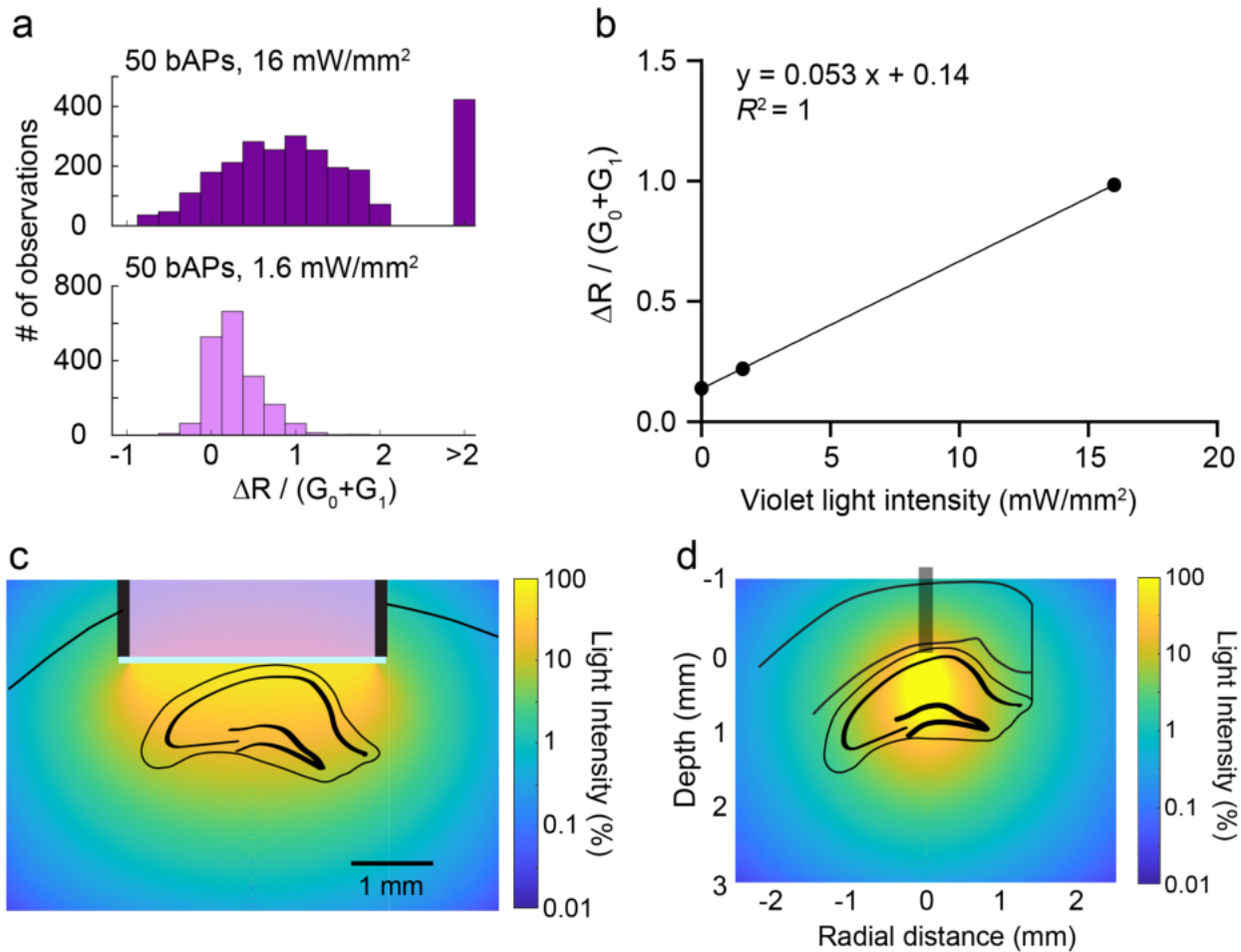
Supplementary Figure 11. Intensity and depth-dependence of photoconversion. (a) Histogram of photoconversion for 50 bAPs with 16 mW mm^{-2} (as in Fig. 4c) and 50 bAPs with 1.6 mW mm^{-2}. **(b)** Photoconversion ($\Delta R/(G_0+G_1)$) shows linear non-proportional relationship to violet light intensity. Median values taken from (a) with the 0 bAP condition shown in Fig. 4c. Black line represents the linear fit to the data. **(c)** Simulation of violet light illumination (405 nm) through a deep cranial window using an 0.8 NA objective (see Fig. 7). Note homogenous intensity throughout hippocampus for a given depth. **(d)** Simulation of violet light injection (10 mW) via 200 μm diameter light fiber with 0.22 NA. Depth attenuation is similar to the cranial window situation, but the intensity drops off more steeply with radial distance (xy).

Discussion

1.0 The role of TRPM4 in hippocampal synaptic function

In this project, I was interested in the role of TRPM4 in hippocampal synaptic transmission. I hypothesized that TRPM4 activation occurs downstream from NMDA receptors and facilitates further depolarization and calcium influx (Figure 9B). I found that TRPM4 does not contribute to basal synaptic transmission at the CA3->CA1 Schaffer collateral synapse in healthy mice. However when EAE is induced, TRPM4 increases synaptic transmission in acute slices made from wild type but not TRPM4$^{-/-}$ mice.

In situ hybridization for TRPM4 in the brain indicate mRNA transcripts in the CA1 region of the hippocampus (Fig. 9A). To confirm protein expression of TRPM4 in the hippocampus, I tested four different antibodies, 3 commercial and 1 from the lab of Dr. Simard, in hippocampal brain slices from both wildtype and TRPM4$^{-/-}$ mice. In all instances, there were no clear differences between genotypes suggesting either that none of these antibodies effectively target TRPM4 or that the hippocampus does not express the channel at detectible levels. Unfortunately, the antibody used in the study from Schattling et al (2012), which was validated using the same TRPM4$^{-/-}$ mouse line, is no longer available. As these antibodies were nonspecific, I did not attempt immunohistochemistry in slices from EAE animals, which would potentially inform us on whether TRPM4 expression is upregulated in the hippocampus and where this upregulation occurs. Recently, a lab published a study in which a TRPM4-IRES-Cre line was created (Eckstein et al., 2020). Access to this line, would allow us to finally determine the expression pattern of TRPM4 not only in the hippocampus but in the entire brain. Distinguishing expression patterns in different cell types would be particularly illuminating for TRPM4 as it is reportedly expressed in neurons, astrocytes, microglia and microvasculature in the brain (Gerzanich, Kwon, Woo, Ivanov, & Marc Simard, 2018; Gerzanich et al., 2009; Kurland et al., 2016; Stokum et al., 2018).

It was unexpected that TRPM4 antagonists had no effect on calcium influx at the synapse or on EPSPs, particularly given that theta-burst LTP is impaired in TRPM4$^{-/-}$ animals (Menigoz et al., 2016). Although when comparing wildtype and TRPM4$^{-/-}$ mice, the authors also reported no change in basal transmission by measuring input/output curves, miniature excitatory postsynaptic currents, and AMPAR/NMDAR ratios. In my experiments I attempted to evoke large synaptic events to increase the likelihood of TRPM4 activation and under pharmacological conditions that might have unmasked a TRPM4 dependent effect. As outlined in the paper, there are a few explanations for the absence of a TRPM4 effect. The first being that there is no TRPM4 protein to antagonize or that we did not activate the channel. It is true that the channel reportedly desensitizes quickly (Nilius, Prenen, Janssens, Voets, & Droogmans, 2004), however this is based on single channel recordings and desensitization *in vitro* is likely modulated by factors like PIP$_2$, calmodulin and internal ATP levels (Nilius, Prenen, Janssens, et al., 2004; Nilius et al., 2005; Nilius, Prenen, Voets, et al., 2004). These factors could potentially be affected by washout from whole-cell recordings, but this does not explain the findings from calcium imaging experiments in which the cells were not patched.

In the hippocampus, calcium-activated nonspecific cation channels have been linked to neuronal burst firing. Most of these studies focus on the involvement of TRPC channels (Arboit et al., 2020; Knauer & Yoshida, 2019) but recent work in the entorhinal cortex indicates other channels like TRPM4 and not TRPC channels may support burst firing (Egorov et al., 2019). Additionally, the theta-burst LTP phenotype points to a role of TRPM4 in lowering the threshold for a postsynaptic neuron to spike or burst. By including QX-314 in the intracellular solution, which blocks voltage-gated sodium channels to prevent action potentials, we may have occluded the action of TRPM4 in action potential generation. However, our study sought to understand the role of TRPM4 in synaptic transmission rather than focusing on cell excitability. In the future it would be worthwhile to examine the role of TRPM4 in cell excitability.

As TRPM4 did not contribute to synaptic transmission in the healthy hippocampus, I hypothesized that perhaps TRPM4 only becomes significantly activated or TRPM4 expression is upregulated in a disease state like EAE. Indeed, TRPM4 is shown to be upregulated in the brain in EAE (Bianchi et al., 2018; Schattling et al., 2012) and in instances of brain injury (Gerzanich et al., 2009; J. M. Simard et al., 2006). In glutamate excitotoxicity assays, antagonism of TRPM4 or absence of the channel is protective against cell death (Bianchi et al., 2018; Schattling et al., 2012). I conducted the same experiments measuring EPSPs from acute slices prepared from wild type and TRPM4$^{-/-}$ mice at the acute stage of EAE. Glibenclamide but not 9-phenanthrol reduced the EPSP peak amplitude exclusively in wild type animals. Although the n-size for the 9-phenanthrol group is a bit low (n=4), it did not point towards a clear trend in any direction. The effect on EPSP amplitude by glibenclamide but not 9-phenanthrol suggests that I may have observed a specifically SUR1/TRPM4 effect rather than exclusively TRPM4. Glibenclamide has a 100-fold higher efficacy against the SUR1/TRPM4 channel than the TRPM4 channel alone (Woo et al., 2013). Due to the lack of available antibodies against TRPM4, I was not able to check for protein expression. To confirm the hypothesis that a SUR1/TRPM4 upregulation is responsible for the increase in synaptic transmission during EAE, a suitable antibody for TRPM4 must be developed or use of a labeled mouse line, such as the TRPM4-IRES-Cre line (Eckstein et al., 2020).

One caveat to these results is the difference in the temperature at which the recordings were conducted. TRPM4 activation is temperature dependent with open probabilities increasing above 30° C (Talavera et al., 2005). I conducted the experiments with slices from healthy animals at lower temperatures 23-25 °C and at 30-32 C° with slices from EAE animals. Optimally, additional experiments at higher temperature from healthy wild types with glibenclamide should be conducted.

2.0 Developing genetically-encoded tools for mapping neuronal and synaptic activity

In "Improved methods for marking active neurons", my co-authors and I developed and characterized the genetically encoded calcium integrator: CaMPARI2. Although CaMPARI1 is new category of sensor that allows the user to tag neurons that are active at a particular time, it has some shortcomings. CaMPARI1 suffers from modest photoconversion contrast and lost much of its signal following chemical fixation (Fosque et al., 2015). CaMPARI2 features improved brightness and better photoconversion contrast in comparison to CaMPARI1. A monoclonal antibody against the red species of CaMPARI2 and the addition of epitope tags to the CaMPARI2 sequence allows for reliable post-hoc analysis in fixed tissue. CaMPARI2 is a useful tool for tagging active neurons but as it is soluble in the cytosol it cannot indicate local calcium, for example at the synapse, as the photoconverted protein will diffuse away from the site of local calcium. In "Freeze-frame imaging of synaptic activity using SynTagMA", we created preSynTagMA by fusing CaMPARI2 to the vesicular protein synaptophysin and we created postSynTagMA by fusing CaMPARI2 to an intrabody against PSD-95, a postsynaptic scaffolding protein. preSynTagMA can be used to distinguish active from inactive axons and postSynTagMA can be used to generate, potentially iterative, maps of synaptic activity across the entire dendritic arbor. The beauty of these sensors is the possibility of decoupling imaging from behavior (i.e. the labeling period), which allows for high resolution imaging with a temporal resolution of approximately two seconds.

I will now remark in more depth on notable features of the sensors and their use. For the sake of clarity, I will use CaMPARI1 when I write specifically about the originally published sensor, CaMPARI2 when I write specifically about the newly developed sensor, and CaMPARI when describing features shared by both sensors. In a similar manner, I will use SynTagMA generally when describing features that apply to both preSynTagMA and postSynTagMA and otherwise I will use the specific naming.

2.1 A narrow window for photoconversion with the improved CaMPARI2

We originally fused CaMPARI1 to synaptophysin (sypCaMPARI) and found that it reliably reported

single APs as shown by the dimming of the sensor (CaMPARI is a reverse indicator) and repeatedly

pairing APs with violet light resulted in increased photoconversion. However, sypCaMPARI and

CaMPARI1 exhibit activity-independent photoconversion (Paper 2, Fig 1; Paper 3, figure 1). Through our

collaboration with the Schreiter lab, I helped to characterize the new CaMPARI2 in neurons. I first

characterized its decrease in fluorescence upon calcium binding by inducing increasing numbers of back-

propagating action potentials at the soma through a patch pipette (Paper 2, supplemental fig. 18). An

unusual feature of CaMPARI is its rather slow kinetics in comparison to other GECIs. The calcium-

dependent dimming peaks approximately 1 second after the stimulus and returns to baseline

approximately 3-15 seconds later. Next, I wanted to understand the relationship between CaMPARI

dimming and photoconversion. I hypothesized that the optimal photoconversion time would correspond

with the rapid millisecond timescale of calcium influx and clearing at the spine (Sabatini, Oertner, &

Svoboda, 2002) or it would fit with the kinetics of the sensor. I carefully tested my hypothesis by pairing

bAPs with 100 ms violet light (395 nm) at multiple delays relative to the bAPs in CaMPARI2 expressing

neurons. I found that the optimal photoconversion time corresponds to the peak of the CaMPARI timing

(Paper 2, supplemental figure 19). We confirmed these findings using a spatial light modulator device to

illuminate quadrants of a sypCaMPARI or preSynTagMA expressing neuron at different delays relative to

the stimulus (Paper 3, fig 2). We found that the optimal photoconversion time was also 1 second for

sypCaMPARI and preSynTagMA but the temporal window for sypCaMPARI extended up to 10 seconds

after the stimulus while preSynTagMA exhibited a much narrower temporal window between 200 ms to

2 seconds after the stimulus. Although a few seconds saved sounds trivial, in terms of activity in the

brain particularly related to behavior, this is a huge improvement. Considering a behaving animal, ten

seconds of integrated neural activity is significantly more neuronal computational intensive period as

compared to two seconds of integrated neural activity.

2.2 Labeling active neurons: Immediate early genes versus CaMPARI2 and nuclear postSynTagMA

Active neurons can be monitored in real-time using GECIs or active neurons can be marked using immediate early genes (IEG) either as a label in fixed tissue or to drive expression of another protein like a calcium sensor or an opsin. IEGs, like *Fos* and *Arc,* are transiently expressed in neurons following neural activity. Their expression requires calcium influx and activation of downstream signaling including the calcium/calmodulin-dependent protein kinases, calcineurin, and Ras-mitogen-associated protein kinase-mediated pathways (Yap & Greenberg, 2018). By using inducible genetic switches like the tetracycline-controlled trans-activator and Cre recombinase under the control of an IEG promotor, it is possible to label neurons that were active during a particular time period. Numerous studies using these methods have been published and have led to groundbreaking discoveries on memory formation, consolidation, separation and extinction in multiple brain areas (Josselyn & Tonegawa, 2020; Tonegawa, Morrissey, & Kitamura, 2018). However, these studies have relatively poor temporal precision. The activity-dependent expression window of *cFos* is approximately 6 hours (unpublished results, Dr. Lamothe-Molina). Inducible systems, like Tet-tag, rely on delivery of tetracycline usually in food/water or by intra-peritoneal injection and tetracycline is also slow to metabolize. These factors extend the potential activity-dependent labeling window to upwards of 12-24 hrs (unpublished results, Dr. Lamothe-Molina). This means that labelling will inherently include behaviors outside of the behavior being studied. CaMPARI2, on the other hand, can afford precise (within 2 seconds before the violet light) labeling of cells active during a particular behavior. We showed that CaMPARI2 can specifically label neurons in the primary visual cortex that are tuned to a particular grating direction.

A drawback to labeling with CaMPARI2 is that the replacement of photoconverted red protein with fresh green protein (i.e. turnover) is approximately 3 days. This limits the frequency of potential re-labeling experiments. A new reversible version of CaMPARI, reversibly switching CaMPARI (rsCaMPARI),

is available. With rsCaMPARI, the active neurons are photo-switched between bright and dark states rather than converted from green to red (Sha, Abdelfattah, Patel, & Schreiter, 2019). Although potentially useful, rsCaMPARI is still a reverse calcium indicator and so when a neuron is active, it will be dim. But the photoswitch label for active neurons is also dark. This will make distinguishing between spontaneously active and labeled neurons difficult. Additionally, alignment of dark or absent signal would be near impossible.

postSynTagMA can be used to mark active neurons similar to CaMPARI2, in addition to marking postsynapses. Our targeting strategy for postSynTagMA uses PSD95.FingR, an intrabody that specifically binds to PSD95 (Gross et al., 2013) and its expression is regulated by a zinc-finger-KRAB(A) sequence. This sequence can drive sequestration of excess protein in the nucleus and suppress further transcription (Wang et al., 2014) (Paper 3, fig. 3). Indeed, postSynTagMA expresses at the postsynapse and is enriched in the nucleus. This serendipitously created an additional labeling compartment that we hypothesized might represent neural activity similar to that measured using untargeted GECIs. Indeed, we found that postSynTagMA can selectively label neurons that were active during a reward presentation and these neurons also experienced high calcium transients during the reward presentation (Paper 3, fig. 7). Unlike CaMPARI2, postSynTagMA at the nucleus turns over with a time constant of 208 minutes (data not shown). Principally, overnight, the red protein should be replaced by fresh green protein and a new activity map can be generated. This turnover rate is a far better compromise and fits well with learning experiments that occur over days, like water maze or reward learning.

2.3 Using preSynTagMA to label active axons

An early approach to imaging at the presynapse used synaptopHluorin whose fluorescence reports vesicular exocytosis (neurotransmitter release) and vesicular recycling (Miesenböck, De Angelis, &

Rothman, 1998). Neurotransmitter sensors for glutamate, dopamine, serotonin and acetycholine make it possible to image release events at single synapses, however these sensors suffer similar limitations as those I described earlier for calcium imaging (Helassa et al., 2018; Jing et al., 2018; Marvin et al., 2019; Patriarchi et al., 2018; Wan et al., 2020). A new sensor, Synaptozip, is genetically encoded "bait" sequence targeted to the vesicular lumen that upon vesicle exocytosis, the bait is available and can specifically bind with a fluorescently labeled added peptide, called Synbond (Ferro et al., 2017). Synaptozip signal accumulates indiscriminate to the temporal dynamics of the presynaptic activity. On the other hand, by timing violet light with the activity of interest, preSynTagMA can report an integral of activity at the bouton with temporal control. PreSynTagMA can be used to distinguish between active and inactive axons (Paper 3, supplemental fig. 1) and potentially differences between individual boutons (Paper 3, supplemental fig. 3). Axonal activity is important for neural computations and tuning to certain stimuli (M. Howe et al., 2019; M. W. Howe, Tierney, Sandberg, Phillips, & Graybiel, 2013; Sun, Tan, Mensh, & Ji, 2016). Plasticity of axonal activity is an important feature in learning and preSynTagMA could be used to map activity iteratively. The time constant for preSynTagMA turnover is 249 minutes and so similar to nuclear postSynTagMA, remapping is feasible the following day.

2.4 Distinguishing active synapses from inactive synapses with postSynTagMA

The propagation of an action potential in the axon is unidirectional and although there may be variability in levels of photoconversion between boutons on an axon relating to the composition of VGCCs between boutons, we expect that if an axon experienced an AP it will propagate through all boutons. In contrast, a postsynaptic neuron receives input from many different axons that will result in significantly different amounts of calcium influx at the postsynapse. As back-propagating action potentials (bAPs), in the presence of synaptic blockers, should principally elevate the amount of calcium evenly across the cell, I paired 0, 3, and 50 bAPs with violet light. I showed that postSynTagMA can reliably report increasing amounts of calcium at single synapses (Paper 3, fig. 4). Using the same pairing

protocol (50 bAPs, 15 repeats) but decreasing the violet light intensity by 10-fold revealed a linear

relationship between violet light intensity and the amount of photoconversion (Paper 3, supplemental

fig. 11).

Interestingly, I observed variability in the photoconversion values between synapses experiencing,

presumably, similar bAP-driven calcium influx. Pursuing this question, I repeated the 50 bAPs

experiments and imaged the entire dendritic tree. I found that photoconversion attenuates in a very

similar manner as the reported using electrophysiological dendritic recordings and using calcium

imaging (Colbert, Magee, Hoffman, & Johnston, 1997; Golding, Kath, & Spruston, 2001). I also confirmed

the same attenuation by imaging individual synapses across the dendritic tree using GCaMP7b (Paper 3,

fig. 5). Although not a new finding, this is one of the first reports of bAP attenuation including the more

thin and oblique dendrites and specifically at all synapses. However, distance from the soma does not

entirely explain variability in photoconversion as the differences are also visible between neighboring

synapses. The composition of VGCCs can vary between synapses (Bloodgood & Sabatini, 2007, 2008;

Yasuda, Sabatini, & Svoboda, 2003) and ER calcium release or uptake at individual synapses may be an

explanation for the observed variability (Holbro, Grunditz, & Oertner, 2009). This highlights a utility of

postSynTagMA for revealing subtle differences between synapses that would be difficult and exhaustive

using traditional spine-by-spine calcium imaging.

2.5 Generating synaptic activity maps with postSynTagMA

There are a handful of existing methods for mapping synapses or monitoring synaptic activity. The

GFP-reconstitution across synaptic partners (GRASP) method uses split GFP tethered to the pre and

post-synapse and only when both are in close proximity, i.e. make a synapse, will the GFP reconstitute

and fluoresce. The method was first demonstrated in drosophila and nematodes, then improved for

mammalian systems (mGRASP), and more recently an enhanced dual GRASP (eGRASP) was published,

which enables labeling of two different presynaptic partners (in cyan and yellow) projecting onto the same postsynaptic partner (Choi et al., 2018; Feinberg et al., 2008; J. Kim et al., 2012). Although these methods have revealed insights into synaptic level connectivity during memory formation, they are purely anatomical. Reports from our lab and the lab of Dr. Simon Wiegert have shown potential toxicity and an increase in synapse number over time when using GRASP methods. This begs the question of whether these tools not only report anatomy but also alter it. We found no alterations in synaptic transmission and spine number between SynTagMA expressing cells and controls (Paper 3, supplemental fig. 4).

Calcium imaging at individual synapses can link anatomy and function but, in intact tissue, we are limited to a small field of view and only a few of the thousands of synapses on a neuron are actually probed. Using postSynTagMA it is possible to visualize the "where" of all active synapses at a moment in time (the labeling window). When using subthreshold activity (i.e. not driving the postsynaptic neuron to spike), we can photoconvert and specifically label the postSynTagMA synapses recruited by the stimulus (Paper 3, fig. 6). The postSynTagMA turnover rate is approximately 30 minutes; markedly faster than preSynTagMA, nuclear postSynTagMA and CaMPARI2. Indeed, this limits the available time to image the generated postSynTagMA map however, it is possible to relabel the same synapses again. This opens up the possibility to follow the stability of a synaptic map over time, particularly under conditions that may drive plasticity.

An ultimate application of postSynTagMA is *in vivo* applications. We demonstrated the basic utility of imaging and photoconversion of postSynTagMA in an anesthetized mouse (P3 Fig 7). However, a limitation for work *in vivo* includes the potential for bAP invasion of the dendrite to interfere with synaptic calcium; resulting in a fully photoconverted dendritic tree. To truly understand this interference, further experiments *in vivo* are necessary. I hypothesize that there may be some "wiggle"

room that allows for the occasional coincident bAP and synaptic calcium influx. Recall that in figure 4 of paper 3, I tested the amount of photoconversion to 0, 3 and 50 bAPs. However, the total number of labeled bAPs is actually higher as the pairing of bAPs to violet light was repeated 15 times in each condition. Meaning that in the 3 bAPs group, the labeled neuron represents the integration of 45 bAPs and in the 50 bAPs group, 750 bAPs. The 3 bAPs group is well below the ceiling of maximum photoconversion. An additional point is that the nonlinear calcium influx driven by NMDARs at the spine may result in stronger photoconversion at the spine than from bAP invasion alone as the coincident calcium from an NMDA-dependent EPSCaT and a bAP is summed (Nevian & Sakmann, 2004).

Even if single synapse labeling without interference from dendritic calcium is not possible *in vivo*, there is considerable interest in dendritic integrative properties, which can be initiated by synaptic activity (G. J. Stuart & Spruston, 2015). I hypothesize that gradients of photoconversion in synapses along a converted dendrite could potentially point towards cooperativity among synapses. Some studies using spine-by-spine imaging *in vivo* have shown synaptic clustering and dendritic and synaptic segregation of information (Frank et al., 2018; Iacaruso, Gasler, & Hofer, 2017; Kerlin et al., 2018; Scholl, Wilson, & Fitzpatrick, 2017). Modeling studies attempt to explain these observed phenomena in a larger system and postSynTagMA may be able to experimentally test modeling studies, particularly those that are interested in how memories are linked across time in both synapses and neuronal populations (Kastellakis, Silva, & Poirazi, 2016)

2.6 Practical tips for working with SynTagMA and CaMPARI2

I would like to spend a bit of time describing the optimal conditions for CaMPARI and SynTagMA acquisition and analysis.

2.6.1 Acquisition

The fluorescent protein that CaMPARI and SynTagMA are built upon, mEos2, has photoswitching properties in addition to photoconversion. Simply put, mEos2 can be switched into a brighter state with a brief violet light illumination (Fosque et al., 2015). I recommend using a short violet light pulse prior to acquiring any image. It is important to remember that the optimal time to shine violet light is 200 ms to 2 seconds after the activity onset. Violet light outside of this window may label additional activity and smear out the temporal resolution. In my hands, I found 500 ms light pulses at a 1 second delay to give excellent results but depending on the experimental conditions, it may be useful to combine shorter or less intense pulses with more pairing events. This could potentially avoid a strong effect of bAP interference. I recommend whenever possible, to image a before and after photoconversion image. It can be difficult to set the laser intensity for the red species for the before image. I recommend increasing the laser power so that there is detectible excitation of the green species in the green channel by the longer 1040 nm wavelength.

The combination of slow kinetics and a decrease in fluorescence upon calcium binding are important factors to consider when working with CaMPARI or SynTagMA. Because the brain is always active, there is always a possibility that an expressing neuron will be spontaneously active (i.e. very dim) when the high-resolution image stack is being acquired. Luckily, because CaMPARI and SynTagMA are ratiometric indicators, the dimming equally affects both green and red species. To mitigate this issue, addition of synaptic blockers or imaging under conditions of low activity, like that observed uising ketamine/xylzine anesthesia, should be considered (Yang et al., 2020). In our experiments, we used two separate wavelengths to excite the green and red species of CaMPARI or SynTagMA (980 nm and 1040 nm, respectively). To improve acquisition speed and reduce motion artifacts, I recommend acquiring stacks by scanning an optical section first with one beam and switching to the other beam and scanning the same optical section. This approach also reduces the possible interference of spontaneous activity, i.e.

dimming, while acquiring stacks. Finally, post-hoc staining against both green and red species would potentially circumvent this issue as the antibody should reveal cells that were dark at acquisition.

As highlighted above, CaMPARI2, preSynTagMA, and postSynTagMA (at the synapses and the nucleus) all feature varying protein turnover rates. These rates determine the available time one has to acquire the labeled map of cells or synapses and the frequency at which one can remap those cells and synapses. The rather short turnover of postSynTagMA at the synapse makes it impossible to use without quick access to imaging; like a cranial window *in vivo* or under the microscope *in vitro*. The other sensors, on the other hand, may be amenable to fiber-coupled photoconversion in a freely behaving animals followed by immunohistochemistry with the red CaMPARI2 antibody.

Another important factor to consider is violet light penetration due to depth-dependent attenuation due to scattering and absorption. I found that there is a linear relationship between photoconversion and light intensity (Paper 3, supplemental fig. 11). Using a published modeling software, I determined the expected violet light penetration through a cranial window and a flat tipped implanted optical fiber. Illumination through the objective gives rather uniform light attenuation with depth whereas, unsurprisingly, light scattering from the fiber occurs in all directions, making it more difficult to interpret photoconversion results. I would recommend normalizing photoconversion between cells or synapses at similar depths. As extended violet light illumination can lead to photodamage, I assessed cell death under conditions used in our paper and found we were well within safe margins (Paper 3, supplemental fig 7), however, it is important to consider these effects when working with these sensors. This is of particular importance as it may limit the number of iterative maps possible.

2.6.2 Analysis

Although the possibility of capturing a complete synaptic activity map is fantastic, labeling on thousands of synapses on a single neuron makes it essential to automatize the analysis (Paper 3 fig. 5). Following

acquisition, the image stacks must be aligned and corrected from chromatic aberration. In optimal

experimental conditions, there is at least one before and after image and even if those images are taken

relatively close in time (~10 minutes), small movements and the motility of spines in tissue requires

alignment of the two images. As these movements occur in three dimensions and are highly localized, a

simple rigid registration insufficient. Inspired by whole brain imaging methods, we applied a software

package developed for functional magnetic resonance imaging, called Elastix (Klein, Staring, Murphy,

Viergever, & Pluim, 2010), to transform and align one image stack to another. Once both images are

aligned, the second obstacle is finding the relevant signal coming from synapses expressing SynTagMA. I

used two different approaches to spot/synapse finding. The powerful image analysis software, IMARIS^{TM}

has a spot locating feature. Using this method, the user defines an object size (in xyz) and the

fluorescent channel to locate the spots. Additional filtering can exclude spots containing fluorescence

from another channel. Although this method is robust and reliable, it is limited to ellipsoid-shaped spots

and requires each described step above to be done in separate steps.

Our open-source software package SynapseLocator is able to align and transform two image stacks

and subsequently find spots. In contrast to IMARIS, SynapseLocator uses machine learning to find spots.

The user creates a training set from real data and trains the classifier for spot finding. With this method,

the spots are fit to their actual shape, which should increase signal fidelity in comparison to the ellipsoid

method.

A final analysis challenge is the presence of autofluorescent objects in tissue, whose emission is

green and particularly red. Synapses have a limited size range and therefore some of the

autofluorescent objects can easily be rejected using size as a criterion, but a proportion of these objects

are similar in size to SynTagMA signals. Fortunately, many of these objects, do not overlap with

SynTagMA (Paper 3, supplemental fig. 8). As autofluorescent objects do not photoconvert most of these

objects can be rejected due to their red fluorescence in the before photoconversion image. Experiments

that use a single post-photoconversion time point may require the use of a morphological marker, like

mCerulean, in order to reject high red objects that do not belong to the neuron.

References

Aittoniemi, J., Fotinou, C., Craig, T. J., De Wet, H., Proks, P., & Ashcroft, F. M. (2009). SUR1: A unique

ATP-binding cassette protein that functions as an ion channel regulator. *Philosophical Transactions
of the Royal Society B: Biological Sciences*, *364*(1514), 257–267.
https://doi.org/10.1098/rstb.2008.0142

Akerboom, J., Chen, T.-W., Wardill, T. J., Tian, L., Marvin, J. S., Mutlu, S., … Looger, L. L. (2012).

Optimization of a GCaMP Calcium Indicator for Neural Activity Imaging. *Journal of Neuroscience*,
32(40), 13819–13840. https://doi.org/10.1523/JNEUROSCI.2601-12.2012

Akerboom, Jasper, Carreras Calderón, N., Tian, L., Wabnig, S., Prigge, M., Tolö, J., … Looger, L. L. (2013).

Genetically encoded calcium indicators for multi-color neural activity imaging and combination
with optogenetics. *Frontiers in Molecular Neuroscience*, *6*(March), 1–29.
https://doi.org/10.3389/fnmol.2013.00002

Amarouch, M. Y., Syam, N., & Abriel, H. (2013). Biochemical, single-channel, whole-cell patch clamp, and

pharmacological analyses of endogenous TRPM4 channels in HEK293 cells. *Neuroscience Letters*,
541, 105–110. https://doi.org/10.1016/j.neulet.2013.02.011

Andersen, P., Morris, R., Amaral, D., Bliss, T., & O'Keefe, J. (Eds.). (2006). *The Hippocampus Book*.

Oxford, UK: Oxford University Press. https://doi.org/10.1093/acprof:oso/9780195100273.001.0001

Arboit, A., Reboreda, A., & Yoshida, M. (2020). Involvement of TRPC4 and 5 Channels in Persistent Firing

in Hippocampal CA1 Pyramidal Cells. *Cells*, *9*(2), 365. https://doi.org/10.3390/cells9020365

Ashcroft, F. M. (2005). ATP-sensitive potassium channelopathies: focus on insulin secretion. *Journal of Clinical Investigation*, *115*(8), 2047–2058. https://doi.org/10.1172/JCI25495

Autzen, H. E., Myasnikov, A. G., Campbell, M. G., Asarnow, D., Julius, D., & Cheng, Y. (2017). Structure of the human TRPM4 ion channel in a lipid nanodisc. *Science*, *232*(January), eaar4510. https://doi.org/10.1126/science.aar4510

Bakker, J., & Leinders-Zufall, T. (2015). The Sense of Smell: Role of the Olfactory Systems in Detecting Pheromones. In *Neuroscience in the 21st Century* (pp. 1–26). New York, NY: Springer New York. https://doi.org/10.1007/978-1-4614-6434-1_29-3

Beenhakker, M. P., & Huguenard, J. R. (2009). Neurons that Fire Together Also Conspire Together: Is Normal Sleep Circuitry Hijacked to Generate Epilepsy? *Neuron*. https://doi.org/10.1016/j.neuron.2009.05.015

Berridge, M. J., Lipp, P., & Bootman, M. D. (2000). The versatility and universality of calcium signalling. *Nature Reviews Molecular Cell Biology*, *1*(1), 11–21. https://doi.org/10.1038/35036035

Bezanilla, F. (2008). Ion Channels: From Conductance to Structure. *Neuron*, *60*(3), 456–468. https://doi.org/10.1016/j.neuron.2008.10.035

Bianchi, B., Smith, P. A., & Abriel, H. (2018). The ion channel TRPM4 in murine experimental autoimmune encephalomyelitis and in a model of glutamate-induced neuronal degeneration. *Molecular Brain*, *11*(1), 41. https://doi.org/10.1186/s13041-018-0385-4

Bliss, T. V. P., & Lømo, T. (1973). Long-lasting potentiation of synaptic transmission in the dentate area of the anaesthetized rabbit following stimulation of the perforant path. *The Journal of Physiology*.

https://doi.org/10.1113/jphysiol.1973.sp010273

Bloodgood, B. L., & Sabatini, B. L. (2007). Nonlinear Regulation of Unitary Synaptic Signals by CaV2.3

Voltage-Sensitive Calcium Channels Located in Dendritic Spines. *Neuron*, *53*(2), 249–260.

https://doi.org/10.1016/j.neuron.2006.12.017

Bloodgood, B. L., & Sabatini, B. L. (2008). Regulation of synaptic signalling by postsynaptic, non-

glutamate receptor ion channels. *The Journal of Physiology*, *586*(6), 1475–1480.

https://doi.org/10.1113/jphysiol.2007.148353

Bovet-Carmona, M., Krautwald, K., Menigoz, A. A. A. A., Vennekens, R., Balschun, D., & Angenstein, F.

(2019). Low frequency pulse stimulation of Schaffer collaterals in Trpm4 −/− knockout rats

differently affects baseline BOLD signals in target regions of the right hippocampus but not BOLD

responses at the site of stimulation. *NeuroImage*, *188*(December 2018), 347–356.

https://doi.org/10.1016/j.neuroimage.2018.12.020

Bovet-Carmona, M., Menigoz, A., Pinto, S., Tambuyzer, T., Krautwald, K., Voets, T., … Balschun, D.

(2018). Disentangling the role of TRPM4 in hippocampus-dependent plasticity and learning: an

electrophysiological, behavioral and FMRI approach. *Brain Structure and Function*, *223*(8), 3557–

3576. https://doi.org/10.1007/s00429-018-1706-1

Brini, M., Calì, T., Ottolini, D., & Carafoli, E. (2014). Neuronal calcium signaling: function and dysfunction.

Cellular and Molecular Life Sciences, *71*(15), 2787–2814. https://doi.org/10.1007/s00018-013-

1550-7

Burris, S. K., Wang, Q., Bulley, S., Neeb, Z. P., & Jaggar, J. H. (2015). 9-Phenanthrol inhibits recombinant

and arterial myocyte TMEM16A channels. *British Journal of Pharmacology*, *172*(10), 2459–2468.

https://doi.org/10.1111/bph.13077

Chen, M, Dong, Y., & Simard, J. M. (2003). Functional coupling between sulfonylurea receptor type 1 and

a nonselective cation channel in reactive astrocytes from adult rat brain. *J Neurosci.*, *23*(1529-2401

(Electronic)), 8568–8577. https://doi.org/23/24/8568 [pii]

Chen, Mingkui, & Marc Simard, J. (2001). Cell swelling and a nonselective cation channel regulated by

internal Ca2+ and ATP in native reactive astrocytes from adult rat brain. *Journal of Neuroscience*,

21(17), 6512–6521. https://doi.org/10.1523/JNEUROSCI.21-17-06512.2001

Chen, T.-W., Wardill, T. J., Sun, Y., Pulver, S. R., Renninger, S. L., Baohan, A., … Kim, D. S. (2013).

Ultrasensitive fluorescent proteins for imaging neuronal activity. *Nature*, *499*, 295–300.

https://doi.org/10.1038/nature12354

Choi, J.-H., Sim, S., Kim, J., Choi, D. Il, Oh, J., Ye, S., … Kaang, B.-K. (2018). Interregional synaptic maps

among engram cells underlie memory formation. *Science*, *360*(6387), 430–435.

https://doi.org/10.1126/science.aas9204

Clapham, D. E. (2007). Calcium Signaling. *Cell*, *131*(6), 1047–1058.

https://doi.org/10.1016/j.cell.2007.11.028

Colbert, C. M., Magee, J., Hoffman, D. A., & Johnston, D. (1997). Slow recovery from inactivation of Na+

channels underlies the activity-dependent attenuation of dendritic action potentials in

hippocampal CA1 pyramidal neurons. *The Journal of Neuroscience : The Official Journal of the

Society for Neuroscience*, *17*(17), 6512–6521. https://doi.org/10.1097/SPC.0000000000000012

Colquhoun, D., Neher, E., Reuter, H., & Stevens, C. F. (1981). Inward current channels activated by

intracellular Ca in cultured cardiac cells. *Nature*, *294*(5843), 752–754.

https://doi.org/10.1038/294752a0

Cox, J., & Witten, I. B. (2019). Striatal circuits for reward learning and decision-making. *Nature Reviews Neuroscience*, *20*(8), 482–494. https://doi.org/10.1038/s41583-019-0189-2

Crowder, E. a, Saha, M. S., Pace, R. W., Zhang, H., Prestwich, G. D., & Del Negro, C. a. (2007). Phosphatidylinositol 4,5-bisphosphate regulates inspiratory burst activity in the neonatal mouse preBötzinger complex. *The Journal of Physiology*, *582*(Pt 3), 1047–1058. https://doi.org/10.1113/jphysiol.2007.134577

Crunelli, V., & Hughes, S. W. (2010). The slow (1 Hz) rhythm of non-REM sleep: A dialogue between three cardinal oscillators. *Nature Neuroscience*, *13*(1), 9–17. https://doi.org/10.1038/nn.2445

Dana, H., Sun, Y., Mohar, B., Hulse, B. K., Kerlin, A. M., Hasseman, J. P., … Kim, D. S. (2019). High-performance calcium sensors for imaging activity in neuronal populations and microcompartments. *Nature Methods*, *16*(7), 649–657. https://doi.org/10.1038/s41592-019-0435-6

Debanne, D., Inglebert, Y., & Russier, M. (2019). Plasticity of intrinsic neuronal excitability. *Current Opinion in Neurobiology*, *54*, 73–82. https://doi.org/10.1016/j.conb.2018.09.001

Del Negro, C. A., Funk, G. D., & Feldman, J. L. (2018). Breathing matters. *Nature Reviews Neuroscience*, *19*(6), 351–367. https://doi.org/10.1038/s41583-018-0003-6

Del Negro, C. a., Morgado-Valle, C., Hayes, J. A., Mackay, D. D., Pace, R. W., Crowder, E. a, & Feldman, J. L. (2005). Sodium and Calcium Current-Mediated Pacemaker Neurons and Respiratory Rhythm Generation. *Journal of Neuroscience*, *25*(2), 446–453. https://doi.org/10.1523/JNEUROSCI.2237-04.2005

Demion, M., Bois, P., Launay, P., & Guinamard, R. (2007). TRPM4, a Ca2+-activated nonselective cation

channel in mouse sino-atrial node cells. *Cardiovascular Research*, *73*(3), 531–538.

https://doi.org/10.1016/j.cardiores.2006.11.023

Dendrou, C. A., Fugger, L., & Friese, M. A. (2015). Immunopathology of multiple sclerosis. *Nature*

Reviews Immunology, *15*(9), 545–558. https://doi.org/10.1038/nri3871

Denk, W., Strickler, J., & Webb, W. (1990). Two-photon laser scanning fluorescence microscopy. *Science*,

248(4951), 73–76. https://doi.org/10.1126/science.2321027

Diekelmann, S., & Born, J. (2010). The memory function of sleep. *Nature Reviews Neuroscience*.

https://doi.org/10.1038/nrn2762

Dreosti, E., Odermatt, B., Dorostkar, M. M., & Lagnado, L. (2009). A genetically encoded reporter of

synaptic activity in vivo. *Nature Methods*, *6*(12), 883–889. https://doi.org/10.1038/nmeth.1399

Duan, J., Li, Z., Li, J., Santa-Cruz, A., Sanchez-Martinez, S., Zhang, J., & Clapham, D. E. (2018). Structure of

full-length human TRPM4. *Proceedings of the National Academy of Sciences*, *115*(10), 201722038.

https://doi.org/10.1073/pnas.1722038115

Dutta Banik, D., Martin, L. E., Freichel, M., Torregrossa, A.-M., & Medler, K. F. (2018). TRPM4 and TRPM5

are both required for normal signaling in taste receptor cells. *Proceedings of the National Academy*

of Sciences, *115*(4), 201718802. https://doi.org/10.1073/pnas.1718802115

Eckstein, E., Pyrski, M., Pinto, S., Freichel, M., Vennekens, R., & Zufall, F. (2020). Cyclic regulation of

Trpm4 expression in female vomeronasal neurons driven by ovarian sex hormones. *Molecular and*

Cellular Neuroscience, *105*(April), 103495. https://doi.org/10.1016/j.mcn.2020.103495

Egorov AV, Hamam BN, Fransen E, Hasselmo ME, & AA., A. (2002). Graded persistent activity in

entorhinal cortex neurons. *Nature*, *420(6912)*(November), 133–134.

https://doi.org/10.1038/nature01030.1.

Egorov, A. V., Schumacher, D., Medert, R., Birnbaumer, L., Freichel, M., & Draguhn, A. (2019). TRPC

channels are not required for graded persistent activity in entorhinal cortex neurons.

Hippocampus, *29*(11), 1038–1048. https://doi.org/10.1002/hipo.23094

Endo, M., Kurachi, Y., & Mishina, M. (Eds.). (2000). *Pharmacology of Ionic Channel Function: Activators

and Inhibitors* (Vol. 147). Berlin, Heidelberg: Springer Berlin Heidelberg.

https://doi.org/10.1007/978-3-642-57083-4

Feinberg, E. H., VanHoven, M. K., Bendesky, A., Wang, G., Fetter, R. D., Shen, K., & Bargmann, C. I.

(2008). GFP Reconstitution Across Synaptic Partners (GRASP) Defines Cell Contacts and Synapses in

Living Nervous Systems. *Neuron*, *57*(3), 353–363. https://doi.org/10.1016/j.neuron.2007.11.030

Ferro, M., Lamanna, J., Ripamonti, M., Racchetti, G., Arena, A., Spadini, S., … Malgaroli, A. (2017).

Functional mapping of brain synapses by the enriching activity-marker SynaptoZip. *Nature

Communications*, *8*(1), 1229. https://doi.org/10.1038/s41467-017-01335-4

Fleig, A., & Penner, R. (2004). The TRPM ion channel subfamily: Molecular, biophysical and functional

features. *Trends in Pharmacological Sciences*, *25*(12), 633–639.

https://doi.org/10.1016/j.tips.2004.10.004

Fosque, B. F., Sun, Y., Dana, H., Yang, C.-T., Ohyama, T., Tadross, M. R., … Schreiter, E. R. (2015). Labeling

of active neural circuits in vivo with designed calcium integrators. *Science*, *347*(6223), 755–760.

https://doi.org/10.1126/science.1260922

Frank, A. C., Huang, S., Zhou, M., Gdalyahu, A., Kastellakis, G., Silva, T. K., … Silva, A. J. (2018). Hotspots

of dendritic spine turnover facilitate clustered spine addition and learning and memory. *Nature Communications*, *9*(1), 422. https://doi.org/10.1038/s41467-017-02751-2

Gao, Y., & Liao, P. (2019). TRPM4 channel and cancer. *Cancer Letters*, *454*(February), 66–69. https://doi.org/10.1016/j.canlet.2019.04.012

Garland, C. J., Smirnov, S. V., Bagher, P., Lim, C. S., Huang, C. Y., Mitchell, R., … Dora, K. A. (2015). TRPM4 inhibitor 9-phenanthrol activates endothelial cell intermediate conductance calcium-activated potassium channels in rat isolated mesenteric artery. *British Journal of Pharmacology*, *172*(4), 1114–1123. https://doi.org/10.1111/bph.12985

Gees, M., Colsoul, B., & Nilius, B. (2010). The Role of Transient Receptor Potential Cation Channels in Ca2+ Signaling. *Cold Spring Harbor Perspectives in Biology*, *2*, a003962–a003962. https://doi.org/10.1101/cshperspect.a003962

Gerzanich, V., Kwon, M. S., Woo, S. K., Ivanov, A., & Marc Simard, J. (2018). SUR1-TRPM4 channel activation and phasic secretion of MMP-9 induced by tPA in brain endothelial cells. *PLoS ONE*, *13*(4), 1–23. https://doi.org/10.1371/journal.pone.0195526

Gerzanich, V., Makar, T. K., Guda, P. R., Kwon, M. S., Stokum, J. A., Woo, S. K., … Marc Simard, J. (2017). Salutary effects of glibenclamide during the chronic phase of murine experimental autoimmune encephalomyelitis. *Journal of Neuroinflammation*, *14*(1), 177. https://doi.org/10.1186/s12974-017-0953-z

Gerzanich, V., Woo, S. K., Vennekens, R., Tsymbalyuk, O., Ivanova, S., Ivanov, A., … Simard, J. M. (2009). De novo expression of Trpm4 initiates secondary hemorrhage in spinal cord injury. *Nature Medicine*, *15*(2), 185–191. https://doi.org/10.1038/nm.1899

Ghajar, J. (2000). Traumatic brain injury. *The Lancet*, *356*(9233), 923–929.

  https://doi.org/10.1016/S0140-6736(00)02689-1

Glatigny, S., & Bettelli, E. (2018). Experimental Autoimmune Encephalomyelitis (EAE) as Animal Models

  of Multiple Sclerosis (MS). *Cold Spring Harbor Perspectives in Medicine*, *8*(11), 1–20.

  https://doi.org/10.1101/cshperspect.a028977

Golding, N. L., Kath, W. L., & Spruston, N. (2001). Dichotomy of Action-Potential Backpropagation in CA1

  Pyramidal Neuron Dendrites. *Journal of Neurophysiology*, *86*(6), 2998–3010.

  https://doi.org/10.1152/jn.2001.86.6.2998

Grand, T., Demion, M., Norez, C., Mettey, Y., Launay, P., Becq, F., … Guinamard, R. (2008). 9-phenanthrol

  inhibits human TRPM4 but not TRPM5 cationic channels. *British Journal of Pharmacology*, *153*,

  1697–1705. https://doi.org/10.1038/bjp.2008.38

Grienberger, C., & Konnerth, A. (2012). Imaging Calcium in Neurons. *Neuron*, *73*(5), 862–885.

  https://doi.org/10.1016/j.neuron.2012.02.011

Gross, G., Junge, J., Mora, R., Kwon, H. B., Olson, C. A., Takahashi, T., … Arnold, D. (2013). Recombinant

  Probes for Visualizing Endogenous Synaptic Proteins in Living Neurons. *Neuron*, *78*(6), 971–985.

  https://doi.org/10.1016/j.neuron.2013.04.017

Grynkiewicz, G., Poenie, M., & Tsien, R. Y. (1985). A new generation of Ca2+ indicators with greatly

  improved fluorescence properties. *Journal of Biological Chemistry*, *260*(6), 3440–3450.

Guinamard, R., Bouvagnet, P., Hof, T., Liu, H., Simard, C., & Sall??, L. (2015). TRPM4 in cardiac electrical

  activity. *Cardiovascular Research*, *108*(1), 21–30. https://doi.org/10.1093/cvr/cvv213

Guinamard, R., Chatelier, A., Demion, M., Potreau, D., Patri, S., Rahmati, M., & Bois, P. (2004). Functional

characterization of a Ca2+-activated non-selective cation channel in human atrial cardiomyocytes. *Journal of Physiology*, *558*(1), 75–83. https://doi.org/10.1113/jphysiol.2004.063974

Guinamard, R., Sallé, L., & Simard, C. (2011). The Non-selective Monovalent Cationic Channels TRPM4 and TRPM5. In *Transient Receptor Potential Channels, Advances in Experimental Medicine and Biology* (Vol. 704, pp. 147–171). https://doi.org/10.1007/978-94-007-0265-3_8

Guinamard, R., Simard, C., & Del Negro, C. (2013). Flufenamic acid as an ion channel modulator. *Pharmacology and Therapeutics*, *138*(2), 272–284. https://doi.org/10.1016/j.pharmthera.2013.01.012

Guo, J., She, J., Zeng, W., Chen, Q., Bai, X. C., & Jiang, Y. (2017). Structures of the calcium-activated, non-selective cation channel TRPM4. *Nature*, *552*(7684), 205–209. https://doi.org/10.1038/nature24997

Haj-dahmane, S., & Andrade, R. (1998). Ionic mechanism of the slow afterdepolarization induced by muscarinic receptor activation in rat prefrontal cortex. *Journal of Neurophysiology*. https://doi.org/10.1152/jn.1998.80.3.1197

Hamill, O. P., Marty, A., Neher, E., Sakmann, B., & Sigworth, F. J. (1981). Improved patch-clamp techniques for high-resolution current recording from cells and cell-free membrane patches. *Pflügers Archiv European Journal of Physiology*, *391*(2), 85–100. https://doi.org/10.1007/BF00656997

Helassa, N., Dürst, C. D., Coates, C., Kerruth, S., Arif, U., Schulze, C., … Török, K. (2018). Ultrafast glutamate sensors resolve high-frequency release at Schaffer collateral synapses. *Proceedings of the National Academy of Sciences of the United States of America*, *115*(21), 5594–5599.

https://doi.org/10.1073/pnas.1720648115

Helmchen, F. (2004). Calcium imaging. In R. Brette & A. Destexhe (Eds.), *Handbook of Neural Activity Measurement* (Vol. 2004, pp. 362–409). Cambridge: Cambridge University Press. https://doi.org/10.1017/CBO9780511979958.010

Henderson, M. J., Baldwin, H. A., Werley, C. A., Boccardo, S., Whitaker, L. R., Yan, X., … Harvey, B. K. (2015). A low affinity GCaMP3 variant (GCaMPer) for imaging the endoplasmic reticulum calcium store. *PLoS ONE*. https://doi.org/10.1371/journal.pone.0139273

Higley, M. J., & Sabatini, B. L. (2012). Calcium Signaling in Dendritic Spines. *Cold Spring Harbor Perspectives in Biology*, *4*, a005686–a005686. https://doi.org/10.1101/cshperspect.a005686

Higley, Michael J., & Sabatini, B. L. (2008). Calcium Signaling in Dendrites and Spines: Practical and Functional Considerations. *Neuron*, *59*, 902–913. https://doi.org/10.1016/j.neuron.2008.08.020

Hille, B. (1987). Ionic channels of Excitable Membranes 2nd edition. *Journal of The Electrochemical Society*. https://doi.org/10.1149/1.2100457

Hires, S. a, Tian, L., & Looger, L. L. (2008). Reporting neural activity with genetically encoded calcium indicators. *Brain Cell Biol*, *36*, 69–86. https://doi.org/10.1007/s11068-008-9029-4

Hodgkin, A. L., & Huxley, A. F. (1952). A quantitative description of membrane current and its application to conduction and excitation in nerve. *The Journal of Physiology*. https://doi.org/10.1113/jphysiol.1952.sp004764

Holbro, N., Grunditz, A., & Oertner, T. G. (2009). Differential distribution of endoplasmic reticulum controls metabotropic signaling and plasticity at hippocampal synapses. *Proceedings of the National Academy of Sciences*, *106*(35), 15055–15060. https://doi.org/10.1073/pnas.0905110106

Homma, R., Baker, B. J., Jin, L., Garaschuk, O., Konnerth, A., Cohen, L. B., & Zecevic, D. (2009). Wide-field and two-photon imaging of brain activity with voltage- and calcium-sensitive dyes. *Philosophical Transactions of the Royal Society B: Biological Sciences*. https://doi.org/10.1098/rstb.2009.0084

Howe, M., Ridouh, I., Mascaro, A. L. A., Larios, A., Azcorra, M., & Dombeck, D. A. (2019). Coordination of rapid cholinergic and dopaminergic signaling in striatum during spontaneous movement. *ELife*, *8*, 1–24. https://doi.org/10.7554/eLife.44903

Howe, M. W., Tierney, P. L., Sandberg, S. G., Phillips, P. E. M., & Graybiel, A. M. (2013). Prolonged dopamine signalling in striatum signals proximity and value of distant rewards. *Nature*, *500*(7464), 575–579. https://doi.org/10.1038/nature12475

Humeau, Y., & Choquet, D. (2019). The next generation of approaches to investigate the link between synaptic plasticity and learning. *Nature Neuroscience*, *22*(10), 1536–1543. https://doi.org/10.1038/s41593-019-0480-6

Iacaruso, M. F., Gasler, I. T., & Hofer, S. B. (2017). Synaptic organization of visual space in primary visual cortex. *Nature*, *547*(7664), 449–452. https://doi.org/10.1038/nature23019

Inoue, M., Takeuchi, A., Manita, S., Horigane, S., Sakamoto, M., Kawakami, R., … Bito, H. (2019). Rational Engineering of XCaMPs, a Multicolor GECI Suite for In Vivo Imaging of Complex Brain Circuit Dynamics. *Cell*, 1–15. https://doi.org/10.1016/j.cell.2019.04.007

Jaffe, D. B., Johnston, D., Lasser-Ross, N., Lisman, J., Miyakawa, H., & Ross, W. N. (1992). The spread of Na+ spikes determines the pattern of dendritic Ca2+ entry into hippocampal neurons. *Nature*, *357*, 244–246.

Jha, R. M., Bell, J., Citerio, G., Hemphill, J. C., Kimberly, W. T., Narayan, R. K., … Simard, J. M. (2020,

January 9). Role of sulfonylurea receptor 1 and glibenclamide in traumatic brain injury: A review of the evidence. *International Journal of Molecular Sciences*. https://doi.org/10.3390/ijms21020409

Jha, R. M., Kochanek, P. M., & Simard, J. M. (2019). Pathophysiology and treatment of cerebral edema in traumatic brain injury. *Neuropharmacology*, *145*(July 2018), 230–246. https://doi.org/10.1016/j.neuropharm.2018.08.004

Ji, N., Freeman, J., & Smith, S. L. (2016). Technologies for imaging neural activity in large volumes. *Nature Neuroscience*, *19*(9), 1154–1164. https://doi.org/10.1038/nn.4358

Jia, H., Rochefort, N. L., Chen, X., & Konnerth, A. (2010). Dendritic organization of sensory input to cortical neurons in vivo. *Nature*. https://doi.org/10.1038/nature08947

Jing, M., Zhang, P., Wang, G., Feng, J., Mesik, L., Zeng, J., … Li, Y. (2018). A genetically encoded fluorescent acetylcholine indicator for in vitro and in vivo studies. *Nature Biotechnology*, *36*(8). https://doi.org/10.1038/nbt.4184

Jochems, A., & Yoshida, M. (2013). Persistent firing supported by an intrinsic cellular mechanism in hippocampal CA3 pyramidal cells. *European Journal of Neuroscience*, *38*(2), 2250–2259. https://doi.org/10.1111/ejn.12236

Josselyn, S. A., & Tonegawa, S. (2020). Memory engrams: Recalling the past and imagining the future. *Science (New York, N.Y.)*, *367*(6473). https://doi.org/10.1126/science.aaw4325

Kandel, E. R., Schwartz, J. H., & Jessell, T. M. (2000). *Principles of Neural Science, fourth addition*. *McGraw-Hill Companies*. https://doi.org/10.1036/0838577016

Karschin, C., Ecke, C., Ashcroft, F. M., & Karschin, A. (1997). Overlapping distribution of K(ATP) channel-forming Kir6.2 subunit and the sulfonylurea receptor SUR1 in rodent brain. *FEBS Letters*, *401*(1),

59–64. https://doi.org/10.1016/S0014-5793(96)01438-X

Kastellakis, G., Silva, A. J., & Poirazi, P. (2016). Linking Memories across Time via Neuronal and Dendritic

Overlaps in Model Neurons with Active Dendrites. *Cell Reports*, *17*(6), 1491–1504.

https://doi.org/10.1016/j.celrep.2016.10.015

Kazemipour, A., Novak, O., Flickinger, D., Marvin, J. S., Abdelfattah, A. S., King, J., … Podgorski, K. (2019).

Kilohertz frame-rate two-photon tomography. *Nature Methods*, *16*(8), 778–786.

https://doi.org/10.1038/s41592-019-0493-9

Kerlin, A., Mohar, B., Flickinger, D., MacLennan, B. J., Davis, C., Spruston, N., & Svoboda, K. (2018).

Functional clustering of dendritic activity during decision-making. *BioRxiv*, 440396.

https://doi.org/10.1101/440396

Kim, J., Zhao, T., Petralia, R. S., Yu, Y., Peng, H., Myers, E., & Magee, J. C. (2012). MGRASP enables

mapping mammalian synaptic connectivity with light microscopy. *Nature Methods*, *9*(1), 96–102.

https://doi.org/10.1038/nmeth.1784

Kim, Y. S., Kang, E., Makino, Y., Park, S., Shin, J. H., Song, H., … Linden, D. J. (2013). Characterizing the

conductance underlying depolarization-induced slow current in cerebellar Purkinje cells. *Journal of*

Neurophysiology, *109*, 1174–1181. https://doi.org/10.1152/jn.01168.2011

Klein, S., Staring, M., Murphy, K., Viergever, M. A., & Pluim, J. P. W. (2010). Elastix: A toolbox for

intensity-based medical image registration. *IEEE Transactions on Medical Imaging*.

https://doi.org/10.1109/TMI.2009.2035616

Knauer, B., Jochems, A., Valero-Aracama, M. J., & Yoshida, M. (2013). Long-lasting intrinsic persistent

firing in rat CA1 pyramidal cells: A possible mechanism for active maintenance of memory.

Hippocampus, *23*(9), 820–831. https://doi.org/10.1002/hipo.22136

Knauer, B., & Yoshida, M. (2019). Switching between persistent firing and depolarization block in

individual rat CA1 pyramidal neurons. *Hippocampus*, *29*(9), 817–835.

https://doi.org/10.1002/hipo.23078

Koizumi, H., John, T. T., Chia, J. X., Tariq, M. F., Phillips, R. S., Mosher, B., … Smith, J. C. (2018). Transient

Receptor Potential Channels TRPM4 and TRPC3 Critically Contribute to Respiratory Motor Pattern

Formation but Not Rhythmogenesis in Rodent Brainstem Circuits. *Eneuro*, *5*(February),

ENEURO.0332-17.2018. https://doi.org/10.1523/ENEURO.0332-17.2018

Kurland, D. B., Gerzanich, V., Karimy, J. K., Woo, S. K., Vennekens, R., Freichel, M., … Simard, J. M. (2016).

The Sur1-Trpm4 channel regulates NOS2 transcription in TLR4-activated microglia. *Journal of

Neuroinflammation*, *13*(1), 130. https://doi.org/10.1186/s12974-016-0599-2

Launay, P., Fleig, A., Perraud, A. L., Scharenberg, A. M., Penner, R., & Kinet, J. P. (2002). TRPM4 is a Ca2+-

activated nonselective cation channel mediating cell membrane depolarization. *Cell*, *109*, 397–407.

https://doi.org/10.1016/S0092-8674(02)00719-5

Lee, C. R., Machold, R. P., Witkovsky, P., & Rice, M. E. (2013). TRPM2 channels are required for NMDA-

induced burst firing and contribute to H2O2-dependent modulation in substantia nigra pars

reticulata GABAergic neurons. *Journal of Neuroscience*, *33*(3), 1157–1168.

https://doi.org/10.1523/JNEUROSCI.2832-12.2013

Lei, Y., Thuault, S. J., Launay, P., Margolskee, R. F., Kandel, E. R., & Siegelbaum, S. A. (2014). Differential

contribution of TRPM4 and TRPM5 nonselective cation channels to the slow afterdepolarization in

mouse prefrontal cortex neurons, *8*(September), 1–14. https://doi.org/10.3389/fncel.2014.00267

Leitz, J., & Kavalali, E. T. (2014). Fast retrieval and autonomous regulation of single spontaneously recycling synaptic vesicles. *ELife*. https://doi.org/10.7554/eLife.03658

Leiva-Salcedo, E., Riquelme, D., Cerda, O., & Stutzin, A. (2017a). TRPM4 activation by chemically- and oxygen deprivation-induced ischemia and reperfusion triggers neuronal death. *Channels*, *6950*(October), 0–0. https://doi.org/10.1080/19336950.2017.1375072

Leiva-Salcedo, E., Riquelme, D., Cerda, O., & Stutzin, A. (2017b). TRPM4 activation by chemically- and oxygen deprivation-induced ischemia and reperfusion triggers neuronal death. *Channels*, *6950*(October), 0–0. https://doi.org/10.1080/19336950.2017.1375072

Li, G., Makar, T., Gerzanich, V., Kalakonda, S., Ivanova, S., Pereira, E. F. R., … Zhao, R. Y. (2020). HIV-1 Vpr-induced Proinflammatory Response and Apoptosis are Mediated through the Sur1-Trpm4 Channel in Astrocytes, 1–16. https://doi.org/10.1101/2020.03.19.999268

Lichtman, J. W., & Conchello, J. A. (2005). Fluorescence microscopy. *Nature Methods*. https://doi.org/10.1038/nmeth817

Liman, E. R. (2014). TRPM5. In *Mammalian Transient Receptor Potential (TRP) Cation Channels* (Vol. 1, pp. 489–502). https://doi.org/10.1007/978-3-642-54215-2_19

Lin, E. C., Combe, C. L., & Gasparini, S. (2017). Differential Contribution of Ca2+-Dependent Mechanisms to Hyperexcitability in Layer V Neurons of the Medial Entorhinal Cortex. *Frontiers in Cellular Neuroscience*, *11*(June), 1–17. https://doi.org/10.3389/fncel.2017.00182

Lin, M. Z., & Schnitzer, M. J. (2016). Genetically encoded indicators of neuronal activity. *Nature Neuroscience*, *19*(9), 1142–1153. https://doi.org/10.1038/nn.4359

Luo, L., Callaway, E. M., & Svoboda, K. (2018). Genetic Dissection of Neural Circuits: A Decade of

Progress. *Neuron*, *98*(2), 256–281. https://doi.org/10.1016/j.neuron.2018.03.040

Lynch, G., Larson, J., Kelso, S., Barrionuevo, G., & Schottler, F. (1983). Intracellular injections of EGTA block induction of hippocampal long-term potentiation. *Nature*. https://doi.org/10.1038/305719a0

Madej, M. G., & Ziegler, C. M. (2018). Dawning of a new era in TRP channel structural biology by cryo-electron microscopy, 213–225. https://doi.org/10.1007/s00424-018-2107-2

Makar, T. K., Gerzanich, V., Nimmagadda, V. K. C., Jain, R., Lam, K., Mubariz, F., … Simard, J. M. (2015). Silencing of Abcc8 or inhibition of newly upregulated Sur1-Trpm4 reduce inflammation and disease progression in experimental autoimmune encephalomyelitis. *Journal of Neuroinflammation*, *12*(1), 210. https://doi.org/10.1186/s12974-015-0432-3

Martínez-Valverde, T., Vidal-Jorge, M., Martínez-Saez, E., Castro, L., Arikan, F., Cordero, E., … Sahuquillo, J. (2015). Sulfonylurea receptor 1 in humans with post-traumatic brain contusions. *Journal of Neurotrauma*, *32*(19), 1478–1487. https://doi.org/10.1089/neu.2014.3706

Marvin, J. S., Shimoda, Y., Magloire, V., Leite, M., Kawashima, T., Jensen, T. P., … Looger, L. L. (2019). A genetically encoded fluorescent sensor for in vivo imaging of GABA. *Nature Methods*, *16*(8), 763–770. https://doi.org/10.1038/s41592-019-0471-2

Masoli, S., Rizza, M. F., Sgritta, M., Van Geit, W., Schürmann, F., & D'Angelo, E. (2017). Single neuron optimization as a basis for accurate biophysical modeling: The case of cerebellar granule cells. *Frontiers in Cellular Neuroscience*, *11*(March), 1–14. https://doi.org/10.3389/fncel.2017.00071

Masoli, S., Tognolina, M., & Angelo, D. (2019). Parameter tuning differentiates granule cell subtypes enriching the repertoire of retransmission properties at the cerebellum input stage. *Communications Biology*, 1–12. https://doi.org/10.1038/s42003-020-0953-x

Mathar, I., Jacobs, G., Kecskes, M., Menigoz, A., Philippaert, K., & Vennekens, R. (2014). TRPM4. In *Mammailian Transient Receptor Potential (TRP) Cation Channels* (Vol. 1, pp. 461–487). https://doi.org/10.1007/978-3-642-54215-2

Menigoz, A., Ahmed, T., Sabanov, V., Philippaert, K., Pinto, S., Kerselaers, S., … Balschun, D. (2016). TRPM4-dependent post-synaptic depolarization is essential for the induction of NMDA receptor-dependent LTP in CA1 hippocampal neurons. *Pflügers Archiv - European Journal of Physiology*, *468*(4), 593–607. https://doi.org/10.1007/s00424-015-1764-7

Miesenböck, G., De Angelis, D. A., & Rothman, J. E. (1998). Visualizing secretion and synaptic transmission with pH-sensitive green fluorescent proteins. *Nature*. https://doi.org/10.1038/28190

Mironov, S. L. (2008). Metabotropic glutamate receptors activate dendritic calcium waves and TRPM channels which drive rhythmic respiratory patterns in mice. *The Journal of Physiology*, *586*, 2277–2291. https://doi.org/10.1113/jphysiol.2007.149021

Mironov, S. L. (2013). Calmodulin and calmodulin kinase II mediate emergent bursting activity in the brainstem respiratory network (preBötzinger complex). *The Journal of Physiology*, *591*(7), 1613–1630. https://doi.org/10.1113/jphysiol.2012.237362

Miyawaki, A., Llopis, J., Heim, R., Michael McCaffery, J., Adams, J. A., Ikura, M., & Tsien, R. Y. (1997). Fluorescent indicators for Ca2+ based on green fluorescent proteins and calmodulin. *Nature*, *388*(6645), 882–887. https://doi.org/10.1038/42264

Mohr, M. A., Bushey, D., Aggarwal, A., Marvin, J. S., Kim, J. J., Marquez, E. J., … Podgorski, K. (2020). jYCaMP: an optimized calcium indicator for two-photon imaging at fiber laser wavelengths. *Nature Methods*, *10*. https://doi.org/10.1038/s41592-020-0835-7

Mrejeru, A., Wei, A., & Ramirez, J. M. (2011). Calcium-activated non-selective cation currents are

    involved in generation of tonic and bursting activity in dopamine neurons of the substantia nigra

    pars compacta. *The Journal of Physiology*, *589*(10), 2497–2514.

    https://doi.org/10.1113/jphysiol.2011.206631

Nakai, J., Ohkura, M., & Imoto, K. (2001). A high signal-to-noise ca2+ probe composed of a single green

    fluorescent protein. *Nature Biotechnology*. https://doi.org/10.1038/84397

Nevian, T., & Sakmann, B. (2004). Single Spine Ca2+ Signals Evoked by Coincident EPSPs and

    Backpropagating Action Potentials in Spiny Stellate Cells of Layer 4 in the Juvenile Rat

    Somatosensory Barrel Cortex. *Journal of Neuroscience*, *24*(7), 1689–1699.

    https://doi.org/10.1523/JNEUROSCI.3332-03.2004

Nicoll, R. A. (2017). A Brief History of Long-Term Potentiation. *Neuron*, *93*(2), 281–290.

    https://doi.org/10.1016/j.neuron.2016.12.015

Nilius, B., & Droogmans, G. (2001). Ion Channels in Nonexcitable Cells. In *Cell Physiology Source Book*

    (Vol. 55, pp. 485–507). Elsevier. https://doi.org/10.1016/B978-012656976-6/50121-9

Nilius, B., Mahieu, F., Prenen, J., Janssens, A., Owsianik, G., Vennekens, R., & Voets, T. (2006). The Ca2+-

    activated cation channel TRPM4 is regulated by phosphatidylinositol 4,5-biphosphate. *The EMBO*

    Journal, *25*(3), 467–478. https://doi.org/10.1038/sj.emboj.7600963

Nilius, B., Prenen, J., Janssens, A., Voets, T., & Droogmans, G. (2004). Decavanadate modulates gating of

    TRPM4 cation channels. *The Journal of Physiology*, *560*(3), 753–765.

    https://doi.org/10.1113/jphysiol.2004.070839

Nilius, B., Prenen, J., Tang, J., Wang, C., Owsianik, G., Janssens, A., … Zhu, M. X. (2005). Regulation of the

Ca2+ sensitivity of the nonselective cation channel TRPM4. *Journal of Biological Chemistry*, *280*(8), 6423–6433. https://doi.org/10.1074/jbc.M411089200

Nilius, B., Prenen, J., Voets, T., & Droogmans, G. (2004). Intracellular nucleotides and polyamines inhibit the Ca2+- activated cation channel TRPM4b. *Pflugers Archiv European Journal of Physiology*, *448*, 70–75. https://doi.org/10.1007/s00424-003-1221-x

O'Malley, J. J., Seibt, F., Chin, J., & Beierlein, M. (2020). TRPM4 conductances in thalamic reticular nucleus neurons generate persistent firing during slow oscillations. *The Journal of Neuroscience*, (May), JN-RM-0324-20. https://doi.org/10.1523/jneurosci.0324-20.2020

Ozhathil, L. C., Delalande, C., Bianchi, B., Nemeth, G., Kappel, S., Thomet, U., … Abriel, H. (2018). Identification of potent and selective small molecule inhibitors of the cation channel TRPM4. *British Journal of Pharmacology*, *175*(12), 2504–2519. https://doi.org/10.1111/bph.14220

Pace, R. W., Mackay, D. D., Feldman, J. L., & Del Negro, C. a. (2007). Inspiratory bursts in the preBötzinger complex depend on a calcium-activated non-specific cation current linked to glutamate receptors in neonatal mice. *The Journal of Physiology*, *582*(Pt 1), 113–125. https://doi.org/10.1113/jphysiol.2007.133660

Partridge, L. Donald, Müller, T. H., & Swandulla, D. (1994). Calcium-activated non-selective channels in the nervous system. *Brain Research Reviews*, *19*(3), 319–325. https://doi.org/10.1016/0165-0173(94)90017-5

Partridge, L. Donald, & Valenzuela, C. F. (2000). Block of hippocampal CAN channels by flufenamate. *Brain Research*, *867*(1–2), 143–148. https://doi.org/10.1016/S0006-8993(00)02275-7

Partridge, L D, & Swandulla, D. (1988). Calcium-activated non-specific cation channels. *Trends in*

Neurosciences, *11*(2), 69–72. https://doi.org/10.1016/0166-2236(88)90167-1

Patel, A. D., Gerzanich, V., Geng, Z., & Simard, J. M. (2010). Glibenclamide reduces hippocampal injury and preserves rapid spatial learning in a model of traumatic brain injury. *Journal of Neuropathology and Experimental Neurology*, *69*(12), 1177–1190. https://doi.org/10.1097/NEN.0b013e3181fbf6d6

Patriarchi, T., Cho, J. R., Merten, K., Howe, M. W., Marley, A., Xiong, W. H., … Tian, L. (2018). Ultrafast neuronal imaging of dopamine dynamics with designed genetically encoded sensors. *Science*, *360*(6396). https://doi.org/10.1126/science.aat4422

Pérez Koldenkova, V., & Nagai, T. (2013). Genetically encoded Ca2+ indicators: Properties and evaluation. *Biochimica et Biophysica Acta - Molecular Cell Research*, *1833*(7), 1787–1797. https://doi.org/10.1016/j.bbamcr.2013.01.011

Picardo, M. C. D., Sugimura, Y. K., Dorst, K. E., Kallurkar, P. S., Akins, V. T., Ma, X., … Id, N. (2019). Trpm4 ion channels in pre-bötzinger complex interneurons are essential for breathing motor pattern but not rhythm. *PLoS Biology*, *17*(2), 1–30. https://doi.org/10.1371/journal.pbio.2006094

Popp, R., & Gögelein, H. (1992). A calcium and ATP sensitive nonselective cation channel in the antiluminal membrane of rat cerebral capillary endothelial cells. *BBA - Biomembranes*. https://doi.org/10.1016/0005-2736(92)90114-2

Qian, Y., Piatkevich, K. D., Mc Larney, B., Abdelfattah, A. S., Mehta, S., Murdock, M. H., … Campbell, R. E. (2019). A genetically encoded near-infrared fluorescent calcium ion indicator. *Nature Methods*, *16*(2), 171–174. https://doi.org/10.1038/s41592-018-0294-6

Raddassi, K., Kent, S. C., Yang, J., Bourcier, K., Bradshaw, E. M., Seyfert-Margolis, V., … Hafler, D. A. (2011). Increased Frequencies of Myelin Oligodendrocyte Glycoprotein/MHC Class II-Binding CD4

Cells in Patients with Multiple Sclerosis. *The Journal of Immunology*, *187*(2), 1039–1046. https://doi.org/10.4049/jimmunol.1001543

Riquelme, D., Silva, I., Philp, A. M., Huidobro-Toro, J. P., Cerda, O., Trimmer, J. S., & Leiva-Salcedo, E. (2018). Subcellular Localization and Activity of TRPM4 in Medial Prefrontal Cortex Layer 2/3. *Frontiers in Cellular Neuroscience*, *12*(January), 1–13. https://doi.org/10.3389/fncel.2018.00012

Ross, W. N. (2012). Understanding calcium waves and sparks in central neurons. *Nature Reviews Neuroscience*, *13*(March), 157–168. https://doi.org/10.1038/nrn3168

Sabatini, B. L., Oertner, T. G., & Svoboda, K. (2002). The life cycle of Ca(2+) ions in dendritic spines. *Neuron*, *33*(3), 439–452. Retrieved from http://www.ncbi.nlm.nih.gov/pubmed/11832230

Sala-Rabanal, M., Wang, S., & Nichols, C. G. (2012). On Potential Interactions between Non-selective Cation Channel TRPM4 and Sulfonylurea Receptor SUR1. *Journal of Biological Chemistry*, *287*(12), 8746–8756. https://doi.org/10.1074/jbc.M111.336131

Schattling, B., Eggert, B., & Friese, M. a. (2014). Acquired channelopathies as contributors to development and progression of multiple sclerosis. *Experimental Neurology*, *262*, 28–36. https://doi.org/10.1016/j.expneurol.2013.12.006

Schattling, B., Steinbach, K., Thies, E., Kruse, M., Menigoz, A., Ufer, F., … Friese, M. a. (2012). TRPM4 cation channel mediates axonal and neuronal degeneration in experimental autoimmune encephalomyelitis and multiple sclerosis. *Nature Medicine*, *18*(12), 1805–1811. https://doi.org/10.1038/nm.3015

Scholl, B., Wilson, D. E., & Fitzpatrick, D. (2017). Local Order within Global Disorder: Synaptic Architecture of Visual Space. *Neuron*, *96*(5), 1127-1138.e4.

https://doi.org/10.1016/j.neuron.2017.10.017

Sha, F., Abdelfattah, A. S., Patel, R., & Schreiter, E. R. (2019). rsCaMPARI: an erasable marker of neuronal activity. *BioRxiv*, 798298. https://doi.org/10.1101/798298

Shimomura, O., Johnson, F. H., & Saiga, Y. (1962). Extraction, Purification and Properties of Aequorin, a Bioluminescent Protein from the Luminous Hydromedusan,Aequorea. *Journal of Cellular and Comparative Physiology*. https://doi.org/10.1002/jcp.1030590302

Shin, J. H., Kim, Y. S., Worley, P. F., & Linden, D. J. (2009). Depolarization-induced slow current in cerebellar Purkinje cells does not require metabotropic glutamate receptor 1. *Neuroscience*. https://doi.org/10.1016/j.neuroscience.2009.01.044

Shpak, G., Zylbertal, a., Yarom, Y., & Wagner, S. (2012). Calcium-Activated Sustained Firing Responses Distinguish Accessory from Main Olfactory Bulb Mitral Cells. *Journal of Neuroscience*, *32*(18), 6251–6262. https://doi.org/10.1523/JNEUROSCI.4397-11.2012

Simard, C., Hof, T., Keddache, Z., Launay, P., & Guinamard, R. (2013). The TRPM4 non-selective cation channel contributes to the mammalian atrial action potential. *Journal of Molecular and Cellular Cardiology*, *59*, 11–19. https://doi.org/10.1016/j.yjmcc.2013.01.019

Simard, C., Sallé, L., Rouet, R., & Guinamard, R. (2012). Transient receptor potential melastatin 4 inhibitor 9-phenanthrol abolishes arrhythmias induced by hypoxia and re-oxygenation in mouse ventricle. *British Journal of Pharmacology*, *165*(7), 2354–2364. https://doi.org/10.1111/j.1476-5381.2011.01715.x

Simard, J. M., Chen, M., Tarasov, K. V, Bhatta, S., Ivanova, S., Melnitchenko, L., … Gerzanich, V. (2006). Newly expressed SUR1-regulated NC(Ca-ATP) channel mediates cerebral edema after ischemic

stroke. *Nature Medicine*, *12*(4), 433–440. https://doi.org/10.1038/nm1390

Simard, J. M., Woo, S. K., & Gerzanich, V. (2012). Transient receptor potential melastatin 4 and cell

death. *Pflügers Archiv - European Journal of Physiology*, *464*(6), 573–582.

https://doi.org/10.1007/s00424-012-1166-z

Simard, J. M., Woo, S. K., Schwartzbauer, G. T., & Gerzanich, V. (2012). Sulfonylurea receptor 1 in central

nervous system injury: a focused review. *Journal of Cerebral Blood Flow & Metabolism*, *32*(9),

1699–1717. https://doi.org/10.1038/jcbfm.2012.91

Simms, B. A., & Zamponi, G. W. (2014). Neuronal voltage-gated calcium channels: Structure, function,

and dysfunction. *Neuron*. https://doi.org/10.1016/j.neuron.2014.03.016

Simon, F., Leiva-Salcedo, E., Armisén, R., Riveros, A., Cerda, O., Varela, D., … Stutzin, A. (2010). Hydrogen

peroxide removes TRPM4 current desensitization conferring increased vulnerability to necrotic cell

death. *Journal of Biological Chemistry*, *285*(48), 37150–37158.

https://doi.org/10.1074/jbc.M110.155390

Singh, A., Hildebrand, M. E., Garcia, E., & Snutch, T. P. (2010). The transient receptor potential channel

antagonist SKF96365 is a potent blocker of low-voltage-activated T-type calcium channels. *British

Journal of Pharmacology*. https://doi.org/10.1111/j.1476-5381.2010.00786.x

Stokum, J. A., Kwon, M. S., Woo, S. K., Tsymbalyuk, O., Vennekens, R., Gerzanich, V., & Simard, J. M.

(2018). SUR1-TRPM4 and AQP4 form a heteromultimeric complex that amplifies ion/water osmotic

coupling and drives astrocyte swelling. *Glia*, *66*(1), 108–125. https://doi.org/10.1002/glia.23231

Stuart, G. J., & Spruston, N. (2015). Dendritic integration: 60 years of progress. *Nature Neuroscience*,

18(12), 1713–1721. https://doi.org/10.1038/nn.4157

Stuart, G., Spruston, N., Sakmann, B., & Hausser, M. (1997). Action potential initiation and back

propagation in neurons of the mammalian central nervous system, *20*(3), 125–131. Retrieved from

http://discovery.ucl.ac.uk/21791/

Sturgess, N. C., Nicholas Hales, C., & Ashford, M. L. J. (1986). Inhibition of a calcium-activated, non-

selective cation channel, in a rat insulinoma cell line, by adenine derivatives. *FEBS Letters*.

https://doi.org/10.1016/0014-5793(86)81056-0

Sun, W., Tan, Z., Mensh, B. D., & Ji, N. (2016). Thalamus provides layer 4 of primary visual cortex with

orientation- and direction-tuned inputs. *Nature Neuroscience*, *19*(2), 308–315.

https://doi.org/10.1038/nn.4196

Suzuki, J., Kanemaru, K., Ishii, K., Ohkura, M., Okubo, Y., & Iino, M. (2014). Imaging intraorganellar Ca2+

at subcellular resolution using CEPIA. *Nature Communications*, *5*(May), 1–13.

https://doi.org/10.1038/ncomms5153

Svoboda, K., & Yasuda, R. (2006). Principles of Two-Photon Excitation Microscopy and Its Applications to

Neuroscience. *Neuron*, *50*(6), 823–839. https://doi.org/10.1016/j.neuron.2006.05.019

Tai, C., Hines, D. J., Choi, H. B., & MacVicar, B. A. (2011). Plasma membrane insertion of TRPC5 channels

contributes to the cholinergic plateau potential in hippocampal CA1 pyramidal neurons.

Hippocampus, *21*(9), 958–967. https://doi.org/10.1002/hipo.20807

Talavera, K., Yasumatsu, K., Voets, T., Droogmans, G., Shigemura, N., Ninomiya, Y., … Nilius, B. (2005).

Heat activation of TRPM5 underlies thermal sensitivity of sweet taste. *Nature*, *438*(7070), 1022–

1025. https://doi.org/10.1038/nature04248

Tian, L., Hires, S. A., Mao, T., Huber, D., Chiappe, M. E., Chalasani, S. H., … Looger, L. L. (2009). Imaging

neural activity in worms, flies and mice with improved GCaMP calcium indicators. *Nature Methods*.
https://doi.org/10.1038/nmeth.1398

Tonegawa, S., Morrissey, M. D., & Kitamura, T. (2018). The role of engram cells in the systems
consolidation of memory. *Nature Reviews Neuroscience*, *19*(August), 1.
https://doi.org/10.1038/s41583-018-0031-2

Tosun, C., Kurland, D. B., Mehta, R., Castellani, R. J., Dejong, J. L., Kwon, M. S., … Simard, J. M. (2013).
Inhibition of the sur1-trpm4 channel reduces neuroinflammation and cognitive impairment in
subarachnoid hemorrhage. *Stroke*, *44*(12), 3522–3528.
https://doi.org/10.1161/STROKEAHA.113.002904

Tsien, R. Y. (1980). New Calcium Indicators and Buffers with High Selectivity Against Magnesium and
Protons: Design, Synthesis, and Properties of Prototype Structures. *Biochemistry*.
https://doi.org/10.1021/bi00552a018

Ullrich, N. D., Voets, T., Prenen, J., Vennekens, R., Talavera, K., Droogmans, G., & Nilius, B. (2005).
Comparison of functional properties of the Ca2+-activated cation channels TRPM4 and TRPM5
from mice. *Cell Calcium*, *37*(3), 267–278. https://doi.org/10.1016/j.ceca.2004.11.001

Valero, M., & de la Prida, L. M. (2018). The hippocampus in depth: a sublayer-specific perspective of
entorhinal–hippocampal function. *Current Opinion in Neurobiology*, *52*, 107–114.
https://doi.org/10.1016/j.conb.2018.04.013

Vennekens, R., & Nilius, B. (2007). Insights into TRPM4 function, regulation and physiological role.
Handbook of Experimental Pharmacology. https://doi.org/10.1007/978-3-540-34891-7_16

Vetter, I., & Lewis, R. J. (2011). *Transient Receptor Potential Channels*. (M. S. Islam, Ed.) (Vol. 704).

Dordrecht: Springer Netherlands. https://doi.org/10.1007/978-94-007-0265-3

Wan, J., Peng, W., Li, X., Qian, T., Song, K., Zeng, J., … Li, Y. (2020). A genetically encoded GRAB sensor for measuring serotonin dynamics in vivo. *BioRxiv*, 2020.02.24.962282. https://doi.org/10.1101/2020.02.24.962282

Wang, W., Cai, J., Lin, Y., Liu, Z., Ren, Q., Hu, L., … Li, W. (2014). Zinc fingers function cooperatively with KRAB domain for nuclear localization of KRAB-containing zinc finger proteins. *PLoS ONE*, *9*(3). https://doi.org/10.1371/journal.pone.0092155

Winkler, P. A., Huang, Y., Sun, W., Du, J., & Lü, W. (2017). Electron cryo-microscopy structure of a human TRPM4 channel. *Nature*, *552*(7684), 200–205. https://doi.org/10.1038/nature24674

Woo, S. K., Kwon, M. S., Ivanov, A., Gerzanich, V., & Simard, J. M. (2013). The Sulfonylurea Receptor 1 (Sur1)-Transient Receptor Potential Melastatin 4 (Trpm4) Channel. *Journal of Biological Chemistry*, *288*(5), 3655–3667. https://doi.org/10.1074/jbc.M112.428219

Wu, J., Liang, Y., Chen, S., Hsu, C. L., Chavarha, M., Evans, S. W., … Ji, N. (2020). Kilohertz two-photon fluorescence microscopy imaging of neural activity in vivo. *Nature Methods*, *17*(3), 287–290. https://doi.org/10.1038/s41592-020-0762-7

Xu, X.-Z. S., Moebius, F., Gill, D. L., & Montell, C. (2001). Regulation of melastatin, a TRP-related protein, through interaction with a cytoplasmic isoform. *Proceedings of the National Academy of Sciences*, *98*(19), 10692–10697. https://doi.org/10.1073/pnas.191360198

Yan, H. D., Villalobos, C., & Andrade, R. (2009). TRPC channels mediate a muscarinic receptor-induced afterdepolarization in cerebral cortex. *Journal of Neuroscience*. https://doi.org/10.1523/JNEUROSCI.1042-09.2009

Yang, W., Chini, M., Pöpplau, J. A., Formozov, A., Piechocinski, P., Rais, C., … Wiegert, J. S. (2020). Anesthetics uniquely decorrelate hippocampal network activity, alter spine dynamics and affect memory consolidation. *BioRxiv*, 2020.06.05.135905. https://doi.org/10.1101/2020.06.05.135905

Yap, E. L., & Greenberg, M. E. (2018). Activity-Regulated Transcription: Bridging the Gap between Neural Activity and Behavior. *Neuron*, *100*(2), 330–348. https://doi.org/10.1016/j.neuron.2018.10.013

Yasuda, R., Nimchinsky, E. a, Scheuss, V., Pologruto, T. a, Oertner, T. G., Sabatini, B. L., & Svoboda, K. (2004). Imaging calcium concentration dynamics in small neuronal compartments. *Science's STKE : Signal Transduction Knowledge Environment*, *2004*, pl5. https://doi.org/10.1126/stke.2192004pl5

Yasuda, R., Sabatini, B. L., & Svoboda, K. (2003). Plasticity of calcium channels in dendritic spines. *Nature Neuroscience*, *6*(9), 948–955. https://doi.org/10.1038/nn1112

Yoshida, M., Knauer, B., & Jochems, A. (2012). Cholinergic modulation of the CAN current may adjust neural dynamics for active memory maintenance, spatial navigation and time-compressed replay. *Frontiers in Neural Circuits*, *6*(March), 1–15. https://doi.org/10.3389/fncir.2012.00010

Zarowny, L., Aggarwal, A., Rutten, V. M. S., Kolb, I., Project, T. G., Patel, R., … Campbell, R. E. (2020). A bright and high-performance genetically encoded Ca2+ indicator based on mNeonGreen fluorescent protein. *BioRxiv*, *3*. https://doi.org/https://doi.org/10.1101/2020.01.16.909291

Zhang, Z., Okawa, H., Wang, Y., & Liman, E. R. (2005). Phosphatidylinositol 4,5-Bisphosphate rescues TRPM4 channels from desensitization. *Journal of Biological Chemistry*, *280*(47), 39185–39192. https://doi.org/10.1074/jbc.M506965200

Zhao, Y., Araki, S., Wu, J., Teramoto, T., Chang, Y.-F., Nakano, M., … Campbell, R. E. (2011). An expanded palette of genetically encoded Ca^{2+} indicators. *Science (New York, N.Y.)*, *333*(6051), 1888–1891.

Appendix

Additional unpublished supplementary figures
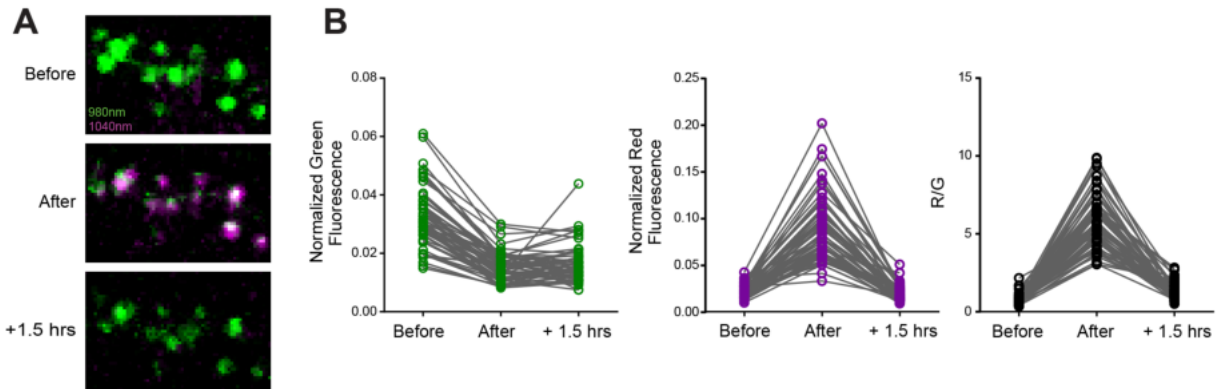
Supplementary Figure 1: Turnover of converted SynTagMA

A CA1 neuron expressing postSynTagMA in an organotypic hippocampal slice culture was exposed to a high potassium ACSF containing 40 mM K^+ in solution to drive bursting activity in the slice. An image of the postSynTagMA signal was taken before High K^+, using 980 nm and 1040 nm, respectively. The slice was exposed to high K^+ for approximately 10 minutes and 1 sec (16 mW*mm^{-2}) of violet light every 30 seconds was shined on the neuron through the objective. After replacing the high K^+ ACSF with fresh ACSF, a second image was acquired in the same manner. Finally, 1.5 hours after the initial photoconversion, a final image was acquired. High K^+ resulted in strong photoconversion along the entire dendritic processes (A). After 1.5 hours post photoconversion, approximately all of the newly red photoconverted postSynTagMA was removed (B). n=1 cell, 48 synapses
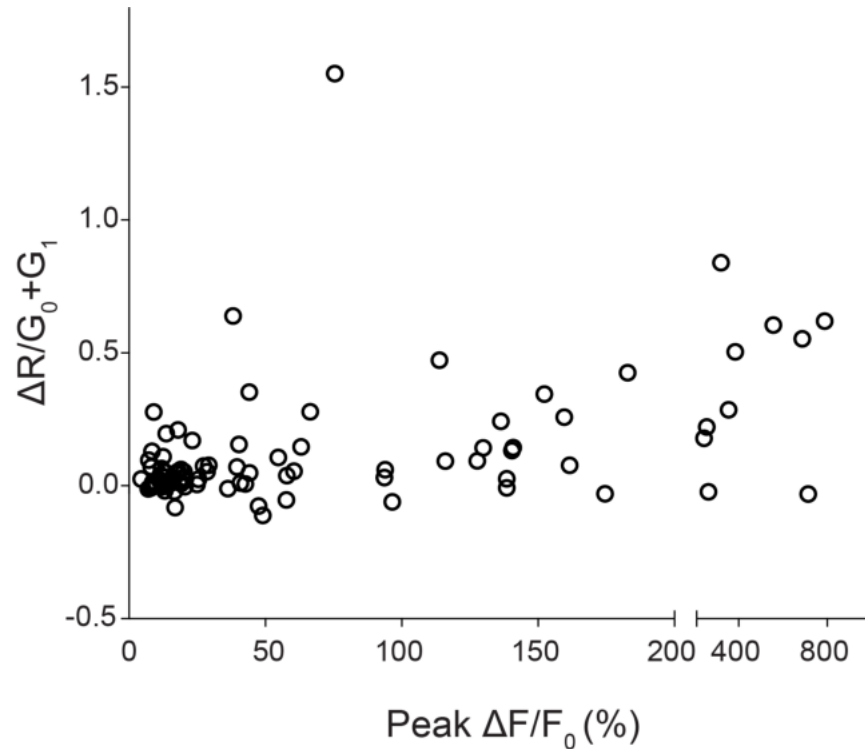
Supplementary Figure 2: Comparing photoconversion at individual synapses to their calcium transients

A stimulating electrode placed in the stratum radiatum to evoke subthreshold (non-spiking) paired pulse EPSPs at the Schaffer collateral synapse; as measured by a CA1 neuron neighboring the postSynTagMA expressing neuron. Before pairing violet light and EPSPs, a pre-photoconversion image was taken. Then EPSPs were paired with 100 ms violet light (1 sec delay, 16 mW/mm^{-2}) 50 times and a post-photoconversion image was taken. Immediately following imaging, the postSynTagMA neuron was patched and filled with Fluo5F and Alexa-594 dye. Putatively converted synapses were surveyed for Fluo5F-dependent calcium transients in response to the same electrical stimulus used for photoconversion. There is no clear relationship between the peak $\Delta F/F_0$ and the amount of photoconversion. This could be due to calcium-buffering of two calcium indicators in a single neuron. n=2 cells, 76 synapses

List of abbreviations

2PLSM	two-photon laser scanning microscopy
ABC	ATP-binding cassette
ACSF	artificial cerebral spinal fluid
ADP	adenosine diphosphate
AMP	adenosine monophosphate
AP	action potential
AOB	accessory olfactory bulb
ATP	adenosine triphosphate
BBB	blood-brain-barrier
CA	*Cornu Ammonis*
CaMPARI	calcium-modulated photoactivatable ratiometric integrator
CBA	(4-Chloro-2-[[2-(2-chlorophenoxy)acetyl] amino]benzoic acid)
CCD	charge coupled device array detectors
CNS	central nervous system
DBX1	developing brain homeobox 1
DISC	depolarization induced slow current
EAE	experimental autoimmune encephalomyelitis
EC_{50}	half maximal effective concentration
EPSP	excitatory postsynaptic potential
ER	endoplasmic reticulum
FFA	flufenamic acid
FP	fluorescent protein
FRET	Förster resonance energy transfer
GABA	γ-aminobutyric acid
GECI	genetically encoded calcium indicator
GFP	green fluorescent protein
GPCR	G-protein coupled receptor
GrC	granule cell
hERG	human ether-a-go-go related gene
IC_{50}	half maximal inhibitory concentration
I_{CAN}	calcium-activated nonselective cation current
IEG	immediate early gene
IP_3	Inositol trisphosphate
K_{ATP}	ATP-sensitive K^+ channel
Kir6.2	inward-rectifier potassium channel
LTP	long term potentiation
MOG	myelin-oligodendrocyte glycoprotein
mGluR	metabotropic glutamate receptor
MS	Multiple sclerosis
NMDA	N-methyl-D-aspartic acid

NSC$_{Ca}$	non-selective cation current of the Ca^{2+}-activated type
NSAID	non-steroidal anti-inflammatory drug
PIP$_2$	phosphatidylinositol 4,5-bisphosphate
PF	persistent firing
PKC	protein kinase-C
PLC	phospholipase C
preBötC	preBötzinger Complex
preSynTagMA	synaptophysin-CaMPARI2
postSynTagMA	PSD95.FingR-CaMPARI2
PSD	postsynaptic density
rsCaMPARI	reversibly switching CaMPARI
sADP	slow afterdepolarization
SNc	substantia nigra pars compacta
SNr	substantia nigra pars reticulata
SK	small-conductance calcium-activated K$^+$
SUR1	sulfonylurea receptor
SynTagMA	synaptic tag for mapping activity
sypCaMPARI	synaptophysin-CaMPARI1
TM	transmembrane
TMEM16A	Transmembrane member 16A
TRP	transient receptor potential
TRPA	transient receptor potential ankyrin
TRPC	transient receptor potential canonical
TRPM	transient receptor potential melastatin
TRPML	transient receptor potential mucolipin
TRPP	transient receptor potential polycystin
TRPV	transient receptor potential vanilloid
TRN	thalamic reticular nucleus
VGCC	voltage-gated calcium channel
VNO	the vomeronasal
VSN	vomeronasal sensory neuron

Acknowledgements

This thesis would not have been possible without the support of many individuals. First, I want to thank Prof. Dr. Thomas Oertner for giving me the opportunity to work in his lab. Through your technical expertise and passion for science I developed deeply as a scientist. Thank you for supporting my career development by supporting attendance at conferences and summer schools. Attending the Cajal summer school both as a student and later as an assistant instructor gave me the confidence to further pursue a career in science. I would like to thank Dr. Christine Gee, my principal supervisor, for the support and mentorship that you've given me over the years. I appreciate the freedom you gave me but also the guidance you always had ready when I needed help or advice. I will always be grateful for the dedication you made to advocating for my success. Dr. Manuel Friese, thank you for giving me the opportunity to work on the collaborative TRPM4 project. I appreciate your willingness to give me the freedom in selecting the direction of the project. Dr. Alberto Perez-Alvarez, I know that my joining the SynTagMA project was not easy and I thank you for your willingness to teach me and share your expertise with me. I developed as a scientist in working with you. Dr. Simon Wiegert, it has been great getting to know you both scientifically and personally. I appreciate the bits of advice you've shared over the years and your belief in my future success. Dr. Christian Schulze, it's been fun discussing and trying to solve analysis challenges together. I also want to thank Iris Ohmert and Sabine Graf whose remarkable technical support made all of these experiments possible. I also want to thank our collaborators, specifically Dr. Eric Schreiter and Dr. Michael Hoppa. It's been a pleasure working with you.

I want to thank all of the Oertner and Wiegert lab members for their role in creating an environment that made me excited to come to work. Dr. Céline Dürst, I appreciate your friendship and support over the years. You taught me that "there are only so many hours in a day" while also inspiring me by your own remarkable work ethic. Silvia, I'm so happy to have met you and your perpetually sunny attitude,

which always lifted me on a dark day. Dr. Laura Laprell, you may not know this but you, a postdoc, asking me, a PhD student, how to do things in the lab and experimental advice, reminded me and confirmed that indeed I have learned a lot over the years. Thank you for that. Paul, I am so grateful for your friendship. Whether dancing at midnight at a festival or emerging from 6 hours of virus injections, I am always inspired by your passion for life and for science. Thank you for consistently listening to my ideas and complaints and grounding me in reality when I needed it.

Outside of the lab, I want to thank my friend Diana. We have been on this scientific journey together since our masters and we are now about to get our PhDs. Your unwavering support and friendship mean the world to me. Of course, thank you with love to my parents, who sadly will not be able to attend my defense due to COVID restrictions. Thank you for supporting my pursuits even when they have taken me halfway around the world. You raised me to be inquisitive and stubborn, crucial personality traits for success in science.

I cannot individually thank everyone, but I'll try and name you! Thank you to: Maru, Kasia, Iris, Mattia, Johanna, Rudy, Andreas, Margo, Oana, Tim, Bas, Aida, Anne, Daniel, Lars, Sergio, Mauro, Wei, Karen, Ale, Jenn, Noemi, Emily, Nichole, Courtney, Amanda and Jenn. All of you in one way or the other supported me.

On one final self-reflecting note, I would like to acknowledge and recognize that part of my success is bound to the inherent privileges I enjoy as an upper-middle class white woman. This is not to say that my achievements are unearned and of less value because of this truth. I rather wish to acknowledge and speak out loud that those achievements came at a lower personal cost and barrier, with regards to assessments of my intelligence, capabilities and access, than it might have for the many young scientists who are Black, Indigenous and People of Color.

Eidesstattliche Versicherung

Declaration on oath

Hiermit erkläre ich, Brenna C Fearey, an Eides statt, dass ich die vorliegende Dissertationsschrift

selbst verfasst und keine anderen als die angegebenen Quellen und Hilfsmittel benutzt habe.

I hereby declare, on oath, that I, Brenna C Fearey, have written the present dissertation by my

own and have not used other than the acknowledged resources and aids.

Hamburg, den   Unterschrift